

DESIGN OF A MODULAR BATTERY PACK FOR ELECTRIC VEHICLES

by

SHASHANK ARORA

Submitted in accordance with the requirements for the degree of
Doctor of Philosophy



Centre for Sustainable Infrastructure,
Swinburne University of Technology, Hawthorn, Australia

May 2017

This page has been intentionally left blank

Abstract

High manufacturing cost and thermal stability of lithium ion (Li-ion) battery cells are currently the two main deterrents to prolific demand for electric vehicles. A plausible solution is a modular/scalable battery thermal management system (TMS). A modular TMS can ensure thermal reliability for battery packs of different nominal capacities without needing major structural revisions and facilitate their mass-production. However, deep understanding of the relationship of heat generation rates with cell capacity is essential for developing a scalable TMS. To facilitate this, a sophisticated experimental set-up for studying heat generation in *LiFePO₄* (Lithium iron phosphate) pouch cells of different nominal capacities is designed in this work. Subsequently, battery heat generation is investigated at various discharge rates using a custom-designed calorimeter for a range of operating temperatures. It is found that the heat generation rates of the studied Li-ion cells become independent of their nominal capacity and thickness if the operating temperature is regulated at 35 °C.

It is however not practical to undertake such comprehensive investigation each time a battery pack of different nominal capacity is to be made available. Hence, a numerical model that can represent the relationship between heat generation rates of a Li-ion pouch cell and its nominal capacity in simple mathematical terms is desirable. Now, the Newman, Tiedemann and Gu (NTG) model is one of the most widely used models for simulating battery thermal behaviour. It has even been adopted by CD-adapco for their proprietary battery modelling software - Battery Design Studio. The NTG model however revolves around an idealised battery cell and may not be applicable to commercial battery cells. In this work, it is noticed that the NTG model underestimates the irreversible heat generation rates for a Li-ion pouch cell. The discrepancy is caused by interphasial polarisation, which is not considered in the NTG model.

Adjustments necessary for improving the accuracy of the NTG model in simulating thermal behaviour of commercial battery cells are subsequently made. In process, a novel and cost-effective technique for estimating interphasial film resistance is also developed.

Further, multi-physics models describing thermal behaviour of these cells are too complex whereas the NTG and other existing numerical models discount the effect of cell capacity on heat generation. Therefore, this thesis proposes a new computational model based on artificial neural network (ANN) for estimating heat generation rate with cell nominal capacity as one of its key inputs along with ambient temperature, discharge rate and depth of discharge. Experimentally measured battery heat generation rates are utilised for training the ANN. Problem of data scarcity is addressed analytically and virtual samples are produced via enthalpy formulation for battery heat generation. Subsequently, the model is trained using Levenberg–Marquardt algorithm. Results disclose that a three-layered feedforward ANN with one hidden layer having six neurons is optimum for this application.

In addition, parasitic power is also one of the key criteria in the selection of the temperature control strategy used for regulating the performance of EV battery packs. For this reason, proof of concept of a scalable TMS that has negative parasitic power requirements is developed in this work. This novel TMS employs phase change material PCM and cannot only maintain uniform battery pack temperature without using power consuming components such as fan, heat exchanger or a pump but also generate electrical power with the aid of thermoelectric devices. Lastly, the key safety features of existing EV battery packs have been closely studied using more than 70 sources including scientific and technical literature and particularly 43 US patents. Finally, the basic mechanical design requirements for a robust and reliable battery packaging system are revealed.

Acknowledgment

This has been an incredible experience for me and it can be aptly described by an ancient Chinese proverb, which states:

When I hear, I forget

When I see, I remember

When I do, I understand

During my PhD candidature, I have done several things and I have understood that inspiration most often strikes those who are hard at work. At the end of this candidature, I would like to thank all who have been a source of inspiration and support to me during this challenging journey.

I would like to begin by thanking my supervisors – Prof Ajay Kapoor and Associate Prof Weixiang Shen for inspiring me to do meaningful and quality work. I probably cannot thank them enough for letting me do what I wanted and for sharing their expertise along with their wealth of knowledge through countless long and stimulating discussions over the past three years. I am grateful to their constant encouragement, inspiring guidance, constructive criticism, and infectious enthusiasm that has resulted in effective and productive finishing of a task that seemed difficult. More importantly, I am thankful to them for teaching me the essential “art of publishing scientific articles”.

Secondly, I would like to thank my supervisor, Prof Romesh Nagarajah for being an invisible pillar of support and giving me the liberty to pursue my research objectives.

Thirdly, I would like to thank Mr. Tim Olding for giving direction and shape to my thoughts during the early stages of my candidature. I would also like to thank Mr. Jason Miller and Ms.

Louisa De Vries for inspiring me to become a better storyteller and for re-imprinting upon me the importance of project planning and quality control. I am also grateful to Dr Gary White, Research Director, AutoCRC, for sharing his inspiring career story and motivating me to let go of the fear of the unknown. I am also thankful to various experts, namely, Dr Mehran Motamed Ektesabi, Arnaldo Sanchez, Antonio Lione, Andrew Miller, Mark Cleave, Dr Fengxian He, Dr Parisa Amiribavandapour, Dr Khay See, Xuidong Xui who spoke to me at length on various technical subjects during these years.

Thanks are also due to Dr Ambarish Kulkarni, Dr Alireza Tashakori and Dr Himani Mazumdar. They not only left some footprints for me to follow but also offered regular counselling sessions at zero cost. In addition, a big thanks to Dr Vidhula Ahire for inspiring me to persevere and push harder during the last leg of my journey. Her ‘light at the end of the tunnel’ theory has been particularly useful. Not to mention, the tips on thesis formatting.

I take this opportunity to acknowledge the Automotive Co-operative Research Centre (AutoCRC) and Swinburne University of Technology scholarship under the *Automotive Australia 2020* scheme, for providing financial assistance, which supported me to perform my work contentedly and securely. I greatly appreciate the provision of using the EV Lab equipment, which facilitated this research. I would also like to thank Alec Papanicolaou, the engineering guru, for his help in preparing the test apparatus used in this research and for allowing me to pull him out of his workshop anytime of the day on numerous occasions.

I am also thankful to Andrew Zammit and Victoria Jandayan from the IT Servicedesk and the facilities team at Swinburne, respectively, for always being available on call. Thanks to the super-active and enthusiastic team of Excellerate Australia (Jacqueline, Patricia, Loren and others) as well for supporting me in my professional development endeavours and providing the necessary administrative support. I would also acknowledge the timely support of Dr

Sylvia Mackie, who has always been kind and generous with her comments on my writing, and Dr Alec Mackintosh in proofreading selected portions of this thesis.

Of course, no acknowledgments would be complete without giving thanks to my parents. They have always inspired me to pursue excellence and taught that hard work pays. They are great role models of resilience, strength and character. I owe everything whatsoever I possess today to my beloved parents. Last but not the least; I want to thank my younger brother, Sudhanshu, for bearing the load of my decisions, without complain. I could not have accomplished this without his unyielding support.

Names that have not appeared are far more remembered without comparison to those who have been listed.

Dedicated to

My amazing brother, Sudhanshu

And my lovely parents: Satayandra Arora and Shobhana Arora

I am who I am, only because of the sacrifices they made!

Declaration

I declare that the work submitted in thesis is a true representation of my own work. I confirm that the work referred to in the thesis:

- contains no material which has been accepted for the award to the candidate of any other degree or diploma, except where due reference is made in the text of the examinable outcome;
- to the best of my knowledge, it contains no material previously published or written by another person except where due reference is made in the text of the examinable outcome; and
- where the work presented is based on joint research or publications, discloses the relative contributions of the respective workers or authors.

Lastly, I warrant that I have obtained, where necessary, permission from the copyright owners to use any third party copyright material reproduced in the thesis (such as artwork, images, unpublished documents), or to use any of my own published work (such as journal articles) in which the copyright is held by another party (such as publisher, co-author). Copies of the copyright statement(s) are included within the appendices of the thesis.

Shashank Arora

May 2017

List of Journal Publications

1. Arora, S., W. Shen, and A. Kapoor, *Critical analysis of open circuit voltage and its effect on estimation of irreversible heat for Li-ion pouch cells.* **Journal of Power Sources**, 2017;350:117-126.
2. Arora S, Shen W, Kapoor A. *Neural network based computational model for estimation of heat generation in LiFePO₄ pouch cells of different nominal capacities.* **Computers & Chemical Engineering.** 2017;101:81-94.
3. Arora, S., W. Shen, and A. Kapoor, *Review of mechanical design and strategic placement technique of a robust battery pack for electric vehicles.* **Renewable and Sustainable Energy Reviews**, 2016. **60**: p. 1319-1331.

Papers under consideration

4. Arora, S., A. Kapoor, and W. Shen, *Application of robust design methodology to battery packs: Identification of critical technical requirements for modular architecture.*
5. Arora, S., A. Kapoor, and W. Shen, *A novel thermal management system for improving discharge/charge performance of Li-ion battery packs under abuse.*

List of Conference Publications

1. Arora, S., W. Shen, and A. Kapoor, *Designing a Robust Battery Pack for Electric Vehicles Using a Modified Parameter Diagram*. 2015, SAE Technical Paper
2. Kulkarni, A., A. Kapoor, and Arora, S., *Battery Packaging and System Design for an Electric Vehicle*. 2015, SAE Technical Paper.

Paper under consideration

3. Arora, S., A. Kapoor, and W. Shen, *A hybrid thermal management system with negative parasitic losses for Li-ion battery packs*. (Submitted for publication in the proceedings of the **International Mechanical Engineering Congress and Exposition 2017**)

Table of Contents

<i>Abstract</i>	<i>i</i>
<i>Acknowledgment</i>	<i>iii</i>
<i>Declaration</i>	<i>vii</i>
<i>List of Journal Publications</i>	<i>viii</i>
<i>List of Conference Publications</i>	<i>ix</i>
<i>Table of Contents</i>	<i>x</i>
<i>List of Figures</i>	<i>xv</i>
<i>List of Tables</i>	<i>xxi</i>

1 Introduction 1

1.1. Prospective Solution.....	2
<i>1.1.1. Modular Battery Pack</i>	3
1.2. Aims and objectives	5
1.3. Methodology.....	6
1.4. Contributions	8
1.5. Organisation of thesis	9

2 Application of RDM to battery pack design 11

2.1. Introduction	13
2.2. Theory of RDM	14
<i>2.2.1. Awareness of Variation</i>	15
<i>2.2.2. Insensitivity to noise factors</i>	16
2.3. Application of RDM to Battery Pack Design.....	17
<i>2.3.1. Creating P-diagram for EV battery pack</i>	17

2.3.2. <i>Discovering the relationship of control factors with CNs</i>	20
2.4. Procedures	20
2.4.1. <i>Determining CNs through Expert Panel Consultation</i>	20
2.4.2. <i>System Boundaries for EV battery pack</i>	22
2.4.3. <i>Characterisation of the impact of noise factors on EV performance</i>	24
2.4.4. <i>Determination of Technical Characteristics</i>	26
2.4.4.1. Light weight.....	27
2.4.4.2. Compact packaging	29
2.4.4.3. Ease of Manufacture.....	30
2.4.4.4. Ease of Assembly	31
2.4.4.5. Structural Stability.....	33
2.4.4.6. Thermal Stability	38
2.5. Results and Discussion	40
2.5.1. <i>Modified P-diagram for an EV battery pack</i>	40
2.5.2. <i>The House of Quality for EV Battery Pack</i>	42
2.6. Conclusion	45
3 Robust battery packaging design for EVs2F	47
3.1. Introduction	49
3.2. Thermal Runaway	54
3.2.1. <i>Thermal barrier</i>	55
3.2.1.1. At module level	56
3.2.1.2. At cell level.....	57
3.2.1.3. The point of egress	59
3.3. Vibration Isolation.....	62
3.3.1. <i>Battery Pack Structure/Mounting Frame</i>	63
3.3.2. <i>Electrode Terminals</i>	66

3.4.	Crash Worthiness.....	67
3.4.1.	<i>Rear Impact</i>	68
3.4.2.	<i>Side Impact</i>	69
3.4.3.	<i>Front Impact</i>	70
3.5.	Material selection for battery pack	72
3.6.	Battery pack placement	75
3.7.	Model design for a robust battery pack	79
3.8.	Conclusions	81
4	Selection of TMS for Modular Battery Pack.....	83
4.1.	Introduction	85
4.2.	Effect of temperature on Li-ion battery cells	88
4.2.1.	<i>Effect of low temperature</i>	88
4.2.2.	<i>Effect of elevated temperatures</i>	89
4.3.	Thermal Management Techniques	93
4.3.1.	<i>Pre-heating Strategies</i>	93
4.3.2.	<i>Conventional temperature control methods</i>	96
4.3.2.1.	Air-cooling	97
4.3.2.2.	Liquid Cooling.....	100
4.3.2.3.	Phase Change Materials	105
4.3.3.	<i>Emerging Techniques</i>	107
4.3.3.1.	Thermoelectric Coolers	108
4.3.3.2.	Thermo-acoustic refrigeration	110
4.3.3.3.	Magnetic Refrigeration.....	112
4.3.3.4.	Internal Cooling.....	114
4.4.	Selection of TMS for Modular Battery Pack.....	116

4.5. Conclusions	119
5 Estimation of heat generation in Li-ion pouch cells	120
5.1. Introduction	121
5.2. Purpose of present investigation.....	123
5.3. Experimental study.....	124
<i>5.3.1. Test procedure.....</i>	<i>128</i>
<i>5.3.2. Problem Formulation.....</i>	<i>129</i>
5.4. Results and Discussion	131
<i>5.4.1. Effect of Temperature.....</i>	<i>132</i>
<i>5.4.2. Comments on the presence of a ‘second discharge plateau’</i>	<i>138</i>
<i>5.4.3. Effect of Discharge rate</i>	<i>141</i>
5.5. Conclusions	147
6 Effect of interphasial film resistance on heat generation3F	149
6.1. Introduction	151
<i>6.1.1. Need for estimating SEI film resistance</i>	<i>153</i>
6.2. Critical analysis of OCV	154
6.3. Experimental set-up.....	157
6.4. Validation through calorimetric tests	160
<i>6.4.1. Design of Calorimeter.....</i>	<i>160</i>
<i>6.4.2. Experimental procedure.....</i>	<i>162</i>
6.5. Results and Discussion	163
<i>6.5.1. Voltage measurement</i>	<i>163</i>
<i>6.5.2. SEI film resistance estimation</i>	<i>166</i>

6.5.3. <i>Calorimetric measurements</i>	171
6.6. Conclusions	175
7 Novel computational model for estimating heat generation	177
7.1. Introduction	179
7.2. Artificial Neural Network Model Design/Construction	181
7.2.1. <i>Data Collection – Experimental</i>	182
7.2.2. <i>Data Generation</i>	185
7.2.3. <i>Artificial Neural Network Paradigm</i>	188
7.3. Results and Discussion	191
7.4. Conclusions	207
8 A hybrid TMS with negative parasitic losses	209
8.1. Introduction	211
8.2. Experimental Set-up	214
8.2.1. <i>Test Procedure</i>	219
8.3. Results and Discussion	221
8.4. Conclusions	235
9 Conclusions and Future Work	236
9.1. Overview	237
9.2. Key Findings and Contributions of this thesis	237
9.3. Recommendations for Future Research	241
<i>References</i>	243
<i>Appendices</i>	265

List of Figures

1.1: Scalable battery solution developed by (a) Valence Technology Inc. for grid energy storage project, and (b) Karlsruhe Institute of Technology for automotive application.....	4
1.2: Illustration of key steps taken en route to completion of project objectives	8
2.1: Difference between robustness and reliability.....	14
2.2: General layout of a P-diagram	15
2.3: System boundary interface for a battery pack	22
2.4: Comparison of mass distribution for different components of a high-power and a high-energy battery cell	27
2.5: Comparison of overall manufacturing cost distributions (excluding pack integration systems) for high-power and high-energy battery packs	31
2.6: Position of electrical connection elements or contacts according to ISO Publicly Available Specification - ISO/PAS 16898:2012for (a) high energy pouch cell and (b) high power pouch cell.....	32
2.7: Battery Packaging architectures (a) T-shaped architecture used in GM Chevrolet Volt and (b) Floor architecture used in Audi e-tron Sportsback concept	36
2.8: Modified P-diagram for a modular EV battery pack	41
2.9: The House of Quality for an EV battery pack	43
3.1: A robust battery pack with one battery module in each battery pack compartment	56
3.2: A cylindrical battery cell assembly with cell spacers.....	57
3.3: An alternate strategy utilising rigid spacer assembly	58
3.4: A battery pack system designed to exhaust the hot gases and material released during thermal runaway event occurring within a section of the battery pack.....	60

3.5: Perspective view of a framing arrangement employed with a compact battery pack design	64
3.6: Perspective view of battery mounting frame	65
3.7: A battery tray being dynamically relocated as the floor deforms.....	68
3.8: Detailed cross-sectional view of the energy absorbing sill insert	69
3.9: Perspective view of primary components associated with a primary and secondary front impact load paths	71
3.10: Nissan Leaf Battery Pack.....	77
3.11: Placement of lithium ion battery pack in Nissan Leaf.....	78
4.1: Causes and effects of battery cell temperature on safety and performance.....	91
4.2: Illustration of thermal runaway process in Li-ion battery cells.....	92
4.3: Classification of different battery thermal management techniques	97
4.4: Schematic of a traditional heat pipe with tubular structure and closed ends.....	103
4.5: Illustration of a thermo-electric cooling module	108
4.6: Cross-section of thermoacoustic refrigerator illustrating various parts.....	110
4.7: Illustration of an active magnetic regenerator used for room-temperature applications.	113
5.1: Battery cell temperature variation measured for different battery cells using a sandwich-structured calorimeter at 10 °C at 2C discharge rate.....	125
5.2: (a) Modified battery calorimeter (b) Surface temperature variation for batteries of different capacities in modified calorimeter at ambient temperature of 5 °C and discharge rate of 3C	127
5.3: Estimated heat generation rates for 8 Ah, 15 Ah and 20 Ah <i>LiFePO₄</i> pouch cells discharged at 3C at ambient temperatures of (a) 50 °C , (b) 20 °C and (c) 5 °C.....	133

5.4: Heat generation rates measured for 8 Ah, 15 Ah and 20 Ah <i>LiFePO₄</i> pouch cells at ambient temperature of 35 °C and discharge rate of 3C.....	137
5.5: Heat generation rates measured for the 20 Ah LiFePO ₄ pouch cell (a) in an ambient environment of 50 °C for different discharging rates (b) effect of ambient temperature on secondary plateauing at discharge rate of 1C and (c) their comparison with heat	140
5.6: Heat generation rates for three test battery cells during the constant current discharge process at a rate of 1C under ambient temperatures of (a) 20 °C, (b) 35 °C and (c) 50 °C	145
5.7: Heat generation rates for three test battery cells during the constant current discharge process at a rate of 0.33C under ambient temperatures of (a) 20 °C, (b) 35 °C and (c) 50 °C	146
6.1: Voltage response recorded during a galvanostatic intermittent discharge test for LFP pouch cell at 27 °C	158
6.2: 20 Ah LFP pouch cell (a) soaked in a PCM for taking potentiometric measurements under isothermal settings (b) surface temperature variation in the test cell at different discharge rates.....	159
6.3: A custom designed battery calorimeter for measuring total heat generated by a 20 Ah LFP pouch cell during charge and discharge cycles	161
6.4: (a) Terminal voltage versus discharge capacity of 20 Ah LFP pouch cell at different discharge rates (b) OCV versus DOD estimated from V-I characteristics of the test battery cell at constant battery cell temperature of 27 °C.....	164
6.5: Comparison of OCV obtained from Gu's method, OCV at equilibrium state and terminal voltage at 0.33C discharge rate and ambient temperature of 27 °C at different DODs	166

6.6: Voltage drop ($= OCV_{t=3600} - OCV_{t=0}$) observed across the SEI film during a constant current discharge test	168
6.7: Variation of SEI film resistance for a 20 Ah Li-ion pouch cell with DOD (markers showing the calculated data points whereas solid line depicts a cubic curve fit).....	170
6.8: Irreversible polarisation for a 20 Ah LFP pouch cell at 27 °C at constant current discharge rate of 0.33C calculated using different OCVs	171
6.9: Total heat generated during charging and discharging process of a 20 Ah LFP pouch cell at operating temperature of 27 °C for C-rates of (a) 0.33C and (b) 0.5C	173
6.10: Comparison of the polarisation heat modelled for a 20 Ah LFP pouch cell by substituting $OCVt = 0$ and then $OCVt = 3600$ consecutively for U in the NTG model with the experimental irreversible heat generation rates estimated at temperature of 27 °C.....	175
7.1: Schematic of the experimental set-up.....	183
7.2: Comparison of measured heat generation rates with those calculated from Eqn. (7.2) for the three test batteries at 1C discharge rate in ambient temperatures of (a) -10 °C, (b) 20 °C and (c) 50 °C	193
7.3: Terminal voltage of the three test cells recorded at varied discharge rates in ambient temperatures of (a) -10 °C, (b) 5 °C, (c) 20 °C, (d) 35 °C and (e) 50 °C.	196
7.4: Variation of enthalpy of reaction of 8 Ah pouch cell with (a) ambient temperature at discharge rate of 0.33C and (b) discharge rate in ambient temperature of 35 °C under different DODs	198
7.5: Effect of the number of neurons in the hidden layer of the network architecture on its performance during training, validation and testing phase of network design	202
7.6: Architecture of the ANN model used for prediction of heat generation rates for Li-ion battery cells.....	203

7.7: Neural Network Performance (Architecture: 1 Hidden layer with 6 neurons).....	204
7.8: Comparison of experimentally measured heat generation rates for the 15 Ah LFP test battery cell with the predicted values from ANN model in different ambient temperatures and discharge rates of (a) 0.33C, (b) 1C and (c) 3C	207
8.1: Schematic of (a) 80 Ah battery pack with upright cells and (b) Casing showing intercellular spacers and electrode slots for battery pack with inverted battery cells; IR window removed for clarity reasons.....	216
8.2: Optical spectrums for the IR window material for (a) visible region, and (b) IR region	217
8.3: Experimental set-up involving battery pack designed with inverted battery cells and a thermoelectric circuit mounted on its top surface (with an ice tray for creating thermal gradient).....	219
8.4: Surface temperature for the internal and the outer battery cells of the battery pack with upright cells shown as a function of time during the abuse test in an operating temperature of 27 °C.....	222
8.5: Thermal images showing temperature distribution in the PCM during abuse test of the Battery Pack with upright battery cells, in ambient temperature of 27 °C	225
8.6: Visible images showing volume fraction of molten phase of PCM in case of abuse test of (a) upright battery cell and, (b) inverted battery cell at 27 °C	227
8.7: Surface temperature history for the internal and the outer battery cells of the battery pack with inverted cell orientation during its abuse test in ambient temperature of 27 °C	228
8.8: Images showing variations in temperature distribution in PCM matrix of battery pack with inverted cells at different stages of the abuse test in ambient temperature of 27 °C	230

8.9: Thermoelectric voltage induced in the TE circuit due to a thermal gradient of approximately 27 °C created due to the presence of molten PCM and battery cells on one side and an ice tray on another.....	233
8.10: Thermal images showing temperature distribution in PCM during various stages of the abuse test of Pack 3, i.e., battery pack designed with inverted battery cells and a TE circuit attached at top surface	235

List of Tables

2.1: Possible failure modes and mechanisms of battery cell failure.....	19
2.2: Details of the expert panel formed to identify implicit customer requirements for EV battery pack.....	21
2.3: USABC commercialisation and long term performance goals for EV battery packs	26
2.4: Comparison of structural characteristics of different types of battery cells	34
2.5: Comparison of different design characteristics of 19.2 kWh <i>LiFePO₄</i> battery pack using different types of battery cells.....	40
3.1: SAE standards governing mechanical design of automotive battery packs	51
3.2: Design solutions critical for a robust battery packaging design disclosed from the patents	53
3.3: Materials used for Battery pack casing in various commercial cars	73
3.4: Battery Pack and its location in some state-of-the-art commercial cars.....	76
3.5: Comparison of energy/power density of Chevrolet Volt with USABC targets	80
4.1: List of OEMs distinguishing those that prefer to use a thermal management system for their EV battery packs from those, which do not.....	86
4.2: List of key incidents involving battery fires and subsequent product recalls by major OEMs	87
4.3: Qualitative analysis of various battery thermal management methods	117
5.1: Physical dimensions of the three test battery cells and the A123 20 Ah control sample used in this investigation	125
5.2: Summary of estimated heat generation rates for three test battery cells under different operating conditions.....	142
6.1: Fitting parameters for both $OCV_t = 0$ and $OCV_t = 3600$ as a function of DODs.....	165

7.1: Battery pack size of commercially available passenger electric cars along with nominal capacity of Li-ion cells used in their assembly.....	181
7.2: Summary of estimated heat generation rates (in Watts) for all the test battery cells under varied operating conditions.....	184
7.3: The properties and parameters of the employed Levenberg–Marquardt optimization algorithm	191
7.4: Enthalpy variation (in J/mol) for different batteries at different temperatures and discharge rates of (a) 0.33C, (b) 1C and (c) 3C	200
7.5: Input layer and hidden layer weights and biases for the trained neural network	204
8.1: Index of refraction and key mechanical properties of the IR window used in this investigation.....	218
8.2: Thermo-physical properties of PCM (RT28HC) used in the present study	218
8.3: Properties of the commercially available thermoelectric module used in the present investigation.....	232

This page has been intentionally left blank

This page has been intentionally left blank

Chapter 1

Introduction

Predictive analysis of greenhouse gas (GHG) emissions indicates that if current trends in energy use are not transformed, average global temperatures in 2050 will be at least 6 °C higher than the long-term average recorded for 2010 [2]. A six-degree rise in the global average temperature could cause irreversible damage to biodiversity and coastal land, and significant shortages of food and water. Therefore, under the Paris Agreement [3], major governments and policymakers have pledged to make decisive joint efforts to limit the global rise in average temperature to below 2 °C. The International Energy Agency (IEA) estimates that in order to conform to the 2 °C pathway, it is essential that by 2030, at least 20% of all road vehicles should be alternative energy vehicles [4]. Therefore, more than 70% of the original equipment manufacturers (OEMs) are investing in vehicle technologies that will connect to the electricity grid and employ electrical energy as their motive power [5].

Currently, electric vehicles (EVs) account for only 0.1% of the global light-duty vehicle stock [2], and large-scale electrification of the road transportation sector seems challenging. The primary issue is the comparatively high retail cost of EVs, which are currently twice as expensive as their internal combustion engine (ICE) equivalents. An EV battery pack accounts for up to 46% of this cost [6-8]. Hence, possible cost reduction techniques, such as modification of the microstructure of existing electrode materials for lithium-ion (Li-ion) battery cells [9-12] and the development of new battery chemistries [13-18] are being pursued extensively by

Introduction

different research groups. These efforts have been partially successful, as the cost of manufacturing an EV battery pack reduced to around USD 268 per kWh in 2015 from USD 1000 per kWh in 2007 - 08 [2, 19]. However, it is understood that the cost of battery packs must be reduced to below USD 125 per kWh to make EV battery packs cost-competitive and to enable large market penetration of EVs. It is therefore assumed that battery packs will continue to be the controlling factor in the costing of electric drive train architecture for next 5 to 7 years [20, 21]. As time-to-market is becoming increasingly important for the success of any new product, it is vital to investigate other means of facilitating the design and manufacturing of battery packs that can provide immediate economic benefits to EV users.

1.1. Prospective Solution

Over the last few decades and across several sectors, including the automotive sector, modularity has emerged as a means to improve the economics of an industry. A modular design would allow OEMs to scale up a battery pack and meet the energy/power requirements of different EV applications, without necessitating major structural modifications to the basic pack architecture. This would enable mass production of battery cells, which in turn would reduce manufacturing costs for EV battery packs.

In addition, it would enable OEMs to accommodate future uncertainties. For example, if a new battery chemistry with higher energy or power density becomes commercially accessible, modularity-in-design will allow EV battery packs to evolve with the new technology easily and at low cost. Other advantages of employing a modular architecture, such as reduced time-to-market and increased ability to diversify production lines, are also well documented [22-24]. More recently, Rothgang et al. analysed the feasibility of a hybrid - modular battery pack for an EV. They confirmed that it is possible to gain significant weight savings at the cell level by adopting a modular architecture for the battery pack [25]. A modular battery pack can therefore

provide the much-needed traction to EVs by turning them into a compelling alternative to conventional ICE vehicles.

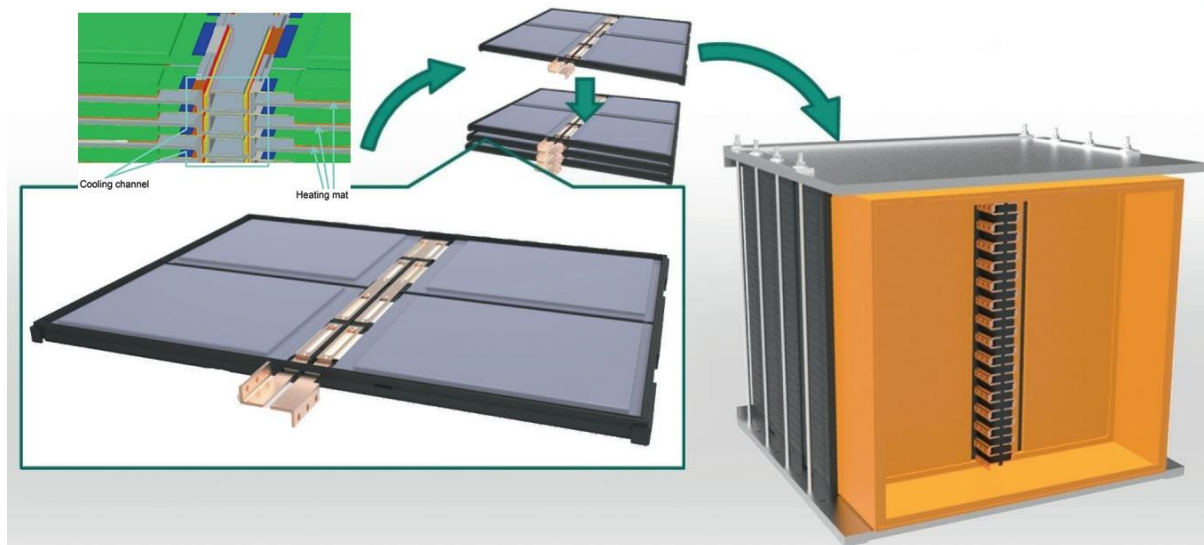
1.1.1. Modular Battery Pack

A modular system can be classified as one of which the fundamental elements are mechanically independent of one another, but work together as a unified “whole” [26]. US patent 5534366, owned by Motorola Inc., first disclosed the conceptual design of a battery pack that could meet this criterion. The patent claims to have modularised the battery pack in such a way that portions of the battery cell cartridge, the circuit cartridge and the housing can be shared and reused. In addition, the battery cell cartridge can be replaced when required, without affecting other components of the system, thus making it a very cost-effective solution for portable electronic devices [27].

Subsequently, Valence Technologies Inc. presented the first scalable Li-ion battery pack for rail application, as shown in **Fig. 1.1(a)**. In series, the Li-ion battery pack is scalable from 12 V to 1000 V and up to several thousands of ampere-hours in parallel. It is equipped with an inter-modular balancing system, but does not include a ventilation/cooling system [28]. At the 2013 IAA International Motor Show in Frankfurt, the Karlsruhe Institute of Technology (KIT) displayed another modular battery concept for electric city buses. In this concept, the size of the battery module can be adapted to different needs by changing the number of cells in each module. In addition, as shown in **Fig. 1.1(b)**, cooling channels are included to regulate the temperature of the electrical contacts in the pack. A distinctive feature of this concept is that instead of using the in-built cooling channels for crash protection, the battery cells themselves function as a crash barrier [29].



(a)



(b)

Figure 1.1: Scalable battery solution developed by (a) Valence Technology Inc. for grid energy storage project [28], and (b) Karlsruhe Institute of Technology for automotive application [29]

Traditionally, single-cell format Li-ion batteries are used for small portable electronic devices. Due to the limited energy content of such cells, it was believed that failure of a single cell, which has been thoroughly investigated and is relatively well understood [30-34], would have little impact beyond its surroundings. However, large or scaled-up Li-ion battery cells are now finding applicability as energy storage systems in vehicle electrification programs and in electric grids. As a result, reports of incidents of single cell failure events cascading to neighbouring cells and damaging entire battery pack are commonplace. A gap lies in our understanding of the behaviour of large Li-ion battery packs under normal and abusive conditions [35, 36].

In order to improve reliability, it is necessary to make Li-ion battery packs insensitive to variations in factors like mechanical vibration and impact and more importantly, ambient temperature. High ambient temperature can cause accelerated cell ageing, whereas low ambient temperatures generally lead to reduced available energy capacity. Further, it has been suggested that the battery cell temperature should be maintained below 50 °C for safety and other reasons [37, 38]. A functional thermal management system (TMS) is essential for Li-ion battery packs. However, TMSs tend to effect the mechanical architecture of the battery packs, which cease to retain their scalability after a TMS is integrated with them. The key is to understand that the notions of mechanical modularity and thermal modularity in EV battery packs are mutually connected.

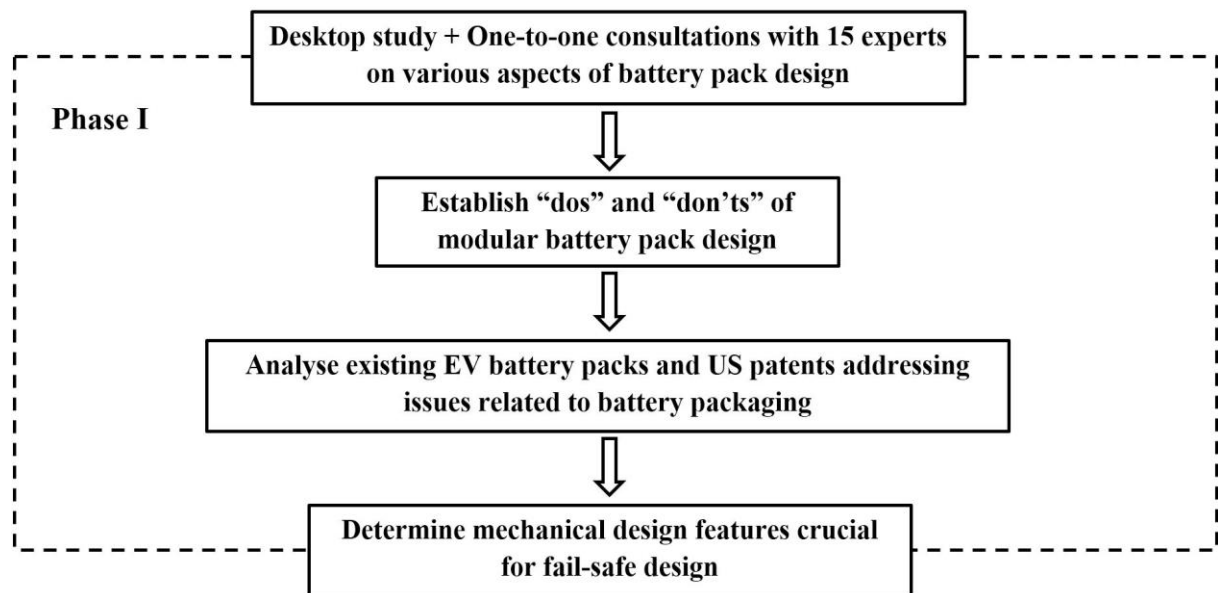
1.2. Aims and objectives

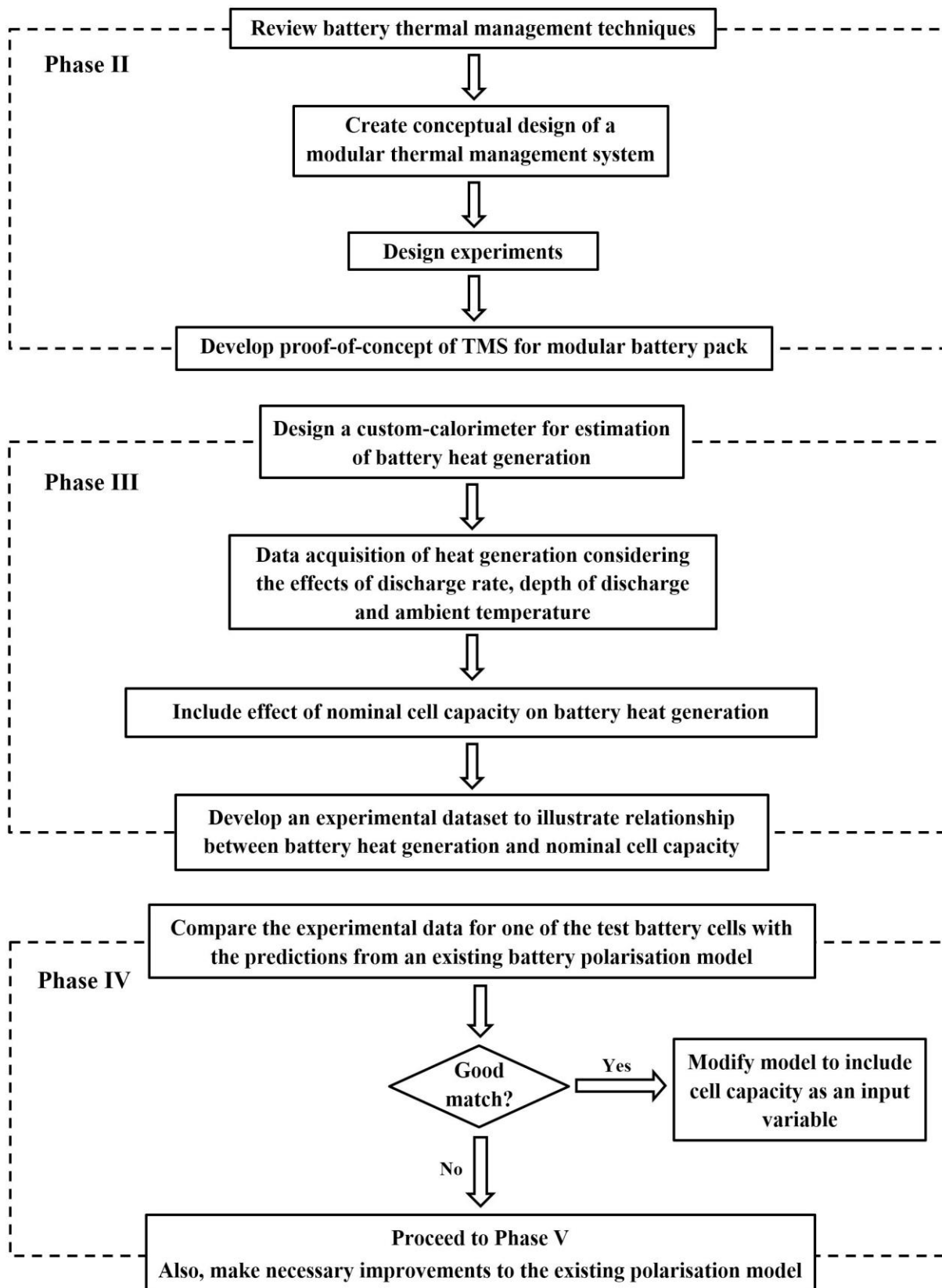
The purpose of this dissertation is to contribute to, develop and deliver tools that can facilitate the design of a modular TMS and thereby a robust battery pack, which is scalable and can meet the energy needs of various applications. The specific objectives of the research described in this thesis can be listed as follows:

- Identify the noise factors and the control factors for an EV battery pack
- Identify the engineering features crucial for reducing the probability of battery pack failure due to exposure to dynamic mechanical and thermal loads
- Investigate the relationship between battery nominal capacity and heat generation, knowledge of which is required for the design of TMSs
- Design a computational model for predicting heat generation in Li-ion battery cells of different nominal capacities; and
- Create a proof-of-concept for a scalable TMS for Li-ion battery packs

1.3. Methodology

A value-based engineering approach is applied to study system interactions with global parameters and to distinguish sources of variability from the control factors. Subsequently, the technical characteristics vital for the design of modular EV battery packs are determined using the House of Quality. Next, an experimental study of the effect of nominal capacity on heat generation is conducted to generate input data for the model development process. Key steps taken to achieve the aims of this dissertation are illustrated in **Fig. 1.2.**





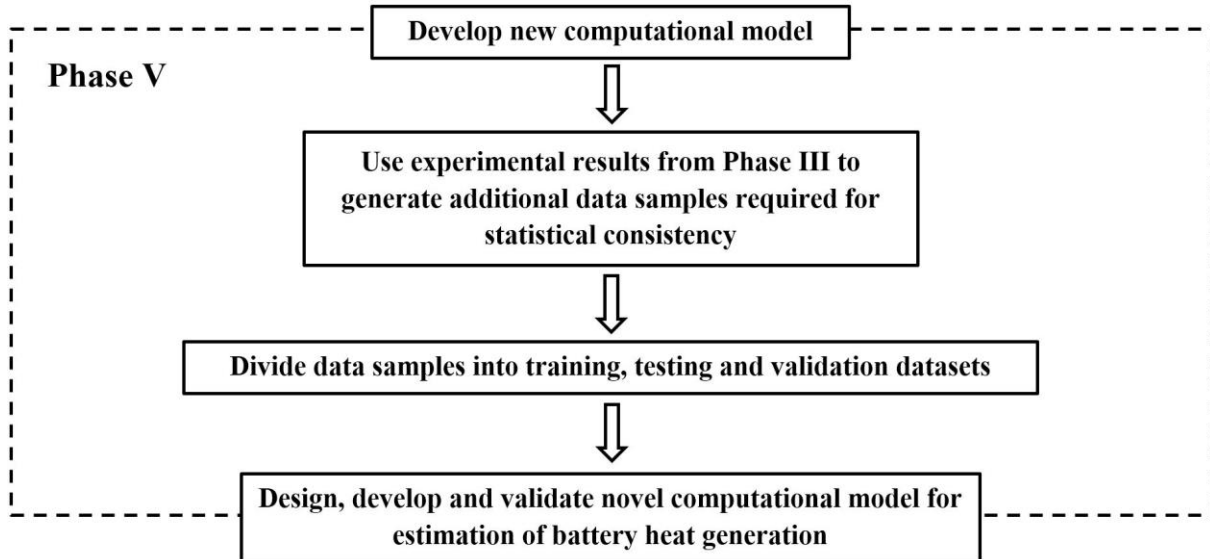


Figure 1.2: Illustration of key steps taken en route to completion of project objectives

1.4. Contributions

The main contribution of this work is the proposal of a novel computational model for the estimation of heat generation rates in Li-ion pouch cells under a range of operating conditions. The model relies on artificial neural network topology and uses cell nominal capacity as one of its key inputs, along with ambient temperature, discharge rate and depth of discharge. The performance of the proposed model is evaluated over a wide cross-section of operating scenarios, including low ambient temperatures and high discharge rates for *LiFePO₄* (Lithium iron phosphate) pouch cells of various nominal capacities. Estimation of heat generation in Li-ion battery cells is crucial for the task of developing TMSs for battery systems with high power requirements. An easy to implement neural network-based model would greatly simplify the procedure and alleviate the necessity of repeating these experiments every time a new application is envisioned for battery packs. Other significant contributions made by this body of work are as follows:

- A framework based on robust design methodology for improving the mass-producibility and reliability of modular EV battery packs has been developed

- Estimation accuracy of one of the widely used battery polarisation models (Newman, Tiedemann and Gu model, also known as the NTG model) has been improved
- A novel, cost-effective and versatile technique for the estimation of solid electrolyte interphase (SEI) film resistance is presented
- The effect of interphasial polarisation on irreversible heat generation rates is quantified
- The effects of battery nominal capacity and cell thickness on battery heat generation rates for Li-ion pouch cells are explained
- A scalable TMS with negative parasitic losses for Li-ion battery packs is presented

The possibility of reducing battery pack weight by improving packaging design and thereby contributing towards the goal of vehicle light weighting will be explored in future work.

1.5. Organisation of thesis

This thesis is concerned with the engineering aspects that can enable the design of a modular battery pack, fit for use in a variety of EV applications. Chapter 1 of the thesis details the motivation for undertaking this work, while Chapter 2 uses a value-based design approach to provide more background information and explain the rationale for the selection of the design aspects addressed in this thesis.

In an EV, thermal runaway, vibration and vehicle impact can all lead to potential failure of Li-ion battery packs. Chapter 3 illustrates through examples that simple mechanical features can be integrated into battery packaging architecture to minimise the possibility of battery pack failure and mitigate the aforementioned safety risks. On the other hand, Chapter 4 discusses various thermal issues affecting Li-ion battery cells. Different thermal management techniques that can be used for improving the thermal stability of Li-ion battery packs are reviewed. This is followed by a qualitative analysis of reviewed techniques for identifying a solution that can meet the design requirements of a modular TMS.

Introduction

The influence of cell nominal capacity on heat generation rates is experimentally investigated in Chapter 5. The results of the investigation are presented in detail in this chapter, providing valuable insights into the relationship between cell nominal capacity and heat generation rates. Chapter 6 scrutinises the effect of open circuit voltage (OCV), a key parameter in the NTG model, on the irreversible heat generation of a commercial cell under a controlled environment by differentiating the OCV recorded immediately after the current stops flowing through the cell and the OCV corresponding to the equilibrium state of the cell. It also presents a cost-effective and versatile method for estimating interphasial resistance.

Chapter 7 proposes a new computational model based on artificial neural networks (ANNs) for the estimation of heat generation rates in LiFePO₄ pouch cells of different nominal capacities. The architecture of the trained ANN for the accurate simulation of the thermal behaviour of LiFePO₄ pouch cells of the nominal capacities from 8 – 20 Ah under various conditions is exemplified. In addition, Chapter 8 presents the design details of a scalable battery TMS with negative parasitic power requirements. The novel TMS proposed in this chapter is a hybrid system employing phase change material and thermoelectric coolers. Therefore, it can not only regulate the battery cell temperature without consuming any power, but also generate electrical energy with the aid of thermoelectric devices.

The main conclusions drawn from the work completed in this research project are reviewed in Chapter 9, and some natural extensions of this work are highlighted.

Chapter 2

Application of RDM to battery pack design¹

¹ A publication was produced based on this chapter. Details are available from - 39. Arora, S., W. Shen, and A. Kapoor, *Designing a Robust Battery Pack for Electric Vehicles Using a Modified Parameter Diagram*. 2015, SAE Technical Paper.

This page has been intentionally left blank

Chapter 2

2.1. Introduction

Customers generally expect an engineering system to deliver the targeted performance each time it is used in the conditions for it was envisioned to operate during the course of its life cycle. However, target performance, which is generally described by design constraints and objectives, may be exposed to a large scatter in various phases of its life cycle. Such scatter not only affects the desired performance level but also adds to the life-cycle costs of the system in the form of inspection, repair and other maintenance costs. Variability is also regarded as the main barrier to mass production [40]. As a result, several authors have maintained that variation over time in the performance metrics of a system creates dissatisfied customers [41-44].

The most critical performance metrics for a Li-ion battery pack are energy density, power density, cost, cycle life, and safety. Deviation of the performance metric from the target value is termed quality loss [45, 46]. Elimination of the factors responsible for this quality loss can often become too difficult, expensive or time-consuming. An alternate solution for minimising this deviation is provided by robust design methodology (RDM). RDM is a systematic and value-based approach to making products insensitive to sources of variability at a low cost. The purpose of this chapter is to propose an RDM framework for an electric vehicle (EV) battery pack. In this framework, a parameter diagram and a House of Quality are developed to identify factors that can be controlled to improve the mass producibility and increase the reliability of EV battery packs. In the process, the chapter discusses several issues, including the selection of cell type and size, packaging solutions, and battery thermal management strategies encompassing the design and assembly of EV battery packs.

2.2. Theory of RDM

RDM is a customer-centric engineering approach, which recommends making a product minimally sensitive to different causes of variability rather than investing in efforts to eliminate them. It involves using a parameter diagram (P-diagram) to identify robustness candidates and facilitate conceptual design generation for a reliable system. Robustness can be defined as the state of insensitivity of an engineering system to factors with negative influences on its performance. It can be measured in terms of the standard deviation of the performance metric around the mean or the target metric value. Reliability, on the other hand, describes the probability of failure of the system to perform the desired operation with minimum loss or damage. This distinction is highlighted in **Fig. 2.1**, where, $E(f)$ is the expected value and $\sigma(f)$ represents the deviation of performance metric around the expected value [41].

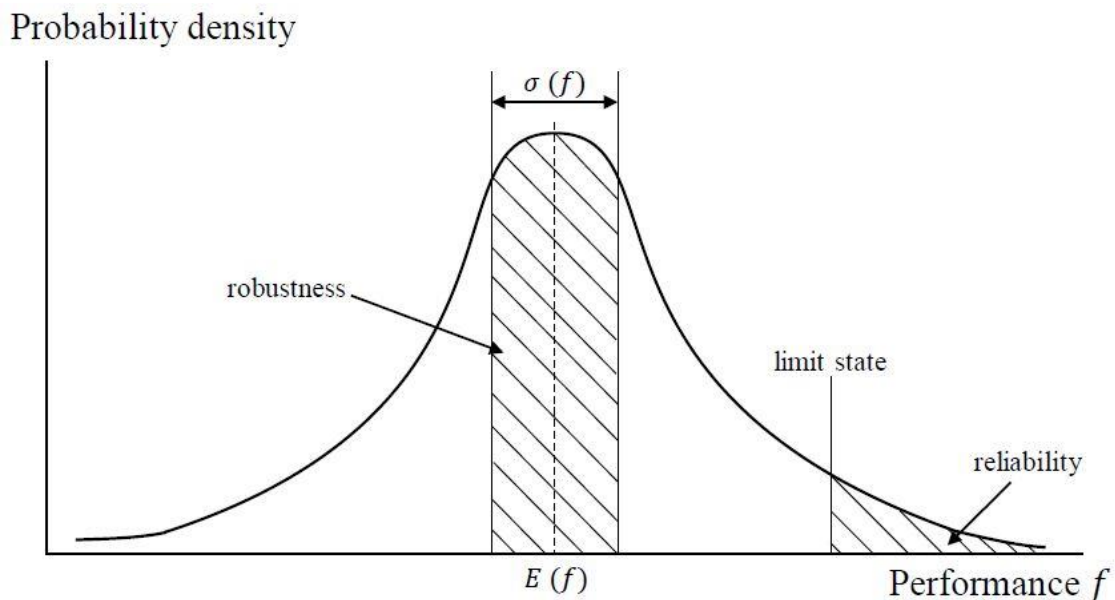


Figure 2.1: Difference between robustness and reliability [41]

According to Arvidsson and Gremyr [47], the actions taken under this approach are focussed either on developing awareness of variation or increasing the insensitivity of the system to noise factors.

2.2.1. Awareness of Variation

It is understood that the smaller the deviation, the better the quality. In accordance with this line of thought, improvement in product quality is nearly always considered as being synonymous with decrease in variation [48]. However, the central problem in design and manufacturing is to extract and gain a better understanding of the information contained in variation. Therefore, in RDM products are often described using a P-diagram, seen in **Fig. 2.2.**

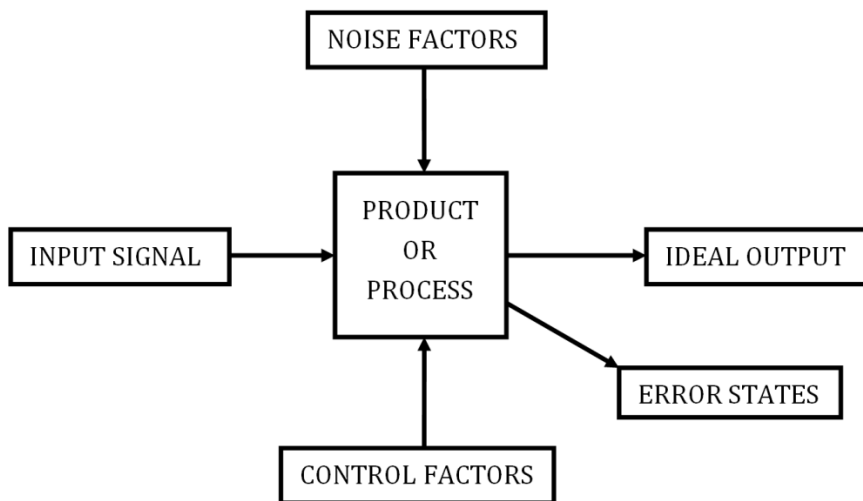


Figure 2.2: General layout of a P-diagram

The P-diagram is a tool, which facilitates the conceptual analysis of a large dataset representing complex interactions of any product or process with global parameters and the generation of reliable design solutions by distinguishing between various factors affecting it. It graphically depicts the input signal, i.e., the energy and other resources invested in the system along with different groups of factors affecting a particular quality trait, ideally expected as an output or a response from the system. Sources of variability that can either not be controlled or are too expensive to control and create disturbance within the system are called noise factors. On the other hand, tunable elements that can be regulated without much impact on technical and financial resource allocation, such as choice of materials, dimensions and the precise weights of different components, are categorised as control factors. In addition, different failure modes

that are a result of a system's interference with existing noises are listed as error states in the P-diagram.

2.2.2. Insensitivity to noise factors

Each of the control factors can have multiple settings, known as levels. Furthermore, the transfer function, which describes the relationship between the ideal output of a system and the factors affecting it, is crucial in the context of the robust design of a system mimicking a relatively well-understood physical phenomenon. Theoretically, it is possible to dampen the effect of noise factors on engineering systems by exploring and modifying the relationship between their response and the control factors [49]. In other words, the control factors are adjusted so that the variability of noise factors has minimum or no effect on the response. Several tools, such as a fault tree analysis, design of experiments, variation mode and effects analysis and quality loss function, are used to accomplish this objective.

The quality function deployment (QFD) technique can also be used for this purpose. QFD is a systematic technique that enables the adaptation of product and technology to end users' needs. It simplifies the conversion of customer needs (CNs) and quality requirements to engineering characteristics or product technical requirements (PTRs). PTRs explain the CNs in the language of engineers and act as a guide on how CNs for the product/system under consideration can be fulfilled. Furthermore, QFD provides an opportunity to include market conditions in the analysis, which makes it an attractive tool for new product design in several industries. It is therefore widely used to identify design targets for the delivery of the expected outcomes considering the technological limitations of the company and the existing market competition [50, 51].

2.3. Application of RDM to Battery Pack Design

RDM is applied to system design in two stages. A P-diagram is created in the first stage to identify the control factors. In the next stage, the interactions of different control factors with ideal system responses are investigated using a technique such as QFD to determine the most appropriate level for each of the control factors. This section discusses these two stages relative to EV battery pack design.

2.3.1. Creating P-diagram for EV battery pack

The key steps taken to create the P-diagram are summarised below:

1. Identification of the system boundaries. It is essential to define system boundaries before starting the procedure of creating a P-diagram. A boundary diagram displays the various component blocks constituting the system. It also allows easy visualisation of the system interface, enabling energy/information exchange with the environment. Hence, it was created based on a careful examination of existing battery packs (Tesla Model S, GM Chevrolet Volt and Nissan Leaf) and the published literature.
2. Definition of the input signal and the ideal response. Since CNs highlight the important product characteristics while informing product designers about ‘what needs to be done’, CNs are listed in the ideal response column of a P-diagram. In EVs, the combination of electrochemical cells or the battery pack receives an input signal from the EV driver in the form of pedal force. The pedal force controls the throttle position, which in turn makes the electrochemical system respond by delivering power, both continuous and peak, as and when required during the drive cycle. It is noteworthy that satisfying only the basic functional requirements, i.e., delivering the power required during the drive cycle and meeting the standard safety requirements, is not sufficient for a modular EV battery pack

Application of RDM to Battery Pack Design

to be considered desirable. An EV user may also have a number of implicit expectations of it. The procedure adopted to identify these requirements is discussed in Section 4.1.

3. Separation of the noise factors from the control factors. The transformation of throttle position to battery output power can be maximized by controlling the interaction of the battery pack with the external environment through various system interfaces. Control over system interactions can be gained by distinguishing parameters that have a direct impact on the system output and adjusting those that lie within its boundary. For example, the effect of temperature on the thermal performance of the battery cells can be reduced by selecting and installing a suitable thermal management system in the battery pack. Battery cell size or layout or packaging clearance can also be modified to make a battery pack more compact, lightweight, and thermally stable, while increasing the ease of manufacture and ease of service at the same time.
4. Establishment of the potential error states. Error states portray the manner in which system failure would be physically noticed in a real-world application. Physical contact between neighbouring cells and the production of smoke or odour during battery operation are examples of potential failure modes for a battery pack in an EV. Other physical indicators defining the state of failure for a battery cell were identified in the literature review and they are listed in Table 2.1. The table also identifies the fundamental physical, chemical, mechanical or electrical stress-inducing mechanisms that may cause an electrochemical cell to fail or battery cell failure.

Observed effect	Potential failure modes	Potential failure causes	Potential failure mechanism	Battery component	Likelihood/Severity		
Reduction of power and capacity	Thickening of solid electrolyte interphase layer	Chemical side reactions between lithium, electrode and solvent	Reduction of chemical reaction and deposition	Active material coating of cathode and anode	High/Low		
	Particle fracture	Intercalation stress	Mechanical stress		Moderate/Low		
	Reduced electrode porosity	Dimensional changes in electrode	Mechanical degradation				
Increased charge transfer resistance	Pitting corrosion of aluminium	Over-charge of battery	Chemical corrosion reaction	Cathode current collector	Low/Moderate		
	Gas generation		Thermally-driven electrode decomposition	Cathode active material	Low/High		
	Decrease in lithium salt concentration	Chemical side reactions between lithium, electrode and solvent	Reduction of chemical reaction and deposition	Electrolyte salt	High/Low		
	Copper plating	Over-discharge of battery	Chemical corrosion reaction and dissolution	Anode current collector	Low/High		
High joule heat generation	Internal short-circuit between anode and cathode	External load on cell	Mechanical stress	Casing	Low/High		
Bloating of the casing							
Drastic voltage reduction	External corrosive path between positive and negative leads	Inadvertent shorting of terminals	Wear out through chemical corrosion reaction				
	Hole in separator	Dendrite formation	Mechanical damage				
		External crushing of cell					
Loss of conductivity between battery and host device	Solder cracking	Circuit disconnect	Thermal, mechanical fatigue and vibrations	Casing	Low/High		
Inability to charge or discharge the battery	Closing of separator pores	High internal cell temperature	Thermally-induced melting of separator	Separator	Low/High		

Table 2.1: Possible failure modes and mechanisms of battery cell failure (based on information available from [52])

2.3.2. Discovering the relationship of control factors with CNs

A QFD analysis is typically conducted through four inter-linked matrices, and each of the four matrices is generated in multiple steps. A detailed description of these steps can be found in [53, 54]. Of the stage, matrix/stage 1 is strategically the most important phase, as it is during this stage that the CNs is translated to PTRs. Therefore, it has been reported that substantial benefits can be achieved by implementing only the first phase of the QFD system [55].

Accordingly, the emphasis of the present study is on the first phase of QFD, commonly known as the House of Quality (HoQ). More specifically, the objectives of the following sections are limited to the identification, understanding and evaluation of the relationship between different CNs and PTRs of an EV battery pack, while the assessment of the correlations among various PTRs will form part of a future study. The strength of these relationships was estimated based on literature surveys, the findings of which were validated using a group decision-making approach. In our case, the success of this approach was ensured by the inter-disciplinary nature of the expert panel guiding the decision-making process.

2.4. Procedures

The methods adopted for acquiring intermediary information required for construction of the P-diagram and the HoQ and the information acquired are presented in this section.

2.4.1. Determining CNs through Expert Panel Consultation

There are several ways to determine what a customer wants as an output of the system, including minimax deviation [56], the minimum mean-square error method [57] and the Delphi method [58]. The Delphi method, which is a structured communication technique for discovering expert opinions and consensus building on a subject, was adopted in the present study because of its simplicity and ease of implementation.

Member ID	Professional Role	Organisation	Reasons for Selection
Member 1	Professor	SUT, Australia	Leading EV R&D program in Australia for the past 10 years
Member 2	Associate Professor	SUT, Australia	Battery pack modelling and design expert
Member 3	Chief Engineer	GM Holden	Led the vehicle electrification program (Commodore) at GM Holden. Worked as a consultant with several other EV enterprises.
Member 4	Specialist Engineer	GM Holden	Was responsible for maintenance and safety of high voltage DC for the GM Volt program and setting up EV training at their Port Melbourne facility
Member 5	Research Director	AutoCRC Ltd.	Mobilising R&D activities for EV development in Australia and the Asia-Pacific region under the Automotive Australia 2020 vision
Member 6	Senior Lecturer	SUT, Australia	Technical leader - Electric bus (eBus) development project for Malaysia
Member 7	Research Engineer	SUT, Australia	PhD in EV motor drives. Headed the control systems development process for the eBus project at SUT
Member 8	Research Engineer	SUT, Australia	Durability engineer with 8+ years of experience in automotive sector
Member 9	Research Engineer	SUT, Australia	PhD in development of lightweight retro-fitted EVs
Member 10	Senior Lecturer	SUT, Australia	Product Design Engineer with over 13 years of professional experience. PhD in lightweight EV drivetrain development
Member 11	Research Scholar	SUT, Australia	Expertise in balancing of battery packs designed for EV applications
Member 12	Post-doctoral Researcher	UOW, Australia	Expertise in developing robust battery management control systems
Member 13	Post-doctoral Researcher	UOW, Australia	Expertise in developing high energy density Li-ion and Na battery cells
Member 14	Manufacturing Engineer	GM Holden	Experience of over 25 years in setting up manufacturing and assembly lines for large automotive project
Member 15	Research Manager	Futuris Automotive	Industry project champion with over 25 years of experience in manufacturing sector. Managed applied technology project worth more than \$20million. Filed two international patents application.

Table 2.2: Details of the expert panel formed to identify implicit customer requirements for EV battery pack where, SUT refers to Swinburne University of Technology; UOW is University of Wollongong and GM stands for General Motors

Application of RDM to Battery Pack Design

As a part of this method, an expert panel comprising fifteen leading professionals from the automotive sector was created. Details of the panel are presented in **Table 2.2**. It can be seen from this table that collectively, the panel had vast experience in the areas of battery pack design, manufacturing, vehicle light-weighting, structural analysis, and project management and quality improvement. Confidential one-to-one discussions were conducted with these experts. The main theme of the discussion was the expected features and quality requirements of the battery pack for their targeted application. Their opinions on EV battery pack performance barriers and preferred strategies for designing a robust battery pack were also recorded. A comprehensive list of implicit customer requirements for EV battery pack was developed based on the experts' opinions.

2.4.2. System Boundaries for EV battery pack

In the case of an EV battery pack, which is essentially a parallel and series combination of multiple electrochemical cells, interactions with the external environment can happen through several interfaces identified in **Fig. 2.3**.

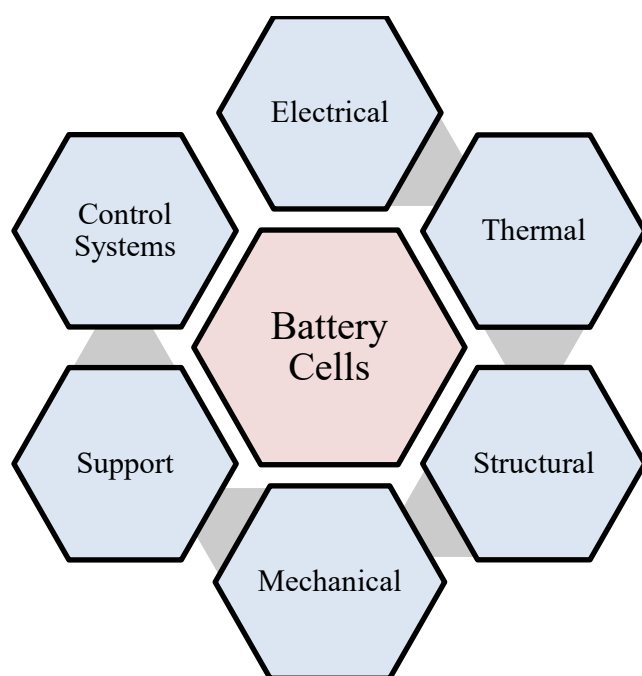


Figure 2.3: System boundary interface for a battery pack

The figure shows a chemical system in the form of a combination of battery cells trading energy with its environment via various interfaces. A brief description of each of these interfaces is provided below.

- A. Mechanical.** This interface represents all the mechanical design features, including cell spacers, damping pads, pressure relief or exhaust valves and seals/gaskets that have been integrated in the battery pack, mainly for safety reasons.
- B. Structural.** A battery pack needs to be contained in a case with a cover to protect it from the effects of humidity, dirt and other environmental factors. In addition, vibration isolation and high crash-worthiness are necessary. Consequently, structural features such as end-plates, tie-rods and cross-members are provided to function as protective members in the battery pack.
- C. Thermal.** The control of the Li-ion battery cell temperature between 25 °C and 30 °C and a uniform thermal distribution across the Li-ion battery pack are required to maximise the energy capacity. To ensure this, a thermal management system including a fluid transfer duct, cooling/heating fluid, insulation coating and auxiliary systems such as fans, pumps, heat exchangers is usually integrated with the battery pack.
- D. Electrical.** A battery pack generates current at a certain voltage to meet the power requirements of an EV drive-cycle. This power is transferred through an electrical circuit comprising bus bar and cables, fuse, circuit breakers, contactors and relays to the EV driveline.
- E. Control Systems.** In battery management systems, sensors for measuring voltage, current, pressure, temperature and humidity are employed to monitor and regulate the state of the battery pack.
- F. Support.** An EV battery pack is generally assembled in the vehicle through mounting brackets and axles, which assist in achieving the required degree of vibration isolation for

reliable operation. Support from the chassis and vehicle body increases the overall crash-worthiness. Similarly, the vehicle floor panel and seats provide isolation of the high voltage components from the passenger cabin.

2.4.3. Characterisation of the impact of noise factors on EV performance

In this study, the noise factors and control factors were mainly identified based on a detailed review of the published literature. Subsequently, the findings were discussed with the expert panel. Final categorization was based on the consensus developed among the panel members.

A. Customer Usage. The driving range of an EV depends on the speed and acceleration characteristics of each trip. Trips with faster acceleration or including ascents over high altitude grades demand more kilowatts per kilometre travelled. Moreover, studies of the driving patterns of EVs indicate that, unlike conventional ICE vehicles, EVs are rarely driven under high-speed motorway conditions and more in rural and urban environments. Consequently, battery packs of EVs that are driven mainly on rural or urban terrain are exposed to a more strenuous life in comparison to those driven over more traditional compositions of road surfaces [59].

B. Vibrations. Driving induces vibration profiles concentrated in the 1 Hz – 25 Hz frequency range with as much as 10% higher energy levels. Pouch cells, which are more common in EV applications, are more prone to localization of vibrational forces. This can in turn cause sharp increases in local stress levels in battery packs, resulting in mechanical and electromechanical failure [60].

C. Ambient Temperature. Another factor that can have a significant effect on the available energy and cycle life of Li-ion batteries is the battery cell temperature. It has been found that with each degree increase in battery cell temperature in the operating range of 30 °C and 40 °C, the cycle life of batteries is reduced by approximately two months [61].

Moreover, an estimate by General Motors indicates that an EV can lose up to 85% of its range at sub-zero temperature if no thermal management system is used[62]. In addition, the rate of self-discharge is also dependent on the storage temperature. The energy capacity of a battery also degrades in response to the ambient temperature and other factors throughout its cycle life [63].

D. Cell-to-Cell Variations. Accidental and practically unavoidable physical and chemical variations among battery cells have a far-reaching effect on the structural dynamics of the battery pack. These random variations lead to the confinement of vibrational energy to a small portion of the cell structure. It is therefore vital to minimise any random cell-to-cell variations in order to define battery performance reliably, as each battery cell will react in a peculiar manner to stimuli received from other sources of disturbance, such as customer usage or the external environment.

E. Auxiliary Load. System interactions, such as heat leakage from different electro-mechanical systems, chassis vibrations, electrical interference, and auxiliary loads like cabin heating/cooling, power steering and air compressors affect the quality of output from battery packs. For example, researchers from the National Renewable Energy Laboratory (NREL) have confirmed that, depending on the ambient environment, the power requirements for managing cabin thermal loads can decrease the driving range of a plug-in EV by 35% to 50% [64].

It should be recalled that the production costs for eliminating these sources of variation in battery cells could be very large. It must therefore be the first priority of any battery pack designer to make the pack insensitive to such variations. Furthermore, changes over time may not be noticeable over a short time-span but it is critical to reduce their influence on battery cycle life for the battery pack to remain on-board diagnostic-compliant.

2.4.4. Determination of Technical Characteristics

PTRs are generally used to assess a product's ability to meet the CNs and must therefore be specified in measurable terms. In addition, they should not be design-specific and have general significance. Benchmarks for evaluating EV battery pack performance have been established by the United States Advanced Battery Consortium (USABC). They are presented in **Table 2.3.**

Parameter (units) of fully burdened system	Minimum goals for commercialisation	USABC long-term goals
Specific energy – C/3 discharge rate, Wh/kg	150	200
Specific power – Discharge, 80% DOD/30s, W/kg	300	400
Specific power – Regen, 20% DOD/10s, W/kg	150	200
Energy density – C/3 discharge, Wh/L	230	300
Power density, W/L	460	600
Specific power to specific energy ratio	2:1	2:1
Normal recharge time, hours	6	4
Life, years	10	10
Cycle life – 80% DOD, cycles	1000	1000
Power & capacity degradation, % of rated spec	20	10
Selling price – 25,000 units @ 40 kWh, \$/kWh	< 150	100

Table 2.3: USABC commercialisation and long term performance goals for EV battery packs [65]

Consultations with various experts contacted during the course of this investigation revealed that, in addition to responding to pedal force, which controls the throttle position, in delivering power to an EV the battery pack must also be:

- Lightweight
- Compactly packaged
- Ergonomic
- Structurally rigid
- Swappable
- Configurable and scalable
- Thermally stable
- Impact-resistant
- Fire-proof
- Easy to manufacture
- Easy to service
- Low-cost

The following sub-sections seek to relate these features to different technical characteristics and other factors that may influence the performance of a modular EV battery pack.

2.4.4.1. Light weight

The total weight of EV battery packs can be reduced by replacing their primary component, i.e., the battery cells, with cells made of novel materials that possess greater gravimetric capacity (mAh/g) or demonstrate a higher operating voltage than traditional active materials [66, 67]. However, an increase in the gravimetric density of electrode materials cannot be scaled linearly to reflect the nominal capacity of commercial battery cells due to the non-negligible weight of inactive cell components. It has been reported that the active material contained in commercial Li-ion battery cells accounts for only 55% of their total weight [68]. In contrast, a thin copper foil, added in the cell assembly to function as a current collector at the anode, can make up to 10% of the total cell weight [69]. **Fig. 2.4** shows a comparison of mass distribution for different components of a high-power and high-energy battery cell.

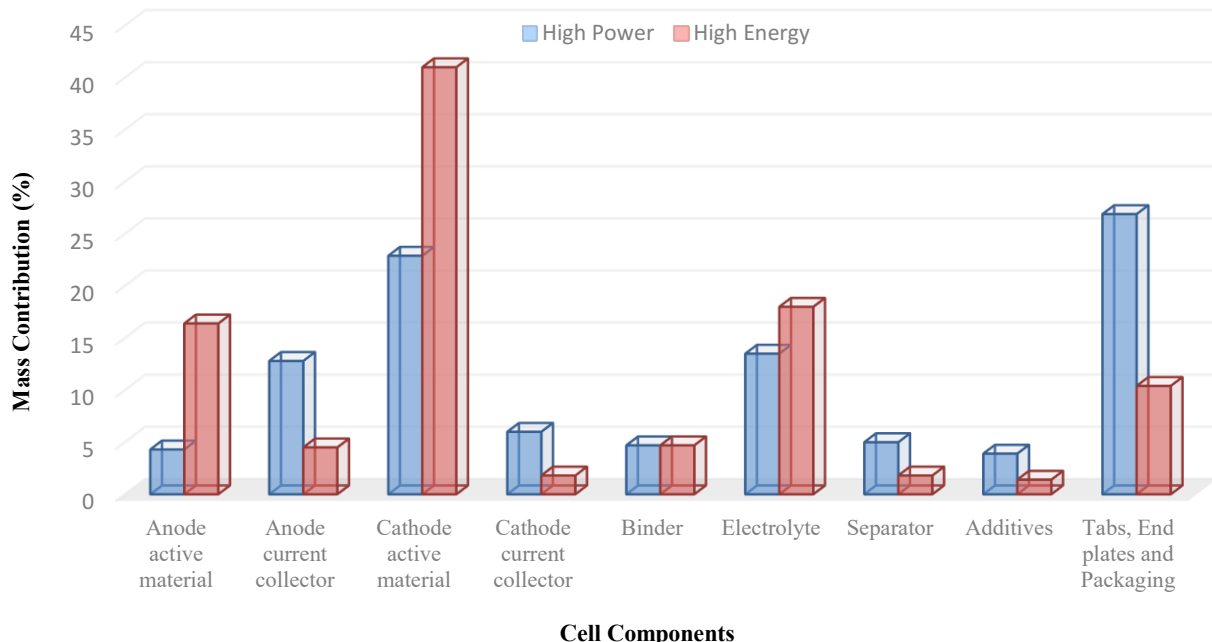


Figure 2.4: Comparison of mass distribution for different components of a high-power and a high-energy battery cell (based on data available from [1])

Application of RDM to Battery Pack Design

Significant improvements in the gravimetric density of Li-ion cells can therefore be achieved by introducing lightweight replacements for inactive electrode components, such as binders, separators, current collectors and cell housings.

Reports show that areal capacities for anode materials that have high gravimetric capacities, e.g. double-walled Si-nanotube, are approximately seventeen times less than the areal capacity of a graphite anode (4.1 mAh/cm^2 [70]). This is equivalent to a material loading of 0.1 mg/cm^2 . Low areal capacity results in the addition of redundant weight in the form of current collectors, separators, interconnectors etc. to the construction of full cell. Non-uniform current distribution and localised active material utilisation are two of the issues affecting the performance of physically large battery cells. An inhomogeneous temperature gradient across the battery cell due to excessive localised material utilisation during high power abstraction can result in permanent damage to the battery cell and even push it into a state of thermal runaway [71]. The selection of battery cells with high areal capacities is therefore crucial, not only for developing a lightweight battery pack but also for safety reasons.

The 24.2 kWh battery pack of the VW e-Golf 2015 was designed using Li-ion pouch cells with nominal capacities of 25 Ah. Subsequently, the manufacturers chose to adopt 35 Ah pouch cells for the pack design and achieved an overall energy storage capacity of 35.8 kWh for the VW e-Golf 2017 without affecting the number of battery cells in the original pack. Similarly, the BMW i3 team is slowly phasing out 60 Ah pouch cells to make way for 94 Ah pouch cells in their battery packs, as the larger cells provide 50% higher energy storage capacity within the same architectural space. The primary reason for the changes in battery cell selection is that as the cell size, i.e., nominal capacity, increases, the number of battery cells required for the design of a battery pack of specified capacity reduces. In addition, the number of cell-interconnections and the quantity of cell protection circuits and wiring required for pack integration is

proportionally decreased, leading to increased weight and volumetric efficiency. Other advantages of the use of larger cell size include lower assembly cost and ease of troubleshooting [72].

2.4.4.2. Compact packaging

Research has shown that small cylindrical cells can conform more easily to the available space and thus have a higher packing density than both the pouch and the prismatic cell types. In fact, packing densities for battery packs comprising of *18650*-type² battery cells, *26650*-type battery cells and large prismatic cells have been reported as $47524.75 \text{ cells}/\text{m}^3$, $22857.14 \text{ cells}/\text{m}^3$ and $416.6667 \text{ cells}/\text{m}^3$, respectively. It has been further reported that while the packing density of the battery pack with *18650* type cells is 114 times more than that of the pack comprising large prismatic cells, the physical density of the former is only 1.5 times greater than that of the latter. Moreover, the packing density of a pouch cell is approximately 2 times less than that of a prismatic cell of similar nominal capacity, mainly because of its smaller thickness and large surface area [73]. It is therefore relatively easier to improve the volumetric efficiency of the battery pack by packaging large quantities of smaller cylindrical cells in the available space than to use large prismatic or pouch cells.

The compactness of packaging design can also have an appreciable influence on the thermal performance of a battery pack. Research shows that increasing the cell-to-cell spacing for a battery pack from 1 mm to 10 mm can lead to a loss of approximately 1°C in the steady-state cell core temperature, for all the three physical formats [74]. According to the NASA Battery Safety Requirements document: JSC 20793 Rev C [75], cell spacing is more critical for pack

² Battery Cell Nomenclature –

Cylindrical: Cell diameter in mm (first two digits) x Height of the cell in tenths of mm (last three digits)

Prismatic: Cell Thickness (first two digits) x Width (next two digits) x Cell Height (last three digits); all in mm

designs employing battery cells of gravimetric energy density greater than 80 Wh/kg. It has further been ascertained that, to alleviate cell-to-cell heat propagation in the instance of a single cell failure or a thermal runaway event, a minimum spacing of 2 mm is required for cylindrical cell formats. In addition, a physical barrier between neighbouring cells is required for the same reasons in battery packs that employ cell formats with side vents [76, 77].

2.4.4.3. Ease of Manufacture

Ease of manufacture depends on the manufacture of battery cells rather than the pack itself. It requires the use of innovative and simple techniques for processing cheap aqueous electrode formulations. One of the suggested techniques involves reducing copper loss and the amount of other inactive components used per unit cell volume by fabricating ultra-thick electrodes with high active material loading. However, high mass loading can often lead to reduced charge transfer rates and increased internal stresses in the electrode layers. In addition, inhomogeneous electrolyte penetration and poor adhesion between dry films of an ultra-thick electrode and current collectors can result in sluggish transport kinetics [78]. Furthermore, 3-D microstructured electrodes are sometimes utilised to achieve higher power density and energy capacity because they demonstrate shorter diffusion lengths and reduced ohmic resistance. However, the fabrication of 3-D microstructures, in addition to being expensive, also involves many complex processing steps, whereas simple manufacturing methods with a minimum number of fabrication steps are generally preferred for commercialisation [79].

The influence of manufacturing scale on cell production costs becomes significant if battery cell design is altered without increasing the annual production quantity. The contribution of material costs to total manufacturing costs increases as manufacturing scale is increased, leading to a substantial decrease in labour and capital costs per unit battery pack, particularly at low production rates. As a result, larger cost benefits can be attained by increasing the

manufacturing scale of battery packs for hybrid vehicles than pure EVs, since the material costs constitute a smaller fraction of the total battery cost for the former, as shown in Fig. 2.5.

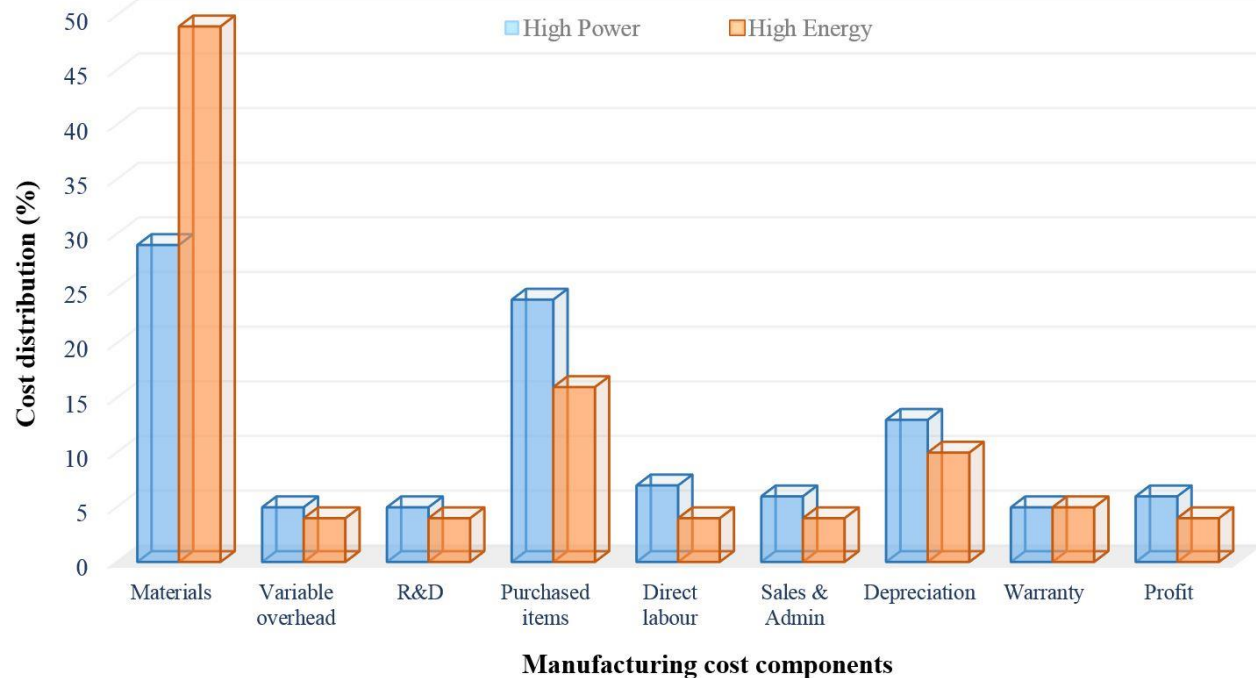


Figure 2.5: Comparison of overall manufacturing cost distributions (excluding pack integration systems) for high-power and high-energy battery packs (based on data available from [1])

2.4.4.4. Ease of Assembly

In accordance with the ISO Publicly Available Specification - *ISO/PAS 16898:2012 Electrically Propelled road vehicles — Dimensions and designation of secondary lithium-ion cells* [80], both the electrical connection elements (contacts) are located on the top side of the Li-ion pouch cells designed for high energy applications. On the other hand, for high-power pouch cells, one of the contacts is located at the top while the other contact is placed on the opposite side of the cells, as indicated in Fig. 2.6. Extra clamping tools are therefore required for the assembly of the interconnections between high-power pouch cells.

This issue also affects cylindrical battery cells, because they also have electrical contacts on both ends. This also renders the external structure design more complex, while increasing the

Application of RDM to Battery Pack Design

wiring complexity and the assembly cost. In addition, punched holes on bare metal terminals of pouch cells are needed to connect them to the copper bus bar using nuts and screws.

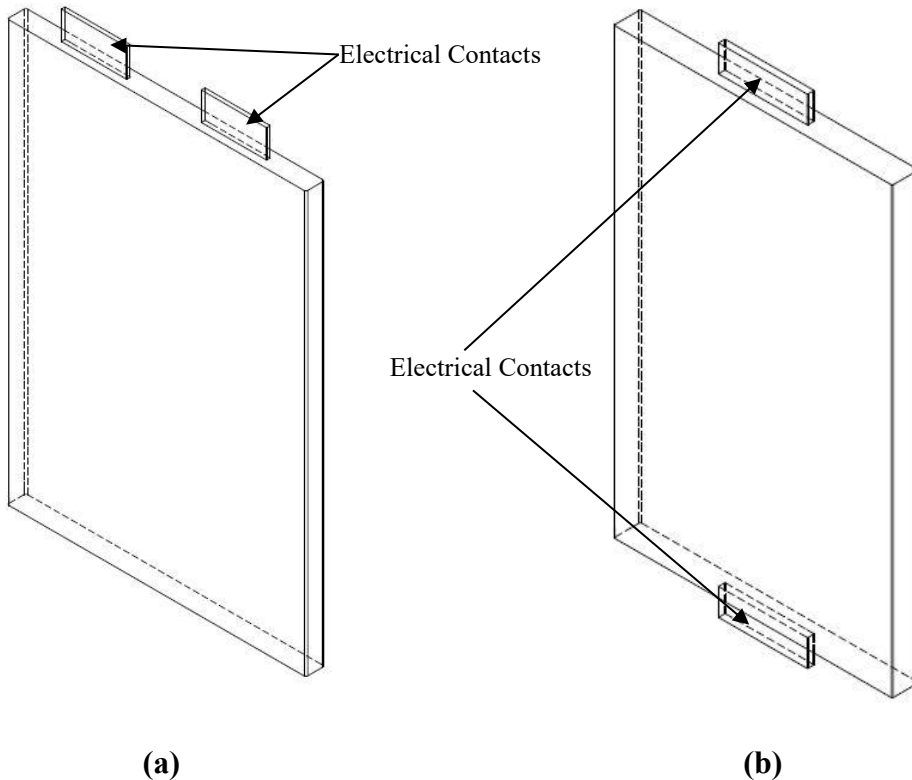


Figure 2.6: Position of electrical connection elements or contacts according to ISO Publicly Available Specification - ISO/PAS 16898:2012 for (a) high energy pouch cell and (b) high power pouch cell [80]

Comparatively, the assembly process of prismatic cells is greatly simplified by the “Poka-yoke” feature included in the design of their male thread terminals. Consequently, only spring washers and nuts are needed to interconnect their terminals. Moreover, the soft packaging of the pouch cells makes it necessary to employ special precautions and handling procedures to minimise rough handling during the assembly of battery cells, as it may lead to local stress development in the cell structure. Delamination of the composite electrode layers is also possible under situations of extreme shock or through the continuous transmission of vibrations during operation. Hence, additional structural members are required in packaging for pouch cells to exert compressive force, to provide vibration isolation and to make them shock-resistant, which in turn incur extra assembly costs. As a result, the cost of assembly of one unit

of pouch cell using mechanical fasteners in the year 2016 was reported to be USD 0.125, as opposed to USD 0.0692 for prismatic cells.

EV battery packs are generally assembled manually, with the assembly cost being proportional to the number of battery cells, cell holders and interconnections and the type of BMS and TMS used. Accordingly, the cost of assembly for one unit of battery pack with *18650*-type battery cells (excluding BMS) has been calculated as USD 424.32 (assuming approximately 85 man-hours at USD 5 per hour). In contrast, estimates indicate that it would cost only USD 3.46 with a process lasting less than 1 hour to assemble a battery pack of equivalent capacity using large prismatic cells excluding BMS. As a result, more economical battery packs can be manufactured, as the assembly process is significantly simplified and the total production time is considerably reduced by using large-format battery cells [73].

2.4.4.5. Structural Stability

In the absence of the adequate compressive force needed to maintain a uniform contact, delamination of electrode layers occurs in pouch cells and prismatic cells, which affects their performance and reliability. Delamination of the electrode layers can be avoided with external structures that may include either hard plates stacked on each side of the battery cell or clamps made of thread rods. Although the stacking plate method has significant advantages during the manual assembly of battery packs, it is more expensive on a mass production basis. In addition, holding clamps may make the pouch cells more vulnerable to mishandling during assembly and to localised stress development due to unbalanced clamping force [73].

The solid structure created by the metallic or rigid plastic casings typically used for prismatic and cylindrical battery cells prevents foreign objects such as nails from penetrating the electrochemical system.

Criteria	Small Cylindrical	Large Cylindrical	Prismatic	Pouch
Casing	Metal	Metal	Semi-hard plastic or metal	Aluminium soft bag
Connections	Welded nickel or copper strips or plates	Threaded stud for bolt or threaded hole for bolt	Threaded hole for bolt	Tabs that are clamped, welded or soldered
Retention against expansion	Inherent from cylindrical shape	Inherent from cylindrical shape	Requires retaining plates at ends of battery	Requires retaining plates at ends of battery
Appropriateness for production runs	Good: welded connections are reliable	Good	Excellent	Excellent
Field replacement	Not possible	Possible	Possible	Not possible
Delamination	Not possible	Not possible	Possible	Highly possible
Compressive force holding	Excellent	Excellent	Poor	Extremely Poor
Local stress	No	No	No	Yes
Safety	Good, integrated with PTC	Good, integrated with PTC	Good, integrated with PTC	Poor, no safety features included
Heat shrink wrapping	Yes	Yes	Depends on casing material	No

Table 2.4: Comparison of structural characteristics of different types of battery cells [81]

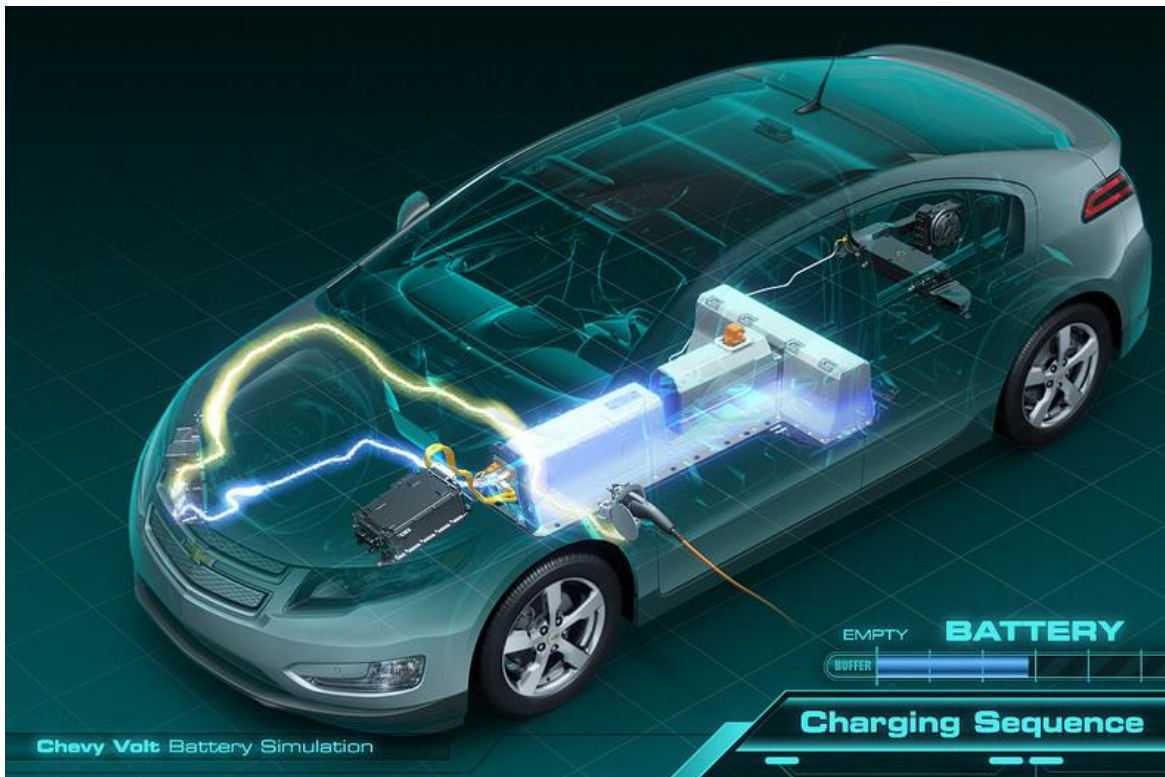
Metallic casings provide a greater degree of tolerance to pressures generated inside the battery cell because of gas generation and venting; a safety feature missing from the pouch cells owing to their soft packaging.

The main structural issue with the prismatic cells is that their corners can be left vacant due to elliptical windings. This result in uneven pressure distribution in electrodes, but the problem can be alleviated by filling vacant corners with solid material. **Table 2.4** compares different battery cell formats according to the structural characteristics considered important from a safety perspective.

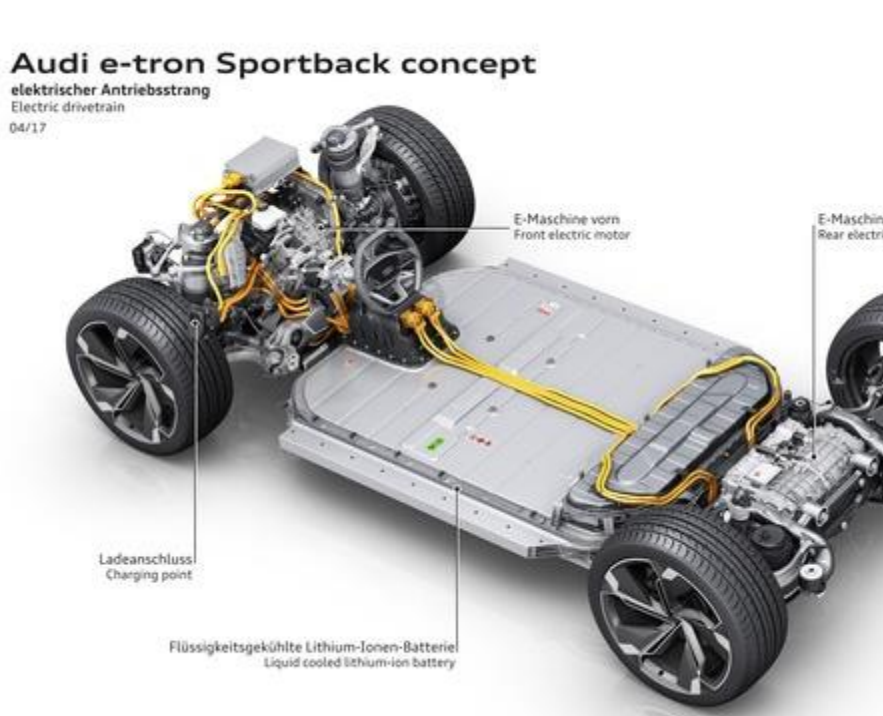
Maintaining the structural integrity of the battery pack during crash conditions is another challenge for EV designers. For this purpose, two packaging architectures, the “T- shaped” architecture and the “Floor” configuration, are primarily utilised for EV battery packs.

The T-shaped architecture seen in **Fig. 2.7(a)** is used in the GM Chevrolet Volt. It enables the battery modules to be arranged inside the primary safe zone of the vehicle, i.e., the area beneath the rear passenger seats and extending along the tunnel between the two rows of seats. It prevents the battery pack from direct frontal impact and side impact loads through the use of the vehicle structure as a crash barrier at the expense of interior cabin space and sometimes passenger comfort.

In contrast, the Floor configuration, used in the Tesla Model S and the Audi e-tron Sportback concept shown in **Fig. 2.7(b)**, involves arranging the battery cells in a slab format under the vehicle floor. This maximises the available cabin space to be used either by the vehicle occupants themselves or for storing their luggage. In addition, this configuration increases the vehicle’s stability during various driving manoeuvres by lowering its centre of gravity. However, it also reduces the ground clearance of the vehicle, thus exposing the battery pack to the dangers of ground or bottom impact.



(a)



(b)

Figure 2.7: Battery Packaging architectures (a) T-shaped architecture used in GM Chevrolet Volt [82] and (b) Floor architecture used in Audi e-tron Sportsback concept [83]

Battery cells are traditionally protected against bottom impact by metal or plastic shell casing enclosures in conjunction with module and battery pack housings and the vehicle body structure, including transverse cross-members, doors and the floor. Furthermore, as the floor panel can only resist impacts of small stones on a gravel road, an armour made of 1mm to 6 mm thick metallic sheet, with a monolithic or a sandwich structure or even their combination is used as a protection against bottom impact. Polymeric coating is applied to it for rust protection. Research has shown that the severity of damage to the protective armour plate is affected by the tip radius of the impacting body, the distance of the indentation point to the nearest boundary of the battery module, and the exponent of the power law-hardening curve. It has further been reported that other thinner protective members of the battery pack rupture soon after the armour is breached, exposing the battery cells to damage from road debris and other sharp objects [84].

To restrict this damage to a minimum, a multifunctional granular battery assembly (GBA) pack, in which the battery cells are organized in a bimodal packing arrangement along with collapsible and sacrificial metal tubes, has been proposed. GBA can function as an energy storage system and a stress control plus energy dissipation unit simultaneously. Simulation studies rate it as 2.6 times more effective than a metal foam structure of equivalent density in reducing the probability of battery pack failure under crash conditions. A reduction of over 5% in the head injury criterion of EVs due to the use of GBAs has also been observed, as opposed to the likelihood of head injury arising from an impact to an occupant of an EV employing traditional battery packs. However, the disadvantages of employing GBA in place of a conventional battery pack include a decline of 35% and 13% in the volumetric capacity and gravimetric capacity of the vehicle, respectively. More importantly, the metal tubes of a GBA add approximately 3% to the gross vehicle weight, which may influence not only the EV's driving range but also its rolling resistance [85].

2.4.4.6. Thermal Stability

In spite of continuous improvements being made in the search for electrochemically- and thermally-stable electrodes and electrolytes, the application of Li-ion battery packs in EVs on a large scale may be constrained by their poor performance at elevated as well as low temperatures. A dedicated thermal management system that minimises the effect of variation in ambient temperature on the battery cell temperature is of vital importance.

It has been observed that it becomes increasingly difficult to transfer heat from/to a battery cell as the heat transfer area available per unit volume of battery cell decreases [34]. Accordingly, a larger base area and a controllable thickness are preferential for pouch cells. Similarly, a taller height and a smaller diameter are recommended to enable efficient heat dissipation through spiral wound cells. However, the longer electron current path in the axial direction may affect cell performance and shorten the cycle life. On the other hand, increasing the cell diameter in order to reduce the height of the cylindrical cell will impede the rate of radial heat transfer, which in turn would also have a negative effect on the cell performance. Optimal cell size is thus chosen as per the module requirement.

A study of the heat rejection properties of 10 Ah battery cells of pouch format (W: 73.35 mm, H: 163.40 mm, T: 10.60 mm), prismatic format (1865140) and cylindrical format (38120) reported their heat transfer areas per unit volume as 228.19 m^{-1} , 156.17 m^{-1} and 105.26 m^{-1} , respectively. Consequently, the thermal management of cylindrical cells was found to be more difficult than that of battery cells of other formats [73]. Insights gained from this study are summarised in **Table 2.4**.

Parameter	Battery Cell Type					
	Cylindrical			Small Prismatic		Pouch
	18650	26650	38120	Small	Large	
Packing						
Number of cells	4800	2400	720	600	50	600
Weight, kg	192	196.8	255.6	171.0	210	172.5
Volume, m ³ (closed pack)	0.101	0.105	0.152	0.131	0.120	0.296
Packing density, cells/m ³	47524.75	22857.14	4736.84	4580.153	416.667	2027.027
Interconnection weight, kg	1.217	0.621	12.11	10.24	1.164	10.75
Weight of cell holder, kg	81.6	40.8	12.24	10.2	1.0	42.22
Physical density of battery pack, kg/m ³	2720.96	2268.77	1841.77	1461.374	1768.033	761.723
Cell cost, USD	≈ 3 - 11	≈ 7 - 18	≈ 20	≈ 20 - 40	≈ 150 - 400	≈ 20 - 40
Assembly of single cell						
α,β Orientation of cell	360°, 0°	360°, 0°	360°, 0°	360°, 360°	360°, 360°	360°, 360°
Cell handing and insertion time, s	3.5	3.5	3.5	3.95	5.0	3.95
α,β Orientation of interconnection	180°, 180°	180°, 180°	180°, 180°	180°, 180°	180°, 180°	180°, 180°
Interconnection handling plus insertion time/cell, s	15.72	15.72	15.72	7.72	7.72	15.72
α,β Orientation of cell holder	360°, 360°	360°, 360°	360°, 360°	360°, 360°	360°, 360°	360°, 360°
Cell holder handling + insertion time, s	7.4	7.4	7.4	7.4	7.4	9.4
Interconnection assembly time (two terminals), s	37	37	46.36	29.72	29.72	60.74
Assembly cost per cell (assumed USD 5 per cell)	0.0884	0.0884	0.101	0.0678	0.0692	0.125
Electrical and Control						
Terminal contact resistance, mΩ	0.4	0.4	0.6	0.6	0.6	0.8
Wiring complexity	—	—	—	—	+	—
Cell monitoring	—	—	—	—	+	—
Reliability	+	+	+	+	—	+
BMS cost	—	—	—	—	+	—
Thermal management						
Heat generated by contact resistance, kJ/cycle (based on NEDC)	2.034	3.935	19.607	23.6747	284.097	34.090
Heat generated by battery pack, kJ/cycle (based on NEDC)	219.906	215.670	193.04	215.440	214.304	218.991
Power consumption of cooling fan	1	0.967	0.380	1.837	6.763	0.604
Complexity of cooling system design	—	—	—	+	+	+

Services and maintenance						
Identification of faulty cell	–	–	–	–	+	–
Ease of cell replacement and service	–	–	–	+	+	+
Uninterrupted operation if one unit cell fails	+	+	+	+	–	+

Table 2.5: Comparison of different design characteristics of 19.2 kWh $LiFePO_4$ battery pack using different types of battery cells [73]

Moreover, the liquid cooling technique has proved to be more effective in regulating battery cell temperatures within the recommended window and in minimising thermal gradients in large battery packs operating at high discharge rates. In this technique, a liquid coolant is passed through built-in mini-channels of a metallic plate kept in close contact with the battery cells. The plate generally has high thermal conductivity and a flat shape, which makes its application easy in the case of battery packs made of pouch and prismatic cells. However, the same shape makes it difficult to transfer heat from cylindrical cells using a cold plate. Inefficiency in heat transfer due to incompatible geometries and marginalised contact areas can be removed via heat pipes or through phase change materials (PCMs). Heat pipes provide a compact cooling solution with high effective conductivity, while PCMs enable greater control over battery cell temperatures. However, the cost of the heat pipes and low thermal conductivity of PCMs needs to be considered in the selection of a suitable thermal management system for EV battery packs.

2.5. Results and Discussion

2.5.1. Modified P-diagram for an EV battery pack

A P-diagram showing the parameters affecting the ideal output of an EV battery pack and the possible failure modes is presented in **Fig. 2.8**.

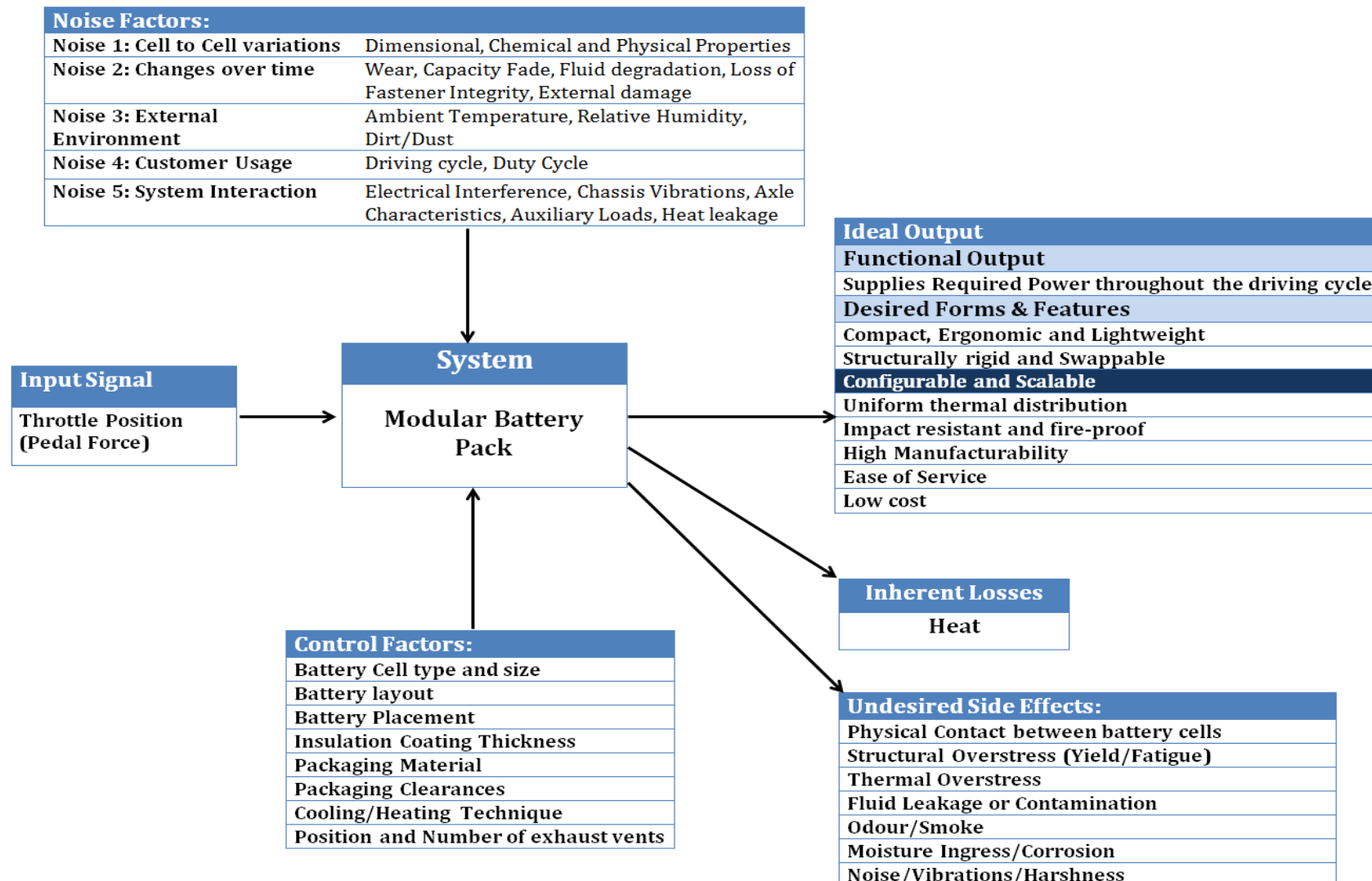


Figure 2.8: Modified P-diagram for a modular EV battery pack

As every engineering system has certain efficiency and corresponding energy losses associated with it, a better design is one that can minimise these energy losses. However, these unwanted but inherent energy losses must be documented in the P-diagram. The heat generated during battery cell operation is a typical example of an inherent loss associated with EV battery packs.

The P-diagram layout illustrated here has therefore been modified (refer to the general layout presented in **Fig. 2.2**) to include this ever-present loss of energy. The modified P-diagram establishes the conversion of part of the chemical and electrical energy to heat as an ineradicable phenomenon during the discharging and charging of battery packs, respectively. It also acknowledges that no real system can be perfectly isolated. Hence, heat flow and thermal interactions between adjacent battery cells or modules are bound to happen. As long as they are within the specified limits, they should be accepted as normal physical behaviour, leaving the battery designer to target the undesired side effects. In addition, the noise factors are arranged according to their level of influence on the battery pack performance. The diagram allows all the factors involved in battery pack design and operation to be visualized at the same time.

2.5.2. The House of Quality for EV Battery Pack

Fig. 2.9 shows the HoQ constructed to illustrate the significance of the relationships between each CN and PTR for an EV battery pack. Left wall or the “What” column of the HoQ matrix documents the CNs for EV battery packs. On the other hand, all the measurable technical characteristics identified as important for meeting the specified CNs, also called the “How”, are collated at the top of the matrix. More importantly, the strength of the relationship between the “whats’ and the “hows” is presented in the central part of the HoQ matrix.

		How						
What	Pack configuration	Cell type	Cell size	Casing (Cell/Pack)	Packaging architecture	Packaging clearance	TMS	Battery placement
	Lightweight	Δ	Δ	⊕	0		⊕	
	Compact	⊕			⊕	0	Δ	
	Structurally rigid			⊕	Δ		0	⊕
	Thermally stable	0	Δ	⊕	0	⊕	Δ	0
	Impact-resistant	0		Δ	Δ		0	⊕
	No odour or smoke	0			Δ		⊕	Δ
	Fire safe		Δ	0	Δ	⊕	Δ	0
	High manufacturability	Δ	⊕		0		⊕	
	Low maintenance	⊕			⊕		Δ	0
	Ease of service	0	⊕		⊕	0	Δ	0
	Low cost		Δ	Δ	0	⊕		
	Configurable				0		0	
	Scalable		0		⊕		Δ	

Figure 2.9: The House of Quality for an EV battery pack (symbols - O , ⊕ and Δ denote weak, moderate and strong correlation, respectively)

Fig. 2.9 was constructed considering all potential customers, including OEMs, production teams, after sales departments, government departments or policy makers, technicians/mechanics and EV drivers and passengers. Equal weight is therefore accorded to each CN in this exercise. The HoQ matrix can also be customised to target specific customer groups, where different CNs are ranked to suit their priorities.

Accurate scoring of these relationships is crucial for new product development. Therefore, as mentioned previously in Section 2.3.2, the representative strengths shown in this study were estimated based on data derived from the synthesis of relevant literature and subsequently validated by a group decision of the expert panel. The symbols 0, \oplus and Δ are used to denote weak, moderate and strong correlations, respectively, while a blank space in the relationship matrix indicates the lack of a relationship between a CN and the corresponding PTR.

Evidently, there are several parameters, namely cell size, casing material and battery pack location in the vehicle, which can be regulated to optimise its performance and reliability. However, the quality matrix also shows that the two most important technical characteristics for an EV battery pack are the packaging architecture and the thermal management system. They both have an appreciable effect on the mechanical and thermal modularity of the battery pack architecture and therefore warrant careful attention during the early design stages.

Battery packs are designed by connecting multiple battery cells in a series-parallel combination. As a result, they can be rescaled simply by modifying the number of battery cells involved in this combination. However, as soon as a thermal management system is integrated with the electrical framework of the batteries, the battery pack loses its configurability. For example, if to meet the energy requirements for a certain application, more battery modules need to be added to the current pack architecture, or if a few modules can be removed from it, the existing battery thermal management system would then be classified as either over-

designed or under-designed for the new application. As a result, it would have to be redesigned using the procedure developed by Pesaran et al. [86], presented later in Chapter 4. It is therefore imperative for a battery pack to have a modular thermal management system for it to retain its scalability. In other words, the mechanical modularity is dependent on the thermal modularity of the system, as heat exchange between neighbouring battery modules cannot be eliminated. Hence, the thermal independence of adjoining battery modules must be ensured so that structural and mechanical design requirements can be satisfied for the battery pack.

The concept of thermal independence at module level for an EV battery pack design has a powerful benefit - to reduce or even eliminate the custom, vehicle-specific thermal analysis that accompanies a traditional system-level vehicle design. If vehicle architecture successfully implements these thermal modularity concepts, then it does not matter where in the vehicle the module is placed. It would be thermally interchangeable, due to its module-level thermal independence; because a module designed like this could be placed anywhere in the vehicle and it would work thermally. This would preclude the necessity for a system-level thermal analysis, or at the very least drastically reduce its scope. Consequently, this would represent substantial savings in the non-recurring engineering associated with the thermal analysis of a particular vehicle. This also provides an opportunity to integrate innovation in the early product design stages and embed the supposed inherent robustness in the product design.

2.6. Conclusion

The International Organisation for Standardisation suggests the mass production of standardised battery cells as a way to overcome high manufacturing costs of EV battery packs and improve the rate of global market capture of EVs. Previous research has established that variability has a negative influence on the mass producibility of any system. Furthermore, the pool of variables that can affect the cycle life, performance and safety characteristics of Li-ion

Application of RDM to Battery Pack Design

battery cells is large. A systematic framework that enables battery pack designers to conceptually analyse elements of this pool, develop a clear understanding of customer needs, and identify factors that can be optimally adjusted to build a reliable battery pack that meets various customer requirements in their entirety is therefore indispensable.

In this chapter, a value-based rapid product development technique, commonly known as robust design methodology, is applied to the evaluation of design aspects related to battery cell type and size, packaging architecture, thermal management solution etc. of modular EV battery packs. In the first stage of this systematic process, a parameter diagram is used to identify and categorise different sources of variability as noise factors and control factors. Next, HoQ is used in the second stage of the process for translating various customer requirements to engineering characteristics correctly.

It is found through HoQ that choices concerning the selection of thermal management strategy and packaging design for the EV battery pack are crucial for the successful implementation of a modular battery pack architecture. In addition, a major technological limitation of EV battery packs is that their mechanical design and thermal design are essentially interrelated. Thermal paths in a module-level design must therefore be adequately isolated after taking into account all mechanical hard points and connections.

Chapter 3

Robust battery packaging design for EVs³

³ A publication was produced based on this chapter. Details are available from - 87. Arora, S., W. Shen, and A. Kapoor, *Review of mechanical design and strategic placement technique of a robust battery pack for electric vehicles*. Renewable and Sustainable Energy Reviews, 2016. **60**: p. 1319-1331.

This page has been intentionally left blank

Chapter 3

3.1. Introduction

Lithium-ion (Li-ion) batteries have become the preferred on-board power source for a pure electric vehicle (EV) due to their high power, high energy density and long cycle life [88]. However, they are also considered sensitive to variations in factors, such as ambient temperature, vibration and pressure. Control of battery temperature and the environment in which a battery pack operates is required to maximise its energy capacity. It has been suggested that the battery temperature must be maintained below 50 °C for safe operation [37, 38]. The vibration frequencies of the battery pack should also be suppressed to avoid resonance at typical natural frequencies of the vehicle suspension system and sprung mass from 0 to 7 Hz, the vehicle powertrain, i.e. driveline and gearbox, from 7 Hz to 20 Hz, and the vehicle chassis system from 20 Hz to 40 Hz [59, 89, 90].

Marginal deviations from the designed boundary can compromise the cycle life of the battery pack. It can also set in motion an uncontrolled chain of exothermic reactions resulting in the release of smoke or toxic gas and the development of high-pressure events leading to premature failure, fire and explosions. These marginal deviations can be caused by excessive heat build-up or physical abuse of battery packs that includes puncturing or crushing the packs [37, 91-93].

Such irregular behaviours were the marked characteristics of Li-ion battery packs during the initial development phase of EVs. On several occasions, they compelled the original equipment manufacturers (OEMs) to withdraw their products from the market. In 2002, EV Global Motors Company received reports of five cases of Li-ion batteries overheating in their electric bicycles.

In three of those cases, the battery packs caught fire. Subsequently, they announced the recall of 2000 Li-ion battery packs through the U.S. Consumer Product Safety Commission [94]. General Motors also called back approximately 8000 units of the Chevrolet Volt sold in the U.S. after incidents of GM Chevrolet Volt's Li-ion battery pack catching fire during the National Highway Traffic Safety Administration crash-safety tests were reported in 2011 [95]. More recently, an explosion of a Li-ion battery pack in GM's test facility in Michigan caused five workers to seek immediate medical help [96, 97]. Tesla Motors also received negative publicity on account of road debris penetrating the battery packs in Tesla Model S and causing fire [98, 99].

Though continual improvements in the safety of large battery packs for EVs are being made, both the general consumer and the OEMS remain apprehensive about accidents during normal use and unintended abuse of EVs [88, 100]. Strict regulations governing the safety of Li-ion battery cells have therefore been stipulated.

Table 3.1 lists various SAE standards relevant to packaging design and performance testing of automotive battery packs [101]. Large scale electrification of private and public transportation sectors however does not seem possible until the behaviour of Li-ion battery packs is properly understood and questions pertaining to their reliability are answered [102, 103]. It is of utmost importance to investigate the design features that can enhance the safety and reliability of a Li-ion battery pack. The significance of this research is accentuated by the fact that the international standard SAE J1797 – Recommended Practice for Packaging of Electric Vehicle Battery Modules is only applicable to lead-acid, nickel cadmium and nickel metal-hydride battery packaging design and not to Li-ion battery packs [104].

Standard	Title	Scope
SAE J240	Life test for Automotive Storage batteries	Life test simulates automotive service when the battery operates in a voltage regulated charging system
SAE J1766	Recommended Practice for EV & Hybrid Vehicle Battery Systems Crash Integrity Testing	Specifies test methods and performance criteria which evaluate battery spillage, retention and electrical isolation during specified crash tests
SAE J1797	Packaging of Electric Vehicle Battery Modules	Provides for common battery designs through the description of dimensions, termination, retention, venting system, and other features required in an EV application
SAE J1798	Recommended Practice for Performance Rating of Electric Vehicle Battery Modules	Common test and verification methods to determine EV battery module performance. Document describes performance standards and specifications.
SAE J2185	Life test for heavy-duty Storage batteries	Simulates heavy-duty applications by subjecting the battery to deeper discharge and charge cycles than those encountered in starting a vehicle
SAE J2289	Electric-Drive Battery Pack System: Functional Guidelines	Describes practices for design of battery systems for vehicles that utilize a rechargeable battery to provide or recover traction energy
SAE J2344	Technical Guidelines for Electric Vehicle Safety	Defines safety guideline information that should be considered when designing electric vehicles for use on public roadways
SAE J2380	Vibration Testing of Electric Vehicle Batteries	Describes the vibration durability testing of an EV battery module or battery pack.
SAE J2464	Electric Vehicle Battery Abuse Testing	Describes a body of tests for abuse testing of EV batteries.
SAE J2929	Electric and Hybrid Vehicle Propulsion Battery System Safety Standard	Safety performance criteria for a battery systems considered for use in a vehicle propulsion application as an energy storage system galvanically connected to a high voltage power train

Table 3.1: SAE standards governing mechanical design of automotive battery packs

It has been reported that among several factors affecting the reliability of Li-ion battery packs, a number of these can arise during the manufacturing process. The most important are: chemical factors such as impurities and concentrations, and joining procedures, i.e. material processing and cell closures, either hermetic or crimp [105]. Another report maintains that in the long term environmental conditions that a battery pack operates in such as ambient temperature, pressure, mechanical and thermal shock, mechanical vibration have a major impact on battery reliability. This report goes on to provide some general battery assembly guidelines [106]. A different study points out that the performance of Li-ion battery packs in EVs strongly depends upon typically uncontrolled ambient operating conditions and therefore cannot be assessed based on laboratory experiments [107]. A more recent work on the other hand suggests that the battery cell temperature also affects the reliability and cycle life of Li-ion battery packs [61].

Despite the fact that different groups hold different opinions about the factors that lead to the unpredictable behaviour of Li-ion battery packs, most of the published work is concentrated towards developing stable electrolytes, new and safe electrode materials, and thermal management solutions for Li-ion batteries. An area that has often been overlooked is the contribution of a robust mechanical design of a battery pack enclosure towards its reliability. Conventional safety devices incorporated in commercial Li-ion batteries were reviewed by a group of researchers, but their work was limited to single cells [108]. In this chapter, we review safety features incorporated in large battery packs in EVs.

A robust and reliable battery packaging design needs to address several design issues pertaining to thermal runaway, vibration isolation and crash safety at cell level as well as at modular level. At each of these levels, there is a need to restrict relative motion between battery cells in order to eliminate potential failures of the battery pack.

Issue	Solution Presented in US Patent	Assignee	Publication Date
Thermal Runaway	8663824	Tesla Motors	March 4, 2014
	8361642	Tesla Motors	January 29, 2013
	8574732	Tesla Motors	November 5, 2013
	8709644	Ford	April 29, 2014
	8679662	Ford	March 25, 2014
	8268469	Tesla Motors	September 18, 2012
	8057554	BYD	May 28, 2009
	8481191	Tesla Motors	July 9, 2013
	8557416	Tesla Motors	October 15, 2013
	8642204	Nissan	February 4, 2014
Vibration Isolation	7507499	General Motors	March 24, 2009
	4169191	General Motors	September 25, 1979
	8268479	BYD	September 18, 2012
	7556656	Nissan	July 7, 2009
	7110867	Nissan - Renault	September 19, 2006
	8304103	Nissan	November 6 2012
	8124276	Nissan	February 28, 2012
	8580427	Mitsubishi	April 5, 2012
	8733492	Suzuki Motor	May 27, 2014
	8702161	Tesla Motors	April 22, 2014
Crash Safety	8696051	Tesla Motors	April 15, 2014
	8424960	Tesla Motors	April 23, 2013
	8393427	Tesla Motors	March 12, 2013
	8286743	Tesla Motors	October 16, 2012
	8733488	Mitsubishi	May 27, 2014
	8276697	Mitsubishi	October 2, 2012
	8012620	Mitsubishi	September 6, 2011
	8037960	Toyota	October 18, 2011
	7921951	Toyota	April 12, 2011
	7717207	Toyota	May 18, 2010
	2013155106 A1	Toyota	October 17, 2013
	20130248267	Suzuki Motor	September 26, 2013
	7070015	Ford	July 4, 2006
	6676200	Ford	January 13, 2004
Strategic Placement	0139527	Renault	June 16, 2011
	8091669	Mitsubishi	January 10, 2012
	7690464	Ford	April 6, 2010
	8592068	Nissan	November 26, 2013
	8561743	Nissan	October 22, 2013
	8517127	Nissan	August 27, 2013
	7743863	Nissan	June 29, 2010
	8770331	Hyundai Motor	July 8, 2014
	4365681	General Motors	December 28, 1982

Table 3.2: Design solutions critical for a robust battery packaging design disclosed from the patents

Strategic placement of the battery pack in an EV can substantially increase the effectiveness of battery packaging design to address the afore-mentioned issues. The following sections will use examples from different patents to illustrate that simple mechanical features can be integrated into the battery packaging design to mitigate these serious safety risks. **Table 3.2** provides a comprehensive list of patents focussing on key issues for a robust battery pack design.

3.2. Thermal Runaway

Thermal runaway is the start of an exothermic chain reaction where the battery cells start to self-heat at a rate greater than 0.2 °C per minute [109]. The excessive heat generation leads to a further increase in the self-heating rate and eventually to a spontaneous combustion of chemical components forming the battery pack. A battery experiencing thermal runaway typically emits a large quantity of gas formed of hydrocarbon vapours, jets of effluent material, and sufficient heat to destroy materials in close proximity to it [105]. Thermal runaway can be initiated by a short circuit within the cell, physical abuse, manufacturing defects, or exposure of the battery cell to extreme external temperatures [109-111]. It is noteworthy that even when a heated battery is in a state of thermal runaway, it can still vent flammable gases [112].

Nonetheless, the risk of any damage to the property and harm to the people becomes significant only after the hot gas escapes the boundaries of the battery pack. The controlling factor here is the auto-ignition temperature (AIT) of the combustible hydrocarbons present in the hot gas. The AIT remains relatively high as long as the gaseous materials are confined to the battery pack. However, it will decrease significantly once the gas expands and comes into contact with the oxygen contained in the ambient atmosphere, potentially leading to their spontaneous combustion. It is at this juncture that the risk to the property and to the vehicle passengers, or to people attempting to control the event, is greatly increased.

Also, as the cells within the battery pack enter into thermal runaway, the associated pressure-rise may lead to a catastrophic failure of the battery pack enclosure. It is therefore important to include at least one failure point that has been designed to fail at a predetermined pressure in the battery packs, to avoid the risk of having an unknown point of failure, which can pose a significant threat to the vehicles and their passengers.

One aspect of mitigating these risks would involve controlling the location or locations where the hot fumes and the effluent material accompanying the thermal runaway event are released. Another aspect would be to control the thermal interactions between regions of the battery pack, thereby avoiding the spread of a single thermal runaway event to the entire pack [113].

3.2.1. Thermal barrier

The increased temperatures associated with thermal runaway may cause the mounting brackets in close proximity to the battery region undergoing thermal runaway to melt or vaporize. As a result, the battery may no longer be held rigidly in its original position. As the affected battery cell/module moves, the spacing between battery components may be diminished, leading to decreased resistance to thermal runaway propagation. Battery cell/module movement may also compromise the battery pack cooling system, thus further increasing the thermal runaway propagation rate. Lastly, it should be noted that if the affected cell/module moves sufficiently, it might come to rest against an adjacent cell/module. If it does, the heat transfer process between the two regions would switch from radiation and convection to a combination of radiation, convection and thermally more efficient process of conduction. Further, in applications where a stacked-type battery configuration, i.e. a layer of battery cells arranged vertically over another layer, is used, gravitational forces may expedite the movement of the top layer once the bracket(s) begins to melt and/or vaporize. It is therefore important to restrict

the movement of the battery cell or module undergoing thermal runaway to minimise the risk of thermal runaway propagation.

3.2.1.1. At module level

US Patent No. 8663824 discloses a design in which the battery pack has been divided into a plurality of battery pack compartments by means of cross members. The packaging design as seen in **Fig. 3.1** includes a central battery pack member which separates the left and right compartments as well as providing a convenient means for running power and data lines [114].

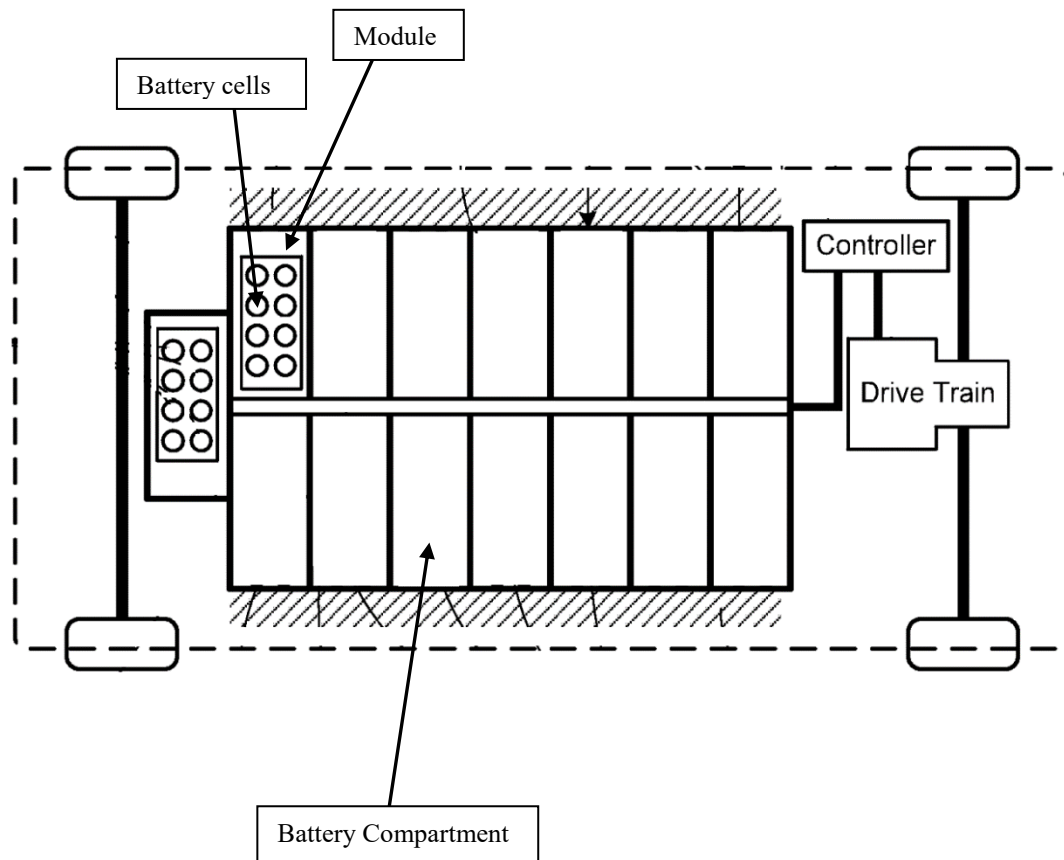


Figure 3.1: A robust battery pack with one battery module in each battery pack compartment [114]

In the design, the lower and the upper cross-members provide a simple means of locating and holding the module in place within the battery pack by capturing the module-mounting flange. Consequently, an air space is created between the modules and the top and the bottom surfaces

of the battery pack. This air space insures that no conductive heat exchange would take place between two adjacent battery modules.

Another design presented in US Patent 7507499 also has a small air-gap between the right and left battery packs that apparently limits the thermal runaway propagation by providing a thermal barrier between groups of cells or battery modules as well as significantly limiting gas flow between compartments. A typical design where a battery pack is divided into several compartments is also reported by Lai et al [115].

3.2.1.2. At cell level

The spacer assembly comprises a plurality of independent and separate rigid spacers. These can be configured to fit between adjacent cells of the battery module, to ensure that each battery cell remains at its predetermined location. The rigid spacers may be friction fit or bonded into their place.

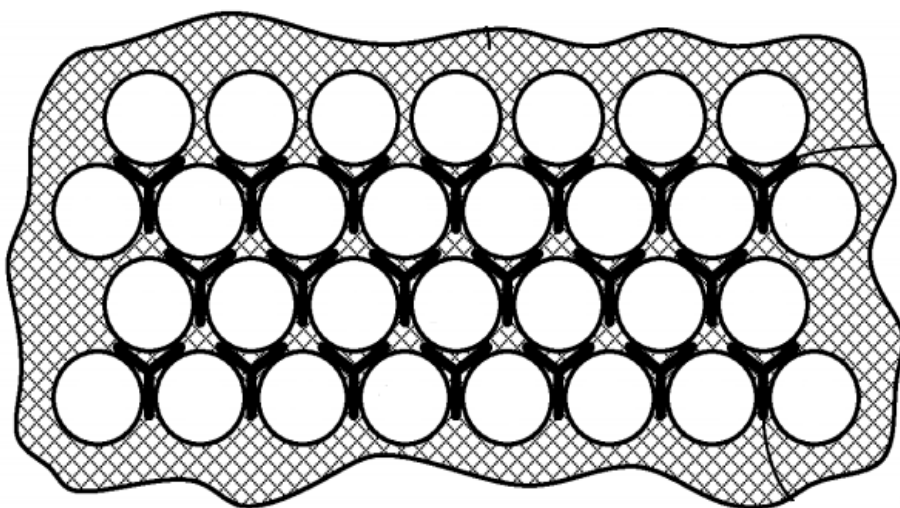


Figure 3.2: A cylindrical battery cell assembly with cell spacers [116]

In general, the spacer assembly selected for integration within the cell-mounting bracket depends on the type and shape of the cells employed within the battery pack. US Patent

8481191 provides a design of a spacer assembly for use with a cylindrical battery cell in a battery pack as seen in **Fig. 3.2** [116]. Each of the spacers has a height between 1% and 5% of the overall battery height.

Since the primary function of cell spacers is to keep the cells fixed in place during thermal runaway, to save mass a pair of much smaller spacers with an upper spacer and a lower spacer as shown in **Fig. 3.3** is preferred over one long spacer running from top to bottom of the cells [116]. Although just one spacer can be used, such as one located near the top or bottom, or near the centre of the cells, use of one spacer is not preferred as it still permits some movement.

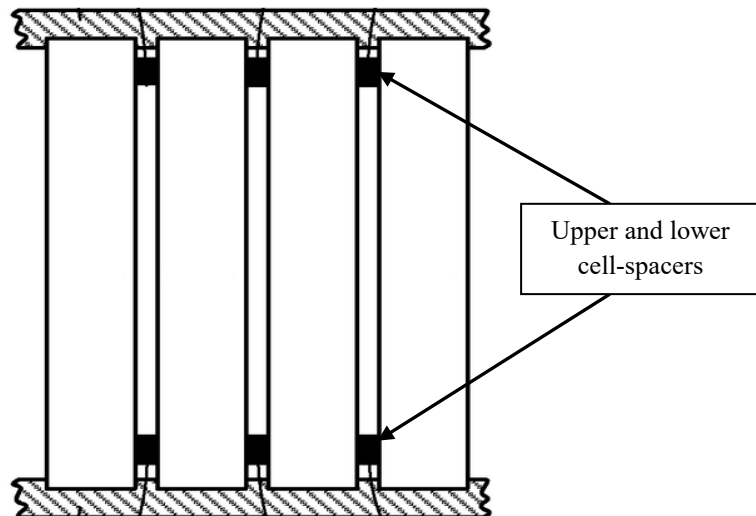


Figure 3.3: An alternate strategy utilising rigid spacer assembly [116]

In addition, the prismatic cells also require the cells to be maintained under a certain amount of binding pressure to prevent the internal spring forces of the cell windings from expanding and damaging themselves and consequently reducing cell life. Battery cell spacers create sufficient binding on the cell sides without covering so much of the cell surface area that cooling becomes ineffective.

US Patent No. 8709644, on the other hand, provides cell spacer design for a battery pack with prismatic cells. The spacers in this design pertain to cartridge-like retainer geometry. The

spacer assembly includes rib supports and a plurality of insulating ribs connected between them. Together they form pockets designed to receive a battery cell. The spacers also include a top and a bottom flange to prevent vertical movement.

The ribs support a battery cell and restrict any movement of battery cell when it is placed in retainer pocket. They also provide a distributed load-bearing surface to the rib supports and a converging inlet and diverging outlet for heating or cooling fluid flow. The fluid inlet and the outlet are parabola-shaped to minimise the pressure drop as cooling fluid flows from varied cross-sectional gaps in front to the back of the cells. Cell spacers further include moulded-in snap-over features at the top inside of the cartridge pocket of spacers. At the instance when battery cell is completely seated in the bottom of the cartridge pocket the snap-over feature locks the cell into separator. As such, the snaps prevent cells from slipping out from the top of the spacers during handling [117].

3.2.1.3. The point of egress

The point of egress of hot gases is controlled by incorporating one or more gas exhaust nozzles that are designed to open during a battery thermal runaway event. The nozzles are placed such that they direct the gas flow and material in a direction away from the passenger compartment and any location where someone could get hurt by the escaping hot effluent, thereby minimizing the vehicle damage and the associated safety risks. US Patent No. 8663824 discloses design of one such exhaust nozzle assembly. To prevent any contaminants such as road debris and moisture from entering the battery pack, a nozzle seal keeps the nozzle closed during normal operation of the vehicle. A pressure equalization valve with a cracking pressure in the range of 0.5 to 1.0 psi, i.e. much less than the pressure encountered during a thermal runaway event, is integrated into the exhaust nozzle to provide a means for handling pressure differentials due to non-thermal events (e.g., due to the vehicle changing altitude). Hollow

structural elements are included in the battery pack configuration to guide the flow of hot gas and material from the cell experiencing the thermal event to the exhaust nozzle.

The nozzle seal that keeps the gas exhaust nozzle closed during normal operations is held in its place by a nut. During thermal runaway, both the pressure and the temperature within the battery pack enclosure increases. Eventually, the nut would melt and/or sufficiently deform to allow the pressure within the pack enclosure to force nozzle seal out of nozzle. However, as the nozzle and its mounting assembly are fabricated from high temperature materials such as steel or ceramic, they do not get affected by increasing temperature and continue to guide the hot gases in a direction that minimizes any personal or property damage [114].

In the configuration described by the patent and illustrated in **Fig. 3.4**, the battery compartments are perforated. During a battery thermal runaway event the gaseous matter generated within the cells, passes through perforations into the cavity or cavities formed within the hollow guide ways of battery pack. The gas then flows through the guide ways to a battery pack gas exhaust nozzle from where it is released out of the battery pack.

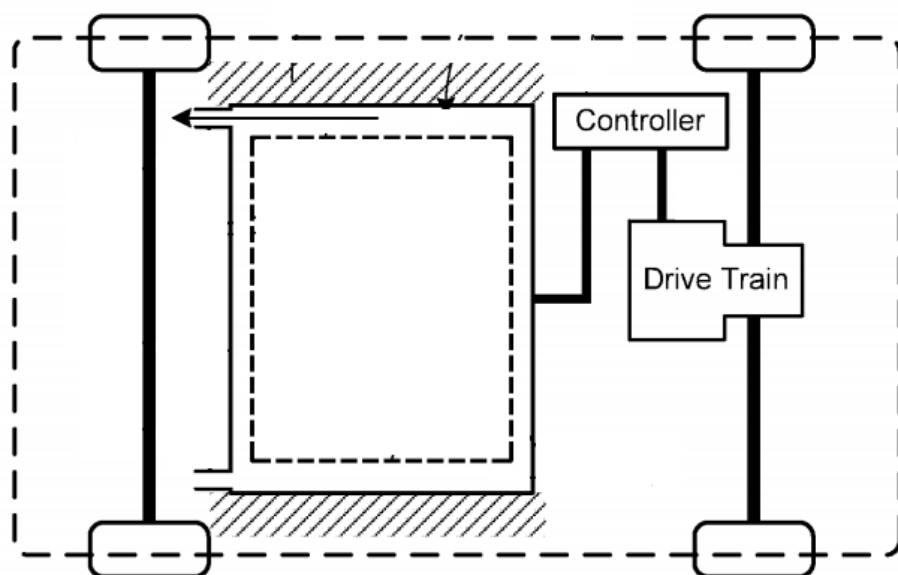


Figure 3.4: A battery pack system designed to exhaust the hot gases and material released during thermal runaway event occurring within a section of the battery pack [114]

Although the design presented in US Patent 8663824 is highly effective in minimising the risks associated with thermal runaway event, exhaust of the hot gases through the exhaust nozzle depends only on the pressure generated by the hot gases released from the cell. For this reason, there is a possibility that when only a limited number of cells are in a state of thermal runaway the pressure generated by the hot effluents might not be high enough to break the nozzle seal. In this case, the hot gasses will not be exhausted from the battery pack. Somehow, the accumulated heat might flow to other battery compartments, increasing the likelihood of the thermal runaway event to propagate throughout the battery pack.

US patent 8642204 provides a high-reliability battery pack that is capable of exhausting the hot gas even when the quantity of the gas released from the cell is small. In this design, a battery pack is formed of battery cells equipped with a pressure relief valve that opens at a certain pressure to release the gas generated by the cell. The relief valves are located approximately at the mid-point of the outer periphery portion in the longitudinal direction, where the pair of the laminated films forming the cells is heat-sealed. They release the gas by opening a heat-sealed part of the laminated films at a pre-determined pressure. The hot gas released from the cell is then exhausted through a gas emission hole to the exhaust duct that carries it to the outside environment.

Under this arrangement, the exhaust gas duct is provided with multiple gas inlets and at least one air intake. The air intake is connected to the cooling airflow passage and sucks in a small portion of the cooling airflow. The gas exhaust duct leads the cooling air flow through the inside passage and exhausts it to the outside environment. Suction of cooling airflow through the air inlet creates a positive pressure in the exhaust duct and starts an air circulation in the gas exhaust duct. So, when hot gas released from the cell reaches the exhaust duct it is immediately exhausted to the outside environment with the cooling air flow. This positive

pressure ensures that the hot gases do not remain in the battery pack for long, thereby providing a highly reliable battery pack [118].

US Patent 8679662 also presents a design for a battery assembly that includes a vent tube and a vent port to define a passageway for gaseous emissions from the battery to the vehicle exterior. The vent tube includes a flexible hose with a proximal and a distal end. The proximal end is connected into the case and receives any emissions that may vent from the cells. The vent port couples the distal end of the tube to the body exterior through a vent aperture that is formed into the floor pan. A gasket is used for sealing the vent port to the floor pan. While sufficient clamping load is provided by the mass of the battery assembly but the use of fasteners is suggested for compressing the gasket and maintaining the seal [119].

3.3. Vibration Isolation

Conventional battery pack structures are not designed to isolate transmission of undesirable vibrations to the assembled battery cells [120]. Accordingly, the frequency of vibrations transmitted from the top portion of the vehicle to the battery pack structure, mounted in a vehicle can be approximately equal to or less than 100 Hz [121]. As a result, dynamic mechanical loads develop on the electrical subsystems such as terminal connectors and bus bars in a battery pack, which can effect in loss of electrical continuity and fatigue failure of the casing. In fact, the lack of proper vibration isolation of electrical and electronic subsystems has been cited as the primary cause of in-market durability failures of battery packs [59]. However, a far graver problem than the loss of electrical continuity arises when natural frequency of the battery structure lies within a frequency range of 100 Hz. The resonance causes an interlayer delamination between the elements of the battery cells to occur wherein the respective layers forming the battery cell disassociate from one another, which is one of the main reasons for the reduced cycle life of the battery [122].

3.3.1. Battery Pack Structure/Mounting Frame

A continuous vertical vibration input of low frequency is transmitted to a vehicle as soon as it makes contact with the highway surface. Also, traveling over uneven surfaces, such as holes, grade crossings or bridge abutments, produces shocks that cause vertical vibrations. Moreover, traversing uneven roadway surfaces can generate lateral forces while longitudinal shocks are encountered during starting and stopping in traffic, or backing the vehicle into a parking facility.

Although vibrations along the Z-axis i.e. the vertical direction are considered most severe, both the vertical and lateral supports must be provided to achieve stabilization of cells within the battery pack enclosure. In order to do so, a compressive force is usually applied to the top surface of the battery packs. US Patent 7507499 illustrates one such design for stabilizing a battery pack in EVs by using a cover-pad-tray retention arrangement. The design comprises of four beams, coupled at a right angle to one another through four connectors to form a rectangular frame structure. Each beam engages one of the four sides of the battery pack. Positive connection between the frame and pack is maintained through tensioning bolts. The arrangement uses two types of damping pads: flat and L-shaped, to absorb vibration and prevent movement of the modules with respect to one another along the Z-axis. The L-shaped damping pads are placed adjacent to each of the corner connectors and bear against the beams to provide relatively small pressure areas at the corners and push the separate battery modules of the battery pack laterally towards one another; whereas, the flat damping pads are positioned at the lower and upper corners of facing sides of the adjacent battery modules. A tray that could be bolted to a part of the vehicle structure provides the support to the battery pack.

The tensioning bolts are fastened after assembling the frame so that the beams are drawn against the corner pads in the longitudinal and lateral directions, i.e. along the X-axis and Y-

axis to peripherally squeeze the battery modules of the battery pack towards one another. This also compresses the damping pads placed between the individual battery modules making them stationary with respect to one another. **Fig. 3.5** presents a perspective view of the design defined in the patent [123].

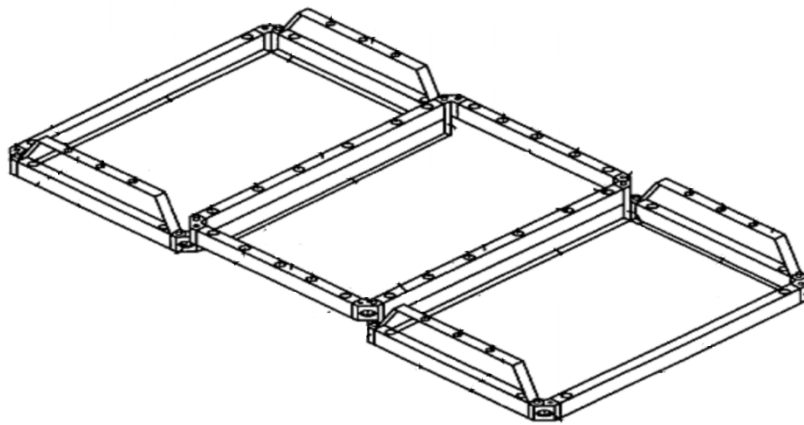


Figure 3.5: Perspective view of a framing arrangement employed with a compact battery pack design [123]

In the design, small packs are packed together to form a larger battery pack. The frame retaining the central battery pack rests on top surfaces of the outer frames so the battery pack in the middle is not in direct contact with the tray's surface. The beam of the central frame is bolted to the outer frames making it a single structure while the beams of the outer frames can be clamped or bolted to the tray. Shallow U-shaped bracket projects from the beams of each of the outer frames to which the cover is attached.

US patent 8642204 also provides a battery pack design in which a hollow structural member is arranged contiguous to the flat surface of the battery pack. It touches the battery module unit through the sealing portion, and functions as a support to the battery modules. The hollow structural member absorbs or attenuates any vibrations that gets propagated to the battery unit and protects the battery modules against the ill-effects of undesirable vibration.

Furthermore, the optimal ride quality with little or no vibration transmission is obtained when a vehicle operates with maximum grip and the maximum grip is obtained when all the tires are loaded equally. US Patent 8561743 discloses details of a battery mounting structure that helps to achieve a uniform weight distribution of the vehicle while maintaining a low centre of gravity. In this design, the battery assembly comprises the battery-mounting frame, the case, the battery modules, the harness, the switch box, the junction box and the control unit.

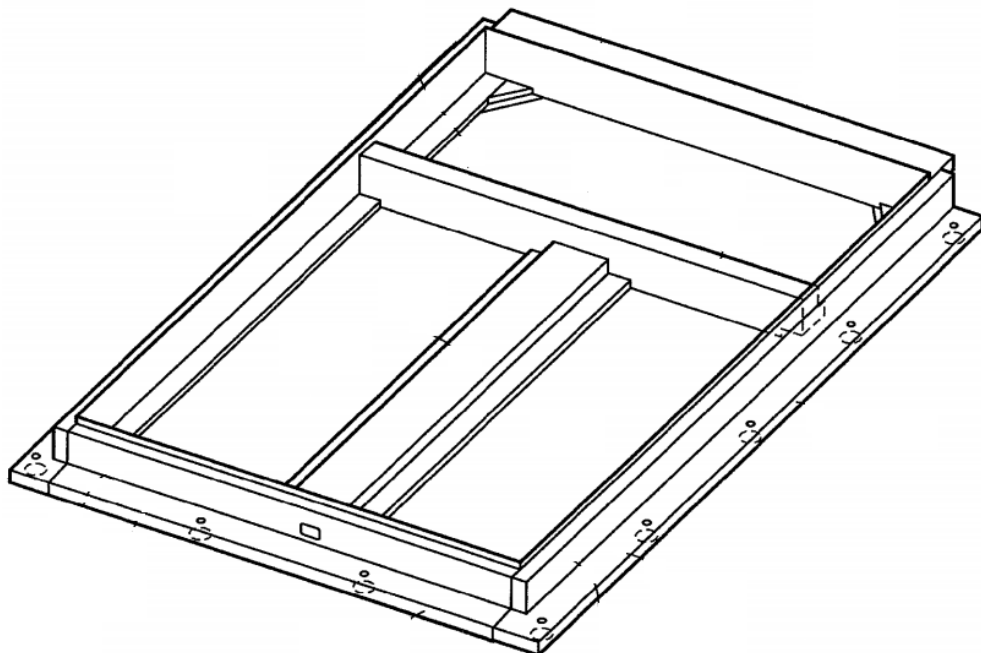


Figure 3.6: Perspective view of battery mounting frame [124]

The design as seen in **Fig. 3.6** makes use of a rectangular mounting frame. It has been divided into two sections, front and rear by a girder that has been welded to the frame [124]. Furthermore, a beam member divides the front section into two equal rectangular areas. In the two front rectangular areas, the batteries are arranged in a vertical direction such that the long side is oriented in the vehicle transverse direction and the short side is oriented in the longitudinal direction of the vehicle whereas the batteries in the rear rectangular section are arranged such that the shortest side is oriented in the vehicle transverse direction. As a result

of this arrangement, the weight of the group of the batteries mounted in the rear section is substantially equal to the total weight of the groups of the batteries mounted in the two front columns. Subsequently, the centre of gravity of the battery assembly is located around an intersecting point of a median of the group of batteries in the vehicle transverse direction and a median of the same in the vehicle longitudinal direction. This point is located to the rear of the graphical centre of the vehicle and is preferable in terms of weight balance of the vehicle in the front-aft direction, considering that the electric motor, the battery charger and the inverter are housed in the front compartment [124]. A clear advantage of this configuration is that the mounting frame can be used for various types of vehicles. This means that even when the layout of the seats of the vehicle is changed; it is possible to realize an optimum weight distribution thereby vibration isolation by simply modifying the number of battery stacks in the group without making major alterations to the dimensions of the battery-mounting frame.

3.3.2. Electrode Terminals

In a battery pack, the connection members such as bus bars are either bolted or welded to the electrode terminals of a battery cell. However, over a period, the bolts are usually loosened and the welding structure may develop cracks due to the transmitted vibrations. For this reason, electrical connections in a battery pack cannot be reliably maintained over its cycle life.

US patent 8580427 discloses a design of a battery pack that can maintain its electrical connections for a long period. In this design, the electrode terminals are formed from an elastically deformable conductive material in a tapered pillar shape with width decreasing gradually from front end towards battery container. In addition, a portion of the front end is divided into segments by cutting a grove in circumferential direction. It allows easy insertion of the electrode terminal into the through-hole of the connection member. As each of the

electrode terminal and the through-hole is formed in tapered pillar shape, separation of the electrode terminals from the connection can be prevented.

Further, the electrode terminals are designed to include a fixing member with a protrusion from the base arranged at the front end of the electrode terminal. The protruding portion fits into the groove and is locked to the connection member. Since the protruding portion widens the width of the groove, the electrode terminal is pressed against the inner peripheral surface of the through-hole of the connection member, the electrode terminal and the connection member can be more reliably maintained connected to each other.

Beryllium copper and A 6000-series aluminium alloy are some examples of the elastically deformable conductive material that can be used to manufacture electrode terminals while the bus bar is a plate-shaped member that can be manufactured using a conductive material such as copper.

3.4. Crash Worthiness

An EV with gross vehicle weight ratio of or less than 4536 kg must conform to the directives laid out by the Federal Motor Vehicle Safety Standard (FMVSS) 305 regarding electrolyte spillage and retention of battery modules in the event of a front, rear and side collisions. The electrolyte spillage provisions defined in SAE J1766 have also been updated to be consistent with FMVSS 305 and reflect international regulatory requirements [125]. To confirm with the stipulated requirements of this standard, integrity of the battery pack mounted adjacent to the seating area of an EV must be preserved in case of a collision impact with sufficient kinetic energy to crush at least a portion of the floor to which the battery tray is mounted.

3.4.1. Rear Impact

US Patent 7070015 discloses a battery mounting system that maintains battery pack's integrity through dynamic relocation of the battery out of the crushing zone during a rear impact. The system uses a motion converter to rotate the battery pack to a different positional elevation which is not parallel to the floor as illustrated in **Fig. 3.7**, wherein the battery is much less likely to be damaged by subsequent crushing of the vehicle's floor [126].

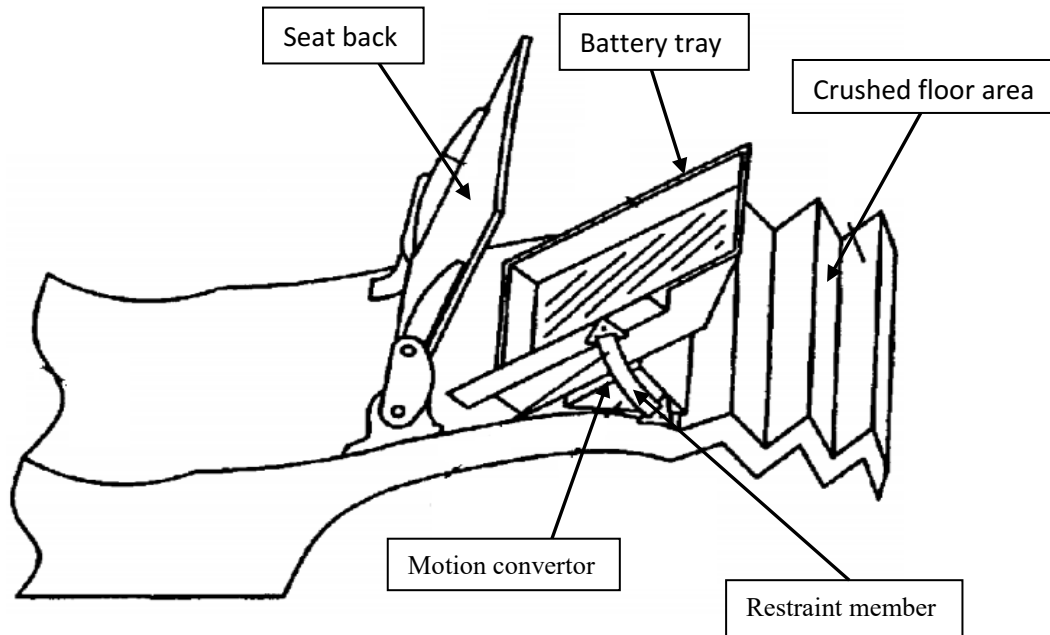


Figure 3.7: A battery tray being dynamically relocated as the floor deforms [126]

The motion convertor involves a first inclined plane that is fastened rigidly to the floor of the battery compartment and a second inclined plane comprising a portion of the battery tray. During an impact, the axial deformation of the floor causes the first inclined plane to slide and engage the second inclined plane, which lifts and initiate rotation of the battery tray in a direction away from the floor. In addition, the inclines have been designed such that a minimum set of predetermined deformation of floor is necessary for the first plane to engage the second. The mounting system also includes a restraining member comprising a flexible member or a

bulkhead that extends from compartment floor to the battery tray. The restraining member resists rotation of the battery tray beyond a predetermined position thereby preventing it from impacting the passenger cabin. Further, the batteries are electrically connected through a conductor wire of such a length that it bends to accommodate its dynamic relocation to a different plane within the compartment [126].

3.4.2. Side Impact

A side impact collision presents a particularly challenging problem to vehicle safety engineers due to the two factors: the relatively low position of the rocker panels on many small vehicles and the difficulty of implementing an impact resistant side structure while taking into account vehicle doors and doorways. US Patent 8702161 provides an energy absorption and distribution side impact system for use with a vehicle. The system, as seen from **Fig. 3.8**, comprises a pair of collapsible side sill assemblies and multiple battery pack cross members to attain a desired level of vehicle side impact resistance [127]. As per the design, a battery pack enclosure extending in dimensions from the front to the rear suspensions and traversing entire vehicle width from rocker panel to rocker panel is mechanically coupled to the left and right hand side sills. The number of battery pack cross-members varies with the number of cell modules to be packaged in the battery pack and with structural characteristics requirement of the battery pack.

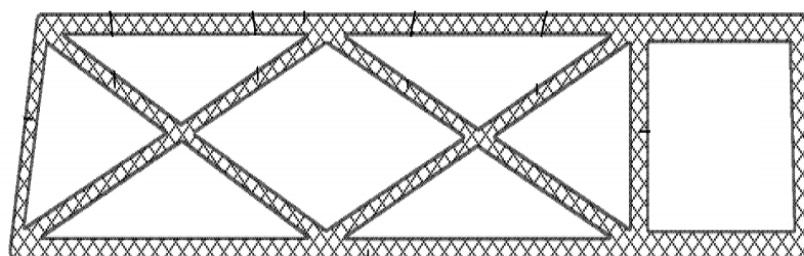


Figure 3.8: Detailed cross-sectional view of the energy absorbing sill insert [127]

In general, hollow cross-members are used to take advantage of high strength to weight ratios of hollow structures. However, it should be appreciated that both the configuration and the material used for the cross member depend on the location it is placed and can vary with it. For example, cross-members located in the centre of the battery pack are thicker than other cross-members to provide additional strength in the areas that are used for seat mounting assembly [127].

Moreover, in EVs with air-cooled batteries, due to large cross-sectional area of the air-ducts, minimal packaging space is available to provide cross-braces for the battery assembly. US Patent 8276696 demonstrates a packaging design in which the inlet/outlet ducts for an air-cooled battery are modified and utilised as structural members to increase the impact resistance of the battery pack. As per the design, the forced air system includes an inlet duct for providing air to the battery and an outlet duct for directing exhaust air from the battery and a fan. At least one of those ducts is configured as a structural member to provide structural support and protect the battery assembly. The duct arrangement extends between opposite sides of the vehicle is attached to the shock tower on each side providing support and protection to the battery assembly. The ducts that are traditionally made of plastic can be made of steel, aluminium, carbon fibre or any other suitable material in EV applications. Due to fewer parts used, it also provides a more efficient and compact packaging solution [128].

3.4.3. Front Impact

In an event of a front impact, the front-side members of EVs absorb significant portion of the impact energy. They minimise vehicle damage or any passenger injuries by controlling the transmission of impact energy to other vehicle structures. However, EVs have a higher body weight than conventional internal combustion engine vehicles. Thus, the strength of the front-side members needs to be increased to absorb the additional kinetic energy, which further adds

to the body weight of an EV. The add-on weight affects vehicle stability, manoeuvrability and more predominantly battery performance in terms of miles per gallon or equivalent.

US Patent 8424960 discloses a design of a front rail configuration for a front structure of an EV in which a large battery pack is integrated into the vehicle frame. **Fig. 3.9** offers a perspective view of the key components associated with a front impact load paths in accordance with the patent [129].

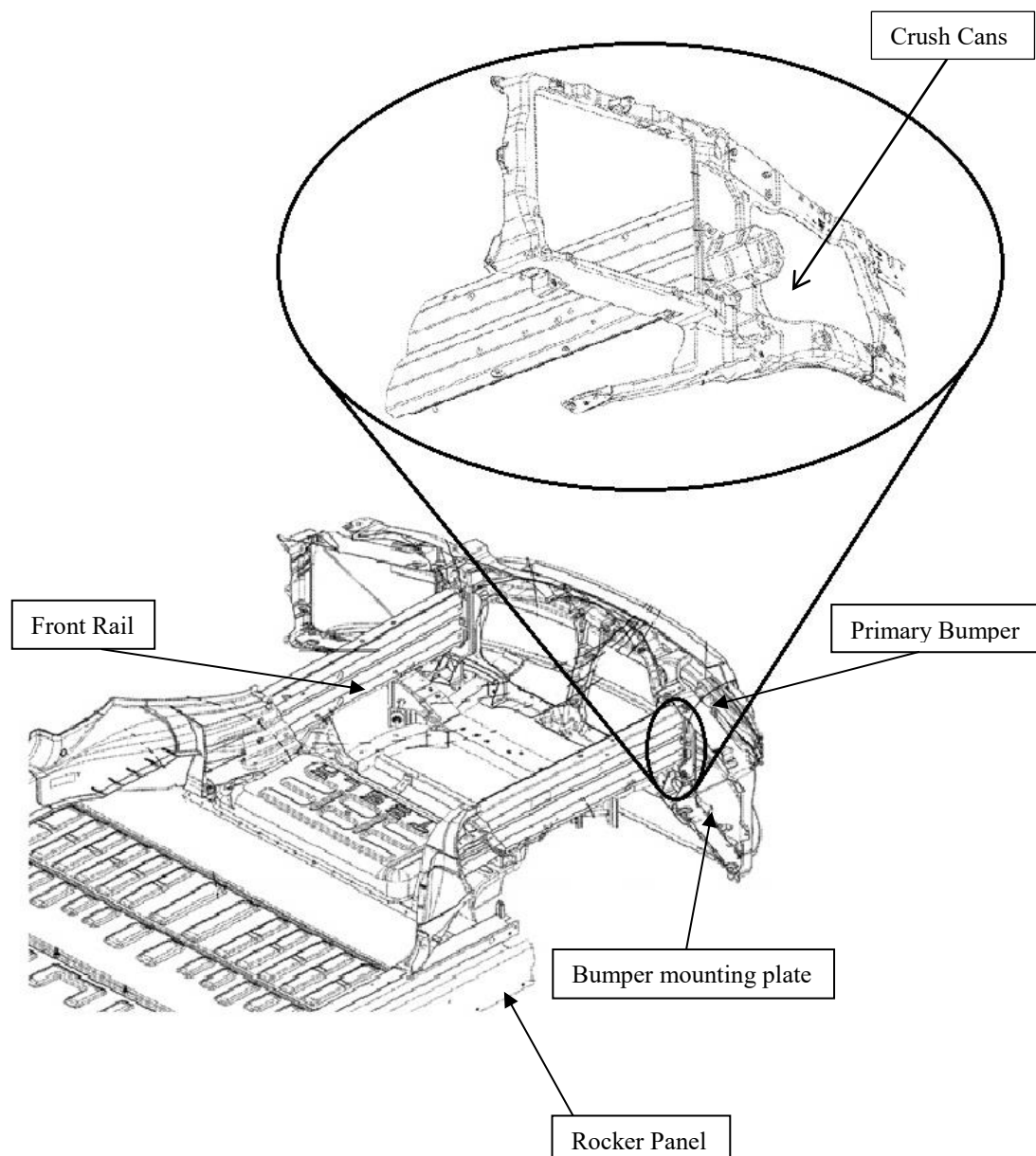


Figure 3.9: Perspective view of primary components associated with a primary and secondary front impact load paths [129]

The design makes use of crush cans that can be made of steel or aluminium or aluminium alloys and achieves improved performance in terms of front impact load distribution, structure weight, vehicle frame rigidity and vehicle manoeuvrability. The design includes a pair of front rails extending lengthwise and spaces apart width wise. One end of each rail is mechanically connected through a crush can to the bumper and the other end is coupled to a torque box. In the design, each crush can is aligned with the upper channel of rails thus achieving a direct transfer of front impact loads from bumper to the top rail channel. Lower rail channel on the other hand adds to load carrying capability of ach front rail while lowering the neutral axis of the rail section. Thus, during a front impact the front rail of the vehicle transfers the impact energy to the crush cans which collapse in response by absorbing some or all of the energy, depending upon the impact force [129].

3.5. Material selection for battery pack

Material of the battery pack plays a significant role in attenuating thermal shocks, mechanical vibrations and other external loads during ride conditions. Therefore, it is vital to select the appropriate materials to meet the functional requirements of a robust and reliable battery packaging design.

It is preferred that the battery pack case i.e. the battery pack side members and the bottom member is fabricated from a lightweight metal, such as aluminium or aluminium alloys. A metal case ensures rigidity or solidity required to support weight of an assembly of cells. In addition, a metal case can adequately withstand high temperature and pressure conditions that a battery pack could get exposed to. Furthermore, since the metals have high thermal conductivity, thermal management of the batteries would be easier. **Table 3.3** presents some examples of the materials that are being used for battery pack case in various EVs.

Vehicle	Material Used for Battery Case
Tesla Roadster	Aluminium
Honda Fit EV	Steel
Chevrolet Volt	Steel
Chevrolet Spark EV	Composite
BMW i3	Aluminium

Table 3.3: Materials used for Battery pack casing in various commercial cars

Battery pack cover or the top member should be made from a material that exhibits electric insulating and high heat dissipating properties. The materials used for the battery pack case and cover should also be chemically stable and should not react with any of the battery components.

The next key component in a battery pack is the rigid spacer assembly used for restricting the cell movements during the thermal runaway. It is essential that the material used for the spacer have a relatively low mass, thus minimising its contribution to overall battery mass. The chosen material should also be electrically insulating and have a relatively low coefficient of thermal conductivity, thus ensuring that it does not allow any thermal energy exchange between the affected and the neighbouring cells.

Preferably, the high temperature spacers are fabricated from a compressible material. The use of a compressible material ensures that the melting or vaporization of mounting brackets near the affected cells does not influence the position of the cells. The degree of compressibility required would depend upon rigidity of the cell mounting brackets since the more inflexible the cells are to movement, the more important it is to use a compressible spacer so that it can be properly located between the cells. Materials that can meet these requirements include alumina-based cloths and felts, aramid paper, and fibreglass cloth that is preferably coated with silicone, acrylic, vermiculite, graphite or polytetrafluoroethylene (PTFE).

Cooling fins or the heat dissipating members are also an integral part of the battery pack and it is crucial to select proper material for them as efficient heat dissipation is critical for battery life. Materials that can be considered for a heat-dissipating member should have good thermal conductivity and vibration absorbing properties. In fact, materials with thermal conductivity in the range of 0.1 to 450 W/mK have traditionally been considered for the design of a heat-dissipating member. The heat-dispersing member could therefore be formed by dispersing a vibration absorbing material into a base material with heat dissipating property. As carbon is recognised for its high damping qualities, any material in which the carbon filler is dispersed into the resin has both superior thermal conductivity as well as high vibration absorbing property.

The damping pads are required to provide sufficient friction force to eliminate any movement in the Z-axis i.e. vertical direction, they should therefore be made of a non-slip material. They should also have sufficient resiliency to absorb vibrational impacts as well as spike impacts. Suitable material for the damping pads are plastics, such as NYLON.RTM., polyphenyl sulfones or polydicyclopentadienes .

Any material that is chemically stable and can resist the hot gases could be used for the gas exhaust duct. The gas exhaust could be formed, for instance, from resin material, elastic material such as rubber-base material, and by combining any of these materials. These materials allow lightweight construction of the gas exhaust duct. Similarly, the exhaust nozzle and the means used to attach the nozzle to the battery pack enclosure are fabricated from a high temperature resistant materials such as steel or a ceramic e.g., alumina, alumina-silica, aluminium oxide, silicon carbide etc.

Regarding the sealing portion or gaskets, it is desirable that the sealing portion be formed from an elastic member or material with high deformability and moisture resistance. O-rings on the

other side should be fabricated from a material with a high temperature resistance such as a fluoroelastomer, a silicone or fluorosilicone material, a perfluoroelastomer, or Teflon.

The material selected for battery mounting brackets needs to meet several design requirements. Primarily, the selected material should be easy to mould and provide ease of fabrication, thus expediting manufacturing while minimizing cost. Secondly, overall mass of the brackets is critical in EV applications. An important requirement from EV components is that they should be relatively low mass. Lastly, in order to minimise the risks of battery short-circuiting; the material should be electrically non-conductive. Accordingly, to meet these design requirements, a conventional battery-mounting bracket is typically manufactured from a polymer, e.g., a plastic such as nylon.

3.6. Battery pack placement

For the purpose of effective space utilisation in an EV, it is necessary that the batteries be placed in a space, which is otherwise unused. From vehicle dynamics point of view, the battery pack should be positioned in such way that the centre of gravity of the vehicle remains low and mechanical stresses and fatigue on mounting frame are minimised.

From a thermal perspective, the battery pack should be placed where an appropriate air circulation to maximise the heat dissipation is possible. While to address the issue of electrical safety the battery pack should be treated as a primary component of electric drivetrain, similar to the engine of an internal combustion engine vehicle. It should hence be located outside passenger compartment so that the high voltage components do not pose any threat to passenger safety.

Vehicle	Battery		Electric Range	Battery Location
	Chemistry	Size (kWh)		
Bolloré Bluecar	Lithium-ion Polymer	30	250 Km (city) 150 Km (highway)	Centre
BMW i3	Lithium-ion	18.8	130 – 160 Km	Centre
Nissan Leaf	Lithium-ion	24	121 Km EPA 200 Km NEDC	Centre
Ford Focus Electric	Lithium-ion	23	122 Km EPA	Rear
Tesla Model S	Lithium-ion	60	335 Km EPA	Centre
		85	426 Km EPA	
BYD e6	Lithium-ion	61.4	300 Km	Centre
Fiat 500e	Lithium-ion	24	140 Km EPA	Rear
Toyota RAV4 EV	Lithium-ion	35	166 Km EPA	Centre
Chevrolet Spark EV	Lithium-ion	21.3	132 Km EPA	Rear
Volkswagen e-Golf	Lithium-ion	24.2	190 Km (NEDC)	Centre
Mitsubishi I MiEV	Lithium-ion	16	100 Km EPA	Centre

* EPA = Environmental Protection Agency; * NEDC = New European Driving Cycle

Table 3.4: Battery Pack and its location in some state-of-the-art commercial cars

In addition, the battery pack should be spaced apart from the front or the rear end of the vehicle structure in order to protect the battery from potential impacts. An ideal space for such storage is in the centre of the vehicle beneath the vehicle floor, but because of the limited ground clearance in passenger vehicles, any such support structure must be carefully designed to use the available space for maximum effectiveness. **Table 3.4** shows the size of the battery packs available in different state-of-the-art commercial cars and their location with respect to the vehicle chassis.

US Patent 8561743 discloses a method to place as many batteries as possible on the EV in the central location without affecting the vehicle dynamics or safety. The patent discloses a battery assembly design in which a group of batteries S1 is located below the front seats, another group S2 is located under the floor between the front and the rear seat, and finally a group of batteries S3 is located below the rear seat.

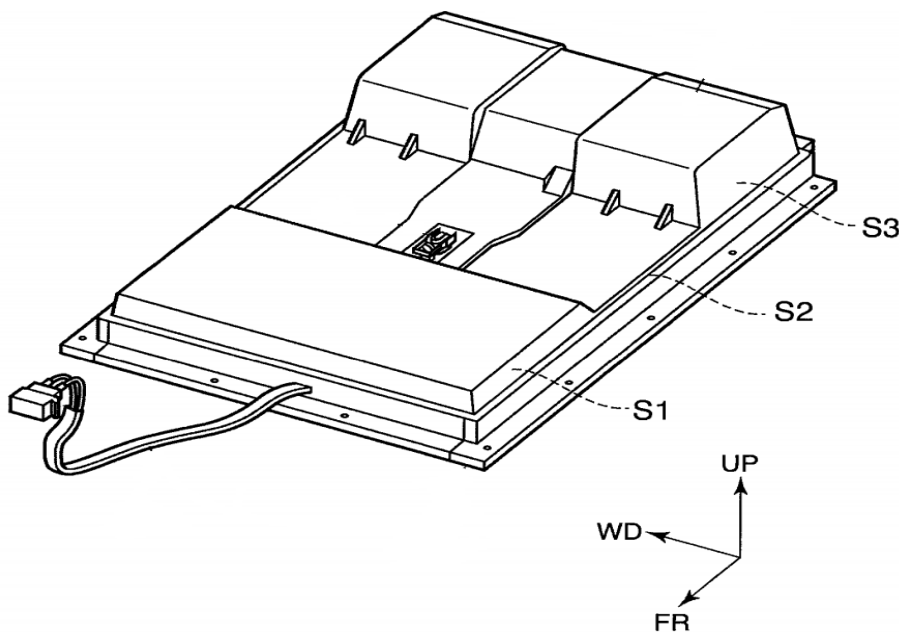


Figure 3.10: Nissan Leaf Battery Pack [124]

In groups S1 and S2, the batteries are stacked in a vertical direction such that the long side is oriented in the vehicle transverse direction and the short side is oriented in the longitudinal direction of the vehicle whereas in the group S3, the batteries are stacked such that the shortest side is oriented in the vehicle transverse direction. Depending upon the width of the lower part of the vehicle body, the number of batteries stacked or the length of the group S3 in the vehicle transverse direction can be minutely adjusted, thus using the space under the rear seat efficiently and placing a large number of batteries on-board. **Fig. 3.10** presents general design layout of prismatic Li-ion battery cells in a Nissan LEAF battery pack [124].

Furthermore, assuming that the height of the group S1 is h_1 , the height of the group S2 is h_2 , and the height of the group S3 is h_3 . Then, by making the height h_1 and the height h_3 greater than the height h_2 , space under the seats can be utilized more efficiently, and a higher number of the batteries can be placed in the vehicle without affecting the space availability for the passengers. In addition, as per this layout, the height h_3 is made greater than the height h_1 . Consequently, the sitting level of the rear seat becomes higher than the sitting level of the front seat which. This arrangement is more preferable as it provides a wide viewing angle for the

passengers in the rear seat [124]. **Fig. 3.11** helps to visualize the sitting level and a better angle of view available for rear passengers achievable through this design configuration [130].

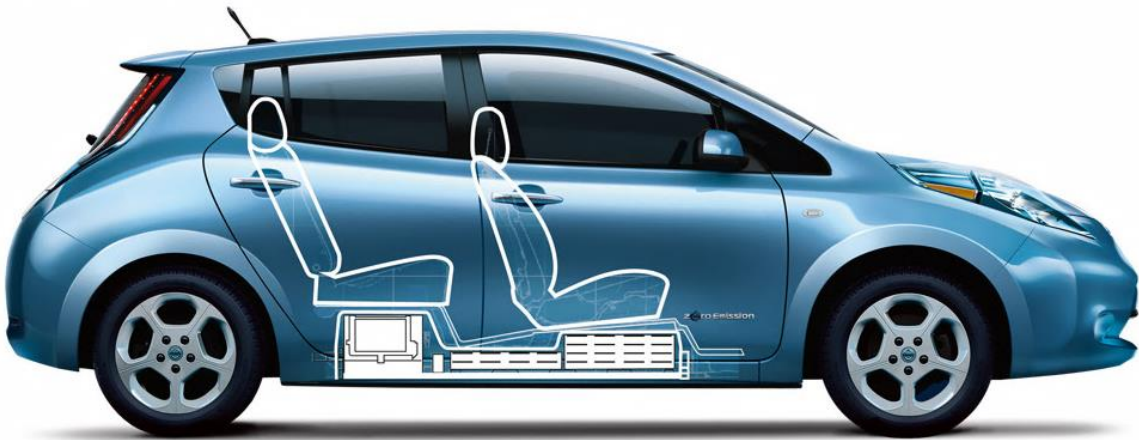


Figure 3.11: Placement of lithium ion battery pack in Nissan Leaf [130]

In view of making effective use of the cabin space and to improve safety in a collision, the battery pack is placed under the seats on the inner cabin side of the floor panel. However, in conventional vehicles, the seats are usually mounted via a mounting fixture on a seat rail for adjusting the available leg space in the vehicle body. As a result, access to the battery pack becomes restricted and if battery pack maintenance or replacement operations are to be performed, the rear seat and seat rails needs to be temporarily removed, rendering the task difficult and inefficient.

US Patent 7743863 is about a battery carrying structure that allows easy access to the battery pack for maintenance and replacement purposes. The carrying structure includes a vehicle floor panel with a stepping portion rising upward towards the rear of the vehicle. The battery is arranged at the step portion and the seats are placed above the battery. The configuration employs a tip-up mechanism, which enables the seat to tip up towards the front of the vehicle. The front part of the seat functions as a rotational pivot in this case. By virtue of this design,

easy access to the battery pack arranged in the stepping portion can be gained by tipping the seat toward the front of the vehicle via the tip-up mechanism [131].

3.7. Model design for a robust battery pack

Battery packs for the Nissan LEAF, the Tesla Model S and the Chevrolet VOLT are among the more advanced and well-designed existing EV battery packs [132-136]. As stated in Section 1, a robust battery pack should be thermally stable, properly insulated from any vibrations and able to maintain its structural integrity in a crash scenario. In view of this, the Nissan LEAF has been excluded from further considerations as it lacks an active battery thermal management system, which compromises its performance under extreme temperatures.

On the other side, the International Organisation for Standardisation is pushing for the standardisation of battery cell design for electric vehicles via the international standard ISO/IEC PAS16898 and the German pre-standard DIN SPEC 91252. The former specifies external dimensions and position of the connector tabs for cells to be used in different classes of EVs i.e. hybrid, plug-in hybrid and battery electric vehicles while the latter specifies the cell capacity. It has been acknowledged that in the longer term, usage of larger battery cells would provide better opportunity for cost reduction due to economies of scale. Consequently, the German pre-standard stipulates that the cells to be used for BEVs should have at least 40 Ah rating [137, 138]. Accordingly, the Tesla Model S battery pack, which uses 3.1 Ah cylindrical cells, might have to be redesigned.

In the Chevrolet Volt battery pack, 288 Li-ion pouch cells accounting for approximately 70% of the battery pack mass and around 55% of the pack volume are placed vertically in a T-shaped steel tray. **Table 3.5** puts the energy and power density of the Volt battery pack into perspective against the USABC 40-mile PHEV requirements. The battery pack is divided in 4 sections or compartments to create a first-level thermal barrier and restrict the thermal runaway event to

the affected compartment only. Further, the non-stacked type cell configuration used for the battery pack would also assist in minimising any gravitational push to the thermal runaway propagation rate.

Parameter	VOLT system level requirement	VOLT cell level requirement	USABC 40mile PHEV requirement
Specific Energy (Wh/kg)	100	145	142
Energy Density (Wh/l)	140	250	230
Specific Power (W/kg)	700	1000	317
Power density (W/l)	1000	1750	-

Table 3.5: Comparison of energy/power density of Chevrolet Volt with USABC targets [139]

In each compartment, foam spacers and repeating frame elements form pockets that are used to hold individual battery cells in place during a crash or a thermal runaway event. Further, thermal stability of Volt battery pack is improved by installing a 1-mm thick aluminium stamped plate between each battery cell as a cooling member such that it is adjacent to one side of each cell to dissipate heat. Each fin has 9 channels of equal length to take the fluid from inlet to outlet manifold insuring consistent heat transfer capacity across the face of each cell. They are all encased in a polyethylene copolymer coated aluminium cover. Not only does the polymer film coating functions as a heat reflector helping in achieving higher thermal performance, the cover also works as an additional isolative layer between the battery modules, passenger compartment and the other components. A silicon gasket seals the battery cover to the battery tray to give an air-tight packaging design [139].

The battery compartments are rigidly connected to each other through c-channel structural bars and end caps. They are then located and secured on the tray through steel hold-down brackets having oversized slots with nylon wedge blocks. The oversized slot makes it convenient to insert the wedge blocks based on the location of the battery sections. External metal strap on

the top and four tie rods at the bottom of each compartment limit their vertical and lateral movement while two end plates, one at each end, provide longitudinal support. Additionally, the lip of the hold-down bracket captures the feet of the repeating frame and eliminates any possible vertical movement of the compartments. Moreover, a higher degree of damping during vibration, shock and impact is achieved by placing rubber isolators in between the battery modules and the surface of the tray that carries them [140].

Lastly, the battery pack is placed in the centre of the chassis under the passenger seats such that it is able to serve as semi-structural element of the vehicle structure. At the same time, it is always kept away from the usual crash zones of the vehicle, i.e. the front and the rear. This strategic placement of the battery pack in Chevrolet Volt, allows it contribute to the 25 Hz bending stiffness of the vehicle body and ensure minimum damage to battery cells in a crash event resulting in higher crash-worthiness of the vehicle [141, 142].

3.8. Conclusions

This chapter reviews the features of a robust battery packaging design that can minimise the probability of battery pack failure. It has been found that:

1. Relative battery cell movement is a characteristic common to battery pack failures due to thermal runaway, mechanical vibrations and vehicle impact. Restricting this movement would provide a higher degree of protection against all of them.
2. There are a number of mechanical design features that are effective in controlling the relative battery cell movement namely cell spacers, rigid battery mounting frame and deformable electrode terminals.
3. The benefits of including a gas venting mechanism are also evident, in that this prevents the development of high-pressure events in the battery pack. Besides, hollow structure

of a gas exhaust duct can provide additional damping to the battery pack against transmitted vibrations during normal vehicle operation and/or vehicle collision.

In addition, a comparison of the design solutions disclosed by different patents with the Chevrolet Volt battery pack design reveals certain features that form the basic mechanical and structural requirements for a robust battery packaging system. These are summarized as follows:

- It is important to have a proper thermal barrier built into the battery packaging design. This means battery packs should be compartmentalized at module level and cell spacers should be integrated at cell level, which provides mechanical protection against thermal runaway propagation.
- Cell spacers are essential to restrict any cell movement that might happen during a thermal runaway event or vehicle impact. They also ensure that the integrity and performance of the battery thermal management system is not compromised during these events.
- Both vertical and lateral supports are necessary for proper vibration isolation. Besides, proper weight distribution can enhance the vibration isolation characteristics of an EV.
- The battery-mounting frame secured to the fixed members of the vehicle architecture helps to increase the rigidity and strength of the vehicle body. The mounting frame with its reinforcing members functions as a transferring path for load input during a vehicle collision.
- The battery pack should preferably be placed in the center of vehicle chassis under the passenger seats away from the usual crash zones of the vehicle structure i.e. the front and the rear.

Chapter 4

Selection of TMS for Modular Battery Pack

This page has been intentionally left blank

Chapter 4

4.1. Introduction

Various chemical reactions and electrochemical transport phenomena characterise the normal charging and discharging processes in a battery cell. Many of these reactions are exothermic in nature [143], highlighting that temperature affects the performance of a battery pack. General Motors estimate that if an EV is operating at sub-zero temperatures, its driving range can be reduced by up to 85% due to the sluggish charge kinetics of the battery pack. On the other hand, if heat transfer from the battery pack to the external environment is not sufficient, excess heat may accumulate in the battery pack, particularly when it is being operated in a hot climate or under an insulating environment. Hot spots can also develop, leading to an uneven temperature distribution across the battery pack, which can alter the discharging and charging characteristics of the battery cells [144, 145]. More importantly, the battery cell temperature may rise beyond the safety limits of 60 °C for Li-ion battery cells with $LiBF_4$ as electrolyte, risking battery pack failure [146].

Previous studies indicate that the battery cell temperature must be regulated within a predefined operating range to sustain a rate of reaction considered healthy for the efficient operation of battery cells. The recommended operational range for Li-ion battery cells is generally between 25 °C and 40 °C [147, 148]. Managing large temperature spikes and non-uniform thermal gradients across the battery pack is therefore the major concern in the design of a scaled-up battery pack essential for supporting an EV driveline. For these reasons, a thermal management system should be integrated with an EV battery pack, although the original equipment manufacturers (OEMs) have followed different approaches. **Table 4.1** separates the OEMs that

are in favour of using a battery thermal management system (TMS) from those who do not use it.

OEMs not using TMS	OEMs using TMS
Nissan	Tesla
BYD	General Motors
Volkswagen	Ford
Mitsubishi	Mercedes
Renault	Fiat

Table 4.1: List of OEMs distinguishing those that prefer to use a thermal management system for their EV battery packs from those, which do not

Several incidents involving battery cells overheating and catching fire have been reported to date. In many cases, the problem of battery overheating has caused OEMs to question the reliability of battery packs and loss of markets for battery-powered products. **Table 4.2** lists major product recalls and incidents of battery-powered products catching fire in recent history.

It is evident that thermal stability is a major issue for Li-ion battery packs. In addition, the high manufacturing costs of battery packs hinder the marketability of EVs. Mass-market appeal of EVs can be improved by using economies of scale generated by the implementation of a modular battery pack architecture. However, the concepts of mechanical and thermal modularity are inter-connected. The thermal independence of each battery cell must be ensured to preserve their interchangeability. In this chapter, different thermal management techniques that can be applied for the regulation of the thermal behaviour of Li-ion battery packs are qualitatively reviewed to ascertain their suitability for potential implementation in a modular system. In order to provide more context for this work, the chapter first presents a brief overview of the main issues that affect the behaviour of Li-ion battery cells in low/elevated ambient temperatures.

Date	Accident details	Reasons identified
November 3, 2016	Battery of Tesla Model S burns and explodes after a high speed impact in Indianapolis, US	Overheating and associated fire risks with battery packs.
September 5, 2016	2.5 million Note 7 phones recalled by Samsung	
August 13, 2016	Tesla Model S catches fire during the 'Electric Road Trip' tour in France	
April 1, 2016	ICAO Air Navigation Commission forbids transportation of Li-ion batteries on passenger aircraft at a state of charge exceeding 30% of their rated capacity	
July 6, 2016	More than 500,000 self-balancing hoverboards are recalled by 10 companies in the US	
January 2, 2016	Tesla Model S catches fire while charging at a supercharger station in Norway	
December 2, 2014	A cargo container packed with 5000 Li-ion batteries explodes after approximately 300 batteries experience escalated heating (Part of FAA tests simulates single battery uncontrolled overheating)	
November 7, 2013	Tesla Model S catches fire after hitting road debris in Smyrna, Tenn.	
March 18, 2013	Mitsubishi i-MiEV catches fire at their Mizushima plant in Japan	
January 7, 2013	A Boeing 747Dreamliner parked at Boston Airport catches fire	
September 2012	Chrysler temporarily suspend their demonstration program involving 109 Dodge Ram 1500 PHEVs	
December 2011	Fisker Automotive recall 239 Karmas delivered in the U.S	
July 18, 2011	EV bus catches fire in Shanghai, China	
April 11, 2011	Zotye M300 EV taxicab catches fire in Hangzhou, China	
September 3, 2010	Boeing B747-400F cargo plane catches fire in Dubai	
April 26, 2010	ACER recall 2700 laptop batteries	
January 2010	Two EV buses catch fire in Urumqi, China	
July 2009	Cargo plane catches fire before flying to USA from Shenzhen, China	
June 2008	Honda HEV catches fire in Japan	
2006 to date	Tens of thousands of mobile phone fires and explosions reported globally	

Table 4.2: List of key incidents involving battery fires and subsequent product recalls by major OEMs

4.2. Effect of temperature on Li-ion battery cells

Li-ion battery cells belong to a category of temperature-sensitive devices, since both their performance and their safety are influenced by their operating temperature [149]. Research has shown that commercial Li-ion battery cells achieve optimum performance near room temperature. This section discusses various challenges associated with operating Li-ion battery cells in temperatures that are far from this ideal range.

4.2.1. Effect of low temperature

It has been reported that *18650* type Li-ion battery cells can supply only 5% and 1.25% of the energy capacity and power capacity available at 20 °C, respectively, in low operating temperatures such as -40 °C [150]. Similarly, the driving range of the 2012 Nissan LEAF has been noted to drop substantially from 138 miles in ideal conditions to 63 miles at -10 °C. Moreover, information presented by different research groups [150-152] on the energy capacity of Li-ion batteries available during constant current discharge/charge tests conducted in low temperatures confirms that the usable battery capacity decreases as the operating temperature is reduced.

It was previously believed that the unsatisfactory performance of Li-ion battery cells at low temperatures was due to their limited electrolyte conductivity, which affects the Li-ion transportation rate between the two electrodes at these temperatures. However, further investigations suggest that inadequate electrode activity can also cause poor low temperature performance in Li-ion battery cells. Electrode activity refers to the combined effect of marginalised Li-ion transfer through surface films on Li-ion battery cell electrodes called the solid electrolyte interphase (SEI), and the high charge-transfer resistance and slow diffusivity of Li-ions within the anode materials [153-157].

Of the control factors, the choice of electrolyte for Li-ion cells is critical to the improvement of their low-temperature performance, primarily because of the intrinsic loss of ionic conductivity associated with low operating temperatures. In addition, SEI film's chemical composition and physical characteristics, such as its resistance and conformability to Li intercalation, depend on the salt forming the electrolyte, and parameters such as the quality of the anode material, and the mode and temperature of the SEI formation [158, 159]. SEI is a surface film approximately 5 Å to 800 Å thick, consisting of both organic and inorganic compounds, which keeps the electrolyte kinetically stable at anode potentials of less than 0.8V. The thickness of the film varies with the degree of anode graphitisation [160, 161]. Interestingly, this anodic film is highly resistive and interferes with the Li-ion transport kinetics at the electrolyte/electrode interphase [162]. Most research activities to date have therefore focussed on improving the conductivity and stability of electrolytes with effective SEI film formation. Approaches that have been central to this improvement are:

1. The use of co-solvents with low viscosity and low freezing temperatures, such as glymes, esters and lactones [163-165]
2. The formulation of new additives for electrolytes to further lower their freezing point [166-169]
3. The substitution of the existing lithium salt LiPF₆ with new mixtures to improve the charge transfer resistance and other characteristics of the SEI film [170-174]

4.2.2. Effect of elevated temperatures

As mentioned in Chapter 2, the United States Advanced Battery Council (USABC) has defined a performance target of 15 years' calendar life for all the battery packs to be used in HEVs, while the targeted calendar life for EV battery packs is 10 years [65]. It is therefore of utmost concern that elevated temperatures, i.e., temperatures greater than 40 °C, trigger battery-ageing

phenomena. Battery ageing refers to the loss of the energy/power retention capacity of a battery as a function of time and inhibits battery packs from meeting the USABC performance goals.

Most electrolytic compounds are not chemically stable at the potentials that exist on the anode, i.e., the negative electrode of a Li-ion battery cell. When a new battery cell is charged for the first time, some of the electrolyte is irreversibly reduced by reacting with free Li-ions near the electrode/electrolyte interphase, forming a thin film of metastable lithium alkyl carbonates, polymers and gaseous products on the surface of the carbonaceous anode. This film is pervious to lithium cations but impervious to electrons and any other chemical species floating in the electrolyte. Electrolytic reduction therefore continues until a steady state is reached where a surface film thick enough to block all the electrons out covers the entire anode surface. It is commonly known as SEI film and prevents the electrolyte from corroding the charged anode due to chemical reduction with little effect on the Li-ion transportation rate through it [175, 176].

It has been reported that at elevated temperatures, impervious SEI film starts to break down and dissolve, leaving the anode surface exposed to electrolytic corrosion accompanied with the irreversible loss of lithium. SEI film dissolution also disturbs the physical equilibrium of the metastable organic components of SEI and initiates their transformation into a more stable inorganic form like lithium carbonate. The ionic conductivity or permeability of the SEI film gradually decreases as the percentage of inorganic carbonates in it starts to increase, marking a significant reduction in the energy capacity and power output of the battery cell [146, 177].

Fig. 4.1 identifies the resulting effects of operating a battery cell at different temperatures and the causes leading to each failure mode.

Battery cell temperature	Cause	Leads to	Effect
High	Electrolyte decomposition	Irreversible lithium loss	Capacity fade
	Continuous side reactions at low rate	Impedance Rise	Power fade
	Decrease of accessible anode surface for Li-ion intercalation		
	Decomposition of binder	Loss of mechanical stability	Capacity fade
25 °C – 40 °C	Maximum cycle life		
15 °C – 24 °C	Superior energy Storage capacity		
Low	Lithium plating	Irreversible loss of lithium	Capacity/ power fade
	Electrolyte decomposition	Electrolyte loss	

Figure 4.1: Causes and effects of battery cell temperature on safety and performance

The electro-chemical breakdown of the SEI film on the anode begins to happen around 85 °C and is the first step of a three-step process that leads to cell meltdown [178, 179]. If insufficient heat is removed from the battery cell at this stage, a point is reached where this process and the governing chemical reactions become self-sustaining. The battery cell then starts to self-heat at a rate greater than 0.2 °C/min and this is classified as thermal runaway [109]. The second phase of the cell meltdown process is initiated when the battery cell temperature becomes greater than 140 °C. This marks the start of exothermic activity at the cathode, i.e., the positive electrode. Oxygen is rapidly released at the cathode and the battery cell now starts to self-heat at approximately 5 °C/min. The process finishes with oxidisation of the electrolyte as the cathode decomposes when the temperature reaches more than 180 °C. Self-heating rates around

11 °C/min have been cited for this phase, but they can increase up to 100 °C/min [180, 181].

The process is schematically described in **Fig. 4.2.**

The onset temperature for the exothermic reactions driving thermal runaway varies with the chemistry of the battery cells and their state of charge. In general, the higher the cell voltage or its state of charge, the lower the onset temperature for thermal runaway. For battery cells with the same chemistry, it varies with the load history of the specific cell and the abuse event [149].

1. Heating starts.
2. Protective layer breaks down.
3. Electrolyte breaks down into flammable gases.
4. Separator melts, possibly causing a short circuit.
5. Cathode breaks down, generating oxygen.

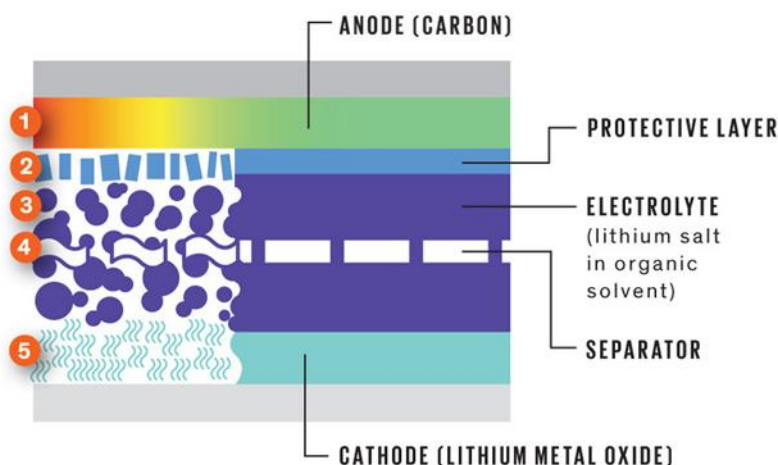


Figure 4.2: Illustration of thermal runaway process in Li-ion battery cells [182]

Research into electrolyte morphology indicates that $LiPF_6$ electrolyte solutions are characterised by increased decomposition at elevated temperatures [183]. It has also been reported that replacing cathode materials like $LiNiO_2$ and $LiNi_{0.8}Co_{0.2}O_2$ with $LiFePO_4$ or $Li[Ni_{3/8}Co_{1/4}Mn_{3/8}]O_2$ [184], or coating the surface of $LiCoO_2$ cathodes with Li_2ZrO_3 by a synchronised lithiation method [185], results in a thermally-stable cell. These positive discoveries have kept the research community motivated in their quest for stable electrolytes and safer cathode materials to improve performance at elevated temperatures. However, an appropriate thermal management strategy may provide additional safety by limiting thermal runaway.

4.3. Thermal Management Techniques

In this section, techniques developed to regulate the battery cell temperature near the pre-specified operating temperature are discussed. The first part presents methods that are exclusively applied for heating the battery cells. These are mainly used in extremely low ambient temperatures and are based on different strategies: internal heating, convective heating and pulse heating. Subsequently, more conventional battery thermal management methods are reviewed with the intent to select a TMS for modular battery packs. These methods are used for managing irregular thermal spikes and maintaining a uniform temperature distribution in the battery pack. Lastly, the suitability of some of the emerging TMSs is also reviewed for modular battery pack application.

4.3.1. Pre-heating Strategies

Ji and Wang [186] recommend pre-heating battery cells to room temperature before normal operation in sub-zero temperature environments. They attribute the sluggish Li-ion kinetics in battery cells to the large change in their impedance at sub-zero temperatures. It has been noticed that at temperatures such as -20 °C the impedance levels can increase by approximately 10 times their value at room temperature and up to 20 times at -30 °C, marking a significant reduction in available energy and power from a Li-ion battery pack [157, 187]. High impedance accounts for large Ohmic heat generation and may induce a notable rise in battery cell temperature and restore the original performance index. The key is to appreciate the strong relationship between the thermal and electrochemical interactions in the Li-ion cells at sub-zero temperatures.

It is noteworthy that the energy balance between the electrochemical heat generation inside the battery given by Equation 4.1 below and the heat dissipated to the surroundings defines the battery cell temperature profile, which in turn regulates the temperature-dependent

electrochemical processes inside the cell [149]. A good understanding of the constantly shifting equilibrium between heat generation and heat dissipation is fundamental to the development of heating techniques for Li-ion battery cells operating in sub-zero temperatures.

$$q = -IV - \sum_l I_l T^2 \frac{d}{dT} + \sum_j \frac{d}{dt} \left[\int \sum_i c_{i,j} RT^2 \frac{\partial}{\partial T} \ln \left(\frac{\gamma_{i,j}}{\gamma_{i,j}^{\text{avg}}} \right) dv_j \right] + \sum_{j,j \neq m} \sum_i \left[\left(\Delta H_{i,j \rightarrow m}^o - RT^2 \frac{d}{dT} \ln \frac{\gamma_{i,m}^{\text{avg}}}{\gamma_{i,j}^{\text{avg}}} \right) \frac{dn_{i,j}}{dt} \right] \quad (4.1)$$

This principle has been utilised by Toyota and a system that uses the internal resistance of the battery to increase its temperature during vehicle operation was disclosed in US patent 6163135. In the design, battery temperature was closely monitored by temperature sensors. As the temperature falls below a predetermined level, a central processing unit performs a controlled charge or discharge of the battery to bring its temperature back up to the required level. The design exploits the basic quality of electrical machines to function as a simple load during the battery-discharge phase, and as a prime mover or generator if operated in reverse, i.e., the charging process. However, the system works only when the vehicle is switched on [188].

The limitation of this system was overcome by the design disclosed in US patent 7154068. The design includes a heater carefully placed between the top and the bottom layer of cells in the battery pack that can be regulated via the vehicle system controller. The heater is a positive temperature coefficient element the resistance of which to current flow increases as the ambient temperature decreases. In addition, the heat generated by it is directly proportional to the current flowing through it. An advantage of this heating mechanism is that it is battery-driven and therefore does not require any power cord to be plugged into an external power distribution system. Furthermore, the vehicle controller switches off the heater if the battery SOC falls below a pre-set value or the vehicle has/had not been in use for a long time to save energy. This

feature is a big advantage when operating an EV in remote locations where distribution boxes might not be readily available [189].

Another way of improving the low temperature performance of a battery pack based on the fluid heating strategy is disclosed in US patent 7264902. The intent of this design is to provide a system that enables rapid heating of the battery pack, especially during the start-up phase, and to permit strict control over the battery cell temperature. Therefore, one or more good heat conductors with heating medium flowing in them are arranged adjacent to each battery cell. This ensures that heat transfer through conduction from the heating system to the battery cells is not affected by the presence of any other medium between them. Each cell is formed in a thin plate shape to enhance the heat conduction rate in the system. Moreover, the liquid electrolyte in the battery cells is replaced with a solid electrolyte. The replacement allows the reduction of the liquid seals used in the pack, thereby minimising its effective heat capacity. This design allows rapid heating and cooling of the battery pack [190].

Pesaran and co-workers compared the various preheating strategies using the finite element modelling technique. The problem was modelled as a pure heat-transfer phenomenon and the non-linearity introduced due to the complex electrochemical-thermal coupling in a battery pack was ignored. The evolution of battery cell temperature as a function of used energy capacity was then studied. Both the studies found core heating to be the most energy-efficient preheating method. Furthermore, only alternating current (AC) signals should be employed, as direct current (DC) pulses can cause damage to the battery core [191, 192]. In addition, Stuart and Hande experimentally analysed the possibility of using AC signals of different amplitudes for the external preheating of battery packs. In their investigation, lead acid batteries and nickel metal hydride batteries were exposed to AC signals of frequencies of 60 Hz and 20 kHz, respectively. It was observed that the speed of heating increases as the amplitude of the AC signal is increased [193].

While several pre-heating techniques for EV battery packs have been proposed, the selection of the most suitable strategy should be done only after ascertaining the cost and effect of heating time on the usable battery capacity and the cycle life of the battery pack.

4.3.2. Conventional temperature control methods

In recent years, a number of techniques for readily removing heat from a battery pack have been tried and tested by various research groups across the globe. They can be classified in various ways, as explained in the following sections:

Medium used: A battery thermal management system can be differentiated by the working fluid used in the cooling loop. They can be:

- A. Air-cooled: unidirectional or reciprocating
- B. Liquid cooled:
 - a. Conventional liquid cooled
 - b. Cold plate
 - c. Heat pipe
- C. Phase change materials
- D. Any combination of the above

Power consumed: If a TMS includes any power-consuming equipment, such as evaporators, blowers and pumps in the cooling loop, it is considered an active system; otherwise, it is classified as a passive system. In addition, TMSs use a working fluid or coolant that absorbs the excess heat and transfers it out of the system. This heat can be absorbed either as sensible heat, thus raising the temperature of the working fluid, or as latent heat, which causes it to undergo phase transformation. In general, all active systems remove heat as sensible heat of the fluid, while passive systems remove it as a latent heat.

Arrangement

- A. Series - Parallel
- B. Direct - Indirect

C. External - Internal

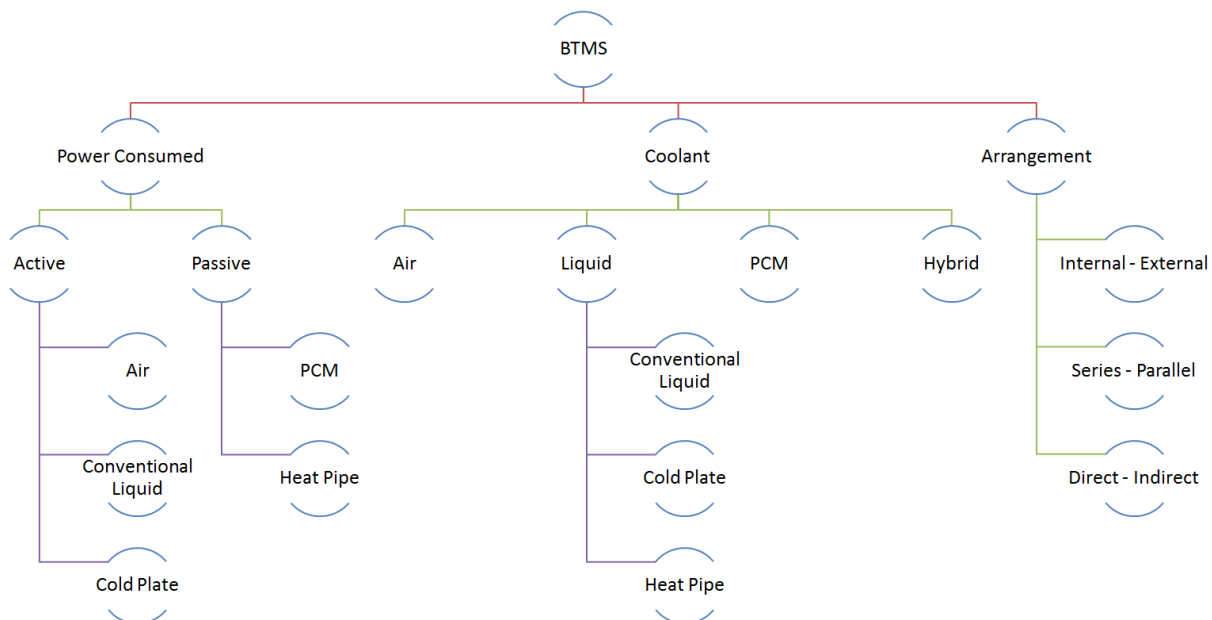


Figure 4.3: Classification of different battery thermal management techniques

4.3.2.1. Air-cooling

Blowing air through a fan [194] or from a wind tunnel [195] over a battery cell is probably the simplest and most cost-effective way of regulating its temperature. It has therefore garnered interest from several OEMs as a prospective thermal management solution for commercial EV battery packs. Many research activities have also been initiated mainly to consider the battery layout and optimise the airflow or the wind speed around it, and minimise the energy consumption and cost accrued. For instance, Xu and He [196] investigated different battery layouts and illustrated that arranging the batteries horizontally rather than longitudinally shortens the airflow path, thereby enhancing the heat dissipation characteristics of an air-cooled battery pack. Their experiments also proved that a double U-type duct could readily satisfy the heat dissipation requirements under a variety of environmental conditions, discharging/charging rates, or SOCs.

Fan et al. numerically studied the transient effect of airflow rate and gap spacing on the performance of an air-cooled battery pack made of eight evenly spaced 15 Ah lithium manganese oxide pouch cells. The Li-ion battery pack was subjected to an aggressive driving test profile represented by the US06 profile scaled by a factor of 1.3. They reported that for a fixed flow rate of $20.4\text{ m}^3/\text{h}$, an improvement of $0.41\text{ }^\circ\text{C}$ in the temperature uniformity within the battery pack was observed as the gap spacing increased from 1 mm to 5 mm. In addition, for a fixed spacing of 3 mm, the maximum temperature rise measured in the pack decreased by $1.8\text{ }^\circ\text{C}$ when the flow-rate in an air-cooled battery was doubled from $20.4\text{ m}^3/\text{h}$ to $40.8\text{ m}^3/\text{h}$ [197].

In another study, Park numerically modelled the effect of an airflow manifold design for a particular battery layout (37 coolant passages 3 mm in diameter formed between 72 battery cells divided equally into 2 rows). Five configurations were studied: rectangular-shaped, tapered manifolds (vertically contracting/expanding from 10 mm \leftrightarrow 20 mm), control design, and lastly, rectangular ventilation hole placed at the outlet of a tapered manifold. He observed that it was possible to achieve the desired cooling effect in an air-cooled pack by including pressure-relief ventilation and a tapered manifold in the wind/cooling tunnel. Further, a decrease from 47 W to 27 W in power consumption of fan was reported due to the presence of a tapered manifold with a ventilation hole [198]. Giuliano et al. studied metal-foam based air-cooled heat exchangers (HXs) for large-capacity lithium titanate battery packs. Their study confirmed that air-cooled HXs consume less power than liquid-cooled HXs and can be used effectively to regulate battery temperature in automotive applications [199].

While simple and sturdy in construction, air-cooled battery thermal management systems generally employ a unidirectional coolant flow in which ambient or conditioned air is admitted through one side of the battery pack and discharged from the opposite side. This is primarily

the reason why air-cooled systems struggle to maintain a uniform thermal distribution and a gradient of less than 5 °C across a battery pack. This was confirmed by Lou, who designed a cinquefoil battery pack containing 5 modules in order to understand heat dissipation through an air-cooled Ni-MH battery pack. He noticed that although the maximum temperature was kept in check, the battery cells near the fan were operating at a lower cell temperature than those further away. In addition, the existence of a thermal gradient higher than 5 °C was confirmed for the battery pack [200].

US patent 7172831 illustrates that it is possible to overcome this basic limitation of air-cooled battery thermal management systems by using bi-directional or reciprocating airflow. Such a system causes the direction of coolant flow to reverse after a pre-set period. As a result, the temperatures of battery cells on opposite sides of the pack averaged over time can be found to be approximately equal. It was further pointed out that the temperature difference between any two adjacent battery cells can be minimised by optimising the duration between the two successive flow reversals [201].

The authenticity of this claim has been verified by Mahamud and Park [194]. They numerically studied the effect of reciprocating airflow on the performance of an air-cooled battery pack made of $LiMn_2O_4/C$ cylindrical cells, using a lumped thermal capacitance model and a two-dimensional computational fluid dynamics model. The computational results were validated using an in-line tube bank set-up. It was found that a reciprocation period of 120 seconds can reduce the maximum cell temperature and temperature non-uniformity in the battery pack by 1.5 °C and 4 °C (equivalent to a 72% reduction), respectively, in comparison with the temperatures recorded for a battery pack with unidirectional air flow. Subsequently, He and Ma [202] developed an observer-based control strategy to regulate the amount of cooling flow required for reciprocating air flow systems. It was demonstrated that the cooling flow

requirement for the reduction of the non-uniformity of thermal gradients existing in the battery pack from 4.2 °C to 1 °C (i.e., by more than 76%), is decreased by 38% if the observer-based control strategy is used to regulate the air flow in reciprocating systems. In addition, He and co-workers [203] also developed a hysteresis controller that can reduce the parasitic power consumption of reciprocating air flow systems by 84%. However, the maximum cell temperature in this case was noted to be 0.7 °C greater than the instance when no control strategy was implemented.

4.3.2.2. Liquid Cooling

Studies have indicated that even extremely high air flow rates may not meet the heat dissipation requirements for an air-cooled EV battery pack that is being discharged or charged at an aggressive rate in a hot ambient environment [204, 205]. Furthermore, the very low thermal conductivity of air may make it hard to cool a battery pack in a hot environment, thus compromising its safety. An alternative way of cooling a battery pack is by circulating a liquid coolant via jackets or through distinct tubes around it or placing, it directly on a liquid-cooled plate. In a slightly different arrangement, battery modules can be submersed in a di-electric liquid to increase the surface area available for heat dissipation. Such a thermal management system has been demonstrated by Pendergast et al., who placed a battery module with Panasonic 18650 cells arranged in an aluminium casing under water for cooling [206]. The higher heat capacity and thermal conductivity of traditional liquid coolants like water, acetone, glycol or oil make a liquid-cooled system more effective than an air-cooled system, despite the added mass, complexity and higher operating costs [207, 208]. However, not every liquid coolant may be as effective as others may for certain applications. For example, Kim and Pesaran found while experimenting with different coolants on cylindrical cells that water–ethylene glycol achieved superior cooling performance to mineral oil in an indirect liquid-

cooled system. However, due to the heat transfer coefficients in the case of a direct-contact cooling system, the performance of mineral oil was comparable to that of other coolants [209].

The previous section has described some examples of studies focussing on conventional liquid-cooled TMSs, which remove heat from a battery module via liquid circulating in a jacket wrapped around it or in channels between the batteries. However, liquid-cooled systems can also be designed using cold plates and heat pipes, and these are described in the following sections

a. Cold Plates

Cold plates are mostly preferred where strict space-limitations apply, such as in EV applications. They are thin-walled metal pressings with inbuilt channels for a liquid coolant to carry heat. In a liquid-cooled TMS with cold plates, metal pressings are generally arranged between adjacent battery cells and a liquid heat-transfer medium is pumped through the inbuilt channels. The liquid coolant then removes all the excess heat from the battery cells and transfers it to an external HX for dissipation to the ambient environment. The cooling performance of a cold plate is assessed in terms of the heat transfer rate, the thermal distribution across the pack, the power consumption depending upon the convective heat transfer coefficient between the plate and the liquid coolant, or the coolant flow rate and ambient temperature.

In the design of cold plates for EV battery packs, different channel designs and geometries may be required for different applications, whereas most current research models of cold plates are based on a square-edged channel geometry. Furthermore, it can be concluded from the concurrent activities in relation to fuel cells that channel geometry is a critical parameter for cold plate design. In addition, the manufacture of square-edged channels is very expensive and sometimes impracticable [210]. This prompted Fisher and Torrance to deviate from square-

edged channels and assess heat transfer through channels with rounded corners. They used the boundary element method to evaluate the performance of rectangular, diamond-shaped and elliptical channels. The results suggested that rectangular channels are more efficient than the other two configurations. Moreover, it was found that although more channels with elliptical design can be accommodated in the same packaging space, the heat transferred through a cold plate with elliptical channels is approximately 5% less than that transferred through a cold plate with rectangular channels [211, 212].

Studies by Yu et al. [213], Choi et al. [214] and Chen et al. [215] confirm that, in addition to the channel geometry, another parameter that can have a significant influence on the performance of a cold plate is the channel configuration, i.e., the route of coolant channels inside the metal pressing. Broad categories under which they can be grouped are - serpentine channels, parallel channels, and multi-channels. Jin et al. designed a thermal management system for EV battery packs using oblique fin cold plates. It was found that in cases of heating loads below 1240 W, this system could maintain the battery cell temperature to less than 50 °C with a flow rate lower than 0.9 l/min [216]. On the other hand, Jarrett and Kim employed cold plates with serpentine channels for the same purpose. Based on a CFD analysis, they discovered that channels of the greatest possible widths are necessary to achieve the lowest average temperature and minimum coolant pressure drop. In contrast, channels with a narrow inlet and gradually widening towards the outlet are required for maintaining thermal uniformity [210]. Huo et al. achieved the best cooling performance for a 5C discharge of a rectangular Li-ion battery cell by directing water into mini-channels on the sides of the electrode at a flow rate of $5 \times 10^{-4} \text{ kg/s}$. However, they also observed an increased risk of failure at ambient temperatures higher than 25 °C and recommended a two-phase TMS for high-temperature applications [217].

b. Heat Pipes

A thermal management system with heat pipes is a passive system driven by capillary action of a wick material lining the internal surface of a vacuum-sealed shell. They have been in existence since 1942 when they were first introduced by R.S. Gaugler, and remove heat through the liquid-to-vapour phase change of a working liquid. The choice of working fluid depends upon the heat pipe shell material characteristics, but commonly used liquids include water, acetone, methanol and ammonia. A heat pipe can be usually divided into three parts; shown in

Fig. 4.4:

1. Hot end or evaporating section
2. Adiabatic part or transport section
3. Cold end or condenser

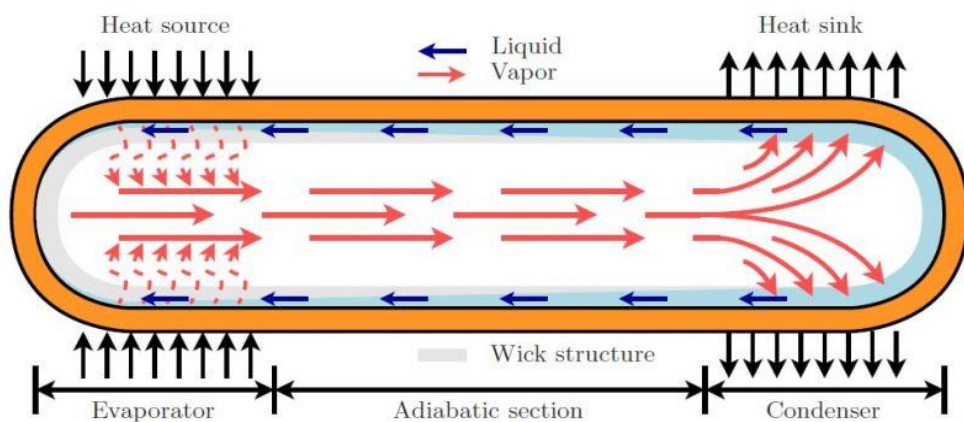


Figure 4.4: Schematic of a traditional heat pipe with tubular structure and closed ends [218]

The liquid within the wick absorbs the excess heat from the battery cells, which are arranged towards the hot end of the heat pipe, and evaporates. The increased vapour pressure and reduced molecular density create a pressure gradient in the pipe that drives the hot vapours to the condensing section where heat is rejected to the HX. The capillary forces developed in the wick draw the condensed liquid back to the evaporator, thus completing the heat transfer cycle. It is noteworthy that since a vacuum exists in the heat pipe, the working fluid vaporizes at a

temperature much below its normal boiling point, allowing the heat pipe to remove large quantities of heat efficiently at much lower temperatures. Furthermore, the flexible geometry, low maintenance requirements and thermal conductivities that are twice the order of magnitude of solid conductors such as aluminium or copper, make them attractive as a TMS option for EVs.

Mahefkey et al. have designed a TMS incorporating heat pipes for Ni-Cd battery cells while Zhang et al. have done this for Ni-MH batteries. Both groups of researchers found that heat pipes can mitigate any thermal excursions in the battery pack [219, 220]. Swanepoel investigated the possibility of using a pulsating heat pipe (PHP) with ammonia as the working fluid to regulate the battery cell temperature of Optima Spirocell lead-acid batteries. Based on experimental results and simulations, he discovered that a PHP with an internal diameter of less than 2.5 mm can successfully manage the thermal variations in the pack [221]. On the other hand, Wu et al. attempted to dissipate heat from a 12 Ah cylindrical Li-ion battery pack using two heat pipes with aluminium fins attached to their cold ends. Their experiments also confirmed that heat pipes can be used to keep battery cell temperatures in a safe range [222].

Various research groups have also tried to combine the benefits of heat pipes as a TMS with other cooling methods, in order to enhance the overall system performance. In one such trial, Jang and Rhi combined a loop thermo-siphon, which works on the same principle as a heat pipe, with forced air-cooling. In their experiments, they managed to control battery cell temperatures under 50 °C and 45 °C with pure water and acetone as coolants, respectively [223]. Rao et al. monitored the influence of cooling the condensing part of a heat pipe on its performance. They reported that the system could maintain the battery cell temperature under 50 °C as long as the heat generated by each cell was less than 50 W [37].

Vibrations ranging between 0 and 100 Hz can be transmitted to the battery pack in an EV from its top body. It is therefore imperative to analyse the influence of vibrations and shocks on the performance of a heat pipe before defining it as fit-for-purpose in EVs. Connors and Zunner studied the behaviour of a flat heat pipe under vibrations. The heat pipe had an internal lining of copper powder to function as a wick material. They reported zero degradation in the cooling performance of a flat heat pipe when exposed to vehicle shock and vibration [224]. Similar conclusions could be drawn from the reports of Guo et al., who studied the effect of mechanical vibrations on the heat-dissipation abilities of rectangular grooves. They observed that the wetting area is enlarged by the vibrating motions of heat pipes. Vibrating motion also intensifies the heat transfer through the microgrooves, which enables the heat pipe to operate without any performance degradation in a vibrating environment [225].

Yet, heat pipes have found limited usage in battery thermal management systems owing to the high capital costs incurred due to the application of copper as a wall and wick material, and the complicated fabrication process. However, recent advances in the manufacture of aluminium heat pipes promise substantial reductions in total system costs [226-229]. In addition, the weight savings realised by replacing heavier copper with lighter aluminum metal will benefit the EV sector.

4.3.2.3. Phase Change Materials

Traditional battery thermal management systems using forced-air cooling and liquid cooling are generally complex and bulky. They also add unavoidable electrical load in the form of fans, pumps, blowers, and HXs to the limited energy storage capacity of an EV. These undesirable disadvantages have increased the expectations for novel thermal management systems. A simple passive solution comprising battery cells placed in a matrix of phase change materials with zero maintenance requirements has therefore been proposed as an alternative by a research

group at the Illinois Institute of Technology. This solution employs the solid-liquid phase transformation of organic/inorganic/eutectic phase change materials (PCMs) to remove the thermal non-uniformities of the battery pack [230, 231].

PCMs require low maintenance and have therefore piqued the interest of several research groups. For example, Khateeb et al. studied a Li-ion battery pack made of eighteen 18650 Li-ion cells and filled with a mixture of PCM and aluminium foam. They examined the thermal behaviour of this pack with the help of a numerical model that was validated through experiments at a later stage. It was also demonstrated through their experiments that the temperature rise in a battery pack can be reduced to half by using a TMS with PCM and aluminium foam, as opposed to the case where no TMS is applied [232]. Mills et al. simulated a laptop battery pack with six 2.2 Ah Li-ion cells and realised a uniform thermal distribution after using expanded graphite saturated with PCM as the thermal management solution [233]. Sabbah et al. compared the performance of a TMS with PCM to that of an air-cooled system using numerical methods and experiments. They demonstrated that the former could keep the temperature of a Li-ion battery cell below 55 °C, even at a constant discharge rate of 6.67C [234]. Kizilel et al. experimented with PCM-filled high-energy Li-ion battery packs and achieved a uniform thermal distribution under both normal and abusive test conditions [235]. Rao et al. also tested eutectic PCMs for 8 Ah prismatic *LiFePO₄* battery cells. The results of numerous experiments simulations indicate that PCMs may be a practical solution to the thermal issues affecting EV battery packs [236]. Li et al. analysed the effectiveness of a PCM-filled copper foam sandwich panel as a cooling system for prismatic power batteries. The tests reflected a lower surface temperature and a better thermal uniformity in the battery module after the integration of the PCM-filled panels [237].

The mechanical behaviour of the thermal management system is equally as important as its thermal performance for making a reliable automotive-grade solution. It is beneficial to have a system design with a higher heat absorption rate, but it also necessary to have the required strength and stability to withstand normal stresses during daily vehicle operation. With this in mind, Alrashdan et al. undertook a systematic study to characterise the effect of the thermo-mechanical properties of eutectic PCMs (paraffin wax/expanded graphite), such as tensile and compression strength and thermal conductivity, on the reliability of Li-ion battery packs. At low as well as room temperatures, improvements in the thermo-mechanical properties, including tensile strength, burst strength, compression strength, and thermal conductivity of the pack were noticed, while they decreased at elevated temperatures [238].

However, phase-change materials have relatively low thermal conductivities. Consequently, they have slower regeneration times and cannot be effective in applications that may include fast charging followed by a quick discharge and then a fast charging of a battery pack in a short time. Several heat transfer enhancement techniques have been investigated for PCMs, which include the following:

1. The use of fixed and non-moving surfaces such as fins and honeycombs [239-243]
2. The employment of composite PCMs [244-246]
3. The impregnation of porous material [247-254]
4. The dispersion of high-conductivity particles in PCMs [255-259]

4.3.3. Emerging Techniques

Several other cooling techniques have been developed in recent times. These techniques offer many advantages, including significant energy and cost-saving potential along with high scalability, over traditional forced-air or liquid cooling methods. In this section, some of these emerging alternatives are discussed in relation to TMS applications.

4.3.3.1. Thermoelectric Coolers

Thermoelectric coolers (TECs) are practically maintenance-free solid-state heat pumps with no moving parts. They utilise doped semiconductor elements, comprising of a series of p-type and n-type thermo-elements, sandwiched in thermally-conductive but electrically-insulating substrates to transfer heat across a junction of two dissimilar materials via the Peltier effect. The p-type material has excess positive charge carriers called holes, whereas n-type material carries more negative charge carriers or electrons. The direction of heat transfer depends on the polarity of voltage applied to the TE modules. An illustration of a TEC module is provided in **Fig. 4.5.**

As voltage is applied to a TEC, electrons jump from a lower energy level of the p-type thermo-element to a higher energy state in the n-type thermo-element by absorbing thermal energy from one side of the module, in effect cooling it. The electrons drop to a stable energy level by rejecting this heat on the other side of the TEC module. Accordingly, the same TEC module can be made to function both as a cooler and as a heater by reversing the direction of current flow across the junction.

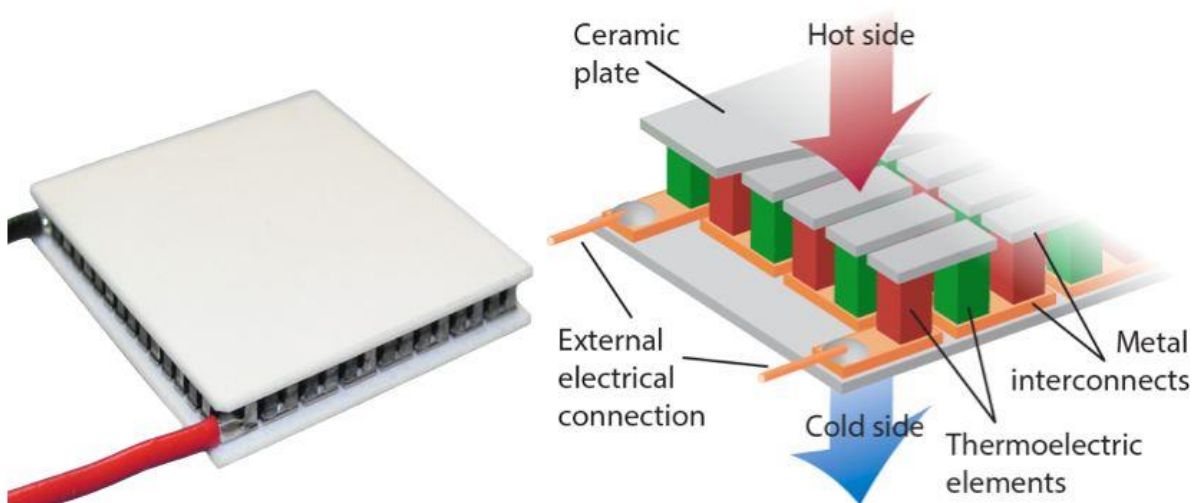


Figure 4.5: Illustration of a thermo-electric cooling module [260]

Other advantages of TEC are:

- It is compact and lightweight
- It is acoustically silent and operates without any vibrations
- It facilitates precise temperature control to within ± 0.1 °C
- It has low manufacturing costs and a wide operating temperature range
- It can cool below ambient temperature
- It is location independent, and can operate in any spatial orientation, at high G-levels or in zero gravity

More importantly, the cooling elements of a TE module are easily scalable [261-263]. For these reasons, TECs have been previously applied for climate control in EVs [62, 264-266]. However, the figure of merit (ZT) for the currently available bellerium telluride based TECs is approximately 1. Consequently, the maximum coefficient of performance obtainable with these devices is limited to 10%. It has been suggested that a ZT close to 4 is required to achieve cooling performance comparable to other thermal management techniques [267]. Research to develop new thermoelectric material and achieve much higher ZT is therefore required to promote TECs as a viable solution for the temperature control of EV battery packs. Nonetheless, the thermoelectric refrigeration method has been used in the new battery thermal management system developed by the Gentherm Incorporation, details of which are disclosed in US patent 8974942. This patent presents the design of a highly integrated yet simplified assembly of thermoelectric modules that can heat and cool separate battery cells simultaneously [268]. It is therefore believed that, owing to their flexible form and scalability, TECs may prove pivotal to the development of modular battery packs.

4.3.3.2. Thermo-acoustic refrigeration

It is known that thermal gradients can result in sound generation; the interaction between thermodynamics and acoustics can therefore also be utilised to produce a refrigerating effect.

Thermo-acoustic refrigerators (TARs) are based on the Stirling cycle. They use resonant high intensity sound waves and a compressible mixture of inert gases as working fluid to pump heat.

A TAR assembly includes a gas-filled resonance tube containing a regenerative unit, called a stack or regenerator for the respective heat pumping processes, and two heat exchangers. **Fig.**

4.6 shows the cross-sectional layout of a TAR with the different components.

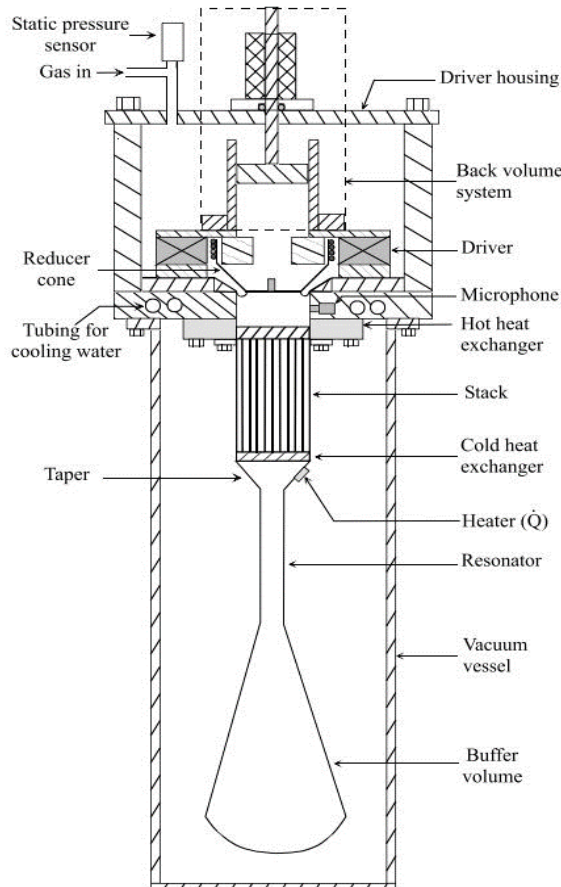


Figure 4.6: Cross-section of thermoacoustic refrigerator illustrating various parts [269]

The regenerative unit is a set of concentric cylinders, square rods or uniformly spaced parallel plates strategically arranged between two heat exchangers, such that they reside between the velocity node and antinodes within the resonance tube. Further, an acoustic driver like an

electric transducer, a moving-coil loudspeaker or a sinusoidal drive mechanism, is placed on one side of the resonance tube while the other end is closed [270, 271]. The selection of the appropriate driver is based on the design requirements, such as light weight, weight-to-volume ratio, high *BI*-factor and low vibration losses [269].

The acoustic driver produces cyclic variations of acoustic pressure in the resonance tube, which causes expansion and compression of the inert gases contained in it. In response, the working fluid starts to oscillate in the resonance tube. Imperfect thermal contact of the regenerative unit with the acoustically oscillating gaseous mixture creates necessary phasing. This enables the regenerative unit to continuously absorb heat from the resonance tube at the end near the velocity antinode and reject it to tube walls closer to the velocity node. This natural phasing also allows the TAR to operate without requiring moving parts other than the oscillating working fluid [272, 273]. TARs can achieve heat transfer either via a standing pressure wave or by means of a travelling pressure wave. These two differ in phasing between pressure and velocity. Because of this phasing, regenerative units with large channels are required in standing pressure wave devices to artificially delay the heat exchange between the tube walls and the stack. Conversely, much smaller flow channels can be utilised for travelling pressure wave refrigerators, as heat transfer starts immediately after the working fluid is subjected to a pressure change. They are therefore more efficient and compact than standing pressure wave pumps.

Thermoacoustic pumps utilising standing pressure waves perform a surface heat pumping process, whereas travelling pressure waves are used in a conventional Stirling-cycle heat pumping process [274, 275]. TARs require no lubrication, sliding seals or expensive components. They can be manufactured using only low-tolerance machined parts. Furthermore, existing vibrations can be readily isolated in TARs, as they use compressors of

low moving mass (approximately 15 gm) and high oscillation frequencies (~ 400 Hz) [272]. The absence of moving parts and vibrations and low manufacturing costs make TARs excellent candidates for battery TMS in EVs.

4.3.3.3. Magnetic Refrigeration

Certain ferromagnetic materials and paramagnetic solids are characterised by the intrinsic coupling of their crystal lattice to the external magnetic field. They are called magnetocaloric materials and this coupling is known as the magnetocaloric effect. Under adiabatic conditions, it is quantified by a reversible temperature change observed in the magnetic solid due to variation in its magnetic entropy upon exposure to a varying external magnetic field [276].

The application of a magnetic field induces spin polarisation in magnetocaloric materials, which makes their molecules more stable, thus reducing their degrees of freedom and magnetic entropy. As the total entropy of a magnetic solid remains constant if adiabatic conditions are maintained, vibrations in the crystal lattice and the entropy of free electrons in the material increase to compensate for the lost magnetic entropy. Consequently, an increase in material temperature is noted. In contrast, a cooling effect is observed as the molecular magnetic ordering returns to the initial alignment state by absorbing thermal energy from the crystal lattice and free electrons when the externally-applied magnetic field is removed [277]. Typically, a field change of 1 Tesla can cause the material temperature to change between 1.5 to 2 K, depending upon the strength of the applied magnetic field and the absolute temperature, but the effect maximises around the Curie or phase transition temperature of the magnetocaloric material [278, 279].

Magnetic refrigerators for room temperature applications utilise active magnetic regenerators (AMRs) similar to that shown in **Fig. 4.7**. An AMR combines the functionality of an indirect heat exchanger with a heating/cooling mechanism. It has a porous structure and is made up of

magnetocaloric materials like gadolinium and perovskite manganese oxides [280], to maximise the adiabatic temperature span associated with the refrigeration cycle.

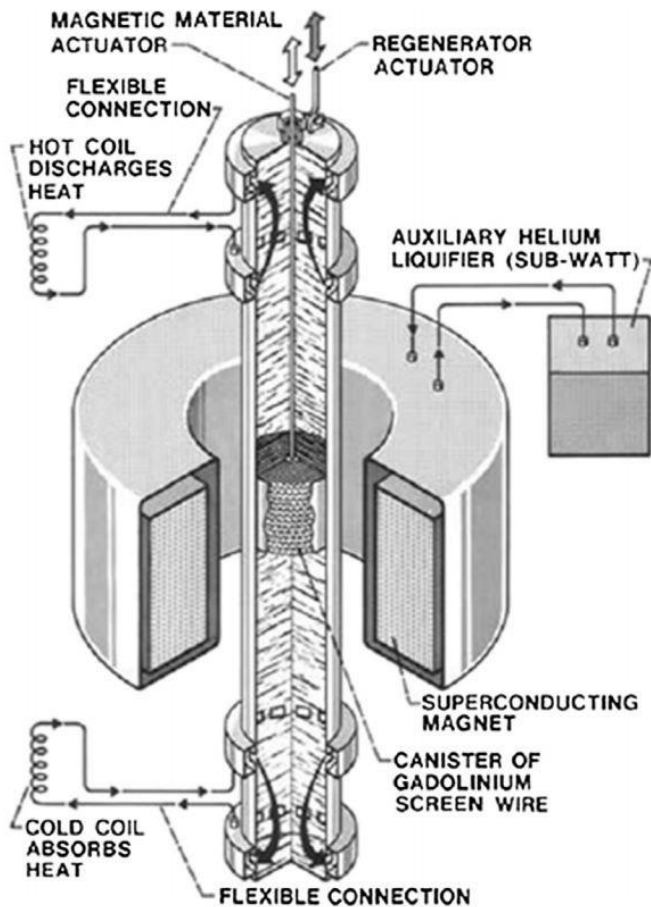


Figure 4.7: Illustration of an active magnetic regenerator used for room-temperature applications [281].

In this device, the regenerator is maintained near the Curie temperature and an external magnetic field is periodically applied to it, making it circle in a magnetic entropy-temperature loop. Subsequently, a heat transfer fluid, usually helium or hydrogen gas or a water-based solution, is circulated through the porous structure of the regenerator from the cold end to the hot end. A thermal wave front is established as the working fluid traverses the structure absorbing heat from it. The heat is then discharged to a hot bath at temperatures greater than the bulk temperature. The fluid flow is terminated when the wave front reaches the hot end of the regenerator, i.e., the exiting temperature drops to the hot bath temperature. This also acts

as a signal to start the adiabatic demagnetisation of the regenerator followed by the circulation of the working fluid in the reverse direction, completing one refrigeration cycle [282, 283].

Magnetic refrigerators can operate at 30 to 60% efficiency of the Carnot cycle without needing much maintenance [284]. Moreover, they do not need components with large mass rotating or reciprocating at high speeds. They can therefore be compact and virtually noise-free. In addition, they can also provide energy savings of up to 50% in comparison with conventional refrigeration methods [285, 286]. Magnetic refrigeration systems with cooling powers between 200 W and 700 W and a quasi-indefinite lifespan are commercially available for applications such as beverage dispensers, medical refrigerators and wine cellars [287]. Therefore, EV battery packs can also benefit from TMSs based on magnetic refrigeration techniques.

4.3.3.4. Internal Cooling

Conventional TMSs minimise thermal gradients across the battery pack by maintaining the exterior cell surface temperature in a pre-specified range. However, a variety of thermal resistances and consequently a large thermal gradient exist in the space separating the heat-generation sites inside the cell from the heat-transfer medium outside it. Estimates for a 26650 Li-ion battery cell suggest that the cell surface temperature and the core temperature may differ by as much as 24 °C for a 10C discharge rate [288]. To address this issue, US patent 6653002 discloses an internal cooling strategy aimed at minimising the thermal resistance between the internal heat-generation sites and the heat-transfer medium.

In one of the embodiments of this invention, microporous TECs are integrated both on the internal and on the external sections of the battery cell. In addition, an array of small heat pipes with a loop or any other open shape is sandwiched between the TECs, forming a cooling module. The open shape of the heat pipes facilitates electrolyte movement in the battery cell. It is also suggested that TECs could be replaced with micro-coolers to accomplish an ultrathin

module assembly. If the temperature inside the battery cell becomes greater than the pre-set threshold values established by a temperature controller, electric current is applied to the TEC module and as a result the Peltier effect develops across it. The hot electrolyte flows through the microporous material of the TEC and comes into thermal contact with a cold junction plate, which is essentially a heat sink. The cold plate removes heat from the hot electrolyte until a lower threshold value is attained. The temperature controller immediately stops current flow to the TEC module and a uniform temperature profile is established inside the battery cell [289].

Driven by a similar objective, Bandhauer and Garimella [290] developed a passive system that uses the liquid-to-vapour phase change process to remove heat generated at local internal locations during battery operation. In their concept, an internal evaporator with micro-channels can be incorporated either directly in the thick current collector or embedded in a sheet of inert material compressed between split current collectors. Excess thermal energy is transferred at the appropriate saturation temperature and pressure to a working fluid flowing through chemically inert micro-channels. The working fluid subsequently undergoes liquid-to-vapour phase change and flows under the buoyancy effect to an external condenser, where it is condensed. The gravitational forces transport the condensed fluid back to the evaporator inlet. The work of these researchers shows that the saturation temperature has a small influence on system performance. More recently, Mohammadian et al. [291] demonstrated that the internal cooling technique involving electrolyte as a coolant flowing in rectangular micro-channels is more effective in decreasing the bulk temperature of a battery cell than a water-based external cooling system. These researchers also showed that the same pumping power for the internal cooling system could achieve up to five times the uniform temperature distribution in a battery cell. Shah et al. [292] also investigated the effectiveness of annular air passages and heat pipes and plain copper rods inserted along the axis of cells as an internal cooling system. They found that, depending on the inner diameter of the heat pipes, it is possible to reduce the cell core

temperature of 26650 Li-ion battery cells by approximately 18 to 20 °C through internal cooling. An appreciable decrease in core temperature can also be achieved by embedding thin copper rods instead of heat pipes in the core of the battery cell. It was noted that internal cooling with heat pipes could delay the onset of thermal runaway events by facilitating rapid heat dissipation from battery cells.

4.4. Selection of TMS for Modular Battery Pack

Previous research studies have established several techniques as suitable candidates for application in battery thermal management systems. The selection of a specific technique can therefore be made only after evaluating all the available alternatives. The factors that are traditionally considered in the TMS trade-off analysis include energy efficiency, capital costs, ease of operation, maintenance requirements and reliability. A comprehensive assessment of these techniques was last presented by Rao et al [94].

According to their assessment, cold plate and thermoelectric devices are not recommended for use in commercial systems, owing to their high thermal resistance and low coefficient of performance, respectively. However, thermoelectric devices are employed by Gentherm Incorporated in their commercial design, whereas cold plates are used in the GM Volt battery pack, signifying that both technologies have improved significantly in recent times.

A trade-off analysis, updated based on new information, is presented in **Table 4.3**. In addition to the traditional factors, TMSs are also evaluated for scalability, development state and associated technical risks in the present study. More importantly, emerging alternatives, such as magnetic refrigeration and thermoacoustic refrigeration, are included in the comparison.

Criteria	Forced Air		Liquid			PCM	Thermoelectric	Thermoacoustic	Magnetic
		Jacket	Cold Plate	Heat Pipe					
Ease of use	High	Low	Moderate	Moderate	High	Moderate	Moderate	Moderate	Moderate
Integration	Simple	Difficult	Intermediate	Intermediate	Simple	Intermediate	Intermediate	Intermediate	Difficult
Energy efficiency	Low	High	Medium	High	High	Medium	Medium	High	
Thermal gradient	High	Low	Moderate	Moderate	Low	Moderate	Moderate	Low	
Cooling level	Small	Large	Medium	Large	Large	Medium	Medium	High	
Regeneration rate	High	Medium	High	Medium	Low	High	Medium	High	
COP @ room temperature	0.4 – 0.7					0.7 - 1.2	Up to 1.0	1.8	
Maintenance	Low	High	Medium	Medium	Low	Medium	Low	Low	
First cost	Low	High	High	High	Moderate	High	Low	Medium	
Scalability	High	Low	Low	Low	High	Medium	Medium	High	
Technical risks	Low	Medium	Medium	Medium	Low	Medium	High	Medium	
Development state	Commercial	Prototype	Commercial	Prototype	Prototype	Commercial	Experimental	Experimental	

Table 4.3: Qualitative analysis of various battery thermal management methods

It is evident from the analysis that none of the thermal management techniques alone can meet the operational requirements of a modular TMS. It can therefore be inferred that a modular TMS would involve a combination of these techniques. In other words, a modular TMS needs to be a hybrid system.

Lastly, there are several approaches to designing a TMS. The most appropriate approach depends on the desired level of sophistication, the availability of information, and the timeline/budget for a particular project. A systematic approach, proposed by Pesaran [86, 207], is adopted for the design of a TMS in this thesis. A summary of the steps involved in this approach is provided below.

1. Establish the desired battery pack thermal performance level including:
 - Average operating temperature
 - Acceptable inter-modular temperature variation
 - Acceptable temperature variation in pack, and
 - Safety and packaging requirements for the vehicle
2. Obtain module heat generation and heat capacity
3. Perform a first-order steady-state energy and thermal analysis to estimate parasitic power required to operate the fan, pump or heat exchanger.
4. Finalise the size of the TMS using a detailed transient analysis for the prediction of battery module and pack behaviour under different operating conditions.
5. Verification of the TMS design through experimental analysis confirming the battery performance and packaging requirements. The size of auxiliary components (fan/pump, HX, heater etc.) is also determined. The significance of factors such as ease of operation, maintenance requirements and reliability is evaluated. The control strategy for operating the TMS is also devised at this stage.

6. Build a prototype battery pack with integrated TMS and conduct bench-top experiments to validate the analysis. A prototype battery pack with integrated TMS is installed in a vehicle to verify the results.
7. Lastly, refine and optimise the TMS design based on the test data and analysis by repeating the previous steps, considering:
 - Battery performance and life
 - Maintenance
 - Reliability
 - Cost

4.5. Conclusions

Different thermal issues affecting the performance, cycle life and safety of Li-ion battery packs are briefly discussed in this chapter, and various thermal management techniques to address these issues are qualitatively reviewed. The purpose of the review is to assess their suitability for a modular battery pack. Most conventional TMSs either have low scalability or deliver marginal performance under challenging conditions (estimated from combined sets of cooling levels and regeneration rates). It is therefore concluded that a robust modular TMS would be a hybrid system, designed through the union of at least two different TMSs. Considering factors such as technical risks, ease of integration, cost and energy efficiency, it can be inferred that PCMs would form an integral part of the modular TMS assembly. Thermoelectric devices also appear to be promising candidates for this application, due to their superior state of development and acceptable COP at room temperatures.

Chapter 5

Estimation of heat generation in Li-ion pouch cells

Chapter 5

5.1. Introduction

The cost of lithium ion (Li-ion) battery packs, the energy storage systems in electronic vehicles (EVs), at present represents 45.3% of the total cost of an EV [6]. The International Organisation for Standardisation (ISO) therefore recommends that in order to obtain a quicker return on investment, a basic standard cell design should be used for all EV battery packs [25, 87]. One of the major drawbacks of this standard design is the thermal stability of Li-ion battery cells. A number of studies have reported that operating a Li-ion battery cell at elevated temperatures can accelerate chemical changes, such as electrolytic corrosion, loss of active material and solid electrolyte interphase growth in cells [293-298]. It can also lead to permanent blockage of Li-ion intercalation sites and the associated decrease in the electrodes' surface area available for electrochemical reaction. This phenomenon is termed irreversible loss of capacity, and according to the estimates of Santhanagopalan et al., it may occur over 5 times faster if the cell is cycled at 45 °C than at 15 °C [299]. Cycling a Li-ion battery cell at temperatures over 85 °C carries the potential risk of the electrochemical breakdown of the anode, ultimately pushing the cell into a state of thermal runaway [178]. On the other hand, Li-ion batteries are also affected by greatly limited electrode activity and poor charge kinetics at low temperatures. For instance, it has been reported that the driving range of the Nissan LEAF 2012 drops substantially from 138 miles in ideal conditions to 63 miles in an operating temperature of -10 °C [186]. Maintaining battery cell temperature within the recommended limits is therefore crucial for the safe and efficient operation of Li-ion battery packs.

The evolution of the cell temperature profile depends on the net energy balance between the heat generated and the heat dissipated from the battery cell via various mechanisms over the period of an EV drive cycle. Therefore, a deeper understanding of the magnitude of the heat generated by a battery cell and the rate at which it is generated is necessary for reliable and safe cell operation. Although the total heat generation in an operational battery is generally approximated by the sum of the reversible heat and the irreversible heat, it also includes other temperature-dependent forms of heat. These are the heat of mixing and the heat of phase transition. Ideally, a numerical model is desirable to analyse the key aspects and behavioural change of different components of the total heat. However, owing to the complexity of an electrochemical system, the importance of experimental studies cannot be under-estimated [300, 301].

The heat generation rate for batteries can be measured experimentally under either isothermal or adiabatic conditions using a commercial or custom-built calorimeter. In an isothermal heat conduction calorimeter (IHC), the battery surface temperature is maintained constant by keeping the cell in full contact with a large heat sink. However, IHCs tend to produce erroneous results at high discharge rates due to the limited heat dissipation ability of the heat sink [302, 303]. As a result, studies involving these calorimeters have been limited to coin cells and small cylindrical cells cycled at low discharge rates [304-313]. Accordingly, the insights gained from them cannot be applied directly to the design of a thermal management system (TMS) for large batteries such as those used in EVs. It is therefore important to refer to a custom-built IHC design, capable of testing comparatively large pouch cells, recently disclosed by Xiao and Choe. The design is based on two thermoelectric devices working as heat pumps and facilitates the measurement of the heat generation rate of a 15.7 Ah LMO/carbon pouch cell [314]. In contrast, adiabatic calorimeters, otherwise known as accelerated rate calorimeters (ARCs), can be used to evaluate battery heat generation rates in normal as well as abusive environments.

ARCs allow the battery cell temperature to increase over time while recording the thermal response of the calorimetric material as it transmits heat rejected by the battery cell during charging/discharging to a constant-temperature heat sink. This information, coupled with the energy balance between the heat sink and the battery cell, is later used to assess the battery heat generation rates [301]. Similar to IHCs, ARCs have also been previously used by several research groups to analyse the thermal behaviour of Li-ion battery cells. A detailed list of all these attempts is available in the report of Schuster et al., along with the data on total heat generated by a 40 Ah LMO/graphite pouch cell for discharge rates ranging between 0.125C and 1C [315]. The work of Chen et al. [300] is of particular interest, mainly because of the wide range of ambient temperatures (-10 °C to 40 °C) and discharge rates (0.25C to 3C) used for analysing the thermal behaviour of A123 20 Ah pouch cell. However, it should be noted that the HDPE slabs, i.e. the calorimetric material, were the only thermal contacts of the test battery cell and no heat sink or any other mechanism for maintaining an isothermal battery surface temperature was incorporated in their calorimeter design. Moreover, according to the details provided, an insulating cover was placed to minimise the heat transfer from the top surface to the surroundings. Schuster et al. still categorise the custom-designed calorimeter used by Chen et al. as an IHC calorimeter in their list. In a subsequent study, Lin et al. used an ARC to investigate the heat generation characteristics of a 40 Ah LiFePO₄ pouch cell discharged at 0.33C, 1C and 2C and at ambient temperatures between -15 °C and 40 °C [316]. Furthermore, a technique based on direct measurements of heat generation rates with a heat flux sensor was recently demonstrated by Drake et al. [288].

5.2. Purpose of present investigation

It should be acknowledged that the heat generated by a battery of specific chemistry depends on reaction kinetics. Reaction kinetics, in turn, are strongly influenced by operating conditions,

namely discharge rate and ambient temperature, and cell design parameters, such as active particle size, Li-ion diffusion coefficient, cell/electrode thickness etc. With the information already available in the public domain, it may not be too difficult to model the effect of operating conditions on the thermal behaviour of a Li-ion pouch cell. However, few researchers have investigated the impact of cell design parameters on the heat generation rates of a battery cell suitable for an EV application. Moreover, it is anticipated that with the ISO recommending a common basic cell design for all EV battery packs, scaling up the basic cell design in order to meet the energy requirements of different applications might soon become general practice. From an engineering perspective, it would thus be beneficial to learn if the nominal capacity of a battery and the associated cell thickness have any affect on battery heat generation rates. The focus of this research project is therefore to examine the heat generation behaviour of $C/LiFePO_4$ pouch cells in relation to their nominal capacities. For the purposes of this investigation, battery cells of different capacities were sourced from the same manufacturer. It is expected that the results of this study will later allow the expression of the relationship between the heat generation rates of a Li-ion pouch cell and its theoretical capacity in simple mathematical terms. This would counter the need to repeat these experiments each time the battery pack is scaled up or down for a new application.

5.3. Experimental study

In this work, a test station was constructed using a 4-channel, 20 V/100 A battery cycler and a programmable thermal chamber. Commercially available $LiFePO_4$ pouch cells with nominal capacities of 8 Ah, 15 Ah and 20 Ah were procured from Benenergy Tech. Co. Ltd., China, to serve as test batteries. In addition, an A123 20 Ah $LiFePO_4$ pouch cell was used as a control sample. The parameters characterising the physical dimensions of these cells are specified in

Table 5.1.

Battery Cell	Model Number	Height (mm)	Width (mm)	Thickness (mm)
8 Ah	BHK – 1280A5	105	80	12
15 Ah	BHK – 11A8F5	155	108	11
20 Ah	BHK – 85C0M7	227	120	9
A123 20 Ah	AMP20M1HD - A	227	160	7.25

Table 5.1: Physical dimensions of the three test battery cells and the A123 20 Ah control sample used in this investigation

The heat generation rates for batteries operating under different conditions are generally estimated using a custom-designed calorimeter with known thermal characteristics. An ARC that can be used for the characterisation of heat generation rates for any pouch cell, regardless of cell chemistry, was proposed by Chen et al. It has a pouch cell sandwiched between two high-density polyethylene (HDPE) slabs, each of them being five times thicker than the pouch cell [300]. However, it was designed for battery cells with high surface area-to-thickness ratios.

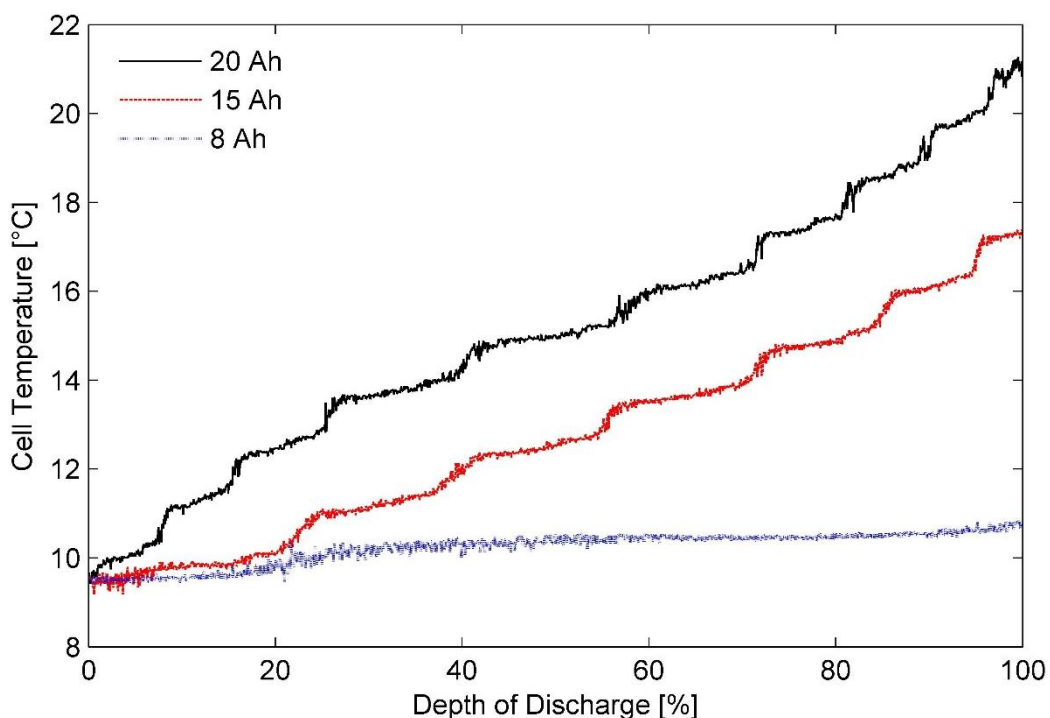


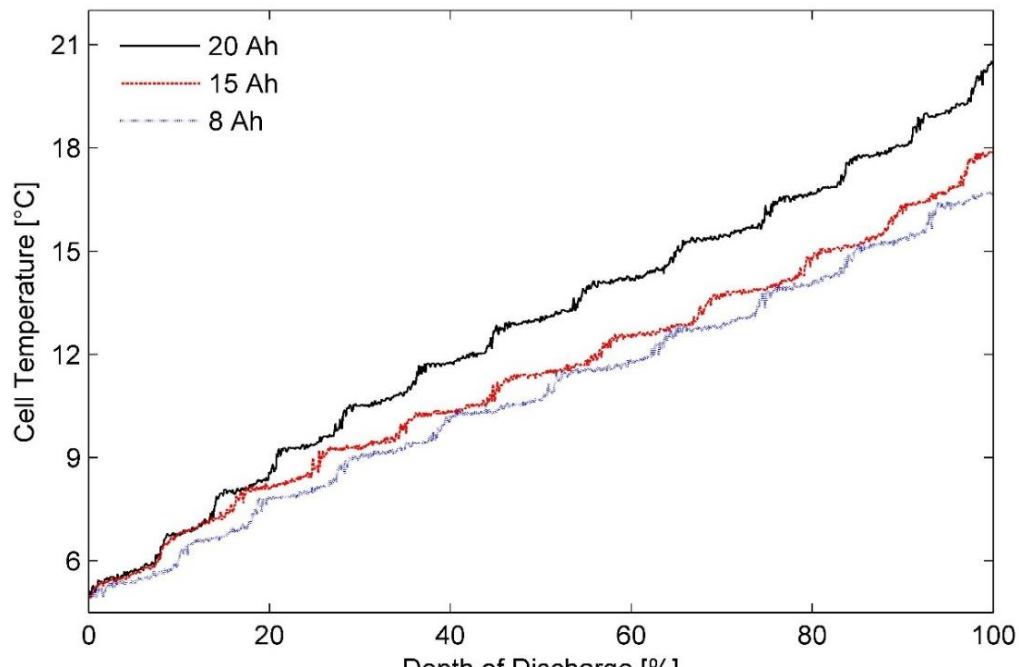
Figure 5.1: Battery cell temperature variation measured for different battery cells using a sandwich-structured calorimeter at 10 °C at 2C discharge rate

Fig. 5.1 shows the surface temperatures recorded for the three test battery cells subjected to a heat generation characterisation procedure in the sandwich-structured calorimeter proposed by Chen et al. The operating temperature is regulated at 10 °C and the constant discharge rate of 2C is maintained using the Arbin BT2000 cycler. Note that for the purposes of this investigation, the operating temperature was the same as the ambient temperature and both terms are used interchangeably here. The steady-state battery surface temperature was 1 ~ 1.2 °C less than the temperature of the thermal chamber for all the experiments. An ARC should not exchange any heat with its surroundings, and should in fact present a large thermal resistance to them [317]. Nonetheless, **Fig. 5.1** illustrates that the thick battery cells are exposed to the ambient environment to a greater degree than the thin pouch cells in the sandwich-structured calorimeter. It is therefore evident that the thickness of pouch cells is a major factor influencing the effectiveness of this design. Accordingly, to minimise the heat leakage in the present investigation, the aforementioned calorimeter was modified by making the battery cells sit in slots, made to their size, in the HDPE slabs.

Fig. 5.2 presents (a) a schematic of the modified battery calorimeter and (b) the surface temperatures measured for the three test batteries at a 3C discharge rate at an operating temperature of 5 °C using the modified set-up. The uniform increase in the surface temperatures for all the three battery cells is seen in **Fig. 5.2(b)**. This reflects the improved capability of the modified calorimeter to test both thick and thin cells, particularly in harsh operating conditions, i.e., low ambient temperature and high discharge rate. The effective heat transfer from the battery cell surface to the HDPE slabs is ensured by the application of a layer of silver metal oxide-based thermal grease (thermal conductivity ~ 3.17 W/m-K and specific gravity ~ 2.4 g/cm³) on the contact surfaces. This modified calorimeter was used in the following test procedure.



(a)



(b)

Figure 5.2: (a) Modified battery calorimeter (b) Surface temperature variation for batteries of different capacities in modified calorimeter at ambient temperature of 5 °C and discharge rate of 3C

5.3.1. Test procedure

The constant current (CC) and constant voltage (CV) mode was adopted to fully charge the battery cells. Under this charging regime, all the three test battery cells were first charged at 0.33C until a maximum allowable voltage of 3.65 V was reached. Thereafter, they were taper-charged to a cut-off current of 0.05C while a constant terminal voltage of 3.65 V was maintained. For the A123 20 Ah cell, the CC-CV mode was applied. However, the current corresponding to the CC stage of the A123 cell was 0.5C and the cut-off current tapered to 0.05C during the CV stage with the cell voltage maintained at 3.6 V. Before starting the test, the test battery cells were fully charged and discharged a few times. For the discharge process, a 0.5C rate was used for all the cells with the lower cut-off voltage set to 2.0 V and 2.5 V for the A123 20 Ah cell and the three test battery cells, respectively. The step serves dual purposes. Firstly, it allows time for the development of the solid electrolyte interphase film and prevents corruption of the measured values due to the absence of film resistance. The cell capacity available for a specific set of discharge conditions stabilises at the end of this step. Secondly, it functions as a quick quality check for expected performance standards for the three test cells.

Prior to the heat characterisation test, the calorimeter was soaked for 12 hours in a constant-temperature air bath provided by the programmable thermal chamber to minimize the temperature gradient between the calorimeter and the surroundings and hence achieve the approximately ideal condition of zero heat transfer. Galvanostatic discharge tests were then conducted for all three test battery cells at ambient temperatures of -10 °C, 5 °C, 20 °C, 35 °C and 50 °C and discharge rates of 0.33C, 1C and 3C. The temperature change in the HDPE slabs was recorded by a thermal sensor strategically placed 6 mm away from the battery surface in the vertical plane passing through the centre of the battery cell and the HDPE slab. Placing the temperature sensor in the central plane limits the edge effects of heat transfer from the slab to the surroundings [300]. Furthermore, a rest phase of an hour after completion of the discharge

process was included in the test procedure to isolate the heat of mixing produced in the discharging operation. This procedure was repeated four times and average readings were used for heat generation estimation.

5.3.2. Problem Formulation

The key to scaling up an electrochemical system successfully is to examine the dynamic thermal response in relation to the battery capacities and strategically manage the exothermic heat released during the two energy transformation processes, i.e. charging and discharging. The modus operandi accepted for collecting the data fit for this study is direct calorimetry. An underlying assumption that all the heat produced by the electrochemical cell is lost to the calorimetric material forms the basis of this technique. Due to this assumption, the source of heating, in isolation, becomes immaterial to the problem. The dynamic heat generation rate and the temperature histories of heat source are subsequently estimated based on transient temperature readings recorded at discrete times at one or more interior points in the calorimeter. Such dynamic heat transfer problems, usually referred to as inverse heat conduction problems (IHCPs), are considered mathematically ill posed. They are also known to be sensitive to random instrumentation errors and the noise present in experiments [300, 318].

Several methodologies, including the convolution theorem, the finite difference method and the finite element method, for solving IHCPs can be found in the research literature [318-324]. However, owing to the inherent complexities and the need for extensive data manipulation, they have been avoided in the present investigation. Instead, the problem formulation was centered on Fourier's law of heat transfer and the fundamental law of conservation of energy. Lateral conduction in the calorimeter was considered negligible in comparison to heat flow in the direction normal to the cell surface, which lends the original problem to a single spatial dimension. This assumption was validated based on readings of a temperature sensor placed 6

mm away from the surface, representing the thickness of the battery, which showed negligible deviation from the bulk temperature. The temperature distribution, T , as a function of time (t) in a slab of homogenous and isotropic material can be described by

$$\frac{\partial}{\partial x} \left(k \cdot \frac{\partial T}{\partial x} \right) = \rho \cdot c \cdot \frac{\partial T}{\partial t} \quad (5.1)$$

where, k (~ 0.49 W/m-K is used in this study) is the thermal conductivity of HDPE, i.e. the calorimetric material, while ρ and c represent its density and specific heat, respectively.

The initial condition of thermal equilibrium between the HDPE slab and the isothermal air bath provided by the thermal chamber is

$$T(x, 0) = T_0(x) \quad (5.2)$$

and the boundary condition of no heat exchange with surroundings at $x = L$, where, L , represents thickness of the HDPE slab is defined as

$$\frac{\partial T}{\partial x} = 0 \text{ at } x = L \quad (5.3)$$

Temperature measurements at $x = x_1$, i.e. the location of the sensor corresponding to discrete time steps, t_i , during the test cycle are given by

$$T(x_1, t_i) = Y_i \quad (5.4)$$

Interestingly, a one-dimensional IHCP with a single unknown surface heat flux at $x = 0$, a known boundary condition at $x = L$ and a temperature history for one internal location can be converted to a case involving two separate problems. Now, for one of these problems concerning the portion of the slab spanning from $x = x_1$ to $x = L$ (say, body 2), the boundary conditions at both of its ends are known. As a result, heat transfer through this region of the slab can be analysed as a direct problem. Heat flux entering body 2, q , which is practically

equal to the flux leaving body 1 (portion of the slab from $x = 0$ to $x = x_1$) via the surface $x = x_1$ is therefore calculated in a direct manner by solving the following equation:

$$q_{x_1}(t) = -k \frac{\partial T}{\partial x} \quad (5.5)$$

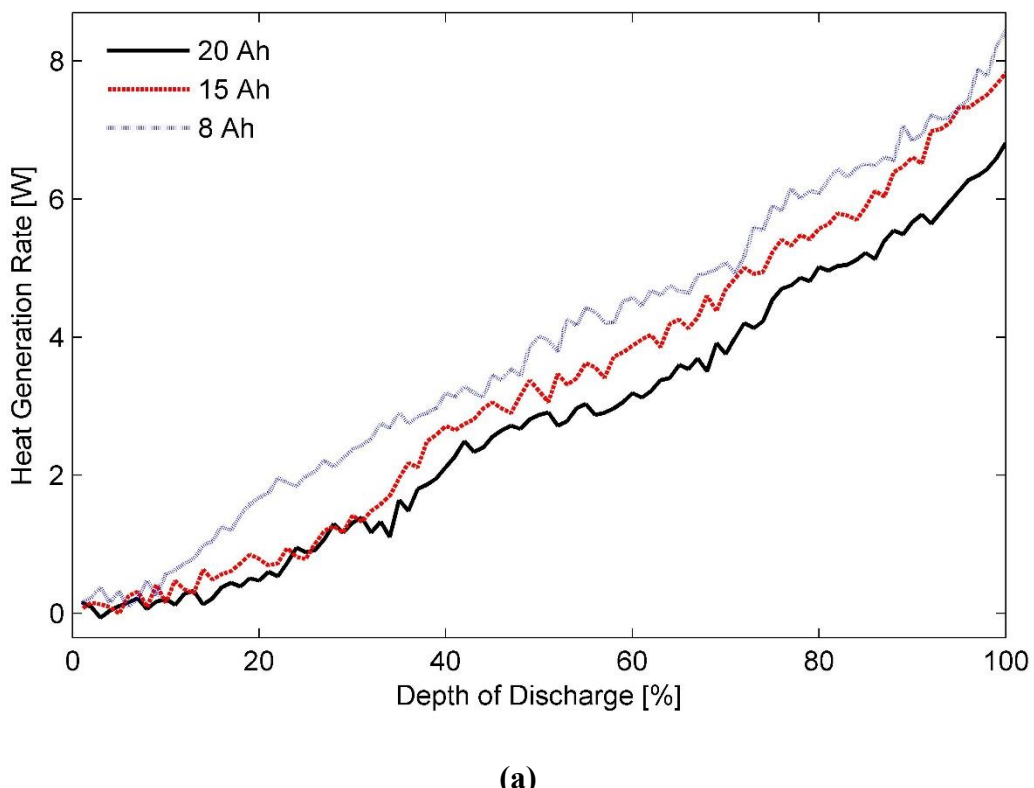
In addition, the battery cell is assumed to be emitting heat equally from both faces. The total heat flux actually generated by it is therefore twice the calculated value [325]. Lastly, the impact of changes in cell thickness on battery heat generation rates cannot be explored if the area of the specific test battery is used for converting the calculated heat flux to the heat energy generated by the cell. Therefore, a transformation constant ($= 0.1 \text{ m}^2$) was determined by comparing the experimental results obtained for the control sample, i.e., A123 20 Ah cell with the values published by Chen et al. [300] for the same cell. These researchers addressed the IHCP problem for an A123 pouch cell by applying Beck's sequential function specification method. This method increases the stability of the problem by including information about future steps in it. Control experiments using the A123 20 Ah pouch cell at the temperature of 10°C and the discharge rates of 0.5C and 2C were performed. A deviation of less than 3% between the heat generation rates estimated herein and those measured by Chen et al. was noted. The difference is judged acceptable in the context of this work.

5.4. Results and Discussion

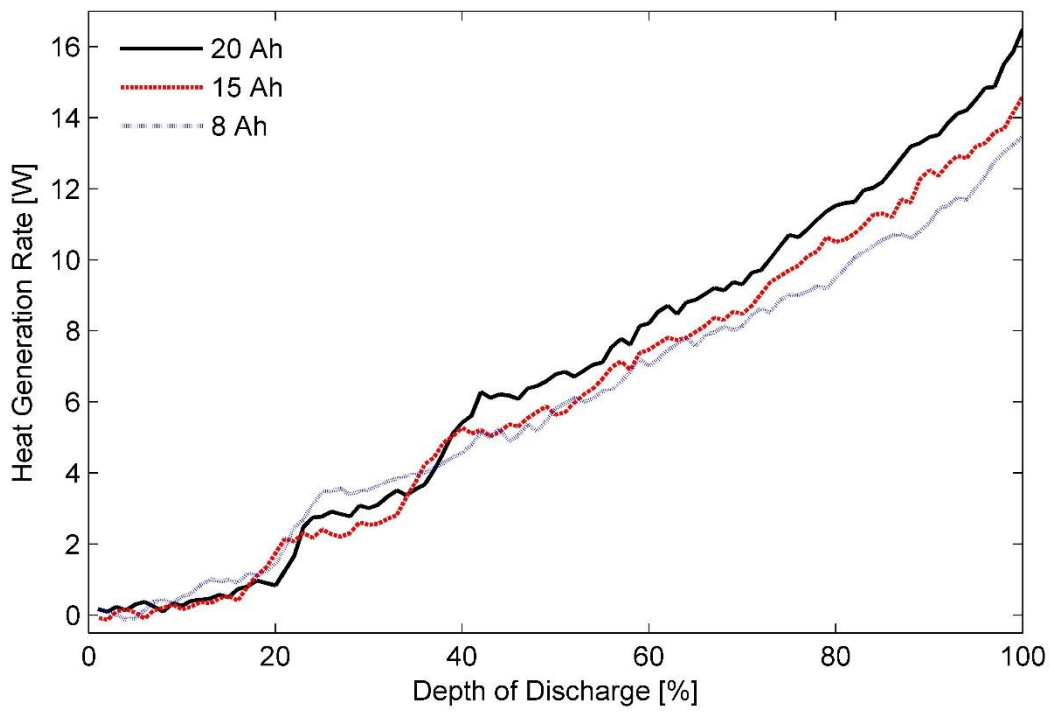
The LiFePO_4 pouch cells were subjected to galvanostatic discharge tests over a range of ambient temperatures between -10°C and 50°C using the experimental procedure described in Section 5.3.1. The following section presents the experimental results to illustrate the observed effects of ambient temperature, discharge current and depth of discharge on the battery heat generation rate when analysed in conjunction with the battery capacity.

5.4.1. Effect of Temperature

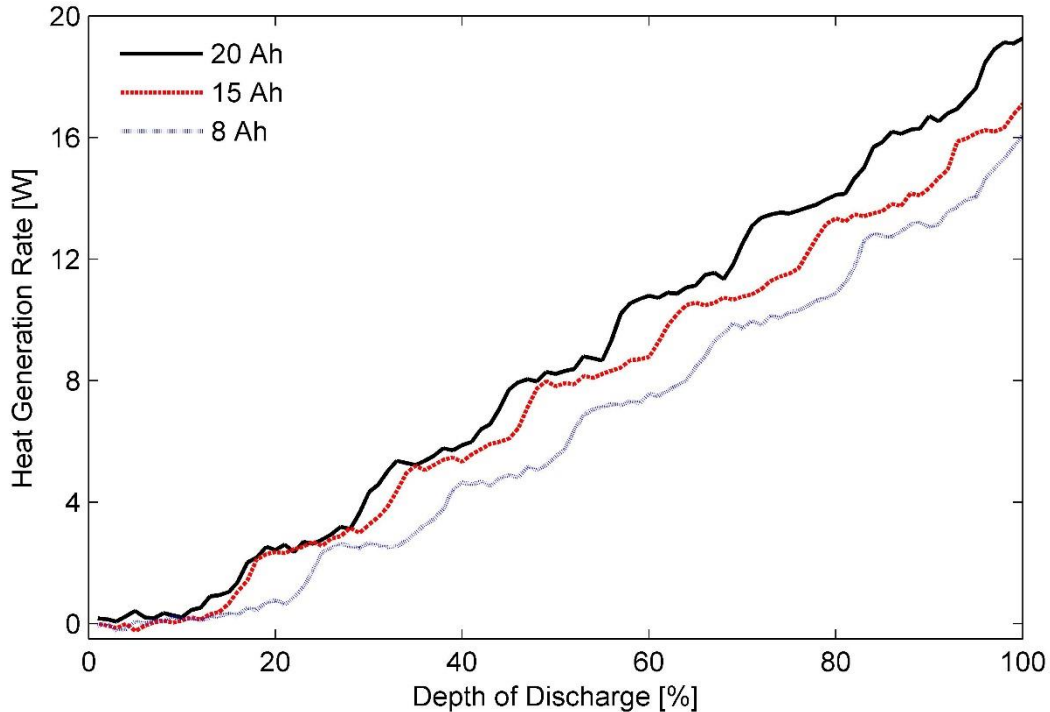
Fig. 5.3 shows the heat generation rates calculated as a function of depth of discharge for the 8 Ah, the 15 Ah and the 20 Ah $LiFePO_4$ pouch cells discharged at a 3C rate in operating temperatures of (a) 50 °C, (b) 20 °C, (c) 5 °C, respectively. It can be seen from **Fig. 5.3(a)** that up to a DOD of 35%, the heat generation rate curves for the 15 Ah and the 20 Ah pouch cell almost overlap, and as the energy stored in these cells is further depleted, the two curves start to deviate. In the DOD range of 40% to 80%, the average heat generation rate determined for the 15 Ah battery cell is larger by 0.65 W than that observed for the 20 Ah pouch cell. The difference increases to 1.1 W at the end of the discharge test. In contrast, the heat generation rate of the 8 Ah pouch cell is considerably greater than that of the other two cells for almost the entire discharge process.



(a)



(b)



(c)

Figure 5.3: Estimated heat generation rates for 8 Ah, 15 Ah and 20 Ah $LiFePO_4$ pouch cells discharged at 3C at ambient temperatures of (a) 50 °C , (b) 20 °C and (c) 5 °C

In fact, the 8 Ah pouch cell generates approximately 1.5 W more than the heat produced by the 15 Ah or the 20 Ah cell per second in the DOD range of 20% to 38% and almost 1 W from thereon until 70% DOD. The figures also show that although the heat generation rates for the 8 Ah pouch cell and the 15 Ah pouch cell are approximately equal at the DOD of 95%, an additional 0.7 W has to be dissipated from the 8 Ah cell at the end of the discharge process if its temperature has to be maintained at 50 °C. This marked dissimilarity in the heat generation rates of the three pouch cells operating under identical test conditions can be attributed to variations in their internal resistance, which is explained in detail later. High internal resistance results in increased heat generation rates and subsequently a higher battery cell temperature, particularly at sections close to the core of the cell.

Upon comparison of the plots shown in **Fig. 5.3(a)** with those in **Fig. 5.3(b)**, a remarkable increase of more than 125% can be noticed in the heat generation rate of the 20 Ah pouch cell as the cell operating temperature drops from 50 °C to 20 °C. This is an indication of the poor electrochemical performance and the substantial drop in the cyclic efficiency of Li-ion batteries at low temperatures. Rather surprisingly, the 8 Ah pouch cell experiences only a 60% increase in the rate of heat generation measured under similar conditions. As a result, the 20 Ah pouch cell appears to be generating more heat than both the 15 Ah and the 8 Ah pouch cells at all stages of the test cycle after a DOD of 40% is reached. By the end of the test, the total heat generated by the 20 Ah pouch cell exceeds the heat produced by the 8 Ah test battery by as much as 2.5 W, warranting careful attention in the design of a TMS for the same cell.

A trend similar to that observed at 20 °C for the heat generation rates of the three test cells is observed at 5 °C, as shown **Fig. 5.3(c)**. In this case, however, a discernible change in the heat generation rates of the 20 Ah pouch cell is evident from the very beginning of the discharge process. Amplification of the total heat is also noticed for all three test battery cells, signifying

a continuous decay in their performance as the operating temperature is decreased. Reduced mass transfer and sluggish charge kinetics can be considered as primary reasons for this. Nonetheless, the ratio of percentage increase in heat generation rates for the 8 Ah pouch cell as a result of shifts in operating temperature from 50 °C to 5 °C is lower than the ratios obtained for the other two test cells. Consequently, the 8 Ah pouch cell, i.e., the thick cell, is more efficient in cold climatic conditions than battery cells with thin geometry. This implies that for the same nominal capacity, Li-ion cells with thicker electrodes in general are better suited for low temperature applications than thin pouch cells. In addition, a thick electrode normally contains more active material than a thin electrode of the same total volume. Accordingly, it delivers a higher capacity at any specific temperature [326].

The transformation of electrical energy to chemical form during charging and vice versa during discharging of an electrochemical cell is a complex process. It happens in multiple stages that involve transportation of the positive and the negative charge carriers across various parts of the battery cell. A portion of the electrical energy stored in the cell is transformed to heat while overcoming the irreversibility associated with these transportation processes. Various components responsible for this irreversible loss can be listed as follows:

- resistance offered to diffusion of Li-ions by the solution phase of the porous electrode
- resistance presented by the cell separator to Li-ion diffusion
- resistance provided by the solid electrolyte interphase to Li-ions
- resistance of the solid phase of the porous electrode to the transfer of electrons across it
- resistivity of the current collectors

All these resistive components are temperature-dependent and can be controlled through judicious cell design. Battery cell design can influence both the electrochemical performance

and the available capacity of the battery under specific operating conditions. For instance, a thick and heavy current collector by virtue of its high conductivity ensures a uniform current distribution in a cell and minimises any thermal gradients across it [327]. Nevertheless, the principal elements that can affect the internal resistance of a cell, and consequently its heat generation rates under varying ambient conditions, are the thickness and the surface area of the electrode.

Theoretically, a thin electrode provides lower internal resistance to Li-ion diffusion in comparison to a thick electrode of the same chemistry and total volume [301, 326]. However, in realistic situations, major portions of the thin electrochemical cell structure can be considered to be in close thermal proximity of the ambient environment. Accordingly, at low ambient temperatures, major portions of the layered structure of a thin pouch cell operate at a lower temperature than the internal sections of a cell with a thick electrode. As the colder regions of an electrochemical cell are typically more resistive than other areas, the high heat generation rates of the 20 Ah or the thin pouch cell relative to the other two test batteries in operating temperatures of 20 °C and below can be explained. Furthermore, the effective current density corresponding to a specific discharge rate is higher in the thick electrode than in the thin electrode because of its smaller surface area. Furthermore, high current density heats up the internal layers of the 8 Ah pouch cell, leading to improved mass transport and charge transfer characteristics, thus contributing to a superior discharge performance. In addition, the large current collector plates and a high current concentration near the tabs can also be a cause of significant heat generation for batteries with a large form factor.

For the same reasons, the physics of the problem are reversed at an ambient temperature of 50 °C, at which a thick cell design becomes responsible for the increased irreversible polarisation noticed in the 8 Ah pouch cell. However, a modular TMS should be able to accommodate cells of different sizes and varied thickness ratios without much difficulty, and certainly without

requiring major structural modifications. It is therefore clear that the success of such a system is dependent on the establishment of a balance between the above-mentioned sources of irreversible heat generation in a Li-ion battery cell. Analysis of the data gained in this study suggests that a TMS designed to regulate the temperature of the studied Li-ion pouch cells at 35 °C could meet this criterion, as is clear in **Fig. 5.4**. More research including other factors such as capacity fade, wear and cycle life is required to validate if, similar to a different grade of engine oil being used for internal-combustion engine vehicles operating in cold climates from those that are used in geographic regions typically associated with hot weather, battery cells for an EV can also be divided into two categories, namely:

- thick battery cells for EVs that are to be driven in low ambient temperatures, and
- thin cells for EVs that can be used in ambient temperatures higher than 35 °C.

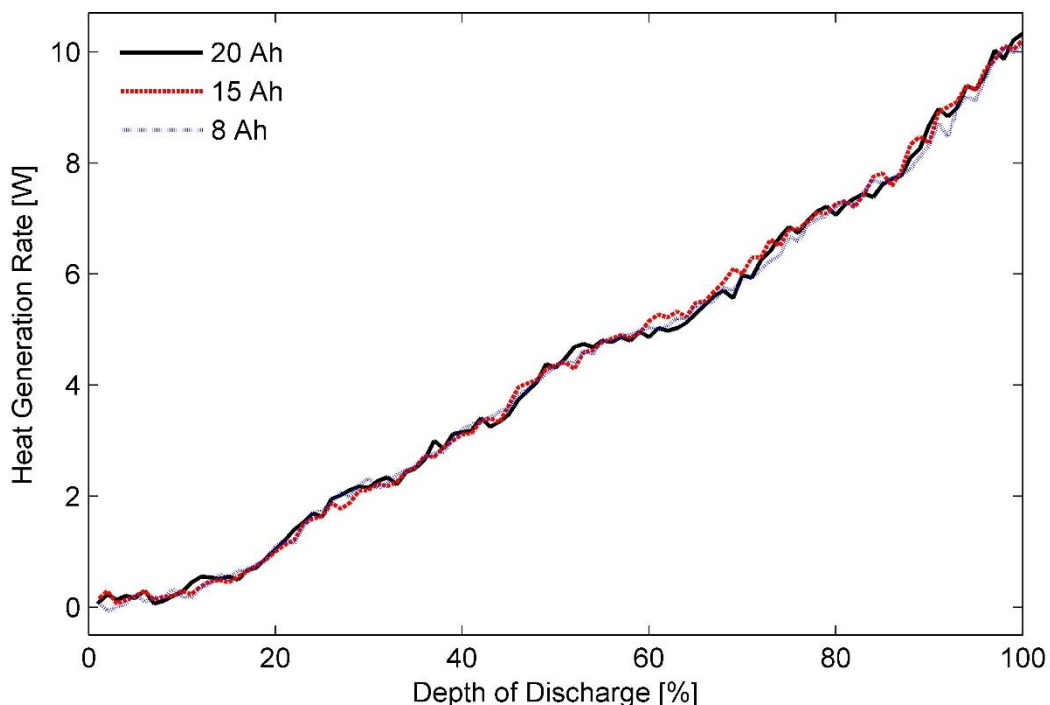


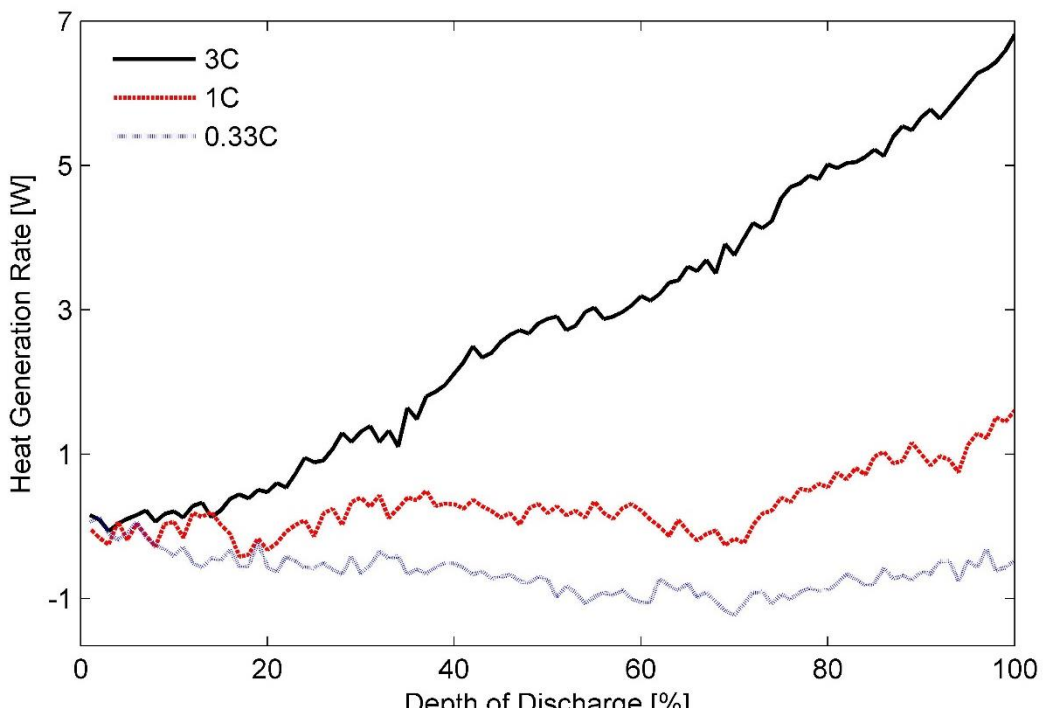
Figure 5.4: Heat generation rates measured for 8 Ah, 15 Ah and 20 Ah LiFePO_4 pouch cells at ambient temperature of 35 °C and discharge rate of 3C

5.4.2. Comments on the presence of a ‘second discharge plateau’

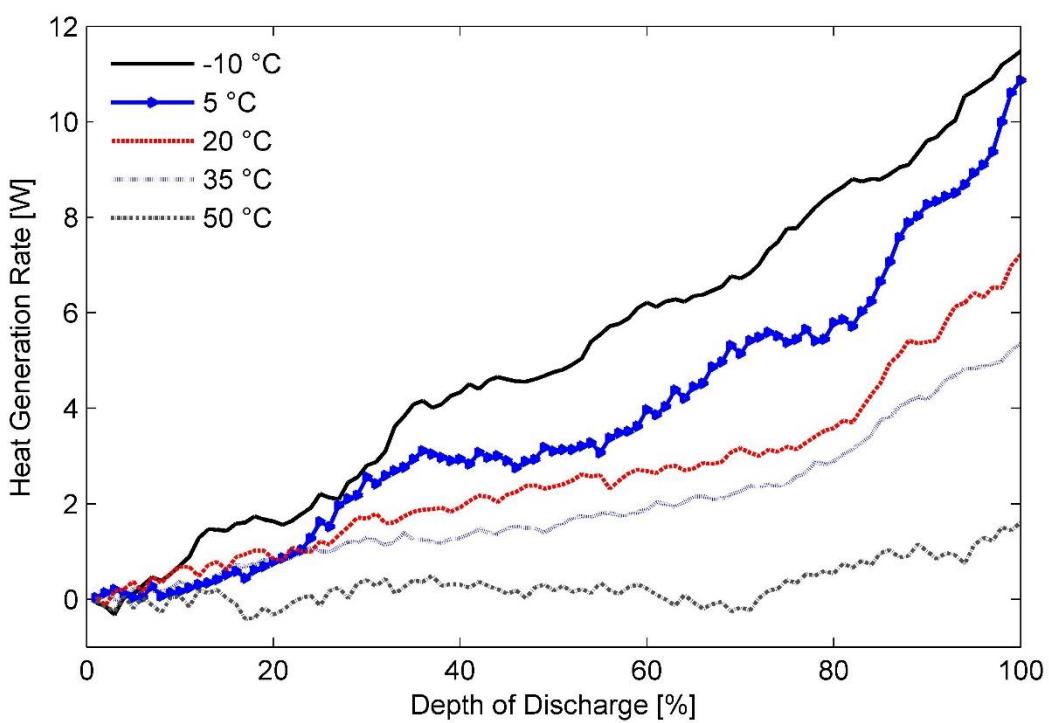
Two low frequency fluctuations in the heat generation curves of A123 20 Ah $LiFePO_4$ cell were reported by Chen et al. [300]. They observed that the fluctuations were more noticeable for battery cells operating with a surface temperature greater than 20 °C. Such waverings giving an impression of a secondary discharge plateau have previously been witnessed for batteries with $LiMnO_4$ electrodes. Their presence in $LiMnO_4$ batteries is generally attributed to a double phase change phenomenon. A hypothesis suggesting the existence of double phase change in $LiFePO_4$ batteries has therefore been formulated by these researchers.

Reports indicating the presence of a second discharge plateau for batteries with $NiOOH$ electrodes can also be found in the research literature [328-331]. Nevertheless, it should be pointed out that the formation of an insulating film at the $NiOOH/substrate$ interface has been suggested as the reason for the appearance of the second plateau. It is believed that the insulating film causes the conductivity of active material to reduce progressively during the discharge cycle until a stage where the electrode resistance becomes constant is reached. A sharp increase in resistance and a resulting increase in heat generation rates is again seen towards the end of the cycle, signifying complete saturation of the active material surface with $Ni(OH)_2$ [332]. Further research investigating temperature-dependent changes in cell topology and microstructure is therefore required to ascertain the primary reason for the fluctuations in the heat generation rates of $LiFePO_4$ cells.

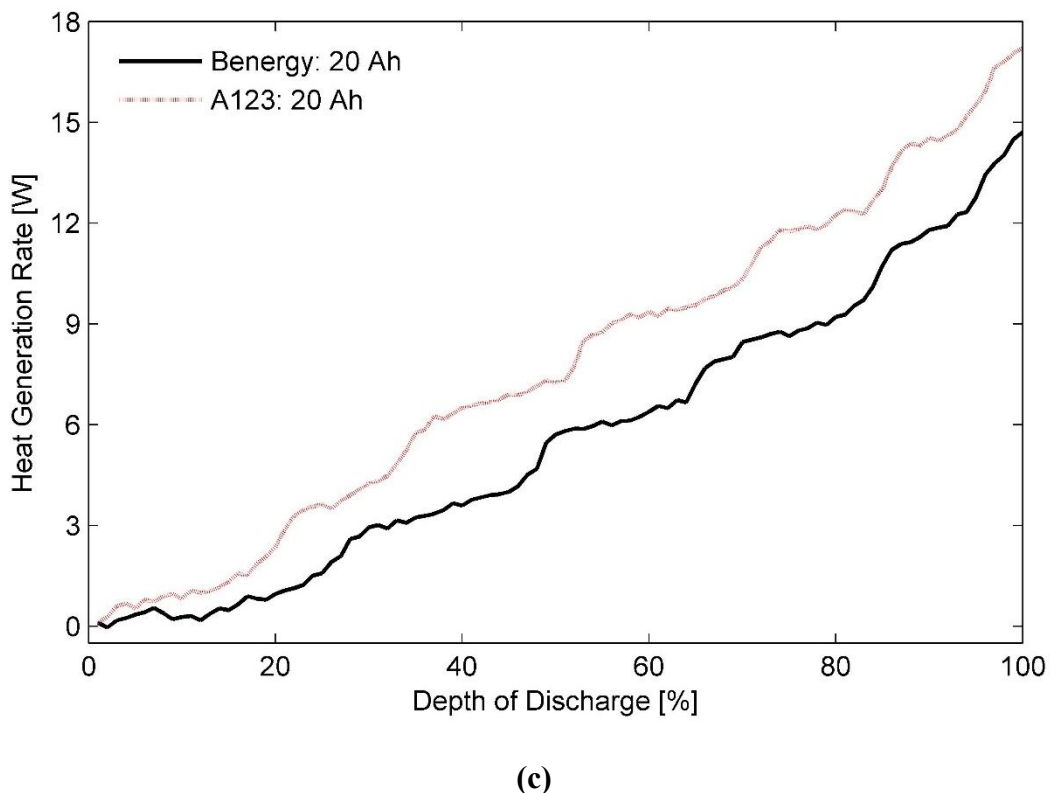
Fig. 5.5 displays the heat generation rates for the 20 Ah test battery (a) at an ambient temperature of 50 °C with different discharge rates of 0.33C, 1C and 3C, (b) at the discharge rate of 1C with the ambient temperatures ranging between -10 °C and 50 °C and (c) at 2C and 10 °C, and their comparison with those measured for the A123 20 Ah pouch cell.



(a)



(b)



(c)

Figure 5.5: Heat generation rates measured for the 20 Ah LiFePO₄ pouch cell (a) in an ambient environment of 50 °C for different discharging rates (b) effect of ambient temperature on secondary plateauing at discharge rate of 1C and (c) their comparison with heat

It can be seen from **Fig. 5.5(a)** that the heat generation rates corresponding to a 0.33C discharge rate are of endothermic nature, which makes it hard to identify the region of double phase change in the cycle. However, at higher discharge rates, a plateau-like feature is visible at a DOD of approximately 35 % and subsequently at around a DOD of 80 %. A second plateau can be seen in the heat generation profiles representing operating temperatures of 20 °C and higher in **Fig. 5.5(b)**. As the same figure indicates, the number of fluctuations increases to 3 or more at low temperatures. The heat generation rates estimated at an operating temperature of 10 °C and a 2C discharge rate for the test battery and the A123 20 Ah cell are therefore compared in **Fig. 5.5(c)**. The results indicate the presence of several heat generation rate plateaus for the A123 20 Ah battery cell, as opposed to the two distinct regions reported by Chen et. al. [300] at low ambient temperatures. It is therefore believed that the noticeable

waviness may be caused by phase lag, i.e., the time lapse between heat generation and heat measurement due to large calorimeter time constants.

More importantly, **Fig. 5.5(c)** shows a remarkable difference of 2.5 W in the heat generation rates measured for the two batteries under these test conditions. In general, reducing the particle size of the positive electrode is known to result in a higher battery capacity. Accordingly, A123 cells employ nanophosphate chemistry with a particle size of 36.5×10^{-9} m [333], as opposed to the average particle size of 300×10^{-9} m used by other manufacturers [334, 335]. However, it has been shown that the influence of active particle size on heat generation rates at discharge rates less than 2C is almost negligible [336]. Therefore, the observed variation in the rates of heat generation can be attributed to the difference in the thickness of the two battery cells. As would be expected, the 20 Ah test battery cell from Benergy Tech. generates heat at a rate much lower than the A123 pouch cell of the same rated capacity but with a 20 % thinner cell design under similar operating conditions.

5.4.3. Effect of Discharge rate

Fig. 5.5(a) is a representation of the heat generation rate plotted as a function of the discharge rate for the test batteries in an ambient temperature of 50 °C. The figure indicates that the magnitude of heat generation rate increases considerably with the discharge rate. Similar behaviour can be expected for all other operating temperatures within the safety margins of Li-ion battery cells.

The estimated heat generation rates as a function of DOD for the three test batteries at a discharge rate of 1C and ambient temperatures of (a) 20 °C, (b) 35 °C and (c) 50 °C are shown in **Figs. 5.6(a), 5.6(b)** and **5.6(c)**, respectively. In addition, inferences about the thermal behaviour of these cells at a discharge rate of 0.33C with different ambient temperatures of (a) 20 °C, (b) 35 °C and (c) 50 °C can be made from the data presented in **Fig. 5.7**. Furthermore,

a concise list of measured heat generation rates for the three test batteries at different ambient temperatures and discharge rates is presented in **Table 5.2**. The table gives an indication of the upper bound and the lower bound for heat generation rates expected from a $LiFePO_4$ pouch cell of specified capacity under typical operating conditions.

Discharge Rate	Nominal Capacity (Ah)	Ambient Temperature (°C)				
		-10	5	20	35	50
0.33C	8	-0.16 to 4.42	-0.98 to 2.20	-0.75 to 1.46	-0.81 to 0.04	-0.75 to 0.13
	15	-0.11 to 4.84	-0.63 to 2.52	-0.65 to 1.97	-0.85 to 0.14	-0.89 to 0.16
	20	-0.01 to 5.19	-1.36 to 2.82	-0.37 to 2.23	-0.84 to 0.13	-1.24 to 0.12
1C	8	-0.07 to 10.46	0.10 to 8.73	-0.07 to 6.23	-0.06 to 5.32	-0.22 to 2.53
	15	-0.25 to 11.05	-0.18 to 10.02	-0.06 to 6.72	-0.07 to 5.41	-0.23 to 2.16
	20	-0.32 to 11.85	0.03 to 10.87	-0.13 to 7.22	-0.01 to 5.35	-0.42 to 1.60
3C	8	—	-0.24 to 16.08	-0.12 to 13.46	-0.07 to 10.13	0.09 to 8.43
	15	—	-0.24 to 17.11	-0.14 to 14.58	0.06 to 10.22	0 to 7.82
	20	—	0.07 to 19.27	0.10 to 16.49	0.06 to 10.32	-0.06 to 6.81

Table 5.2: Summary of estimated heat generation rates for three test battery cells under different operating conditions

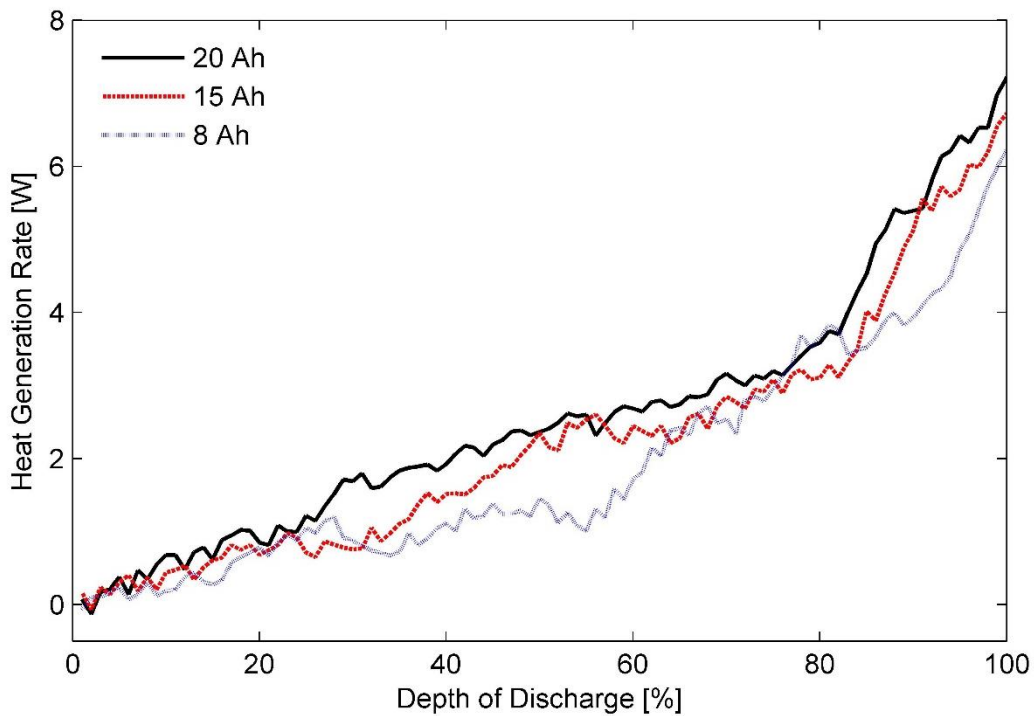
The heat generation rates for a battery cell with a porous electrode are influenced by the transportation rate of Li-ions from the particle surface to the reaction site, driving the de-intercalation process at the negative electrode and the intercalation process at the positive electrode/electrolyte interface. It has also been identified that because of the large difference in the value of the Li-ion diffusion coefficient in the solid ($D_{Li} < 10^{-10} \text{ cm}^2 \text{s}^{-1}$) and the liquid phase ($D_{Li} \sim 10^{-5} \text{ cm}^2 \text{s}^{-1}$), transients in the solid portion of the electrode and in the bulk of the electrolyte are of different orders of magnitude [337]. Consequently, for reaction

rates of 1C or less, Li-ion diffusion in the negative electrode acts as a rate-limiting mechanism for the discharge process. At a discharge rate of 3C, it switches to Li-ion transport in the electrolyte. In addition, Li-ion motion occurs along a non-linear trajectory, owing to constraints provided by the olivine-type structure of $LiFePO_4$ particles [338].

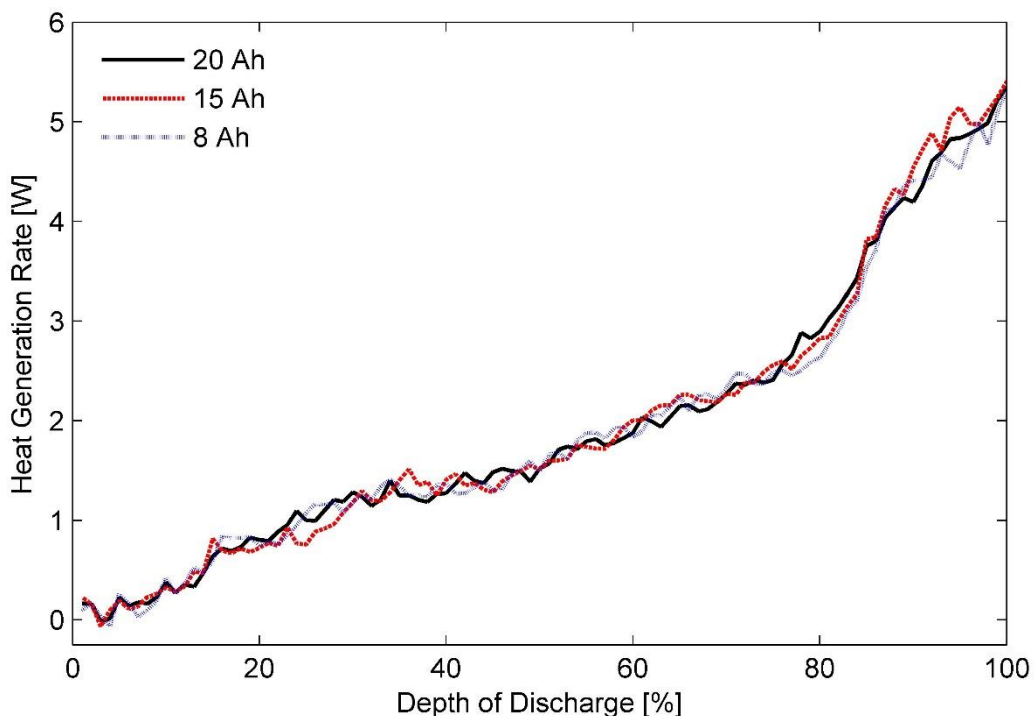
As a result, reducing the electrode thickness reduces the instant diffusion thickness, which is the distance from the internal phase boundary to the particle surface, and the material utilisation, as the particles do not have sufficient time to absorb the charge carriers. In contrast, increasing the cell thickness while keeping the cell capacity constant increases the effective active material loading per unit volume. As a result, electrode porosity is decreased whereas the active-material coating thickness is increased, which causes the Li-ion diffusion path in the solid electrode to become longer, causing an increase in the concentration polarisation and subsequently the heat generation rates [332, 337]. This may explain the almost overlapping heat generation rates for the three test batteries at certain stages of the characterisation test performed at discharge rates lower than 1C. However, judging by the profiles shown in Figs. 5.3-5.7, it can be concluded that the effect of electrode thickness on battery heat generation rates overshadows the influence of dissimilar transients for the solid and electrolyte phases of a battery cell on its thermal behaviour.

Furthermore, the predominantly non-linear heat generation profiles recorded for a 1C discharge process, shown in Fig. 5.6, can be described by an S-shaped curve. It has been noted in the research literature that the variation of entropic coefficient with DOD for $LiFePO_4$ electrodes exhibits a similar trend [301]. It is magnified in the form of entropic heat and is subsequently reflected in the heat generation rates. However, the ratio of reversible heat to irreversible heat is an inverse function of current. Consequently, the effect of reversible heat

on the profile of total heat diminishes progressively as the discharge rate is increased, leading to the quasilinear behaviour seen in **Fig. 5.3**.



(a)



(b)

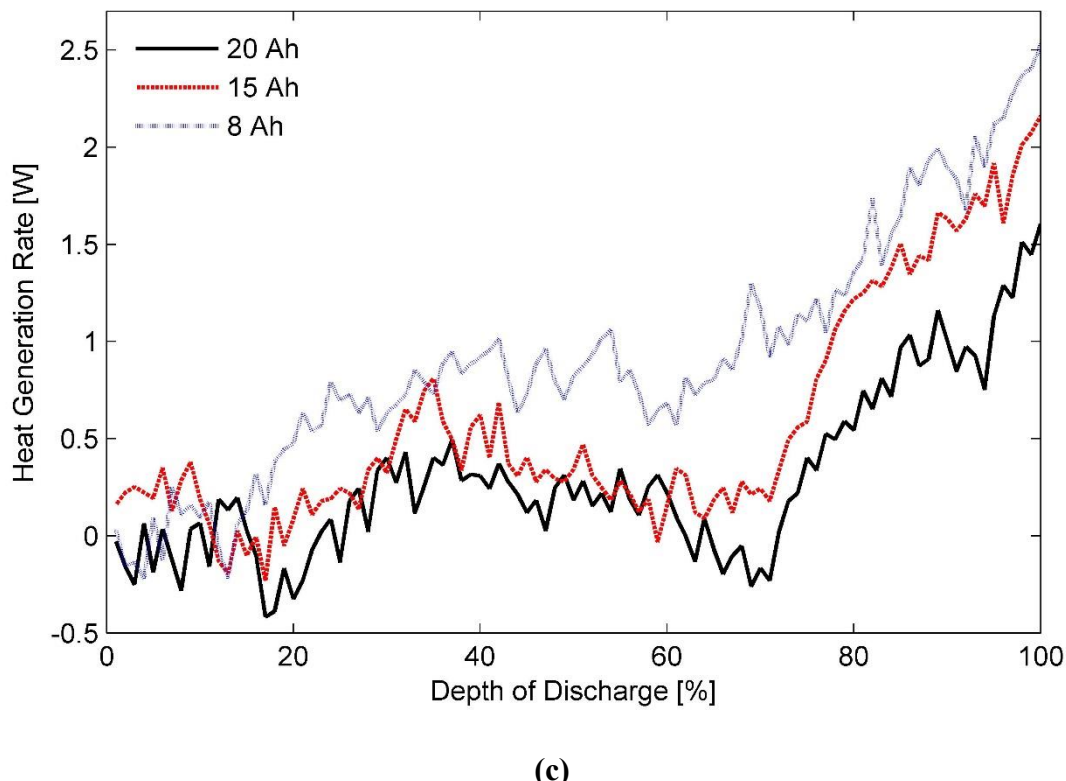
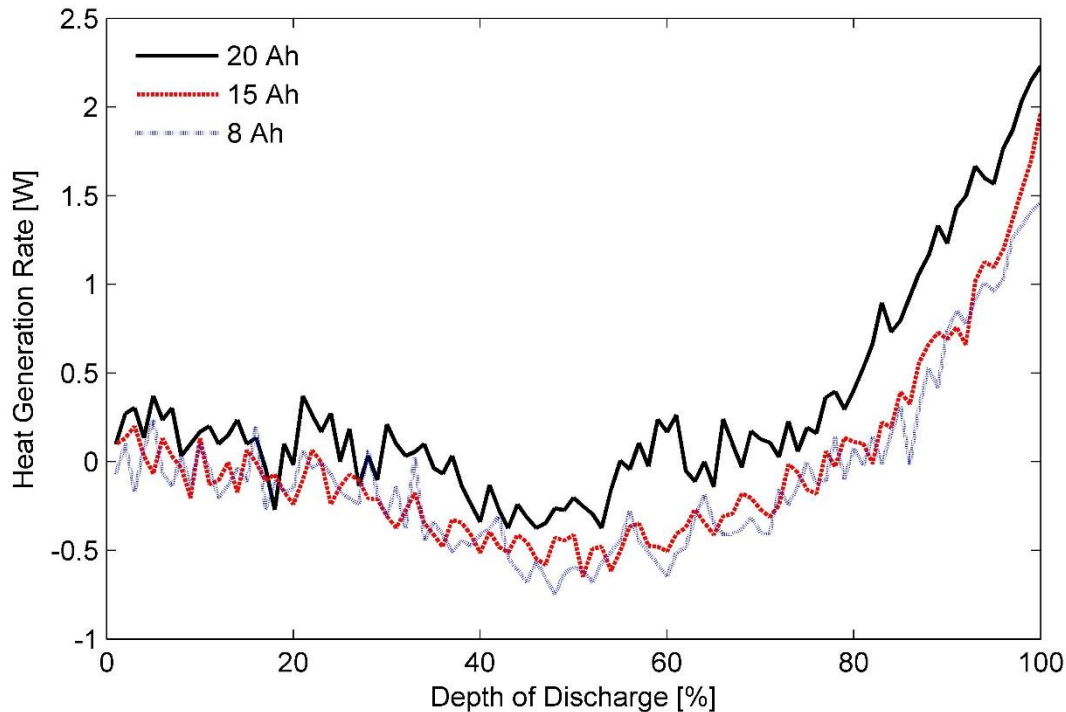
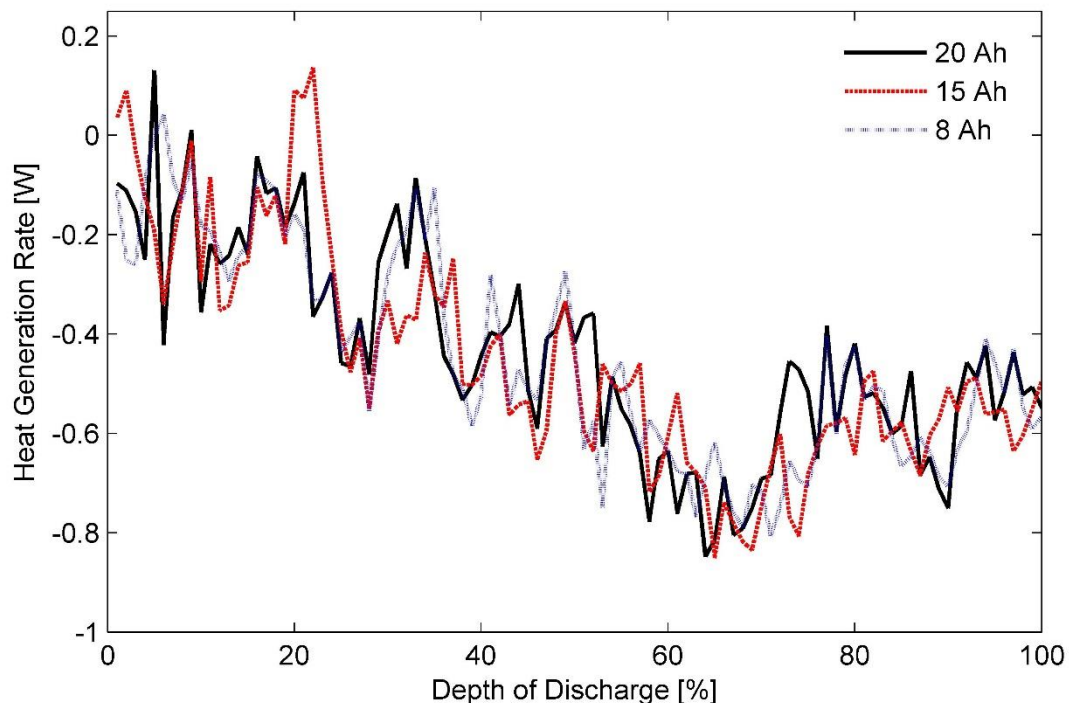


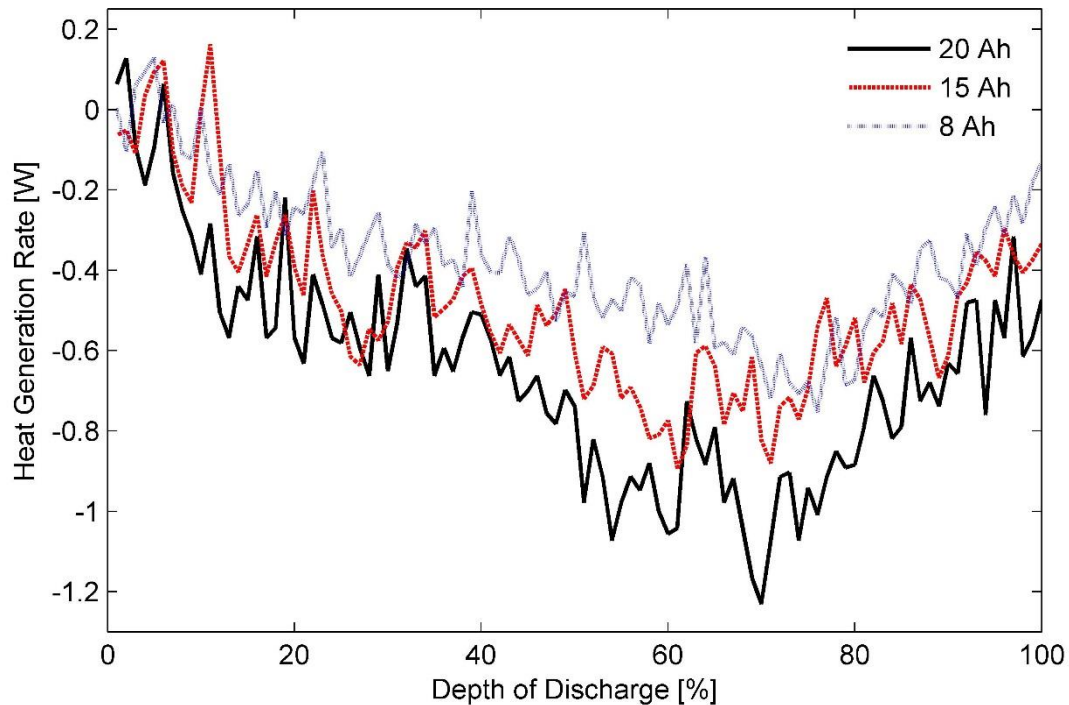
Figure 5.6: Heat generation rates for three test battery cells during the constant current discharge process at a rate of 1C under ambient temperatures of (a) 20 °C, (b) 35 °C and (c) 50 °C



(a)



(b)



(c)

Figure 5.7: Heat generation rates for three test battery cells during the constant current discharge process at a rate of 0.33C under ambient temperatures of (a) 20 °C, (b) 35 °C and (c) 50 °C

Lastly, it can be seen in **Fig. 5.7(a)** that for an operating temperature of 20 °C and at a discharge rate of 0.33C, the total heat generated by $LiFePO_4$ is endothermic for the initial half of the discharge cycle. Afterwards, it switches to an exothermic mode in the second part of the cycle. In contrast, it is endothermic throughout the whole cycle for operating temperatures of 35 °C and 50 °C, as shown in **Figs. 5.7(b)** and **5.7(c)**, respectively. Accordingly, a smaller-sized TMS is required to maintain the Li-ion battery pack at a uniform temperature of either 35 °C or 50 °C than for example at 25 °C. However, from a safety perspective, an operating temperature of 35 °C takes precedence over an operating temperature of 50 °C. Therefore, operating the battery TMS at 35 °C not only facilitates a modular battery TMS design but also assists in vehicle light weighting by restricting the passive load of an EV to the minimum level.

5.5. Conclusions

Heat generation rates for Li-ion battery cells are known to exhibit a strong dependency on discharge rate, ambient temperature and DOD. However, it is anticipated that this relationship may change with the nominal capacity of a battery cell. Therefore, in the present study, the heat generation rates for $LiFePO_4$ pouch cells, with different energy capacities, were experimentally measured at various DODs under an assortment of operating conditions described by a set of values for ambient temperature and discharge rate. The effect of cell/electrode thickness on battery heat generation rates was also included in the analysis. To facilitate accurate measurements, a custom-designed calorimeter was used. It is an improvement over the previous calorimeter proposed by Chen et al [300], and enables heat generation estimation for pouch cells of different surface area-to-thickness ratios. The experimental results reveal that for operating temperatures greater than 35 °C, the heat generation rates for thin battery cells are lower than the rates measured for thick battery cells of equivalent nominal capacity. In contrast, the transformation of electrical energy to chemical

energy in ambient temperatures lower than 35 °C is much more efficient for battery cells with thick electrodes than for thin battery cells. The difference increases as the discharge rate is increased, regardless of the cell operating temperature. In addition, the effect of the Li-ion transportation rate-limiting mechanisms on battery heat generation rates is negligible in comparison to the effect of electrode thickness. Lastly, at an operating temperature of 35 °C, the heat generation rates for all three test battery cells, irrespective of their nominal capacities, are equal. The phenomenon is shown for all the test discharge rates.

Chapter 6

Effect of interphasial film resistance on heat generation⁴

⁴ A publication was produced based on this chapter. Details are available from - 339. Arora, S., W. Shen, and A. Kapoor, *Critical analysis of open circuit voltage and its effect on estimation of irreversible heat for Li-ion pouch cells*. Journal of Power Sources, 2017. **350**: p. 117-126.

This page has been intentionally left blank

Chapter 6

6.1. Introduction

Electrical energy available from an electrochemical cell is a product of its nominal capacity and the working voltage. Understandably, the impetus is largely on the development of lithium ion (Li-ion) batteries with higher operating voltages [340, 341]. One method of achieving this is through replacement of traditional active materials such as spinel lithium manganese oxide and layered lithium cobalt oxide with cathode materials that exhibit higher redox potentials vs. lithium reference electrode (Li^+/Li) [342]. A comprehensive list of such materials is accessible from [343]. On the other hand, capacity reduction for commercially available Li-ion cells due to voltage loss caused by battery polarisation still remains a major issue [344]. This voltage attenuation can be as high as 1V for the lithium conversion process at low temperatures and high charge/discharge rates in transition metal (Fe, Ni, Co and Cu) electrodes [345, 346]. As polarisation directly affects the heat generation characteristics of a Li-ion cell, it can at times become a safety concern and thus needs to be quantified [347].

In view of this, Tiedemann et al. examined the potential distribution on the bare lead-acid battery grid by applying a resistive network model to it [348]. The model was later expanded by Tiedemann and Newman to analyse the transient behaviour of an idealised battery cell. In the model, an empirical function given in eqn. (6.1) is used to describe the irreversible polarisation between the two electrodes of the lead-acid battery [349].

$$\frac{I_t}{A} = Y(U - \phi_+ - \phi_-) \quad (6.1)$$

where $I_t/A=0$ is the current density transferred locally through the separator from the negative electrode to the positive electrode, U is the open-circuit voltage (OCV) of the battery

Effect of Interphasial Film Resistance on Heat Generation

cell, i.e., cell voltage when there is no current flow through it and is mathematically calculated by the intercept of a tangent line on the polarisation curve at $I_t / A = 0$, Y is a reaction rate constant of an electrochemical reaction determined by the reciprocal of the slope of the voltage-current (V-I) curve for the battery cell, ϕ_+ and ϕ_- are the potentials of the positive and negative electrodes, respectively; their difference ($\phi_+ - \phi_-$) is the measured voltage of the battery cell.

Tiedemann and Newman's method of estimating the OCV of a battery cell is based on a premise that the gap between the two electrodes of an idealised cell is filled by an ionic conductor whose concentration is always constant. Accordingly, concentration polarisation is considered negligible in their formulation. As per their assumptions, all the changes in concentration of the electrolyte are restricted to regions within the pores of the lead electrode [350]. The same method was later employed by Gu to experimentally determine the polarisation between the electrodes of a Zn/NiOOH cell [327]. Subsequently, it was referred as the NTG (Newman, Tiedemann and Gu) model and is now one of the most frequently used models for predicting thermal behaviour of Li-ion batteries [61, 71, 288, 351-362]. Moreover, it has even been implemented in the framework of voltage model of a commercial battery simulation software - Battery Design Studio/CD-adapco [363, 364].

However, interphasial polarisation is neglected in the NTG model. This is not justifiable for real or commercial battery cells. Ignoring interphasial polarisation would introduce errors in estimation of battery polarisation and consequently would cause underestimation of heat generation rates of commercial battery cells. Accurate estimate of battery heat generation rates is a pre-requisite for designing a robust and reliable battery thermal management system, responsible for regulating Li-ion battery cell temperature in a safe limit and maintaining their cycle life [37, 365, 366]. It is therefore necessary to check the influence of the interphasial polarization on the OCV used for calculation of heat generation rates via the NTG model. To

the best of authors' knowledge, this effect has not yet been quantified. The present chapter firstly serves this purpose.

Secondly, solid electrolyte interphase (SEI) film resistance is an important parameter in the study of charge transfer kinetics of a Li-ion battery. The passive film affects the diffusion process of Li-ions. As such, it becomes essential to include film resistance in battery modelling. However, the traditional method of measuring the SEI film resistance is costly and time consuming. An indirect approach for quick estimation of interphasial resistance is thus also presented in this chapter.

6.1.1. Need for estimating SEI film resistance

The first few charge and discharge cycles are critical for an unused Li-ion electrochemical cell. Various organic and inorganic species in the electrolyte react with the electrode surface forming a 5 Å to 800 Å thick reaction film during these cycles. It is an ion-conducting and electron-insulating passive film, which can have a considerable affect on the resultant electrode activity. Recent investigations confirm that the Li-ion charge carrier flow is hindered by a film on the external boundaries of the solid portion of the porous electrode while negligible charge-transfer resistance is offered by its solution phase. Retarded surface reactions due to the presence of a passive surface film, commonly referred as SEI film, is therefore among the list of key factors for poor performance of Li-ion battery cells particularly at low temperatures.

It is important to realise that the interphasial impedance has a noticeable influence on the transfer rate of Li-ion under the effect of electrical field. Knowledge of electrical resistance of SEI film is therefore essential for predicting battery performance accurately. Neglecting it may introduce uncertainties in the determination of transport properties such as Li-ion diffusion coefficient and electrolyte conductivity [337].

The transport properties of an electrochemical system can be assessed either via the dependency of voltage and current in a time domain or can be quantified in terms of impedance or admittance on a frequency chart. Noteworthy is that the data acquisition in time domain is relatively straightforward and requires simple instrumentation; measurements in the frequency domain on the other hand contain visual information that can be related back to different transfer processes ongoing simultaneously in a Li-ion battery cell. Owing to this high level of detail available from the impedance spectrum generated by the electrochemical impedance spectroscopy (EIS) technique, it is typically utilised for determination of the SEI film resistance in batteries.

However, obtaining good quality images at very low frequencies is a time consuming process as the impedance bridge is required to be set and balanced for each frequency with costly instrumentation [367, 368]. Furthermore, it is essential to perform several control experiments in parallel to be able to distinguish impedance changes due to factors like initial electrode contamination or additional differential pulse voltammetry or cyclic voltammetry measurements from those due to specific electrochemical interactions and transfer process [369]. For these reasons, a simple and an indirect approach that avoids using impedance spectra for estimation of the SEI film resistance of Li-ion batteries is demonstrated in this chapter. The approach is primarily based on Ohm's law and builds on the foundation developed by Churikov and Ivansishev [370].

6.2. Critical analysis of OCV

An energy balance equation for a battery cell with negligible thermal mass and operating in an insulating environment can be written as [371]

$$\frac{I}{nF} \Delta H = -VI \quad (6.2)$$

The term on the left symbolizes power released from the chemical mass of the cell while the term on the right depicts electrical power available from the cell. ΔH is the enthalpy of the reaction which represents the amount of energy released or absorbed during discharging or charging of the cell, n is the number of moles of electrons per mole of reactant, F is the Faraday's constant, V is the terminal voltage of the cell and I is the charging/discharging current flowing through the cell. Moreover, electrical energy required to overcome the irreversibility involved in transportation of Li-ions from one side of an electrochemical cell to the other corresponds to the change in Gibbs free energy or free enthalpy ΔG of the cell. It is noteworthy that at constant temperature and pressure, the equilibrium voltage of an electrochemical cell is an indicator of the Gibbs free energy change ΔG when no current flows through the cell. Their relationship is mathematically described by

$$E_{eq} = -\Delta G/nF \quad (6.3)$$

Also, the Gibbs free energy change ΔG at an absolute temperature T can be expressed by the difference between the enthalpy ΔH and entropy ΔS of the cell that characterises the reversible energy loss or gain from the electrochemical process as shown below

$$\Delta G = \Delta H - T\Delta S \quad (6.4)$$

Polarisation refers to the mechanism of displacing the potential of an electrochemical cell from its equilibrium during a chemical reaction. It can be divided into three categories: Ohmic polarisation, concentration polarisation and activation polarisation. Together they result in a reduced cell performance. Polarisation can be derived by re-modelling the energy conservation eqn. (6.2) via replacement of the enthalpy ΔH with the equivalent terms from eqns. (6.3) and (6.4) as follows

$$\frac{I}{nF}T\Delta S = (E_{eq} - V)I \quad (6.5)$$

Although both the terms $(E_{eq} - V)$ in eqn. (6.5) and $(U - \phi_+ - \phi_-)$ in eqn. (6.1) describe battery polarisation, the OCV used for E_{eq} in eqn. (6.5) and the OCV used for substituting U in eqn. (6.1) are determined in a different manner. U in eqn. (6.1) is calculated by the intersection of a tangent line on the polarisation curve at $I_i / A = 0$. The OCV obtained from this extrapolation method is a potential corresponding to an instant when the summation of all the currents associated with a set of reversible reactions in the electrochemical system becomes equal to zero. It is however a time variant value that changes as the concentration gradient is relaxed, indicating that the cell has not yet reached an equilibrium state. On the other hand, in eqn. (6.5), the OCV specified is representative of the Gibbs free energy change. It is a thermodynamically established value unique to a state of an electrochemical system and estimated via a galvanostatic discharge test as explained in Section 6.3.

It is vital for an accurate estimation of the change in free energy of a system that the condition of local chemical equilibrium is maintained. For this, the kinetics of the intercalation and the de-intercalation reactions should be sufficiently fast in comparison to the disturbance caused by the measurement [372]. If a concentration gradient exists in a battery cell held in an open circuit state, the ‘activation’ energy associated with the redox reactions induces an ionic return current. The induced current restores the uniformity in the charge distribution of the solution phase of the two porous electrodes.

It should be noted that the OCV can be a good approximation of the equilibrium potential only when the return current is insignificant in comparison to the applied current [373]. It can however take anywhere from several minutes to hours for restoration of the concentration balance after the applied current is switched off [374]. Gu’s method, i.e., the NTG model,

ignores this relaxation period even though the return current may be high enough to have a significant effect on the final results during this phase. The effect is illustrated through a comprehensive experimental study discussed in subsequent sections. Difference between the OCV and the equilibrium voltage of the cell is also outlined in the process. Details of the test procedure and the results are presented in the following text.

6.3. Experimental set-up

A 20V, 100A data acquisition system with 4-channels from Arbin Instruments (BT2000) is used to measure the irreversible polarisation for a Li-ion battery cell during a constant current discharge cycle at 27 °C. A 20 Ah lithium iron-phosphate (LFP) thin pouch cell (Model No.: BHK-85C0M7) manufactured and supplied by Benergy Tech Co. Ltd., China, is chosen as a test battery for this study. With the set-up, the OCV is first calculated in a more traditional manner by galvanostatic intermittent discharge method and subsequently estimated via Gu's extrapolation method [327]. The two OCV values are then substituted in eqn. (6.1) to calculate the irreversible heat generation for the test battery cell.

To prepare the test, the new pouch cell is charged and discharged six times to allow formation of the solid electrolyte interphase layer and stabilisation of battery nominal capacity. In the intermittent discharge test, voltage of the test battery is measured under static conditions. A static condition is when there is no current flow through the cell while an electrochemical cell is considered to be in an equilibrium state when the OCV change rate becomes less than 0.1 mV/30 min [375]. Voltage response of a LFP battery cell at 27 °C, seen in **Fig. 6.1**, indicate that a cell has to remain in open circuit state for at least one-hour in order to fulfil this criterion. Subsequently, the fully charged battery cell, maintained at 27 °C by a programmable thermal chamber, is galvanostatically discharged for 6 minutes at a current of 20A, i.e., 1C of the battery, and thereafter allowed to rest for one hour, each discharge approximately equalling a

Effect of Interphasial Film Resistance on Heat Generation

10% reduction in the depth of discharge (DOD). Such discharging is repeated until a cut-off voltage of 2.5V is reached. The OCV measured at the last second of every rest phase is logged as the equilibrium voltage. In this manner, the OCV is measured at nine different DODs between 0 and 100%, i.e., the fully charged and the fully discharged states, respectively.

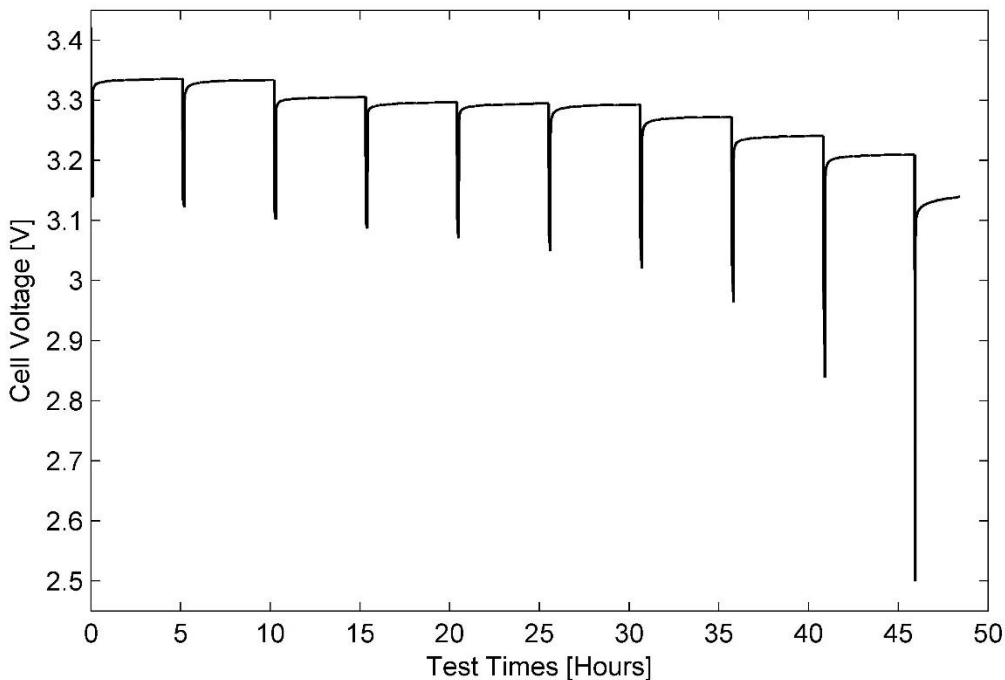
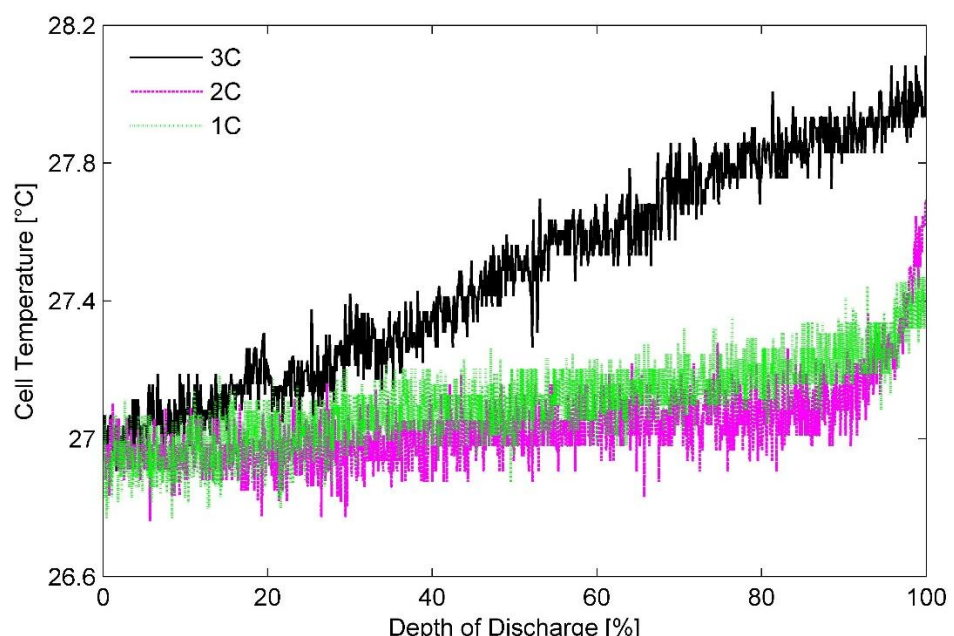


Figure 6.1: Voltage response recorded during a galvanostatic intermittent discharge test for LFP pouch cell at 27 °C

In a second set of these tests, the OCV for the 20 Ah Li-ion pouch cell at 27 °C is estimated from its V-I characteristics as demonstrated by Gu [327]. The problem with this method however is that at high current densities, battery cell temperature rises rather rapidly and introduces errors in the measurement. Previous studies have demonstrated phase change materials (PCM) as an effective thermal management system for Li-ion batteries [235, 236, 244]. To increase the precision of test data, PCM (RT28HC) from Rubitherm GmBH, with a melting point in the range of 27-29 °C, is therefore used as a cooling solution. The fully charged cell is successively subjected to galvanostatic discharge cycles at varying rates starting from 0.01C to 3C to identify the voltage-current characteristics of the cell in a re-designed set up.



(a)



(b)

Figure 6.2: 20 Ah LFP pouch cell (a) soaked in a PCM for taking potentiometric measurements under isothermal settings (b) surface temperature variation in the test cell at different discharge rates

Fig. 6.2 shows (a) the experimental set-up with the 20 Ah LFP test battery soaked in the PCM contained in a polycarbonate casing and (b) resulting surface temperatures recorded during the constant current discharge tests. A maximum deviation of 1.11 °C corresponding to a 3C discharge rate is observed in the cell surface temperatures shown in **Fig. 6.2(b)**. It is thus confirmed that the designed experimental set-up involving PCM can successfully maintain a near-isothermal environment even at high discharge rates.

6.4. Validation through calorimetric tests

Commercially available calorimeters, be they isothermal heat conduction calorimeters or accelerated-rate calorimeters, impose tight restrictions on the size as well as geometry of the battery cells that can be tested. Also, they are generally expensive. Consequently, many of the previous studies concerned with heat generated by Li-ion batteries are based on data extracted from testing small coin or cylindrical battery cells at low discharge rates [304, 305, 307, 376-378]. In this study, a custom-designed adiabatic calorimeter has therefore been used to simulate thermal behaviour typically expected in large battery cells. The findings are later used to validate parameter selection for the NTG model.

6.4.1. Design of Calorimeter

An adiabatic calorimeter functions by minimising the flow of thermal energy between its contents and their environment through the calorimeter material, which acts as a thermal barrier. As such, desirable material for a battery calorimeter should have high thermal resistance in the test temperature range to be able to approximate an ideal solution. Chen et al. confirmed that high-density polyethylene (HDPE) is such a material. They also indicated that HDPE slabs approximately five times the thickness of the battery cell would be required for characterising its heat generation behaviour accurately [300].



Figure 6.3: A custom designed battery calorimeter for measuring total heat generated by a 20 Ah LFP pouch cell during charge and discharge cycles

In view of this, two 50 mm HDPE slabs are bolted together to construct this calorimeter. A 227 x 120 x 4.5 mm deep feature is cut in each of the two slabs for the battery to sit in as shown in **Fig. 6.3**. A layer of thermal grease (thermal conductivity $\sim 1.93\text{W/m-K}$) is applied to the contact surface in order to ensure effective heat transfer from the battery surface to the HDPE slabs. The temperature measurements in the calorimetric material are collected from a sensor strategically placed 6 mm away from the battery surface, in the plane passing through the centre of the battery cell and the HDPE slab to avoid any inaccuracies due to edge effects of heat transfer.

6.4.2. Experimental procedure

The heat of mixing and the phase change have been neglected for the purpose of this investigation. Thus, it is assumed that the heat generated during the discharge cycle of a Li-ion battery includes only the reversible and the irreversible heat components. The former represents the portion of the total heat, which is generated because of entropic changes in the battery structure while the latter signifies the energy consumed in overcoming mass-transfer and charge-transfer limitations, as well as the ohmic losses suffered during the test cycle.

The calorimeter is placed overnight in an isothermal environment of 27 °C created with the assistance of a programmable thermal chamber to achieve a steady state temperature distribution throughout the calorimeter. The standard constant current constant voltage (CCCV) charging method is adopted to fully charge the battery cell. Under this charging regime, the battery cell is initially charged at a 0.33C rate to the maximum allowable charged voltage of 3.65V. Subsequently, the cell is taper-charged to 0.05C while maintaining a constant terminal voltage of 3.65V. As for the discharge cycle, a constant current discharge rate of 0.33C is used as well while the cut-off voltage is set to 2.5V. The cell is allowed to rest for an hour between the charge and the discharge cycles. This rest phase prevented the assumption about the total heat from becoming void by shielding the heat generated during the discharge process from the effect of heat of mixing produced in the charging operation. The process is later repeated with a constant current charge and discharge rate of 0.5C.

Total heat generated by the 20 Ah pouch cell at 27 °C and charge/discharge rates of 0.33C and 0.5C is calculated for both the charge and the discharge operations separately. The calculations are based on the principles of the inverse heat conduction problem and the Fourier's law of heat transfer described in [325]. Furthermore, the irreversible heat for both these processes is

assumed equal. Hence, the reversible heat could be estimated from discharge and charge calorimetric data as follows:

$$Q_{reversible} = \frac{Q_{discharge} - Q_{charge}}{2} \quad [6]$$

The assumption about the irreversible heat is valid until the current used for charge and discharge is same. However, charging algorithm used in this study includes a constant voltage (CV) portion as well, where current gradually decreases to 0.05C. Jannesari et al. determined that the CV mode of the algorithm could account for up to 13% of the total energy delivered to the cell during charging [379]. Consequently, heat generated within the DOD range of 20% and 80% only is used for validation.

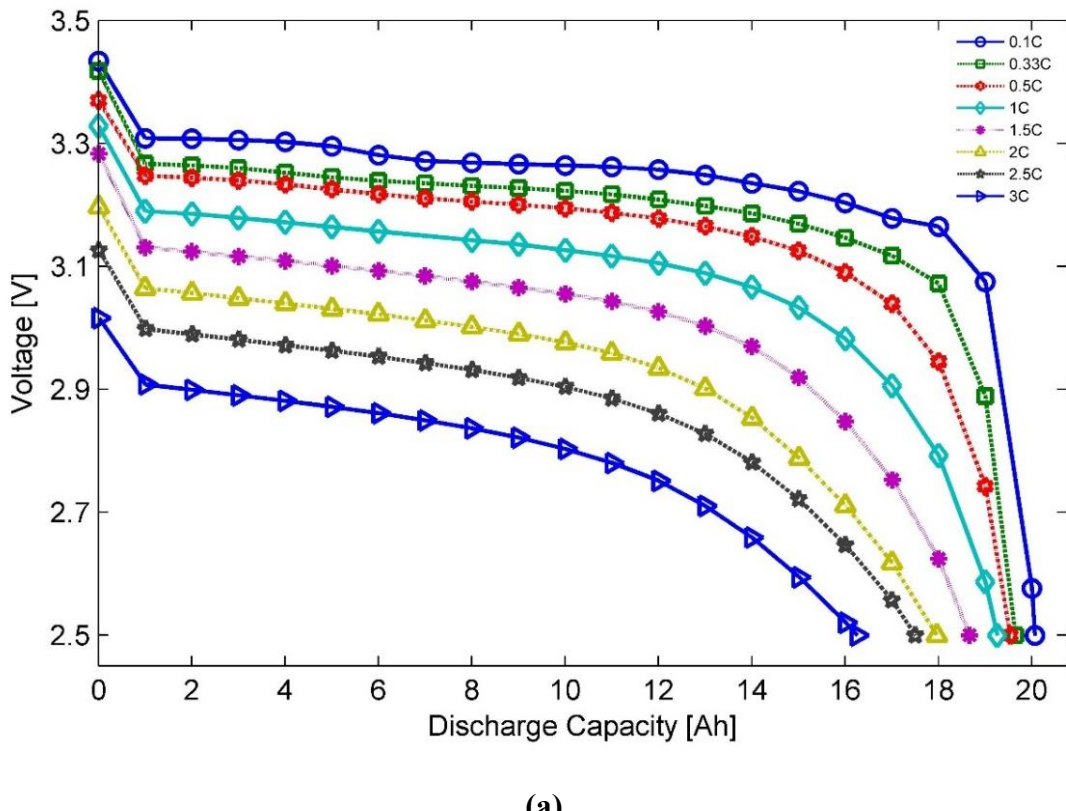
6.5. Results and Discussion

6.5.1. Voltage measurement

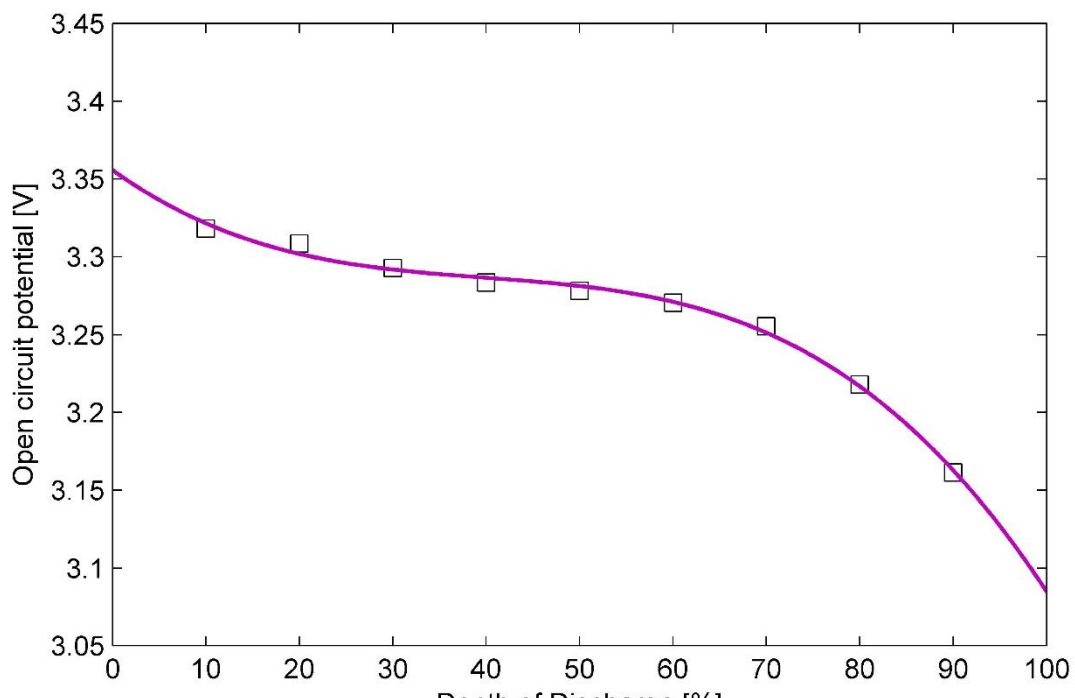
The voltage response recorded at C-rates of 0.1C, 0.33C, 0.5C, 1C, 1.5C, 2C, 2.5C and 3C versus DODs for the test battery cell are shown in **Fig. 6.4(a)**. During this cyclic process, the battery cell temperature is regulated at 27 °C using the set-up shown in **Fig. 6.2(a)**.

It is considered that a discharge rate of 0.1C is slow enough for a LFP pouch cell to allow for complete utilisation of all the active material available in the cell. The available discharge capacity of 20.032 Ah at 0.1C is therefore used as the theoretical capacity to estimate the depth of discharge for further analysis. As a result, discharge capacity in **Fig. 6.4(a)** can be converted into the DOD for different discharge rates and then the OCV at various DODs can be estimated from the V-I characteristics of the test battery via the extrapolation technique, i.e., Gu's method mentioned in Section 3.2. The estimated OCV values are illustrated in **Fig. 6.4(b)**.

Effect of Interphasial Film Resistance on Heat Generation



(a)



(b)

Figure 6.4: (a) Terminal voltage versus discharge capacity of 20 Ah LFP pouch cell at different discharge rates
 (b) OCV versus DOD estimated from V-I characteristics of the test battery cell at constant battery cell temperature of 27 °C

The dependency of the calculated OCV on DODs can be expressed in a polynomial form as shown in eqn. (6.7). Third-order or cubic polynomials are generally preferred due to their ability to capture important details and superior computational efficiency. Coefficients of the third-order polynomial used in this study are listed in **Table 6.1** along with the coefficients of a polynomial fitted to the OCV measured one hour after the applied current is switched off.

$$OCV_t = \sum_{m=0}^3 A_m \cdot DOD^m \quad (6.7)$$

Parameter (V)	Equilibrium Voltage ($OCV_{t=3600}$)	OCV Instantaneous ($OCV_{t=0}$)
A3	$-6.0638 * 10^{-7}$	$-8.0682 * 10^{-7}$
A2	$7.913 * 10^{-5}$	$9.6591 * 10^{-5}$
A1	- 0.0041512	- 0.0043017
A0	3.3833	3.3559

Table 6.1: Fitting parameters for both $OCV_{t=0}$ and $OCV_{t=3600}$ as a function of DODs

A comparison is drawn between the OCV measured one hour from the instant applied current flow is discontinued through the battery cell and the derived OCV from the V-I characteristics in **Fig. 6.5**. It also shows the terminal voltage recorded for a constant current discharge of test battery at 0.33C rate at the operating temperature of 27 °C. The two OCV values can be differentiated by the measuring points in time. While the former, i.e., OCV at $t = 0$ s, is the voltage at the instance when the applied current is turned off, the latter or OCV at $t = 3600$ s is the voltage measured along the two electrodes of a cell sitting in an open circuit state for an hour and corresponds to its equilibrium state. The disturbance created in a pool of charge carriers by the applied current stabilises during this resting period thereby contributing to recovery of the electrode potential. The data collected suggest that the $OCV_{t=3600}$

corresponding to 10% DOD state of the 20 Ah LFP test battery cell is larger than the instantaneous OCV or $OCV_{t=0}$ by 0.028V. On the other hand, 0.0479V is regained by $OCV_{t=3600}$ in the one hour rest phase post current cut-off at a DOD of 90%.

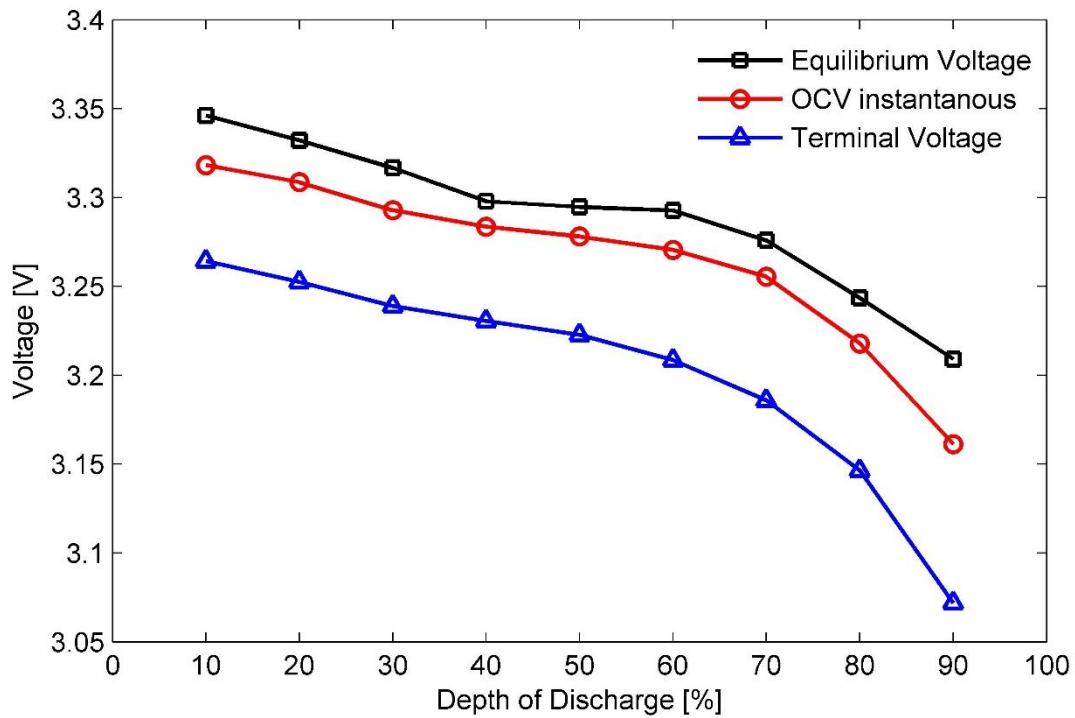


Figure 6.5: Comparison of OCV obtained from Gu's method, OCV at equilibrium state and terminal voltage at 0.33C discharge rate and ambient temperature of 27 °C at different DODs

6.5.2. SEI film resistance estimation

The total irreversible polarisation developed upon current flow in an electrochemical cell is comprised of the Ohmic potential drop across the solid portion of the electrode and in the electrolyte, the potential drop across the solid electrolyte interphase film and a potential shift caused by concentration change due to continuous dissolution and deposition of the potential determining Li-ions. It has been reported though that the diffusion relaxation time constant for lithium components is $10^1 - 10^3$ s [380]. On the other hand, under normal conditions the transient processes in an SEI film on lithium and its alloys would take $10^{-4} - 10^{-3}$ s to complete [381]. A comparative evaluation of these two time frames reveals that in comparison to the

characteristic diffusion relaxation time scales, polarisation across the solid electrolyte interphase film of a Li-ion battery cell develops virtually at the instant a current pulse is applied to a lithium-carbon film electrode.

Furthermore, diffusion coefficient for Li-ions in the liquid phase of the porous electrode, i.e., the electrolyte, is $10^{-5} \text{ cm}^2/\text{s}$. Consequently, concentration polarisation developed in the battery cell as a response to a current pulse of low amplitude and duration of the order of 10^{-4} s may be negligible [337, 382]. For cases involving a longer current pulse, the disturbance caused in the redox electrochemical system would induce an ionic return current which is responsible for reinstatement of a uniform charge distribution in the Li-ion battery cell. It would however take anywhere from a few minutes to several hours for restoring the concentration balance in the battery cell after the applied current is switched off and for the cell to recover from this loss in working voltage. This duration increases as the percentage of lithium in the intercalate increases [380].

Activation polarisation, on the other hand, is the drop in electrode potential sustained while overcoming the energy barrier posed by the slowest step involved in the electrochemical process. It is equivalent to a threshold barrier that Li-ions have to break in order to become mobile. It would therefore come into play each time the electrical circuit including a Li-ion cell is closed, regardless of the cell being in an equilibrium state or not. In other words, difference between OCV instantaneous and terminal voltage of the cell includes the activation polarisation. Thus, the difference between the $OCV_{t=0}$ and the $OCV_{t=3600}$ can be attributed to the interphasial polarisation, which evidently from **Fig. 6.5** cannot be accounted for by the OCV estimation technique proposed by Gu.

Interphasial polarisation, i.e., the potential drop across the SEI film is thus calculated using the difference between the equilibrium voltage and the OCV derived from the extrapolation of V-

I curves to the y-axis, i.e., $I = 0$ at time = 0 in the chronopotentiograms shown in **Fig. 6.4(a)**.

The corresponding voltage drop observed for the 20 Ah test battery as a result of the SEI film resistance is presented in **Fig. 6.6**.

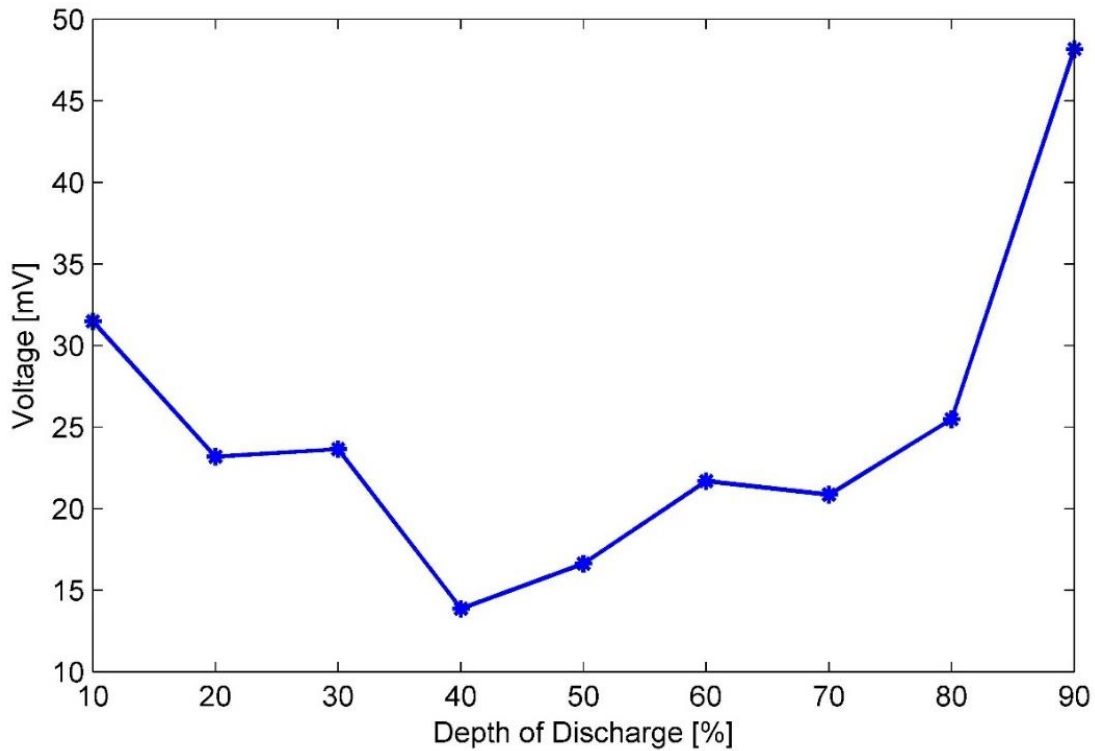


Figure 6.6: Voltage drop ($= OCV_{t=3600} - OCV_{t=0}$) observed across the SEI film during a constant current discharge test

The task of estimating the SEI film resistance can be accomplished by defining a linear approximation between the kinetic current and the battery potential as per the Ohm's law described in eqn. (6.8).

$$R_{SEI} = j^{-1} \cdot \Delta E \quad (6.8)$$

An additional condition confirming $j = \text{constant}$, where, j is the current density and ΔE is the potential step across the SEI film, has to be imposed on the system. Moreover, the kinetic current is considered independent of the Li-ion concentration in the porous electrode matrix. As such, the only influencing factor is the ionic conductivity or the electrical resistance of the

passive SEI film. The benefit of this approach is that it is phenomenological in nature. Within its framework, accurate detailing of the microscopic diffusion process of Li-ions across the SEI film is therefore not required. Accordingly, complexity of the problem is greatly reduced.

However, application of high current or potential steps to the SEI transition region may result in a sharp rise of Li-ion concentration gradient across its thickness. Also, applying a current pulse unavoidably causes a disturbance in the concentration pool of Li-ion whose magnitude is much greater than that of the disturbance created in response to a potential step. As the Ohm's law and the condition of linearity is only valid for cases of small perturbation of electrode potential, it becomes crucial to determine the appropriate amplitude for current/potential pulse.

In a current density spectrum of $0 - 5 \text{ mA/cm}^2$ and a potential step of 10 mV, Churikov et. al have shown that initially (after threefold cycling) the linearity holds true for the entire spectrum of current densities. However, it starts to deviate as current densities greater than 1 mA/cm^2 are applied to a redox system kept in storage for 2 months [380].

Subsequently, a current density of 0.001 A/cm^2 , that can be considered as a current tending to zero, is used. Lastly, interphasial resistance for a 1.13 nm thick SEI film of lithium-carbon film electrodes obtained through EIS technique is $0.0053 \text{ Ohm}\cdot\text{m}^2$ and $0.0093 \text{ Ohm}\cdot\text{m}^2$ for a film with 1.95 nm thickness [379, 383]. It can be noticed from **Fig. 6.7** that the magnitude of calculated SEI film resistance is consistent with that measured for LFP pouch cells using impedance spectroscopy. It can also be seen from the graph that the average value of SEI film resistance for the 20 Ah LiFePO_4 test cell defined with respect to DOD can be taken as constant during the discharge cycle. This is characteristic of a stable film.

Effect of Interphasial Film Resistance on Heat Generation

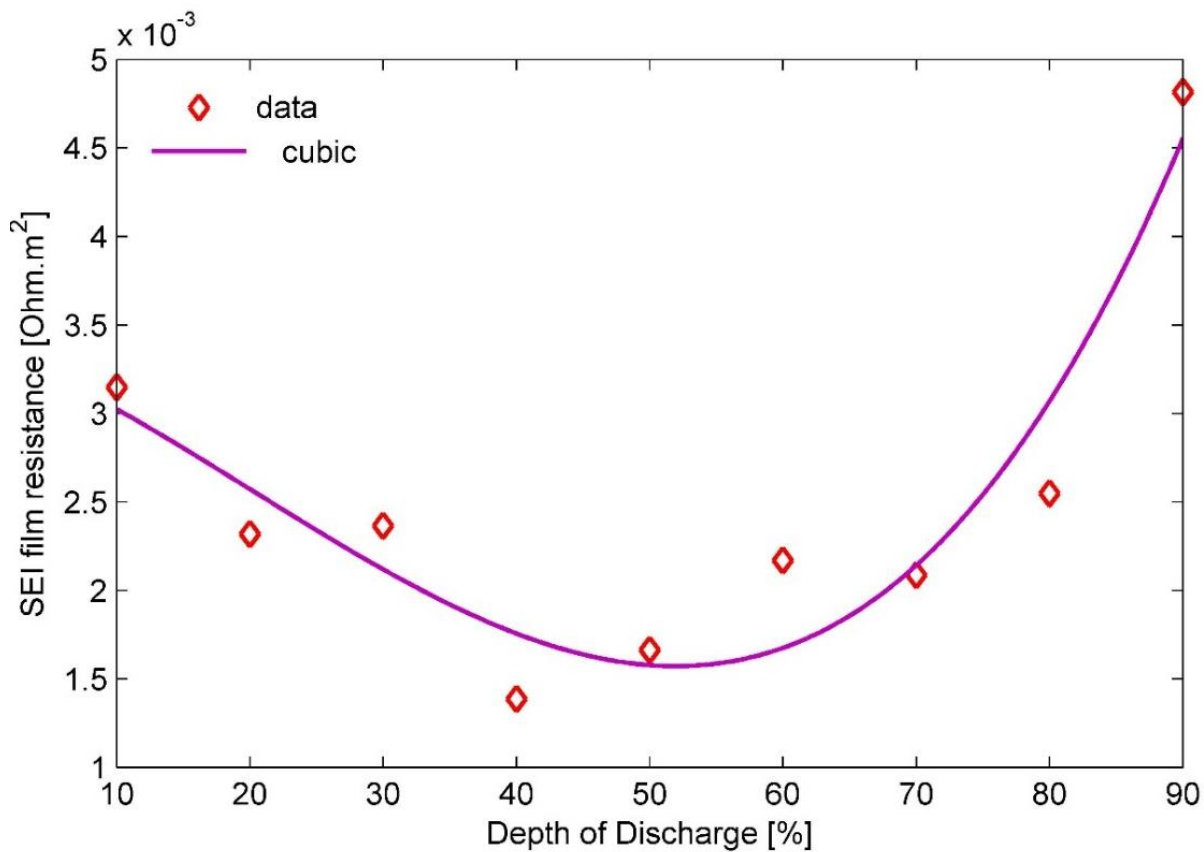


Figure 6.7: Variation of SEI film resistance for a 20 Ah Li-ion pouch cell with DOD (markers showing the calculated data points whereas solid line depicts a cubic curve fit)

However, little variations in its permeability may be noticed at different stages of discharge as phase transformation occurs. The permeability of SEI film is greater in the range of 40% to 70% DOD when both the iron phosphate phases, i.e., $FePO_4$ and $LiFePO_4$ coexists. In contrast, it offers higher resistance to Li-ion diffusion in the beginning and towards the end of discharge process when a monophase, i.e., $FePO_4$ at 0% DOD and $LiFePO_4$ near to 100% DOD, dominates the electrode composition [384]. This dependency, described by the solid line shown in **Fig. 6.7**, is governed by the following relation

$$R_{SEI} = 1.544 \times 10^{-8} * DOD^3 - 9.332 \times 10^{-7} * DOD^2 + 2.805 \times 10^{-5} * DOD + 0.003384 \quad [9]$$

6.5.3. Calorimetric measurements

Irreversible polarisation calculated using the equilibrium voltage and the OCV obtained via the Gu's method for the 20 Ah LFP test battery cell discharged in ambient temperature of 27 °C at a rate of 0.33C is shown in **Fig. 6.8**. It can be seen from the figure that application of Gu's method for OCV estimation leads to underestimation of the irreversible polarisation by 40% to 65% in the DOD range of 10% – 90%.

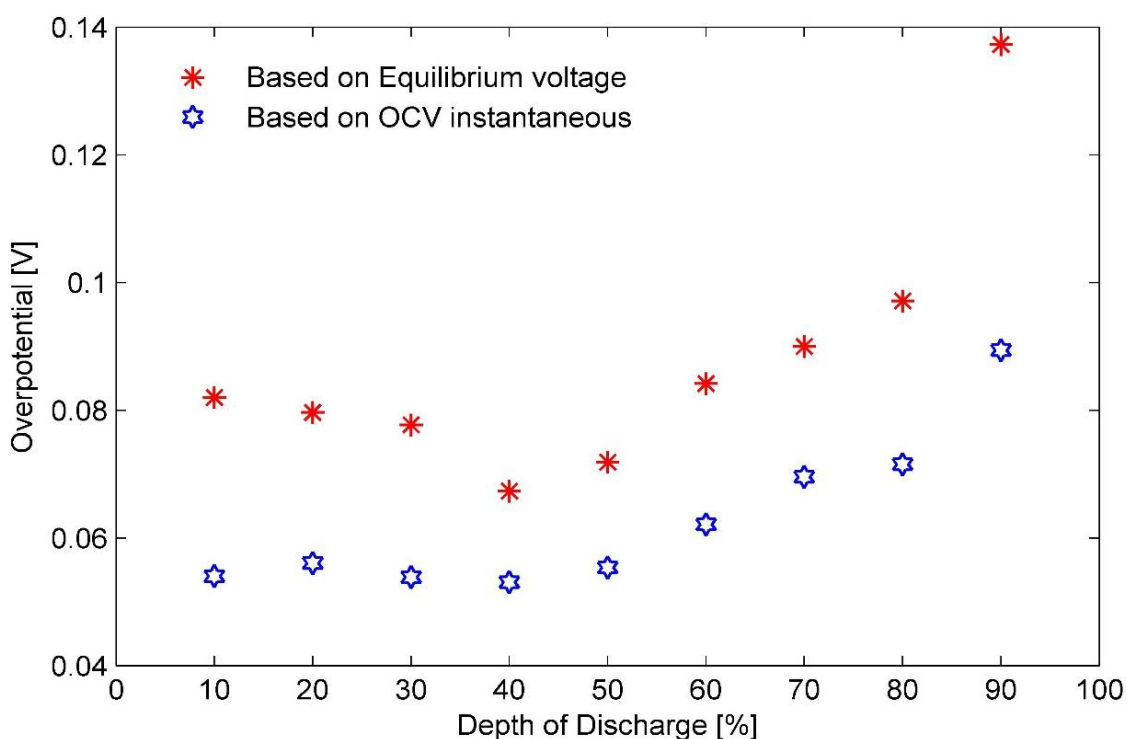


Figure 6.8: Irreversible polarisation for a 20 Ah LFP pouch cell at 27 °C at constant current discharge rate of 0.33C calculated using different OCVs

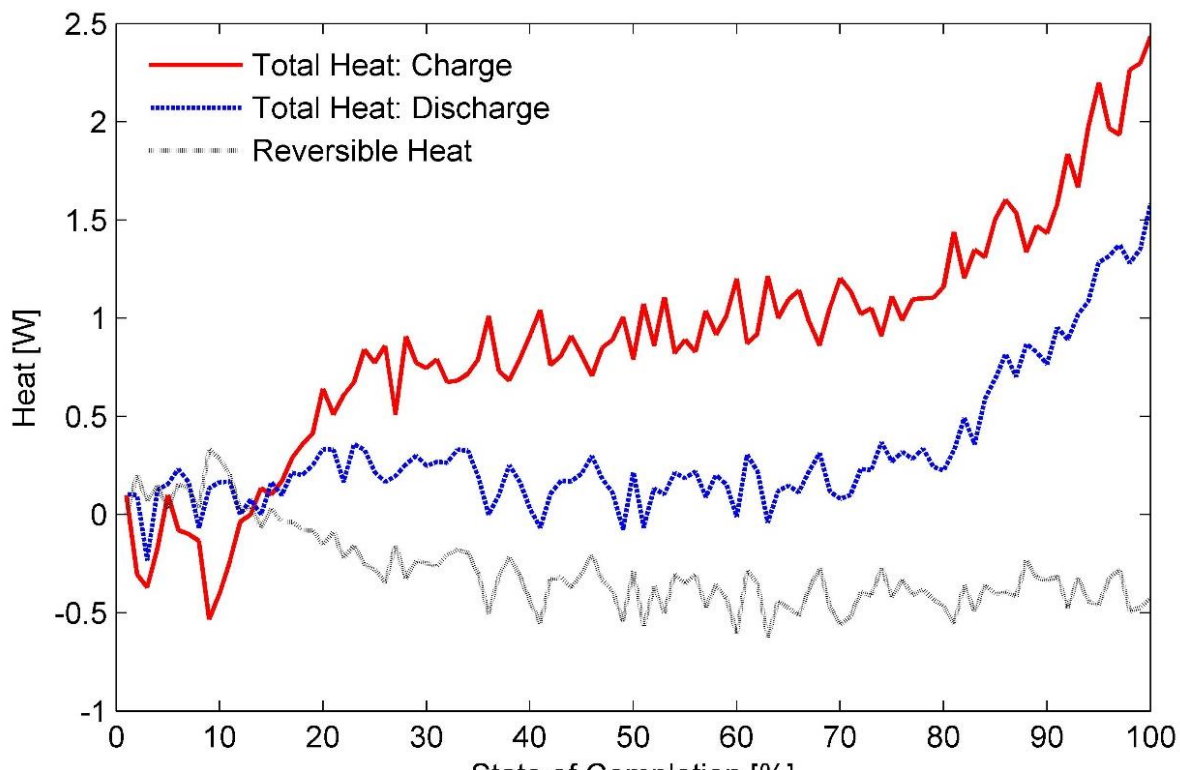
Fig. 6.8 also shows that from the three resistive components mentioned previously in Section 2, different components have a dominating effect on the irreversible polarisation during different stages of the discharge cycle. For example, the necessity to supply the minimum energy required to bring Li-ions to a condition where they can undergo physical transport from one electrode to another results in a relatively higher polarisation at the beginning of the cycle. Similarly, a large increase in the concentration polarisation owing to depletion of all the active

Effect of Interphasial Film Resistance on Heat Generation

material in the anode is observed near the end of the discharge process. It may thus no longer be possible to sustain the reactions at a current rate of discharge.

Figs. 6.9(a) and 6.9(b) illustrate the influence of entropic heat over the total heat generated during charge and discharge processes at an operating temperature of 27 °C at 0.33C and 0.5C, respectively. It can be seen from these figures that the reversible heat has its maximum values in the DOD range of 35% – 75% and appears to be an exothermic quantity functioning as a heating source augmenting the irreversible heat generated during the charging cycle.

In contrast, it works as a heat sink or an endothermic member opposing the irreversible heat during the discharge cycle. Similar observations about the nature of reversible heat have also been reported by Chen et al. [300] alongwith Bandhauer et al. [301].



(a)

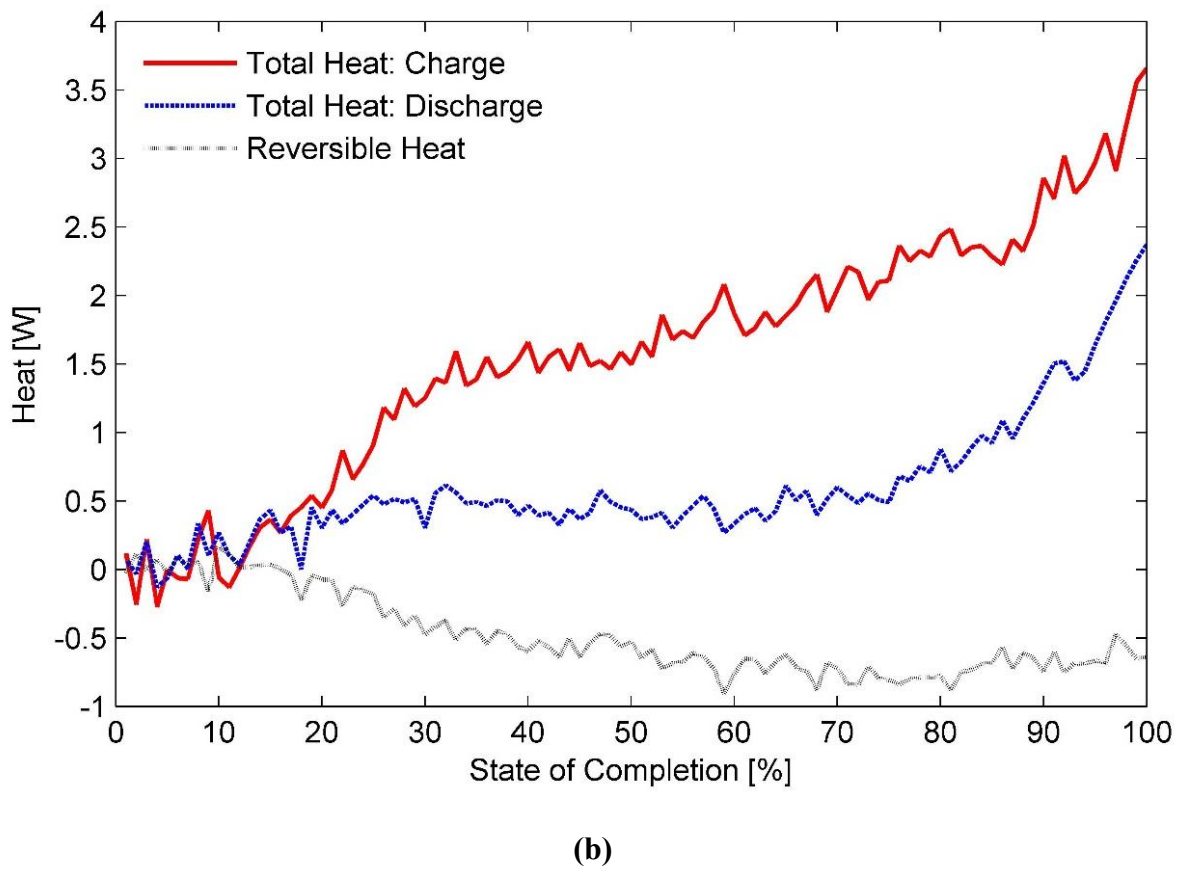


Figure 6.9: Total heat generated during charging and discharging process of a 20 Ah LFP pouch cell at operating temperature of 27 °C for C-rates of (a) 0.33C and (b) 0.5C

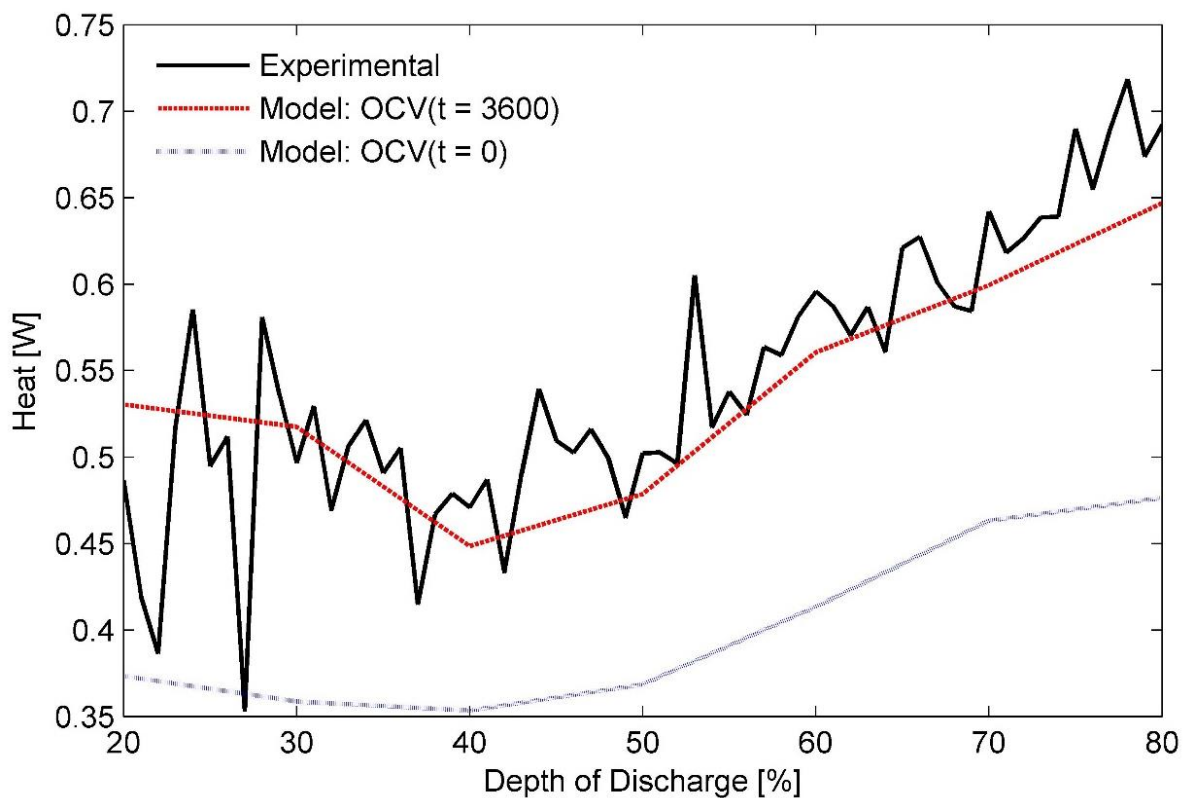
As a result, the total heat measured for the discharge process is only about 36% of the total heat generated while charging the battery in this stage. The ratio relatively improves as the end of the cycle approaches. In this case, the heat generated towards the end of the discharge cycle is almost 65% of the heat produced during charging. This is because of a major increase in the irreversible polarisation after the test battery is discharged by 80%.

Lastly, the irreversible heat calculated based on the assumed energy balance between the experimental data for charge and discharge obtained from the calorimetric tests conducted at cycling rates of 0.33C and 0.5C and ambient temperature of 27 °C and are shown in **Fig. 6.10(a)** and **Fig. 6.10(b)**, respectively. In particular, **Fig. 6.10(a)** shows the experimentally measured heat generation rates curve in relation to the polarisation heat modeled using the NTG formulation and the irreversible heat derived in accordance with eqn. (6.5). Similarly,

Effect of Interphasial Film Resistance on Heat Generation

irreversible polarisation heat, corresponding to a discharge rate of 0.5C and an ambient temperature of 27 °C, calculated by multiplying discharge current with the irreversible polarisation values estimated on the basis of OCV instantaneous and the equilibrium voltage respectively, are plotted against the experimentally measured values in **Fig. 6.10(b)**.

It can be seen from these figures that the average value of polarisation heat predicted through the NTG model is smaller than the experimentally measured heat generation rate at 0.33C discharge rate by approximately 0.15 W. The difference between the two values increases to approximately 0.22 W for a 0.5C discharge rate. Conversely, in both the figures, good agreement can be seen between the experimentally determined battery polarisation and the polarisation curve obtained by replacing the $OCV_{t=0}$ with the $OCV_{t=3600}$ values in the DOD range of 30 and 70%. The two curves start to deviate further as the concentration polarisation becomes a dominating factor towards the end of the discharge cycle.



(a)

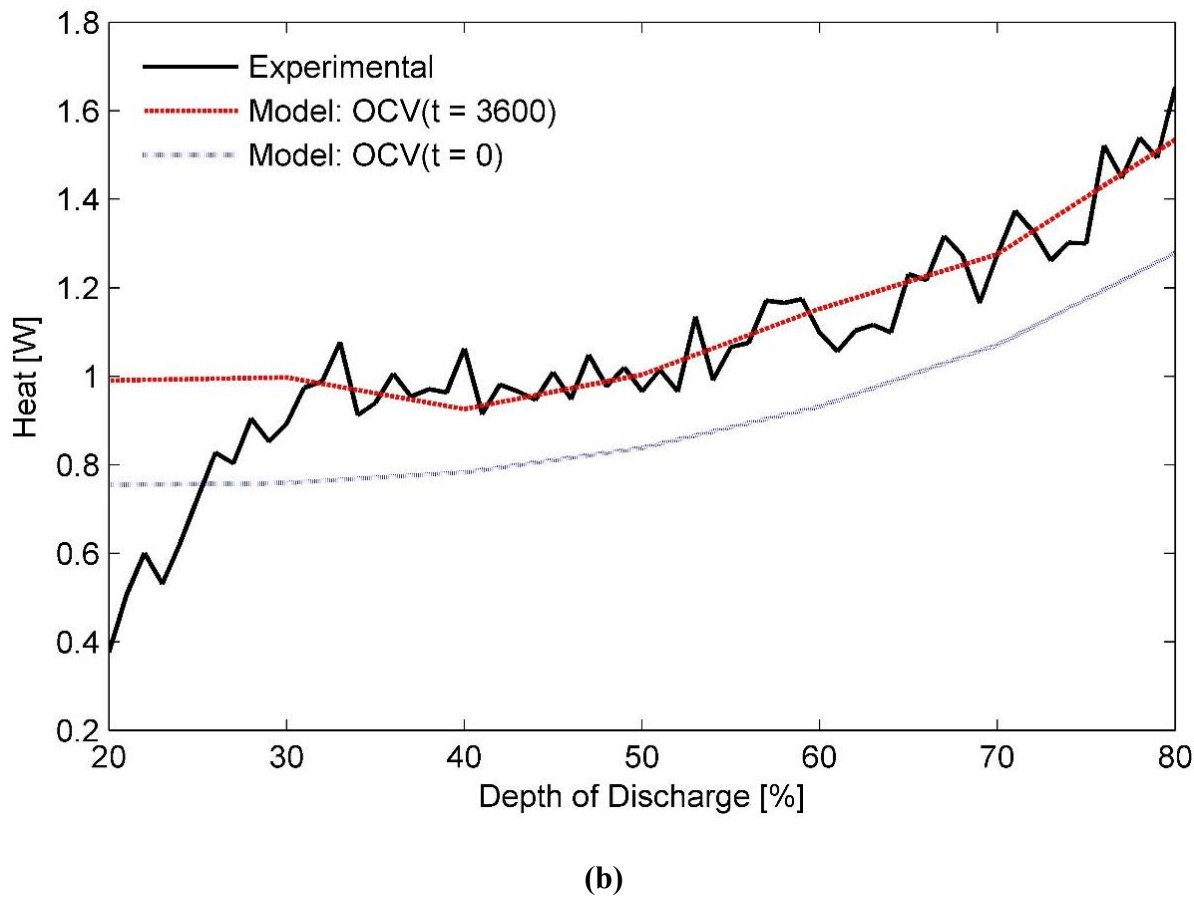


Figure 6.10: Comparison of the polarisation heat modelled for a 20 Ah LFP pouch cell by substituting $OCV_{t=0}$ and then $OCV_{t=3600}$ consecutively for U in the NTG model with the experimental irreversible heat generation rates estimated at temperature of 27 °C

The aforementioned results not only explain the underestimation of irreversible polarisation by the NTG model but also highlight the noticeable influence of interphasial impedance on the transfer rate of Li-ions in an electrochemical system under the effect of an electrical field.

6.6. Conclusions

In this chapter, the hypothesis behind the battery polarisation model developed by Newman, Tiedemann and Gu has been critically evaluated. For this purpose, the open circuit voltage for a Li-ion pouch cell is first derived from the V-I characteristics of a test battery at constant current discharge as shown by Gu and secondly via the galvanostatic intermittent current discharge method. The results obtained confirm that the OCV, which is relevant to characterisation of irreversible heat generation rates in Li-ion batteries, can deviate

significantly from the true value, if it is calculated in a manner suggested within the framework of the NTG model, i.e., extrapolating the tangent on the V-I characteristics of the cell to obtain voltage at current cut-off. The findings also demonstrate that neglecting the effect of interphasial polarisation on the OCV of cells discharged between 10% and 90% could lead to underestimation of the battery polarisation by as much as 65%. The corresponding error in the irreversible heat generation rates for the 20 Ah test battery is observed to be 0.15 W for a 0.33C discharge rate and 0.22 W for a discharge rate of 0.5C at 27 °C. It also shows that the same polarisation model could predict the irreversible heat generation rate for batteries with greater confidence after the OCV values calculated from V-I curves are replaced by those measured one hour after the current is switched off during the galvanostatic intermittent current discharge tests. A necessary change concerning selection of the appropriate OCV measurement technique in the framework of voltage model of commercial battery design software, that have the NTG model running in the background, is thus recommended.

In addition, a novel methodology for estimating solid electrolyte film resistance of Li-ion batteries is also presented in the present chapter. In the first step of this method, interphasial polarisation developed across the SEI film of a Li-ion battery cell is determined. The interphasial polarisation in this study is defined as the difference between the equilibrium voltage and OCV at $t = 0$ where ‘ t ’ is the time after switching off the applied current. Ohm’s law is then used to calculate the SEI film resistance. Using this technique, SEI film resistance for a 20 Ah $LiFePO_4$ pouch cell is calculated and the values are found consistent with the published data for a similar cell. The technique may therefore be applied with good confidence to other battery chemistries or cell types as well for an approximate estimation of SEI film resistance.

Chapter 7

Novel computational model for estimating heat generation⁵

⁵ A publication was produced based on this chapter. Details are available from - 385. Arora, S., W. Shen, and A. Kapoor, *Neural network based computational model for estimation of heat generation in LiFePO₄ pouch cells of different nominal capacities*. Computers & Chemical Engineering, 2017. **101**: p. 81-94.

This page has been intentionally left blank

Chapter 7

7.1. Introduction

From cell to pack level, lithium ion (Li-ion) batteries are characterised by a complex set of physicochemical processes. These processes are influenced by operation temperature and usage history, which in turn affects performance, cycle life and above all safety of Li-ion energy storage systems. Hence, temperature inside the functional assembly of a Li-ion battery pack needs to be effectively managed at each level from cell to pack regardless of the application anticipated for the battery system [87, 386]. Information pertaining to thermal properties and heat generation of battery pack under diverse operating conditions is a prerequisite for developing a thermal management system (TMS) required for maintaining battery cell temperature in a safe limit [86, 234]. Experimental methods for measuring heat generation rates are an integral part of TMS design process, they are however time-consuming and require a costly set-up. Another issue needing attention is the technical feasibility of testing samples of large battery cells that are still in their preliminary stages of development [387]. In view of these issues, a computational model, for analysing battery behaviour under various operating conditions in a controlled and safe manner, becomes highly desirable.

Over the years, numerous electrochemical models have been developed to represent the charge transfer kinetics of Li-ion battery cells via coupled non-linear partial differential equations. Among them, pseudo two-dimensional (P2D) model is probably the most frequently used model for battery simulation [388-393]. The P2D model is based on concentrated solution theory and can be used to calculate potential and concentration variations for the solid and the electrolyte phases within the porous electrode. It also allows estimating transients across the cell separator. Notably, inclusion of several internal variables makes it complex and as a result, very powerful computing resources are required to process this model. Coupling thermal

effects to the P2D model further increases the complexity level. It also makes validation of the model more difficult in case of high energy/power applications [394].

Besides, data pertaining to cell design parameters called by electrochemical-thermal coupled models such as electrode dimensions, porosity, transference number, precise mass and properties of constituent materials, diffusion coefficient, etc. is rarely disclosed and made available in public domain by battery manufacturers. For this reason, sophisticated experimental measurements are required to determine internal design variables before such models can be used to predict thermal behaviour of a battery cell [347]. Due to the added complexities and the need for prior data measurements, thermal equations are usually decoupled by applying a global energy balance principle to the existing multi-physics model. It has to be noted though that the global energy balance principle is valid only for battery cells with uniform current distribution [394]. In this context, previous studies indicate that a temperature gradient develops rapidly across the cell as battery size increases, leading to a non-uniform reaction rate. Non-uniform current distribution can also result from mass-transfer limitations and poor charge kinetics [71, 395].

In addition, the ISO (International Organisation for Standardisation) recommends employing a standard cell size larger than 40 Ah for one class of pure battery electric vehicles (BEV1) and a minimum size of 60 Ah for the other class of pure BEV (BEV2) [25]. **Table 7.1** lists nominal capacity of a Li-ion battery cell forming the energy storage system of passenger electric cars available in market. This list highlights the large variation present in the cell size of commercial EV battery packs. However, the major limitation of current thermal models is that they do not take into account the effect of nominal cell capacity on heat generation rates. Considering this, a thermal model with an ability to estimate heat generation rates relative to nominal cell capacity would be of utmost importance.

Vehicle	Pack Capacity (kWh)	Cell capacity (Ah)	Reference
Chevrolet Spark EV 2016	19	23.75	[396, 397]
Chevrolet Bolt	60	50	[398]
VW e-Golf 2015	24.2	25	[399, 400]
VW e-Golf 2017	35.8	37	[401]
Tesla Model S	60 and 90	3.4	[402]
Ford Focus Electric	23	15	[403, 404]
Mercedes-Benz B-class ED	36	3.4	[405, 406]
Kia Soul EV	27	38	[407, 408]
BMW i3 2017	33	94	[409, 410]
Mitsubishi iMiEV	16	50	[411, 412]
Nissan LEAF 2016	30	32.5	[413, 414]

Table 7.1: Battery pack size of commercially available passenger electric cars along with nominal capacity of Li-ion cells used in their assembly

The aim of this chapter is therefore to propose a new computational model that is easy to implement and accepts cell nominal capacity as one of its key input parameters. The proposed model is based on the artificial neural network (ANN) and can be used to simulate thermal behaviour of Li-ion pouch cells of nominal capacities ranging between 8 Ah and 20 Ah under varied operating conditions accurately.

7.2. Artificial Neural Network Model Design/Construction

Artificial neural networks are statistical/analogous models that can effectively generalise input to output functional relationships that are hidden and difficult to define in an empirical format [415]. Such models are seldom concerned with the mechanistic details of actual physicochemical phenomena occurring in target system and aim to ascertain an overall correlation between various process drivers [416]. ANNs are also considered more robust, adaptable and less sensitive towards external noises and errors in comparison to other statistical modelling techniques. More importantly, unlike symbolic manipulation techniques ANNs can

accept numeric data structures directly. It is a crucial requirement as converting numeric data to non-numeric nominal values carries risks such as loss of associated information, inappropriate data intervals and even the possibility of generating entirely different mining results [417, 418]. Another important feature of ANN is that they allow incremental mining in contrast to majority of statistical modelling methods that are typically batch oriented. This feature allows accommodation of new data input, whenever it becomes available, to a trained ANN model without reprocessing it. However, they may involve issues like long training time and a risk of overfitting associated with them or increasing difficulties in replicating a stable solution at the expense of training time. Selection of a right combination of input parameters and collecting sufficient data is therefore vital for successful execution of this computing approach.

7.2.1. Data Collection – Experimental

Prior investigations have shown that heat generation during discharge process of a Li-ion battery cell is strongly dependent on depth of discharge (DOD), discharge rate and ambient temperature [300, 301]. Consequently, boundary values for different input parameters used in this chapter are defined as 0% and 100% for DOD signifying fully charged and fully discharged state of the battery cell, respectively; 0.33C and 3C for discharge rate; ambient temperature controlled between -10 °C and 50 °C. Particularly, this study includes the nominal capacities ranging from 8 Ah to 20 Ah in the input of ANN for considering the influence of cell nominal capacity on heat generation behaviour.

The selected boundary values are coincident with the extreme values specified by the cell manufacturer for each parameter. This ensures that the training set will be inclusive of all possible operating conditions thereby making it highly unlikely for the ANN model to be used for extrapolation.

The dataset is developed by taking average of readings from four repetitive galvanostatic discharge tests involving $LiFePO_4$ (LFP) pouch cells of nominal capacities 8 Ah, 15 Ah and 20 Ah, manufactured by Benergy Tech Co. Ltd., China, in a controlled environment using a 100 A/20 V programmable battery cycler and a 4-channel data acquisition system from Arbin Instruments (BT 2000). Battery cycler functions as both a battery charger and a variable electronic load. This system is combined with a programmable air-bath and a custom-designed calorimeter, made of high-density polyethylene slabs, to measure the heat generation rates for different test battery cells galvanostatically discharged under various test conditions. Representative schematic of the experimental set-up is provided in **Fig. 7.1**.

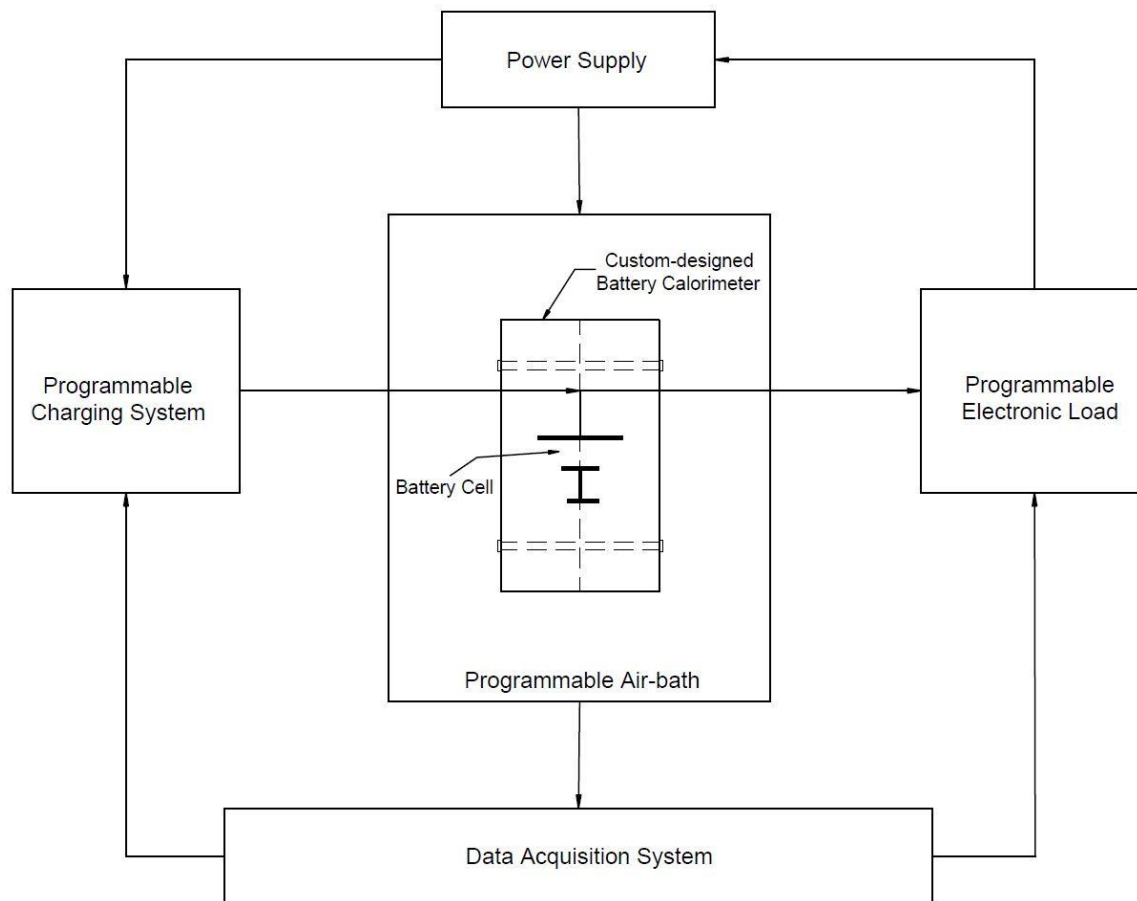


Figure 7.1: Schematic of the experimental set-up

Discharge Rate	Rated Capacity (Ah)	Ambient Temperature (°C)				
		-10	5	20	35	50
0.33C	8	-0.16 to 4.42	-0.98 to 2.20	-0.75 to 1.46	-0.81 to 0.04	-0.75 to 0.13
	15	-0.11 to 4.84	-0.63 to 2.52	-0.65 to 1.97	-0.85 to 0.14	-0.89 to 0.16
	20	-0.01 to 5.19	-1.36 to 2.82	-0.37 to 2.23	-0.84 to 0.13	-1.24 to 0.12
1C	8	-0.07 to 10.46	0.10 to 8.73	-0.07 to 6.23	-0.06 to 5.32	-0.22 to 2.53
	15	-0.25 to 11.05	-0.18 to 10.02	-0.06 to 6.72	-0.07 to 5.41	-0.23 to 2.16
	20	-0.32 to 11.85	0.03 to 10.87	-0.13 to 7.22	-0.01 to 5.35	-0.42 to 1.60
3C	8	—	-0.24 to 16.08	-0.12 to 13.46	-0.07 to 10.13	0.09 to 8.43
	15	—	-0.24 to 17.11	-0.14 to 14.58	0.06 to 10.22	0 to 7.82
	20	—	0.07 to 19.27	0.10 to 16.49	0.06 to 10.32	-0.06 to 6.81

Table 7.2: Summary of estimated heat generation rates (in Watts) for all the test battery cells under varied operating conditions

Details of the experimental test procedure are available from [300] while the calculation of heat generation rates is based on the principles of the inverse heat conduction problem and the Fourier's law of heat transfer described in [325].

Table 7.2 provides summary of the estimated heat generation rates from experimental data for the three test battery cells, discharged at rates corresponding to 0.33C, 1C and 3C in ambient temperatures of -10 °C, 5 °C, 20 °C, 35 °C and 50 °C.

After the process drivers have been identified and the data samples have been collected, it is important to evaluate information content of the available dataset for completeness as at times it may not be sufficient or suitable for ANN learning purpose and extracting significant information from it is crucial. As per the central limit theorem, a well-regarded statistical theory, the sample size of less than 30 is considered inadequate for performing an intelligent inference [419]. It can be seen from **Table 7.2** that only 5 unique measurements for ambient temperature and 3 each for discharge rate and nominal capacity are available from the experiments conducted in this study, which is considerably less than 30.

7.2.2. Data Generation

Data scarcity is one of the major reasons behind poor performance of many of the data mining and machine learning algorithms. A possible way of resolving this issue is by incorporating prior knowledge of the system into learning procedure and creating virtual data samples [420, 421]. In so doing, the training set size is systematically increased to mitigate the data scarcity problem. Consequently, a similar methodology is employed to improve generalisation ability of the designed ANN model, details of which are presented in the following text.

The most commonly used thermal model for estimating heat generation rates for electrochemical cells is described as

$$q = I_d(U - V) - I_d \left(T \frac{\partial U}{\partial T} \right) \quad (7.1)$$

The term ‘ I_d ’ in eqn. (7.1) indicates the discharge current; ‘ U ’ symbolizes the equilibrium voltage of the cell approximated by its open circuit voltage while ‘ V ’ is the terminal voltage at a specific DOD and ‘ T ’ is the absolute temperature. It is a simplified version of the energy balance equation proposed by Bernardi et al. [422]. The first term on right hand side in eqn. (7.1) represents the irreversible heat while the reversible heat is derived from the second term. Simplifications have been made by disregarding the effects of phase change and heat of mixing on the total heat. However, equation (7.1) requires fitting parameters for both the open circuit voltage and its derivative with respect to temperature. On the other hand, a good correlation between the estimated values and the experimental data can be established by specifying a single parameter - enthalpy of reaction (ΔH) in the equation shown below

$$q = - \frac{I_d \Delta H}{nF} - VI_d \quad (7.2)$$

Equation (7.2) is the mathematical identity of eqn. (7.1) [373]. It defines the heat generation rate for a battery cell as the balance between the energy generated by chemical transformation reaction and the energy supplied to the load per unit time, where, the rate of energy generation via the chemical reaction characterising the discharge process is quantified by the product of enthalpy of reaction (ΔH) and rate of reaction, which is proportional to the discharge current. Therefore, in accordance with the principle of parsimony, eqn. (7.2) is given preference over eqn. (7.1) for generating virtual samples. Subsequently, appropriate ΔH values are fitted to the thermal model based on eqn. (7.2) as demonstrated in [373]. After confirming accuracy and measurability of the virtual samples corresponding to the experimental measurements, empirical models are used for determining the one-to-one relationship of heat generation rate separately with each of the input variables identified previously in Section 7.2.1. To do so, a

polynomial of $(n-1)^{th}$ degree, n being the number of unique measurements available from the experimental dataset for the concerned input variable, is used to fit the dataset comprising of these unique measurements and the associated enthalpy values. The coefficients of the fitted polynomial are listed in Appendix. This polynomial is subsequently used for generating additional virtual samples. Number of additional samples generated is such that the final number of the dataset available for each input, i.e., experimental measurements + virtual samples generated, is greater than or equal to 30. Subsequently, 23221 samples are prepared through various permutations and combinations of the four input parameters. Lastly, total samples available are divided into two sets: one containing 2835 samples representing data obtained just for the 15 Ah battery cell and the second set containing the remaining 20386 samples. The latter is further divided randomly into three sets comprising 70%, 15% and 15% of 20386 samples. They are used for training, validation and testing of the ANN model, respectively, whereas the former is used for an independent assessment of the accuracy of the trained network.

As ANN models are function approximators, data representation is crucial to their operation. Consequently, the generated samples cannot be forwarded to the ANN model in a raw format [417]. Data samples are therefore scanned for outliers and then transformed to an appropriate form, i.e., between 0 and 1, as required by the ANN transfer function. Such function is based on first-differencing scheme described by

$$X_{tr} = \frac{(X_i - X_{\min})}{(X_{\max} - X_{\min})} \quad (3)$$

where, X_{tr} is the transformed value, X_{\min} and X_{\max} are the minimum and the maximum values in the data set, respectively and X_i is the original measurement for the concerned parameter.

7.2.3. Artificial Neural Network Paradigm

ANN topology resembles a human brain structure and contains multiple layers of several elaboration units called neurons that are interconnected by a set of modifiable weights. Neurons function as knowledge banks and assist the ANN in accumulating experience. It learns to react to a particular stimulus by analysing the sum of weighted impulse from a specific group of neurons and provides desirable response in controlled environment. Acquired modality allows the ANN model to identify any linear or nonlinear relationship existing between the case data within a multi-dimensional information spectrum and for this reason they are known as universal function approximators [423, 424].

Neurodynamics and architecture work in conjunction to define the ANN model organisation. While properties of each neuron in an ANN are described through neurodynamics, architecture controls the number of neurons in each layer and their interconnections [417]. As each independent variable is characteristically represented by a separate neuron, the proposed structure of the ANN model for calculating battery heat generation rates comprises of an input layer with four neurons, with each representing one of the four aforementioned input variables, namely DOD, temperature, nominal capacity and discharge rate. The model produces a single output corresponding to the battery heat generation rates, i.e., the dependent variable.

Theoretically, an ANN model with sufficient neurons in one hidden layer can approximate any continuous function to an acceptable degree. Nonetheless, there is no universal rule for estimating the right number of neurons in the hidden layer. As per the geometric pyramid rule, hidden layer of a three-layered ANN should have $\sqrt{(n * m)}$ neurons, where, n and m are the number of neurons in the input layer and the output layer, respectively [425]. On the other hand, Bailey and Thompson suggest that for optimal operation of the ANN model, the number of the neurons in the hidden layer would be 75% of the number of input neurons whereas Katz

reckons that it could range anywhere from one-half to three-times the number of neurons in the input layer [426, 427]. These guidelines however cannot warrant an effective ANN architecture [428]. Accordingly, the number of neurons in the hidden layer is estimated through a trial and error approach and the existing methodologies can be categorised as: fixed, constructive or destructive. In the fixed technique, several networks, each with a different number of the neurons in the hidden layer, are created and trained separately. Subsequently, the trained networks are tested independently and the architecture of the model with superior performance, measured in terms of an error function, is adopted. In contrast, to save time, the other two methodologies involve varying the number of the neurons in the hidden layer during the training phase instead of creating, training and then testing multiple architectures. Constructive approach refers to the mechanism of adding neurons to the hidden layer and conversely in the destructive scheme they are removed till the performance of ANN model begins to deteriorate [417]. The fixed approach is applied to design the architecture of the proposed ANN in this work for ease of implementation through MATLAB.

Transfer functions are mathematical formulations that constrain the ANN outputs from attaining large values that might push it into a paralysed state by impeding its further training. It has been shown that an ANN model with sigmoid transfer function can predict the average behaviour of a non-linear function more efficiently whereas a network with hyperbolic tangent transfer function is better suited for applications that involves modelling deviations from the average [429]. As the proposed model intends to estimate average heat generation rates for Li-ion batteries, sigmoid transfer function is utilised to describe the dynamic properties of neurons in the input and the hidden layers.

Lastly, a suitable learning algorithm is required to train the ANN model. ANN training is a numerical process to identify the network's connection strength, described by biases and

weights of different neurons in various layers of the ANN. Further, a validation dataset is incorporated in the training process to minimise the risk of overfitting. The error function in the training dataset and the validation are continuously monitored throughout the learning process. Initially, a decrease is noticed for functions of both the training error and the validation error. ANN training process is terminated when the validation error starts to increase or reduces to a magnitude smaller than the convergence tolerance, where the tolerance setting of 10^{-7} is used in this work. Several learning algorithms have been developed for ANN training purposes. The gradient descent method functions by optimising the connection strength parameters in the direction of negative gradient. In this method, the target function converges quickly during the initial iterations but the descending rate becomes very slow as the function approaches an optimal value. On the other hand, the Newton method identifies an ideal search direction in the vicinity of an error minimum so that the iterations can run at relatively faster rate. Levenberg–Marquardt (LM) algorithm integrates the aforementioned algorithms and is therefore the fastest learning algorithm for a feedforward ANN [430]. It is expressed by:

$$x_{k+1} = x_k - [J^T J + \mu I]^{-1} \cdot J^T e \quad (4)$$

where, x_k represents weights and biases vector, J is Jacobian matrix containing first derivatives of network errors with respect to the weights and biases, I is unit matrix, e is the vector of network errors and μ is test scalar. When μ is zero, the LM algorithm becomes similar to the Newton's method whereas when μ is large, it behaves like gradient descent method with a small step size. The LM algorithm has high convergence rate, accuracy and can be efficiently launched from MATLAB platform [431, 432], which is adopted to train the proposed ANN in this study. Neurodynamic and architecture parameters applied to the network topology constructed in MATLAB environment are listed in **Table 7.3**.

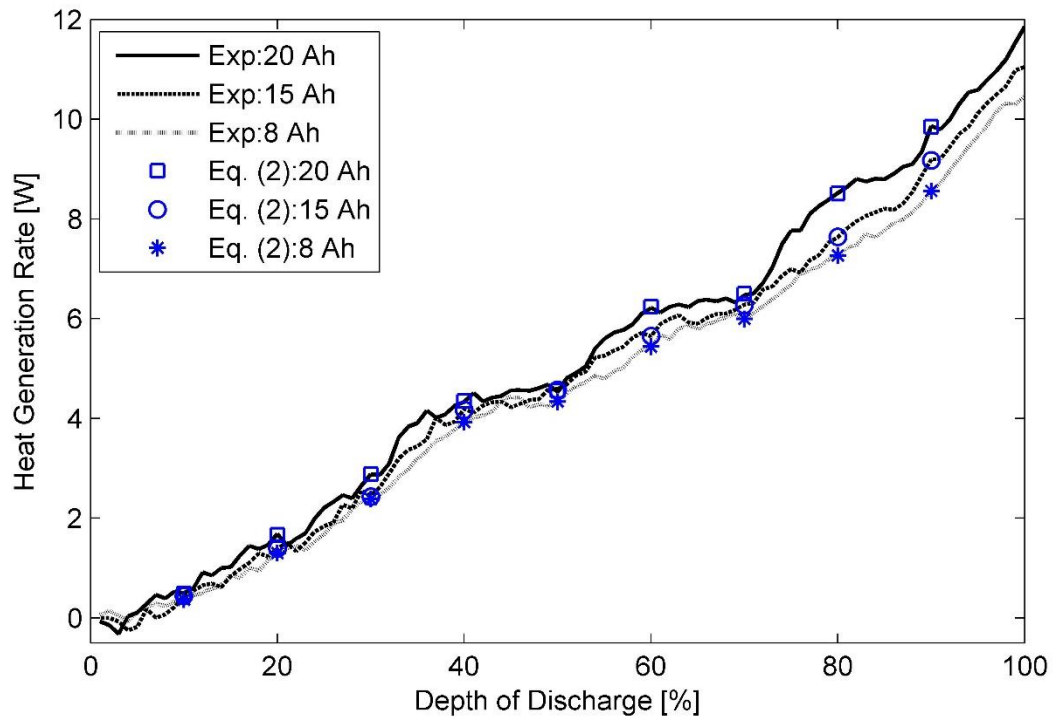
Properties	Parameters
Learning rate	0.01
Momentum constant	0.9
Performance goals	0.005
Activation function in hidden layer	SIGMOID
Activation function in output layers	PURELIN
Maximum number of epochs	1000

Table 7.3: The properties and parameters of the employed Levenberg–Marquardt optimization algorithm

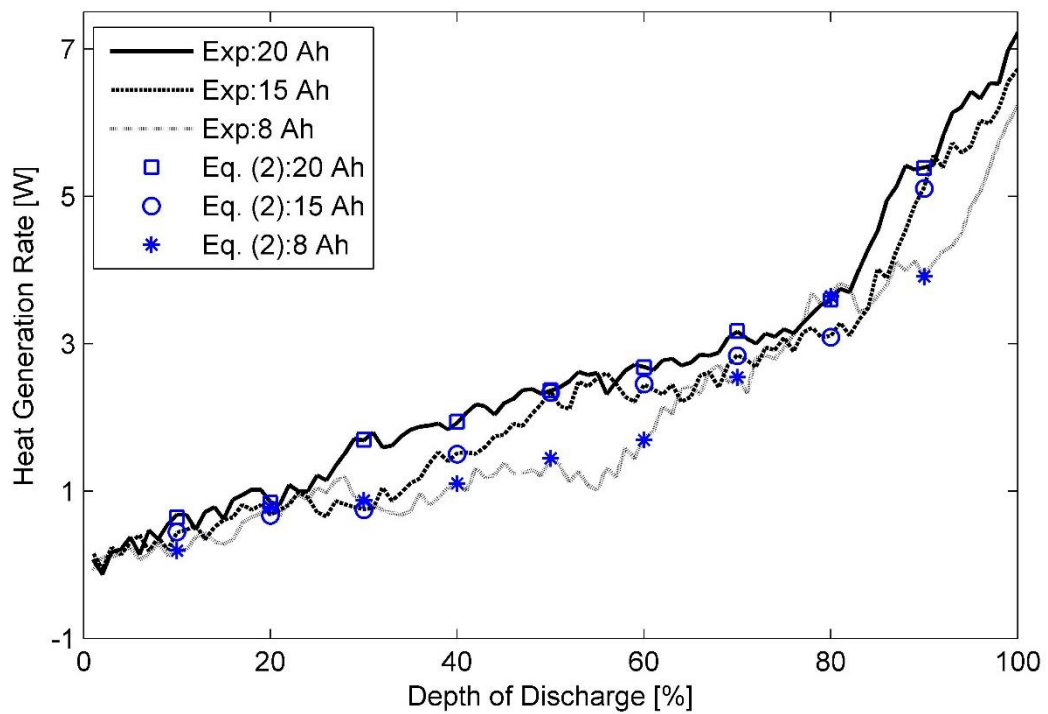
7.3. Results and Discussion

Fig. 7.2 shows the estimated heat generation rates, obtained by substituting a suitable value for ΔH in eqn. (7.2), superimposed on the plots of experimental data measured for different test batteries at a discharge rate of 1C under the ambient temperatures of (a) -10 °C, (b) 20 °C and (c) 50 °C, respectively.

It can be seen that the heat generation rates for a Li-ion pouch cell discharged at 1C rate resemble an S-shaped profile, demonstrating a largely non-linear behaviour. More importantly, the graph shows that the heat generation rate for 20 Ah pouch cell after the completion of discharge process is approximately 1 W and 1.4 W more than the rate measured for 8 Ah pouch cell of the same chemistry in the ambient temperatures of 20 °C and -10 °C, respectively. In contrast, the 8 Ah pouch cell is observed to generate heat at a rate of 2.53 W at the end of discharge cycle in an ambient temperature of 50 °C as opposed to 1.60 W generated by the 20 Ah test battery cell under similar operating conditions.



(a)



(b)

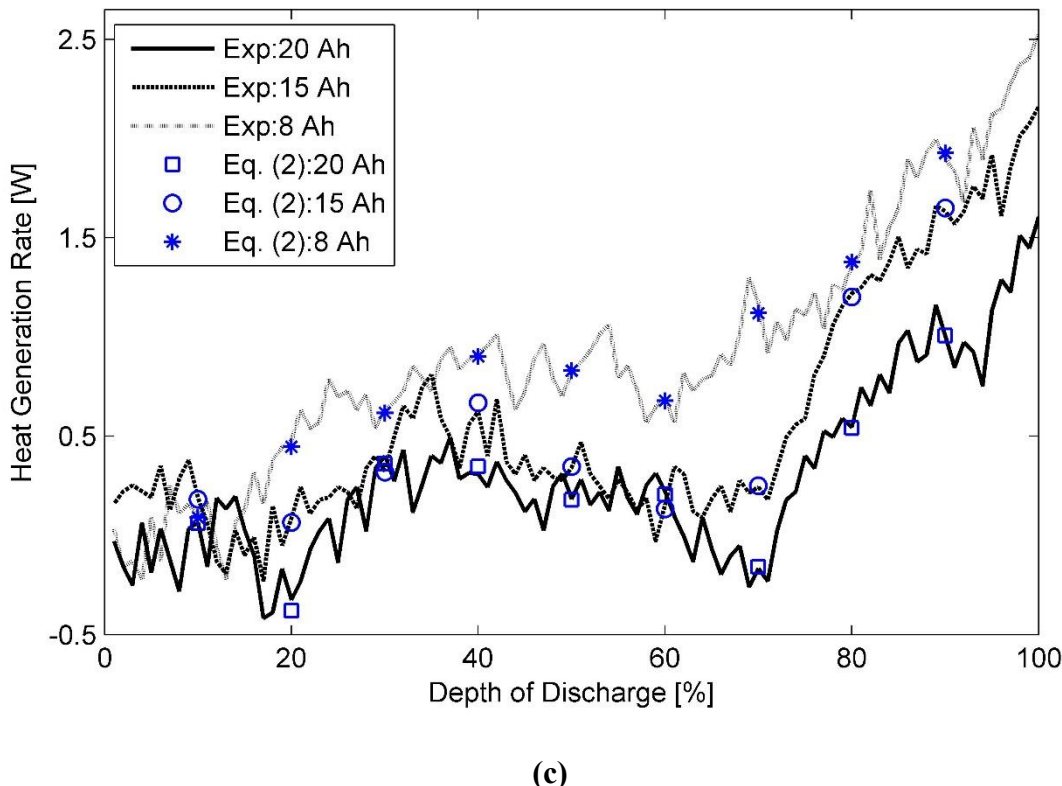
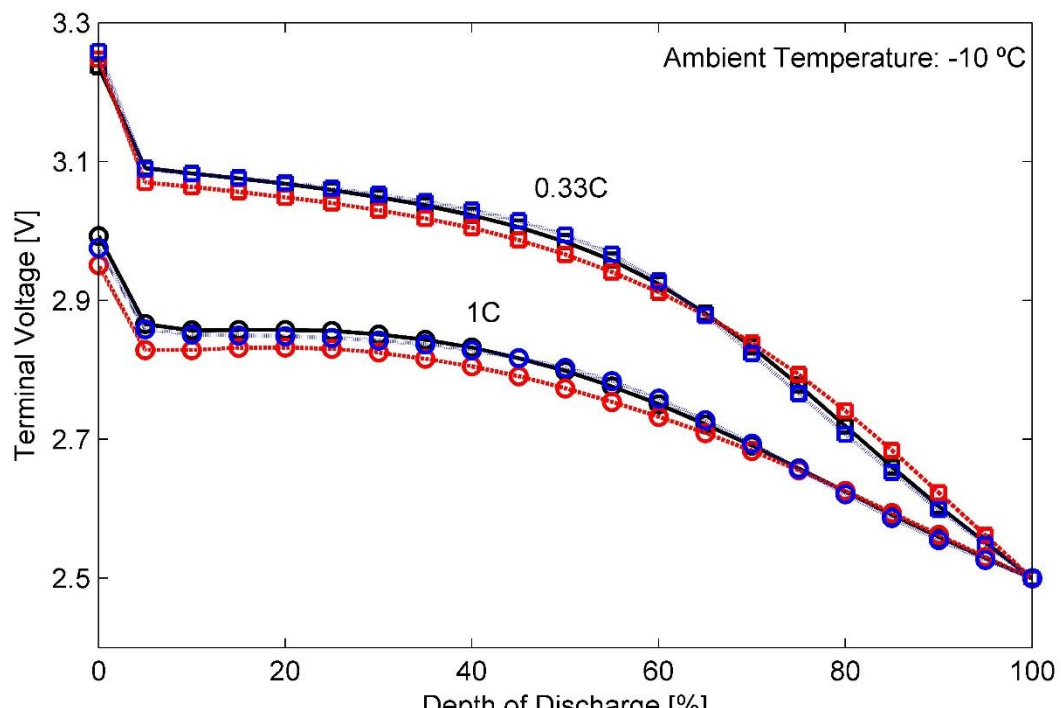


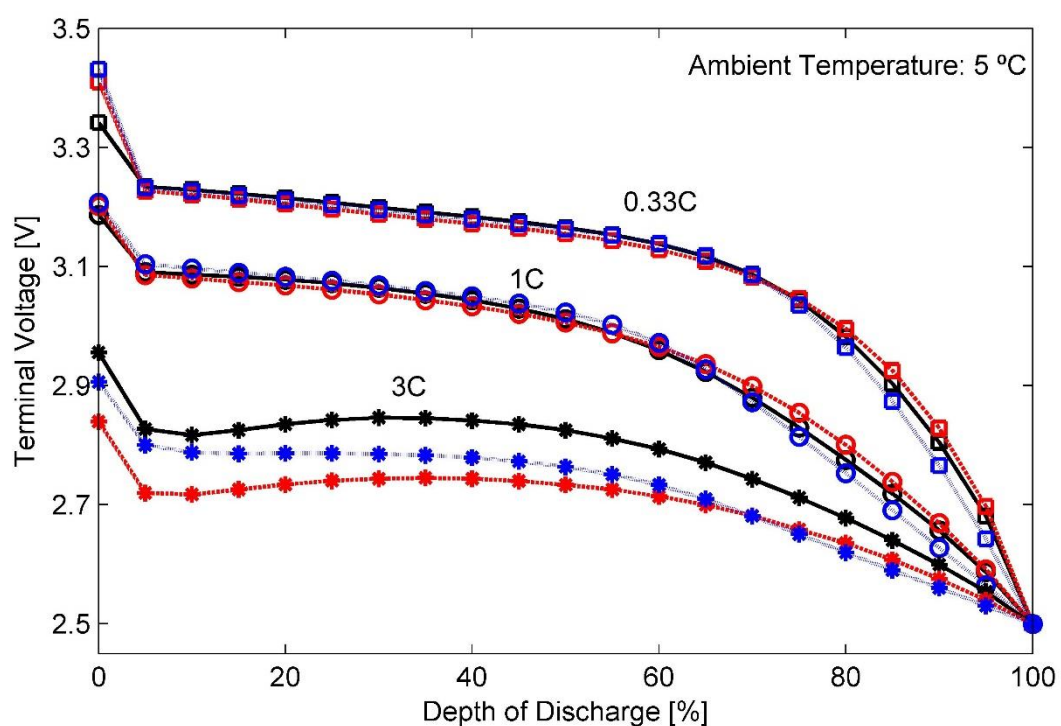
Figure 7.2: Comparison of measured heat generation rates with those calculated from Eqn. (7.2) for the three test batteries at 1C discharge rate in ambient temperatures of (a) -10 °C, (b) 20 °C and (c) 50 °C

This flipping in relative magnitudes of heat generation rates of the three test battery cells can be attributed to variations in charge and mass transfer resistance because of cell/electrode thickness and operating temperature as well as their effect on various physicochemical processes ongoing in the battery cells. A balance between these competing mechanisms is established at an operating temperature of 35 °C and as seen from **Table 7.2**, the phenomenon is witnessed for all discharge rates in the test battery cells.

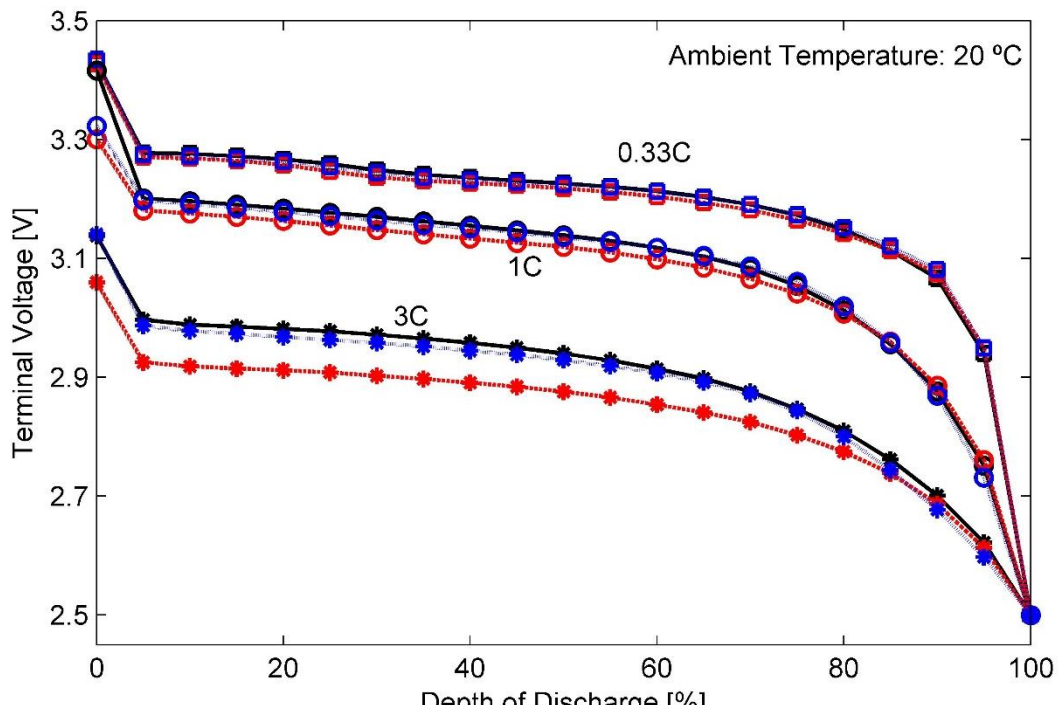
As to the process of generating virtual samples via eqn. (7.2), selection of ΔH is driven with an objective of restricting the error in the estimated heat generation rates to less than 0.05 W. For this purpose, power delivered by the battery cell is determined from the data available through **Fig. 7.3**, which shows the terminal voltage recorded for the three test battery cells under different operating conditions at various stages of discharge process.



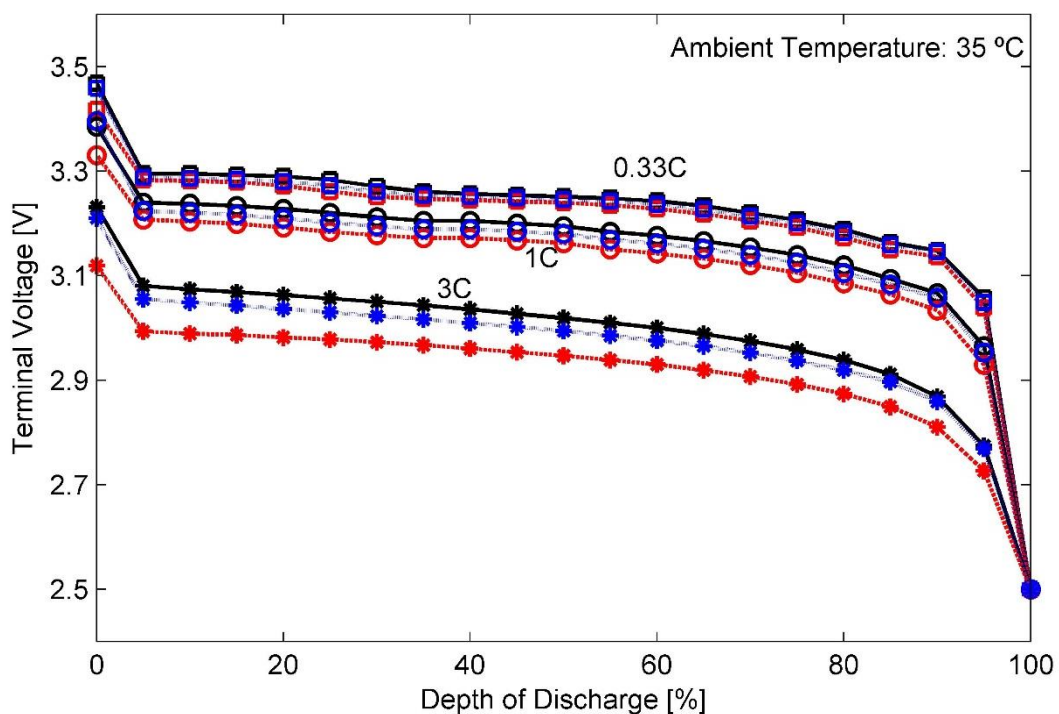
(a)



(b)



(c)



(d)

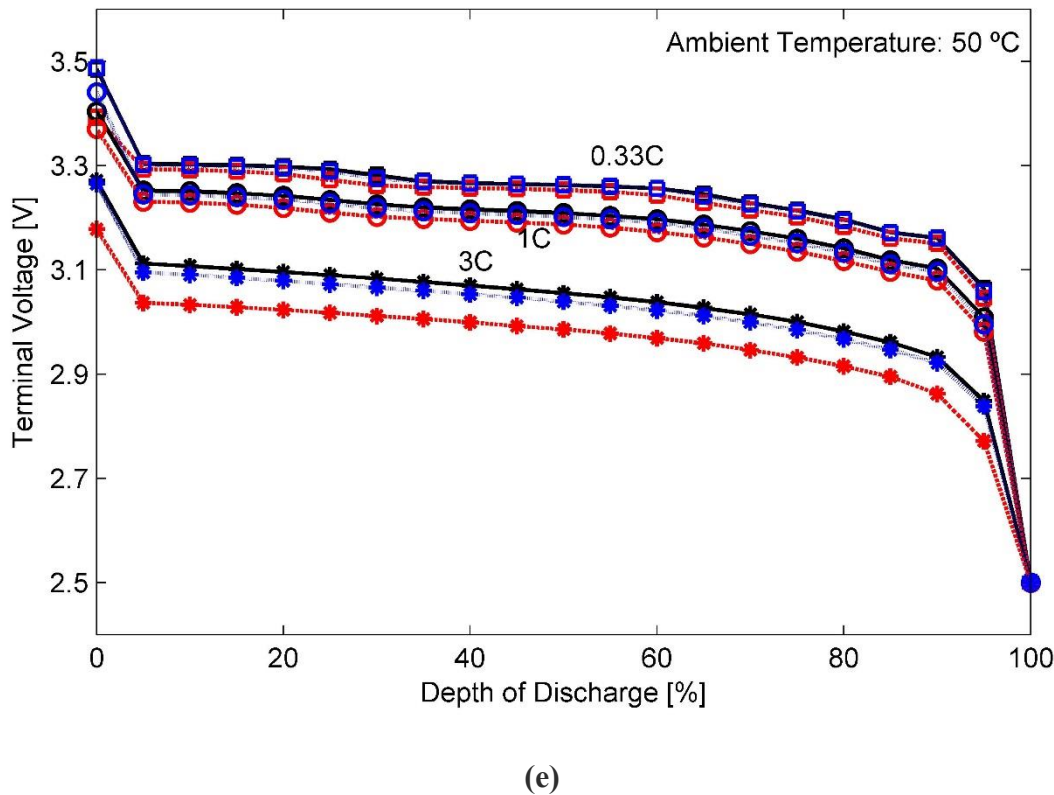
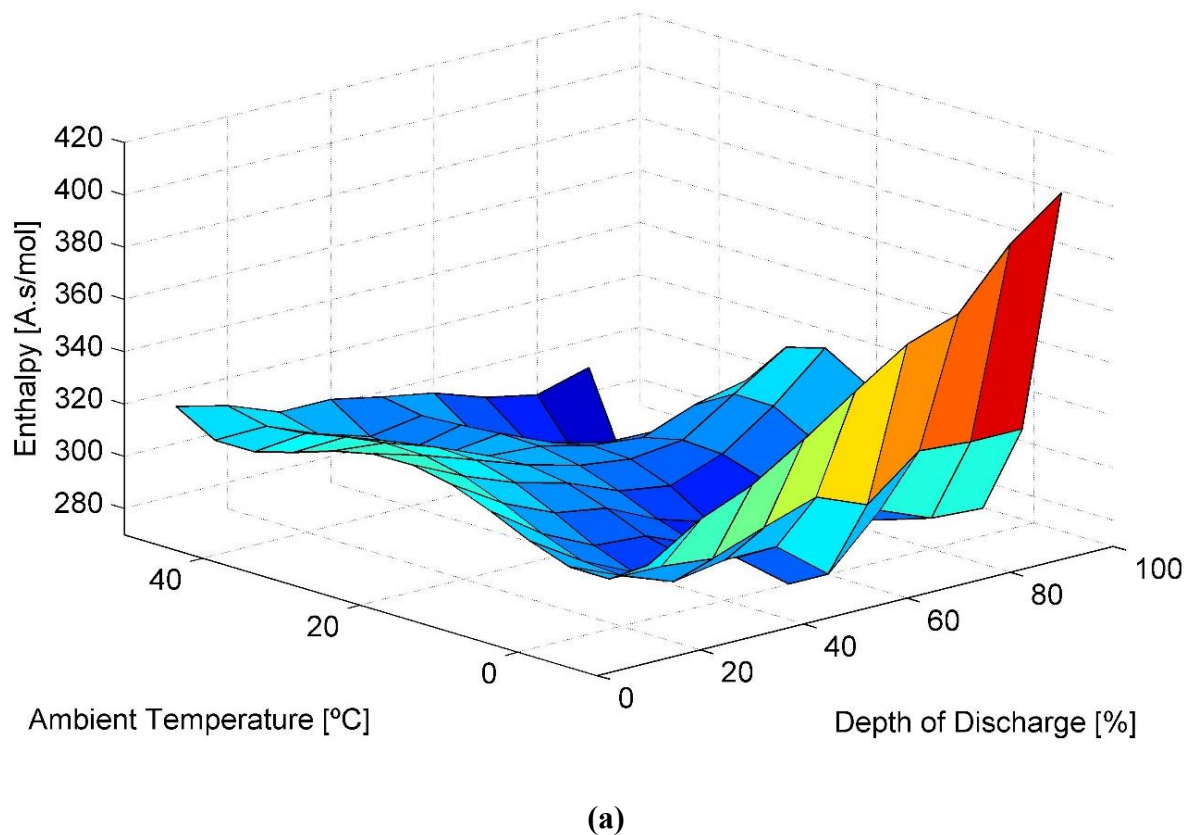


Figure 7.3: Terminal voltage of the three test cells recorded at varied discharge rates in ambient temperatures of (a) -10 °C, (b) 5 °C, (c) 20 °C, (d) 35 °C and (e) 50 °C. (Solid black line represents 20 Ah cell, dotted red line represents 15 Ah cell and dashed blue line shows data for 8 Ah cell. Also, square markers correspond to 0.33C discharge rate, circles are for 1C discharge rate and lastly, asterisk is representing 3C discharge rate)

A downward shift is noticed in the voltage plateaus of all the test cells with increasing discharge rates and decreasing ambient temperatures. This shift is more discernible at discharge rate of 3C for 15 Ah battery cell. It is indicative of hindered charge transfer kinetics due to increased internal resistance of Li-ions cells which results in partial utilisation of active material at high discharge rates and low ambient temperatures. In fact, a jump of over ten times has been reported in the internal resistance of commercial cells cycled at -20 °C in comparison to those operating in an ambient temperature of 20 °C [186, 433]. Increased internal resistance induces more heat generation inside the battery cell and consequently causes the rise of the cell temperature, which in turn causes a slight increase in its terminal voltage as seen from Figs. 7.3(a) and 7.3(b) in the DOD range of 15% to 55%.

More importantly, the enthalpy of reaction is a sum of Gibbs free energy of the system and entropy of the reaction. They are state functions. In this context, the full discharge cycle of an electrochemical cell can be analysed in terms of several distinct stages defined by the DOD of the cell. Therefore, in contrast to Catherino's approach [373] where a single value of ΔH was selected to model the whole discharge cycle, discrete values of ΔH corresponding to different DODs, that are multiples of 10, are identified. Owing to this, extent of conformity of the modelled heat generation rates with the experimentally recorded profiles, as seen from **Fig. 7.2**, is much higher over the entire domain than that achieved by Catherino via single-value fitting approach. Corresponding variation of enthalpy of reaction with (a) ambient temperature and (b) discharge rate is shown in **Fig. 7.4** for a complete discharge cycle of an 8 Ah pouch cell in perspective of the power drawn out of the cell at that operating stage.



(a)

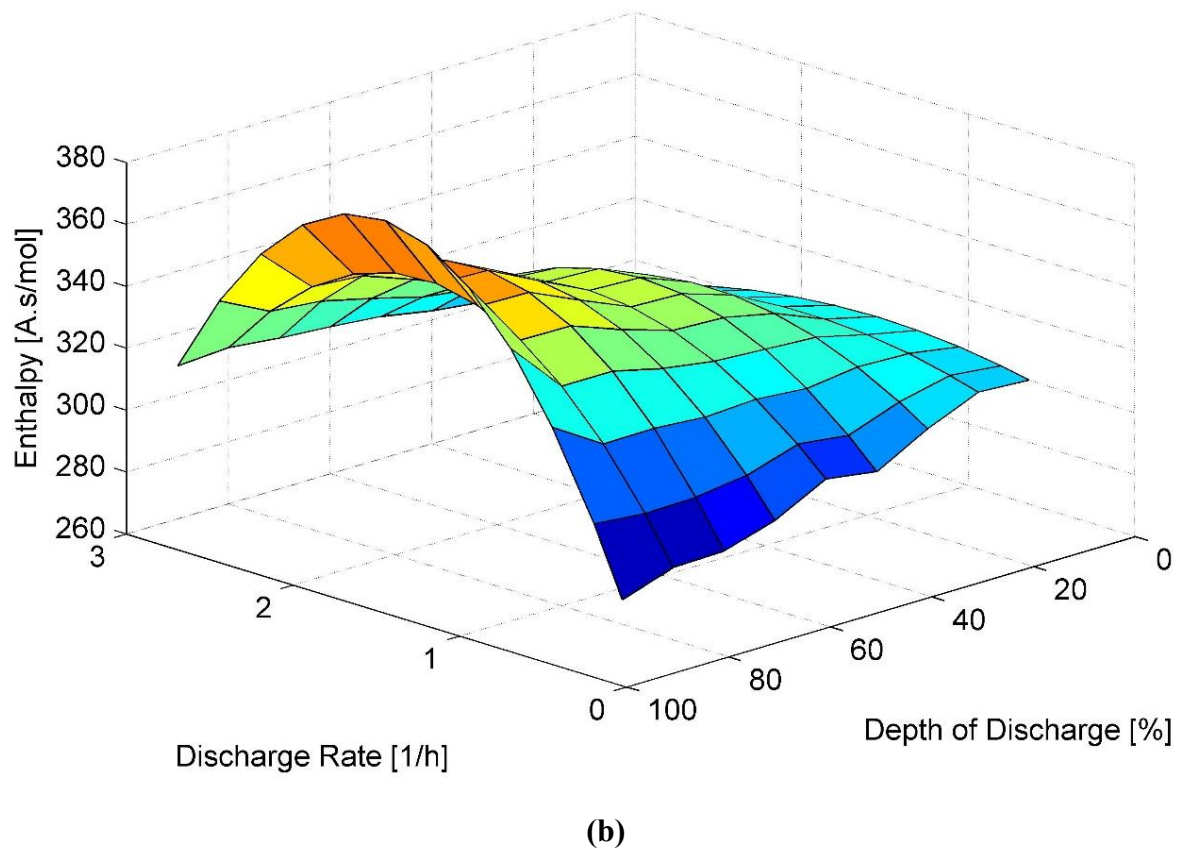


Figure 7.4: Variation of enthalpy of reaction of 8 Ah pouch cell with (a) ambient temperature at discharge rate of 0.33C and (b) discharge rate in ambient temperature of 35 °C under different DODs

Fig. 7.4(a) shows that enthalpy of reaction decreases as the cell operating temperature slowly shifts from -10 °C to 50 °C, suggesting improved electrochemical performance and reduced heat generation rates for Li-ion battery cells at high temperatures for any DODs. Moreover, a sharp increase in the enthalpy of reaction of the test battery can be noticed as it is discharged in an ambient temperature of -10 °C, highlighting exothermicity of the process at low temperatures. On the other hand, the enthalpy gradually declines as the discharging process continues in an environment of 50 °C. The fall in ΔH indicates that heat generation rates for the 8 Ah test cell are endothermic in nature, which is consistent with the results of previous studies involving Li-ion batteries [300, 301].

Ambient Temperature (°C)	Cell Capacity (Ah)	Depth of Discharge (%)								
		10	20	30	40	50	60	70	80	90
-10	8	307.5	320	328	340.5	354	367	373.75	395.5	410.25
	15	311	314	307.5	304	304	300	295	293.5	293
	20	313	315.5	312.75	307.75	307.75	303.75	300.75	301.5	292.75
5	8	303	290.5	281.25	282	277	262	281.25	276.75	281.25
	15	303.25	305.25	300.5	298	293	302.5	300.75	291.75	291.5
	20	305	301.75	294.5	287.5	293	292	295.75	292	279.5
20	8	318.75	309.5	302	297	289	286	293.25	306.75	324
	15	318	309.5	306.5	301.5	302.5	299.5	301.75	305.25	310
	20	318.25	315	316.5	307.5	308.5	312.5	309.75	309.5	313.75
35	8	310	311	304	295	297.5	289	284	283.5	278
	15	311	314	307.5	304	304	300	295	293.5	293
	20	313	315.5	312.75	307.75	307.75	303.75	300.75	301.5	292.75
50	8	314	309.5	302	302	298	294.5	288	284	289.5
	15	313	309	304.5	304.5	302.5	298	294.5	297	292.25
	20	314	310	307.25	307.25	304	299	293.5	295.5	295.75

(a)

Ambient Temperature (°C)	Cell Capacity (Ah)	Depth of Discharge (%)								
		10	20	30	40	50	60	70	80	90
-10	8	279.5	290.5	303	320.25	322.75	331.75	332.25	340.5	349.75
	15	275.75	282.25	288.25	297.5	297	300	299.25	302.5	306.25
	20	278	283.75	289	294.25	292	295.5	291	294.25	294.5
5	8	307.5	308.25	314.75	322.75	332.25	326.5	322.25	337	332.5
	15	298.5	298.25	307.75	310	307.75	307.25	315	307.75	305.75
	20	298.5	300.75	308	307.75	305.5	304.75	302.5	295.75	296.25
20	8	310.25	316	315.75	317.25	320	321.25	328.5	335.25	324
	15	309.25	310.5	315.75	318.5	317.75	314.75	314	310	311.25

	20	311.5	311.25	314	313.75	314.25	313.75	312.75	308	303.5
35	8	315	318.5	322.5	323.5	324.5	327	331	331	348
	15	311.25	312.5	314	314.5	314.5	316	316	316	321.75
	20	315.5	316.5	317.25	316.25	316.25	316.75	316.25	316.25	317.25
50	8	314	317.5	318	320.5	319	316	319	319	322
	15	312.75	311	311	312.5	309.75	307	305.5	308.5	307.75
	20	314	311	313	312	310.5	309.5	305.5	305.75	304.25

(b)

Ambient Temperature (°C)	Cell Capacity (Ah)	Depth of Discharge (%)								
		10	20	30	40	50	60	70	80	90
5	8	269.5	272	279.25	286.75	288.75	294	297.75	296.5	299.5
	15	262.5	268.75	271.75	276.25	280.5	280.75	281.75	283	279.25
	20	272	277.5	281.5	283.5	285.75	287	284.75	281	277.75
20	8	289.25	292	299.5	302.5	306	308.75	309.75	308.25	302.5
	15	282	284.75	285.5	290.25	289.5	291.5	290.75	290.25	286
	20	288.75	289	291.5	292	294.5	294.25	292.5	289.75	282.25
35	8	295	297	301	303	306	307.5	308.75	310.5	309.5
	15	289	289.75	291.5	292.25	293.5	293.75	293.25	292.75	289
	20	297	297.25	297.75	298	298.25	297.25	296.75	294.75	290.75
50	8	300.5	304	305.5	307.5	309.5	310	310	310.5	309.5
	15	293	293.5	293.5	295.25	295	294.75	294.5	293.25	290.25
	20	300.25	299.5	299.5	299.5	299.5	298.25	297	295.75	292

(c)

Table 7.4: Enthalpy variation (in J/mol) for different batteries at different temperatures and discharge rates of (a) 0.33C, (b) 1C and (c) 3C

Nonlinearities embedded in the relationship of battery heat generation rates and discharge rate are evident from **Fig. 7.4(b)**. It presents change in enthalpy of reaction with discharge rate and DOD of an 8 Ah Li-ion pouch cell for a galvanostatic discharge test in an ambient temperature of 35 °C. It can be seen that for discharge rates lower than 0.5C, ΔH decreases with DOD implying endothermic behaviour for Li-ion battery cells as low discharge rates and high ambient temperatures. Conversely, exothermic heat generation behaviour can be expected as discharge rates are increased. Increase in ΔH is therefore observed as higher discharge rates are selected, corresponding to any DODs.

However, exothermic heat generation associated with high discharge rates causes the cell temperature to rise, which is responsible for faster charge transfer kinetics and better cell performance. Consequently, enthalpy of reaction and battery heat generation rates at high discharge rates are relatively lower than those that would be estimated by a linear function of discharge rates. Similar results are obtained for the other two test batteries as well. A summary tabulation of the fitted ΔH values covering the operational domain for all the three test battery cells is presented **Table 7.4**.

A three-layered feed-forward ANN model is analogous to a conventional non-linear regression model. Weights connecting neurons of adjacent layers are equivalent to the regression curve parameters while the bias term used in an ANN model can be viewed as the intercept term of a regression equation. Overarching aim of regression analysis is minimisation of the sum of squared errors between the actual value and the estimated output for the statistical problem. Hence, mean squared error is chosen as the evaluation criterion for assessing the performance of the proposed ANN model and is defined by

$$Q_{mse} = \frac{1}{N} \sum_{n=1}^N (q_m(n) - q_p(n))^2 \quad (4)$$

where, Q_{mse} is the MSE between the actual and the predicted heat generation rate, N is the total number of data samples used for the respective step, i.e., training, validation or testing of ANN model, $q_m(n)$ represents the measured/actual values for heat generation rates and $q_p(n)$ signifies the heat generation rate projected by the ANN model.

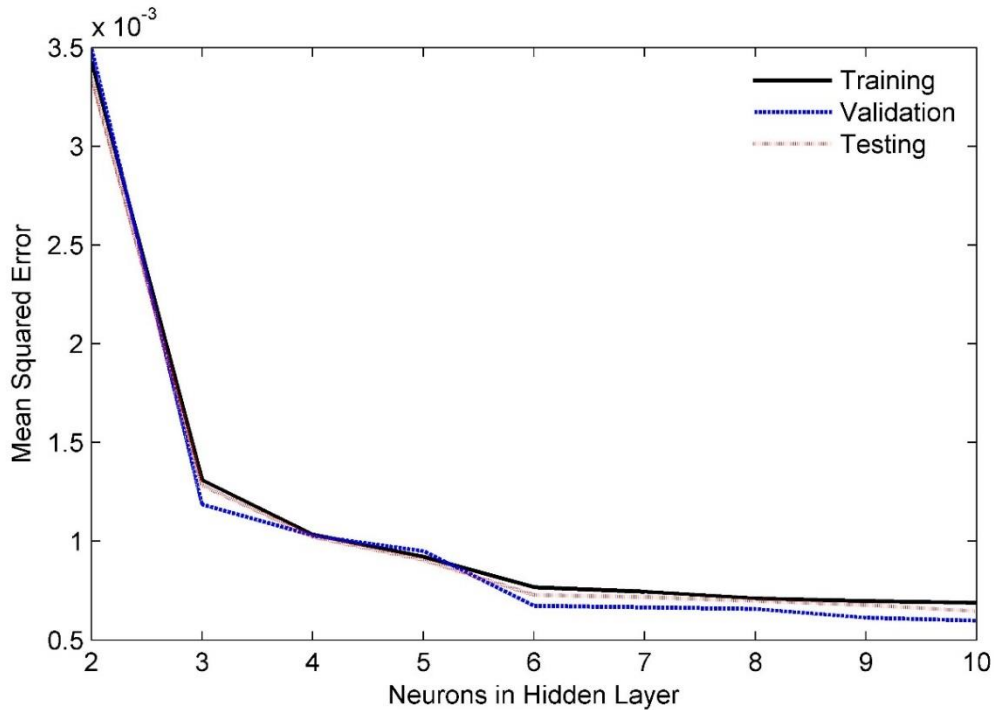


Figure 7.5: Effect of the number of neurons in the hidden layer of the network architecture on its performance during training, validation and testing phase of network design

Fig. 7.5 illustrates the improvement in accuracy, expressed in terms of mean squared error, realised during training, validation and testing of the ANN model for this case when the number of neurons is increasing in its hidden layer during construction phase of the network. As seen from the figure, the mean squared error in forecasts of the trained ANN model, with two neurons in the hidden layer, is reduced by 64% if the number of neurons in its hidden layer is modified to three. A further improvement of 40% in the accuracy of forecasting is achieved by doubling the number of the neurons in the hidden layer from 3 to 6 in the architecture of the ANN model. It is observed that the slope of the error curve becomes too low from that point onwards and thus not much benefit is attained in accuracy of the model. In addition, the

negative influence of adding more neurons to the hidden layer on complexity, computational time, efficiency and cost of the ANN model cannot be overlooked. Therefore, architecture with a single hidden layer having six neurons, shown in **Fig. 7.6**, is therefore adopted for the ANN model. Additionally, input weights and layer weights for different neurons of the trained network are provided in **Table 7.5**.

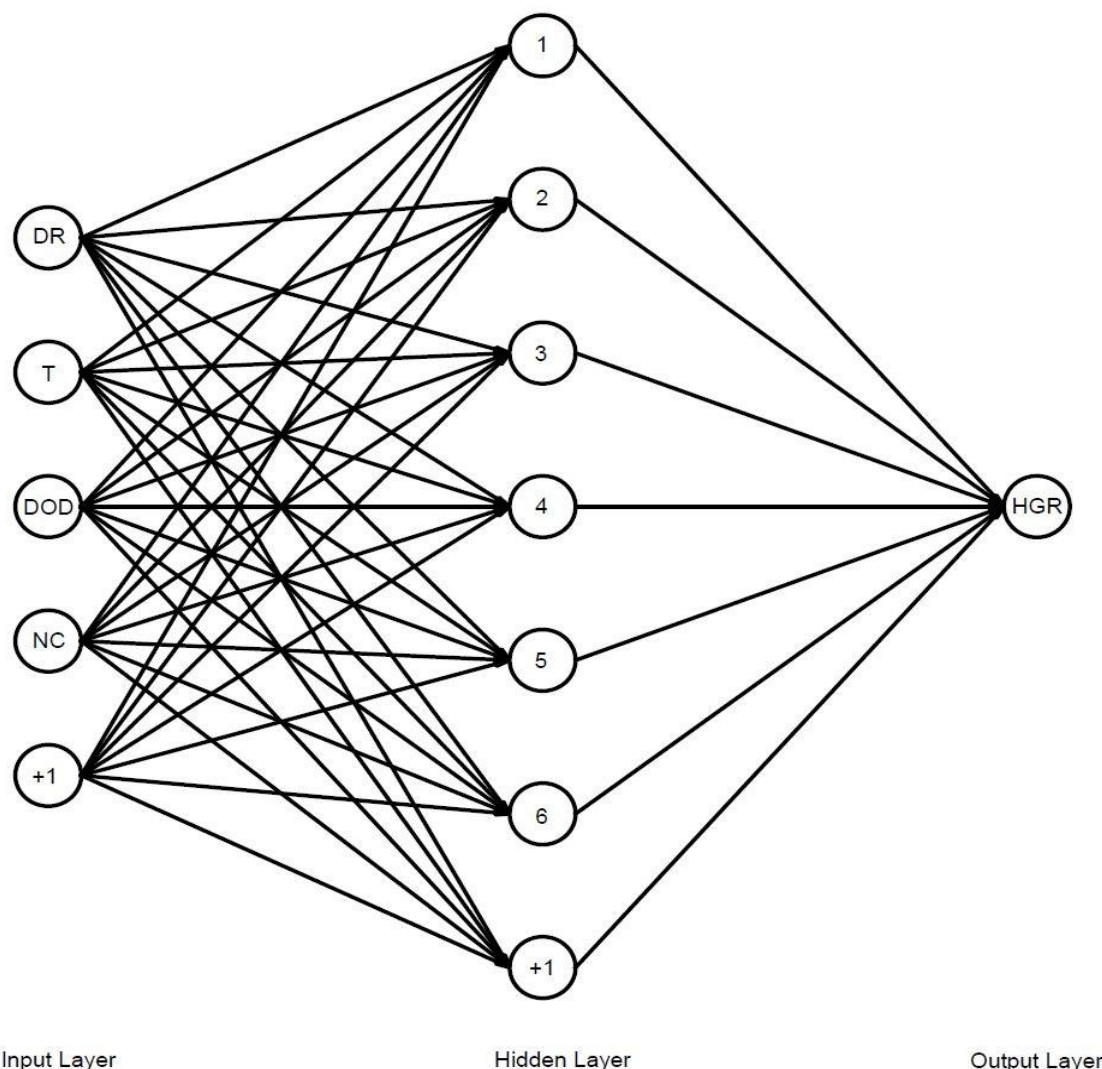
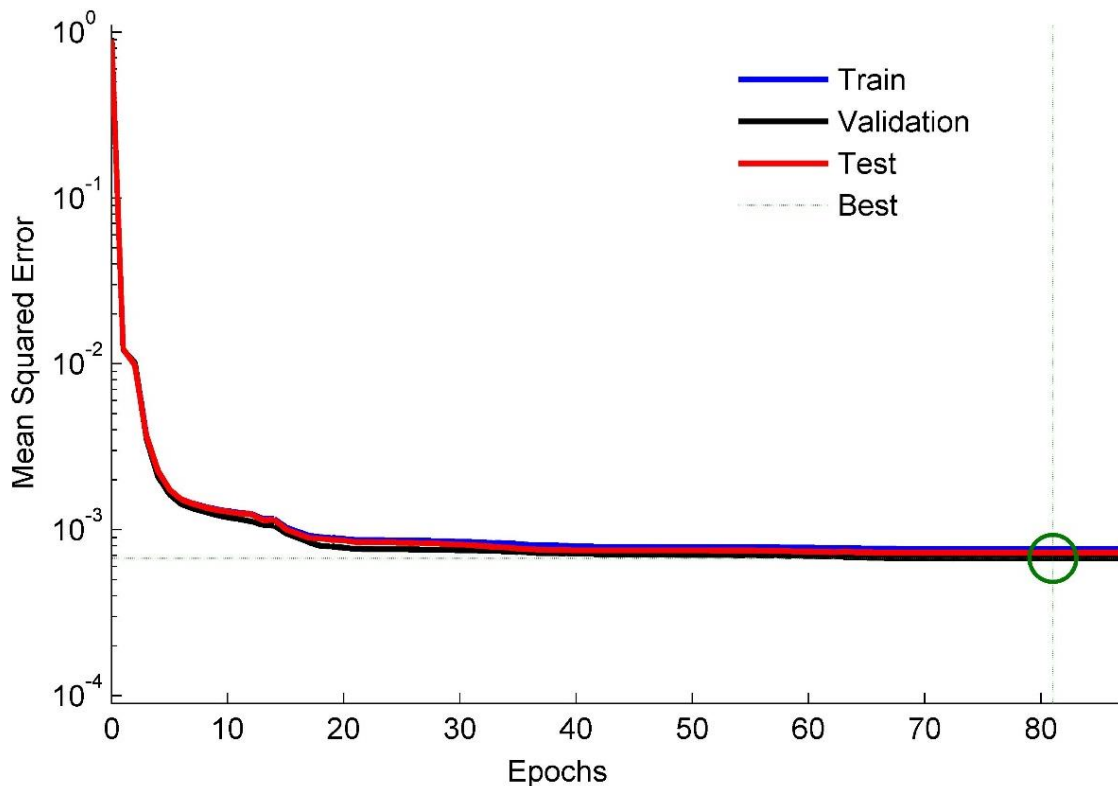


Figure 7.6: Architecture of the ANN model used for prediction of heat generation rates for Li-ion battery cells. The input layer accepts discharge rate (DR), ambient temperature (T), depth of discharge (DOD) and nominal capacity (NC) of the battery cell as inputs whereas heat generation rate (HGR) is provided as an output by the output layer of the model. A bias term, which constantly emits 1, is added to the input layer and the output layer.

Input Layer Weights				Hidden Layer Weights	Biases	
DR	T	DOD	NC		Input	Hidden
0.3024	-0.6414	-1.3740	4.1422	-0.1848	1.5672	-0.5428
0.0090	0.8948	-0.5330	0.5850		0.7009	
0.0647	0.8308	-0.2044	-0.4773		3.2047	
0.8529	-1.5338	4.5306	8.1262		0.0918	
-0.0542	-0.7024	0.5130	0.4600		3.2411	
0.0164	0.1292	1.4145	-3.8653		0.1873	
					1.9309	

Table 7.5: Input layer and hidden layer weights and biases for the trained neural network

Performance of the adopted ANN is shown in **Fig. 7.7**. It is seen that the mean squared error in model predictions decays exponentially with increasing number of training passes or epochs.

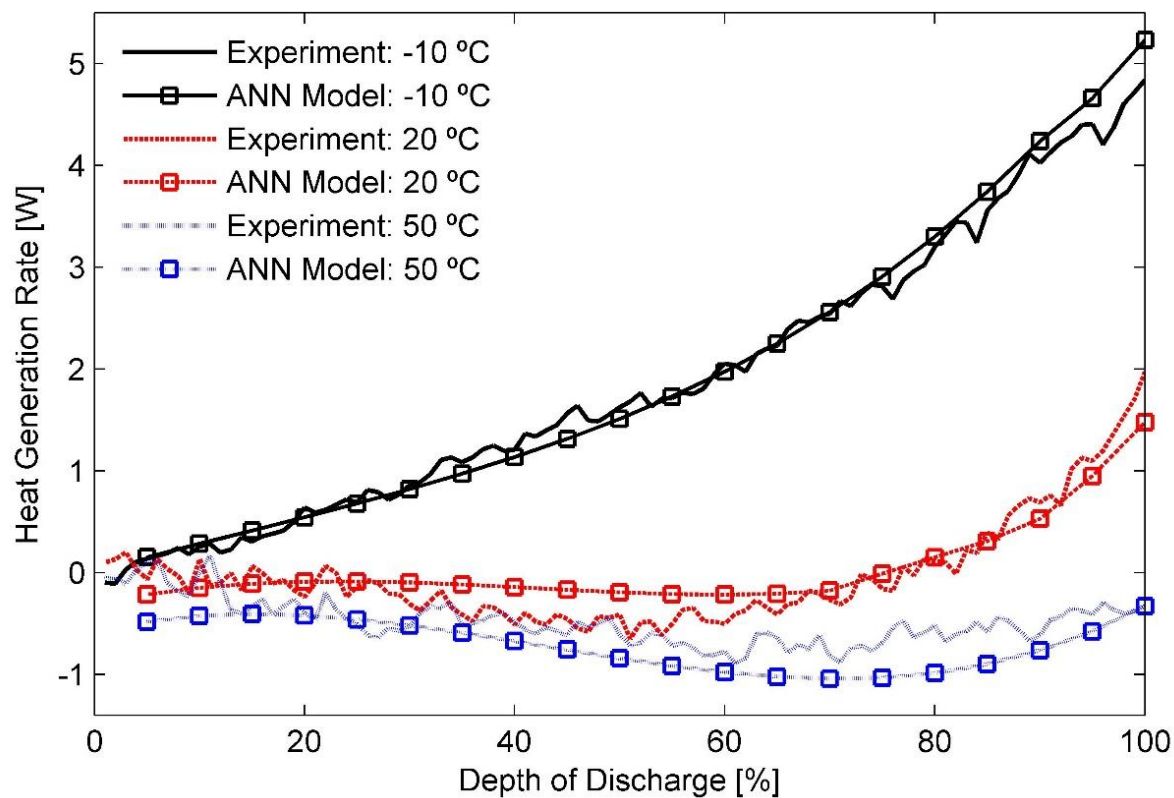
**Figure 7.7:** Neural Network Performance (Architecture: 1 Hidden layer with 6 neurons). Best Validation Performance is 0.00067335 at epoch 81

Minimum mean squared error of 0.00067335 is noted for an independent validation test of the network at epoch 81. Subsequently, it can be inferred that the unbiased ANN model is capable

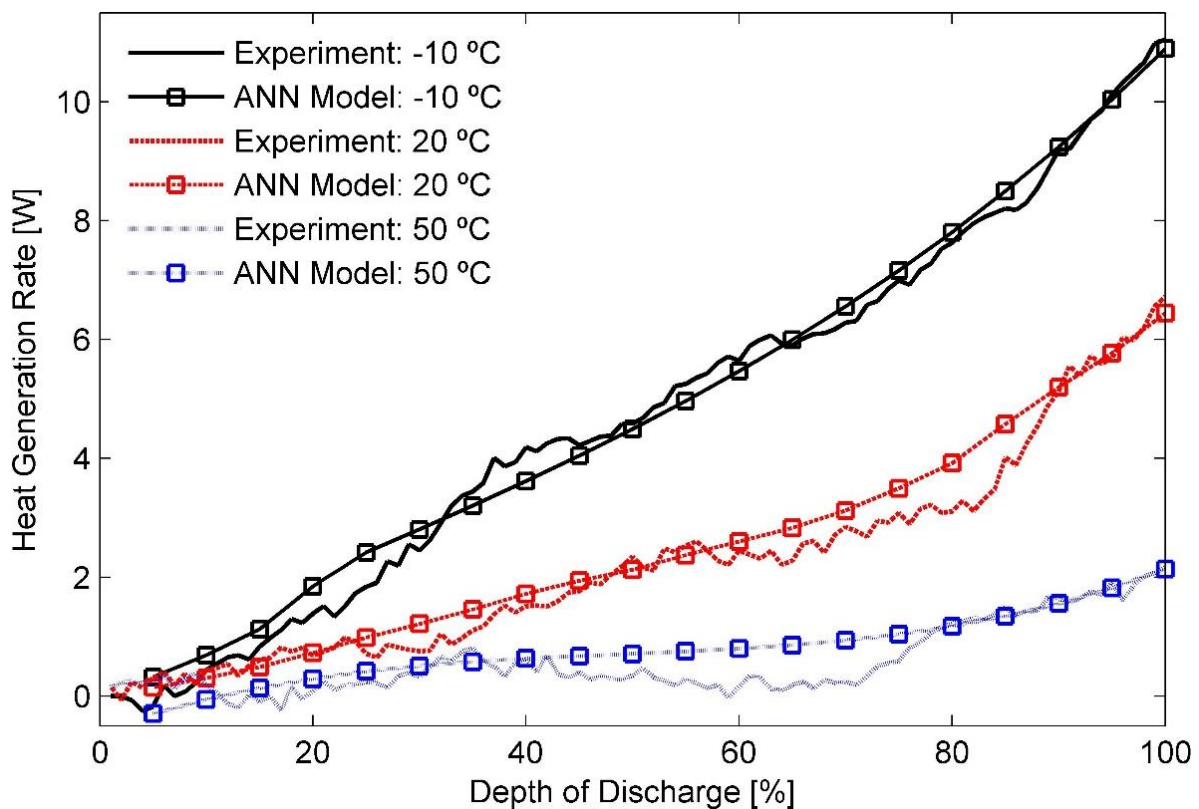
of estimating heat generation rates for any operating states within the pre-defined input parameter boundaries accurately. The acquired ability is a direct result of a training process that involves the designed ANN learning the patterns present in dataset supplied to it.

It has to be noted that the dataset used for training the ANN model is developed using new and healthy battery cells. The performance of the trained neural network may therefore deviate as the battery cells age. A possible way to make the ANN model more robust would be to monitor the thermal behaviour of the cells throughout their cycle life and update the ANN training set as more data becomes available.

Lastly, effectiveness of the proposed ANN architecture for heat generation rate estimation is analysed through a separate test schedule. As a part of it, the trained and validated ANN model is used to calculate the heat generation rates for a 15 Ah $LiFePO_4$ pouch cell discharged in ambient temperatures of -10 °C, 20 °C and 15 °C, information regarding which was purposely omitted from the sample dataset initially used to train the network. **Fig. 7.8** shows the response of the ANN plotted against the experimental results obtained for the 15 Ah test cell at these operating temperatures and discharge rates of (a) 0.33C, (b) 1C and (c) 3C. It can be seen that a good agreement between the predicted and the measured heat generation rates with a correlation coefficient of 0.98627 can be observed. Maximum deviation from the experimental values recorded for the ANN output during the entire test schedule is ± 0.56 W.



(a)



(b)

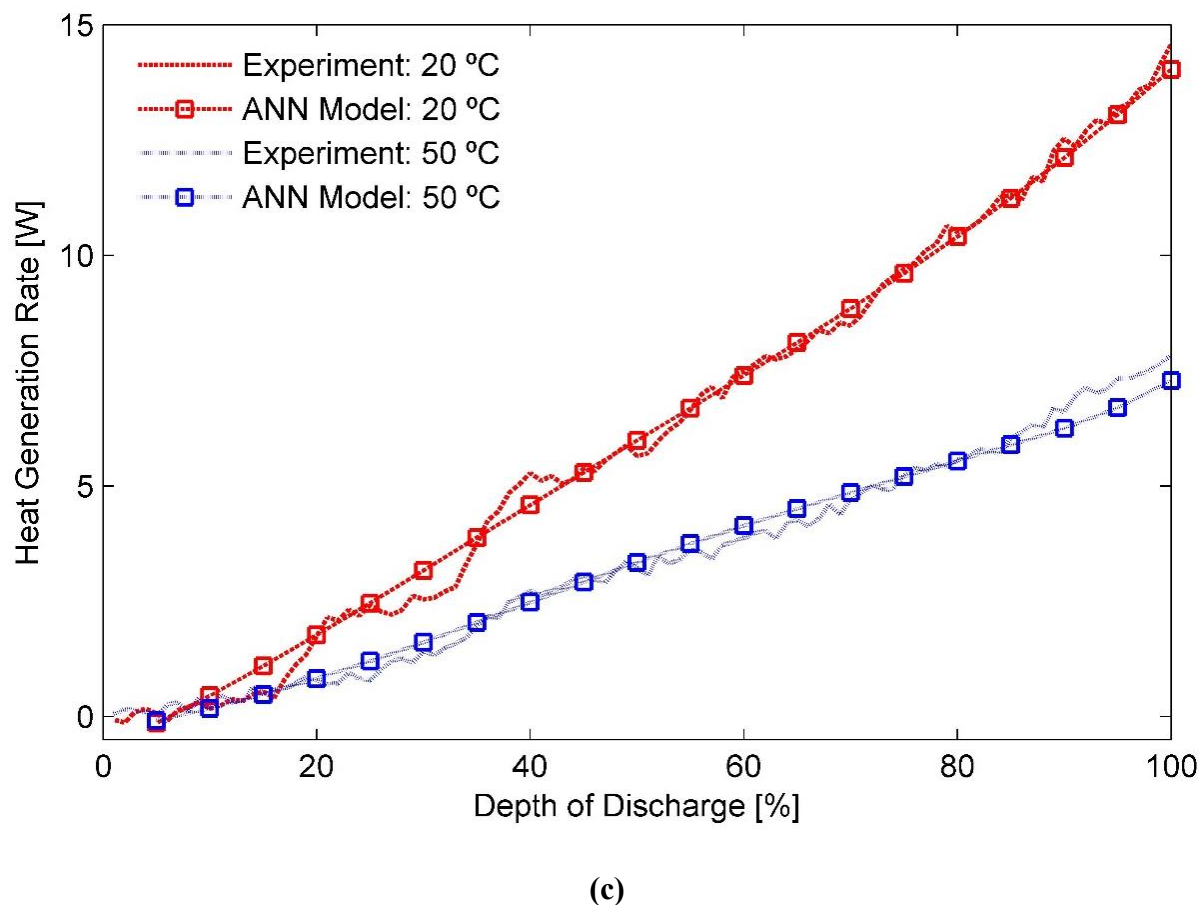


Figure 7.8: Comparison of experimentally measured heat generation rates for the 15 Ah LFP test battery cell with the predicted values from ANN model in different ambient temperatures and discharge rates of (a) 0.33C, (b) 1C and (c) 3C

It is understood that besides feedforward ANNs there are other ANN architectures as well such as recurrent ANNs, self-organizing maps, radial basis function ANNs and deep ANNs. The feedforward ANN may not be the best choice for the heat generation rate-predicting problem. Therefore, the performance of different ANN modelling techniques would be compared in future research.

7.4. Conclusions

In this chapter, an ANN-based parametric computational approach for estimating heat generation rates of Li-ion battery cells is developed. This feedforward network has been

designed and trained using the Levenberg–Marquardt algorithm on the dataset generated through calorimetric experimental technique and subsequently expanded via an empirical formulation. It puts particular emphasis on the effect of nominal battery capacity on heat generation rates of Li-ion battery cells in addition to the effects of discharge rate, depth of discharge and operating temperature. This is significant owing to wide variability in cell sizes used for commercial EV battery packs and large dissimilarities in their operating environment.

The optimal ANN architecture for this application is found to be a three-layered structure consisting of an input layer with four neurons, followed by a hidden layer made up of 6 neurons and finally an output layer with one output neuron. The test results confirmed the validity and accuracy of the proposed model architecture. It is observed that the designed network can estimate heat generation rates for Li-ion pouch cells of rated nominal capacities between 8 Ah and 20 Ah accurately, with a mean squared error of 6.7335×10^{-4} , for operating states represented by a discharge rate in between 0.33C and 3C and an ambient temperature within the range of -10 °C to 50 °C. Future work would focus on extending the span of boundary parameters defined for ANN model predictions. In addition, another dimension may be added to the model by including the ageing effects on battery heat generation rate.

Chapter 8

A hybrid TMS with negative parasitic losses

This page has been intentionally left blank

Chapter 8

8.1. Introduction

Driving range, performance and mass-market appeal of electric vehicles (EVs) are directly related to energy capacity, power density and cycle life of their battery packs. A key factor that can significantly affect the available energy capacity and the cycle life of a Li-ion battery based energy storage system is battery cell temperature. Sluggish charge kinetics in sub-zero ambient temperatures on one side and serious safety risks associated with operating Li-ion battery cells at a cell temperature of over 60 °C on another are a cause of major concern for battery pack designers [37, 38]. It is suggested that Li-ion battery cells operate at their maximum efficiency near room temperature environment. However, system irreversibility can cause a part of electro-chemical energy to transform to heat energy and correspondingly lead to an appreciable deviation in the battery cell temperature from the target value during the charging and the discharging processes [1, 434].

Severity of the issue increases as the number of scaled-up Li-ion battery cells assembled in the battery pack increases due to difficulty in removing heat from central sections of the battery pack [435, 436]. Furthermore, heat transfer between neighbouring cells of the battery pack needs to be minimised so as to reduce the probability of single cell failure events cascading to neighbouring cells and damaging the entire battery pack [35, 36, 87]. For these reasons, integration of a battery thermal management system (TMS) with the battery pack is essential. This would maintain temperature of individual battery cells within a pre-specified range and minimise heat transfer between adjacent battery cells.

A Hybrid TMS with Negative Parasitic Losses

It has been reported that up to 40% of the battery pack's energy capacity may be required to support auxiliary electrical loads such as fans, blowers or pumps in forced air-cooling and liquid-cooling TMSs [437]. In view of this, parasitic power, which is the energy required to operate the TMS, is generally one of the key criteria in selection process of the temperature control strategy that should be used to regulate the performance of EV battery packs. This criterion has driven the research requirements for simple and energy-efficient passive TMSs like heat pipes and phase change materials (PCMs) [230, 438], please see Chapter 4, Section 3.2 for details. PCMs are preferred over the heat pipes because of their low initial and operating costs and easy integration process [94]. However, PCMs are generally characterised by low thermal conductivities and slow regeneration rates [255]. Long regeneration times can render such systems ineffective under abusive conditions. Abuse conditions are defined as continuous cycling at fast charge/discharge rates with minimal rest (cooling-down) periods.

Numerous research studies are thus focussed on investigating methods for improving thermal properties of PCM-based TMSs. For instance, Zhao et al. [248] noted that thermal conductivity of a composite system of paraffin wax (RT58) and copper foam is much higher than the thermal conductivity of paraffin-wax alone. Similarly, Khateeb et al. [259] found that embedding aluminium foam in a PCM matrix can also improve its heat transfer properties. Wang et al. [439] compared the surface temperatures for air-cooled 16.5 Ah LiFePO₄ battery cells with surface temperatures for battery cells (a) soaked in paraffin (melting range of 46 °C to 52 °C) contained in an insulated quartz container, and (b) embedded in a composite of paraffin wax and four aluminium foams with porosity between 70% and 90%. All the battery cells were charged at a rate of 1C in an ambient temperature of 20 °C. They reported the maximum battery cell temperatures for the three test cases as 36 °C, 29.5 °C, and 26.1 °C, respectively. Further, the highest surface temperatures recorded for a charging rate of 2C were 46.0 °C, 36.8 °C, and 32.4 °C, respectively. Li et al. [237] also attained promising results by using a combination of

commercial paraffin wax and metallic foam. However, a larger than 3 °C inter-cellular gradient was observed in their experiments.

Cellular structure of metal foams typically resembles a honeycomb. It is suggested that the porous structure of metal foams cannot be refilled uniformly after PCMs go through a phase change cycle. Metal wire mesh plates are thus recommended as a replacement for metallic foam structures in the PCM composite. Azizi et al. [440] positively tested a composite system of Polyethylene glycol 1000 and aluminium wire mesh plates with a very high voidage as a TMS for Li-ion battery pack made up of LiFePO₄ cylindrical (38120) cells operating in the ambient temperatures between 50 °C and 55 °C.

Thermal conductivity of PCM matrix can also be enhanced via addition of highly conductive powders. The powders can be categorised into: (a) macro-doped powders, (b) micro-doped powders, and (c) nano-enhanced powders. Macro-doped powders are prepared after metallic materials are injected with PCMs. They are however susceptible to heterogeneity as air may sometimes be trapped in the composite. Further, latent heat of the macro-doped powders decreases as the percentage of metallic particles increases [256]. This problem can be resolved by using nano-enhanced materials. Special care is required in preparation of nano-PCM composites though, as a high-percentage of nano-particles can lead to agglomeration and homogeneity is crucial for efficient functioning of nano-enhanced mixtures [239, 441, 442].

It can be seen that these thermal conductivity-enhancing techniques involve use of complex fabrication processes and require addition of dead weight in form of metallic/foreign compounds to PCM matrix, which results in partial loss of latent heat storage capacity of the PCMs. Furthermore, it is a common understanding that heat generation sites are non-uniformly distributed across the battery cell surface with more hot spots occurring in the top portion, i.e., the area closer to the electrode terminals. Nevertheless, battery cells in the majority of battery

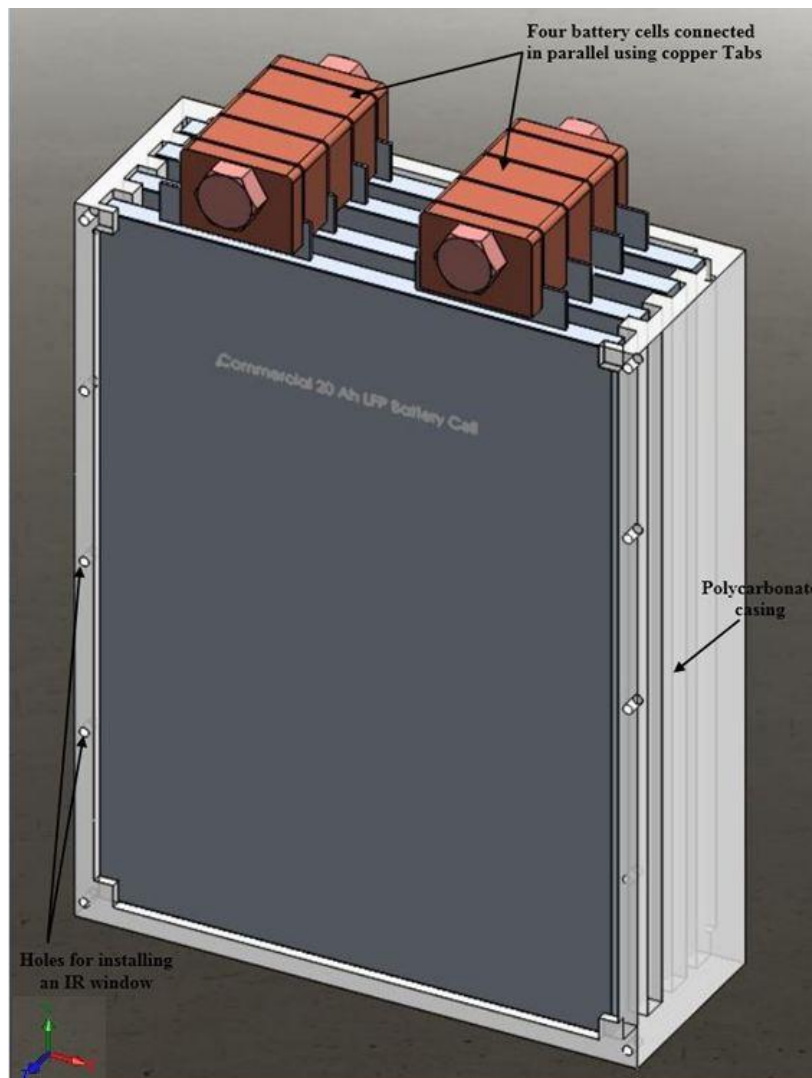
pack designs are arranged in an upright position. Such an arrangement suppresses convective heat transfer through the battery pack and affects average thermal conductivity of the PCM-based TMSs.

In this chapter, we investigate the effect of battery cell orientation on the performance of PCM-based TMSs in abusive conditions. Energy efficient solution is presented that employs convection heat transfer mechanism to improve average thermal conductivity of such systems. Additional improvement to the performance of TMS is made by connecting Seebeck devices, commonly known as thermoelectric coolers, to the battery pack. The thermoelectric coolers reduce the regeneration time for the PCM matrix by recovering a portion of the waste heat and transforming it to electrical energy, which can be used elsewhere. The novel TMS presented in this chapter can thus be regarded to have negative parasitic power requirements and a noticeable influence on driving range of the EV. The experiments described in the following sections will present more details of this heat transfer system.

8.2. Experimental Set-up

Commercially available $LiFePO_4$ (lithium iron phosphate) thin pouch cells of 20 Ah nominal capacity have been selected as test battery cells for substantiating the validity of the TMS design formulated in this chapter. Subsequently, two different 80 Ah Li-ion battery packs are constructed by connecting four battery cells in parallel using copper tabs. Battery pack 1, shown in **Fig. 8.1(a)**, is constructed by arranging the battery cells in a vertically upright position, i.e., electrode terminals projecting through the top surface of the pack. In contrast, the battery cells are placed in an inverted position in battery pack 2 such that the terminals protrude through 1.5 mm wide slots made in the bottom surface of the battery pack's rectangular casing, as seen in **Fig. 8.1(b)**.

Casings for both the battery packs are designed with a 6 mm thick polycarbonate sheet because polycarbonate provides excellent visible light transmission and high strength to weight ratio at low price. Inter-cellular spacing in the pack is maintained at 6 mm using spacers made out of the same sheet. On the other hand, gap between internal surface of the casing and front side of the first battery cell in the pack and similarly the gap between the casing's internal surface and rear surface of the last cell in the battery pack are restricted to 3 mm.



(a)

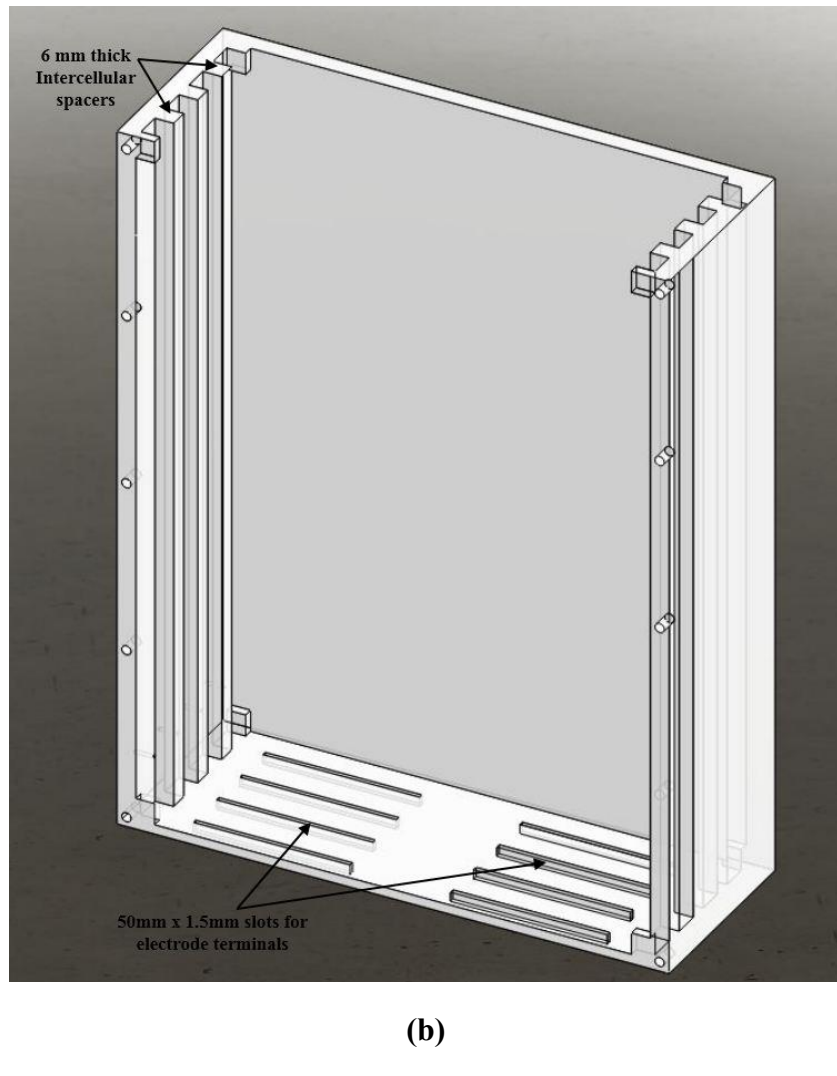
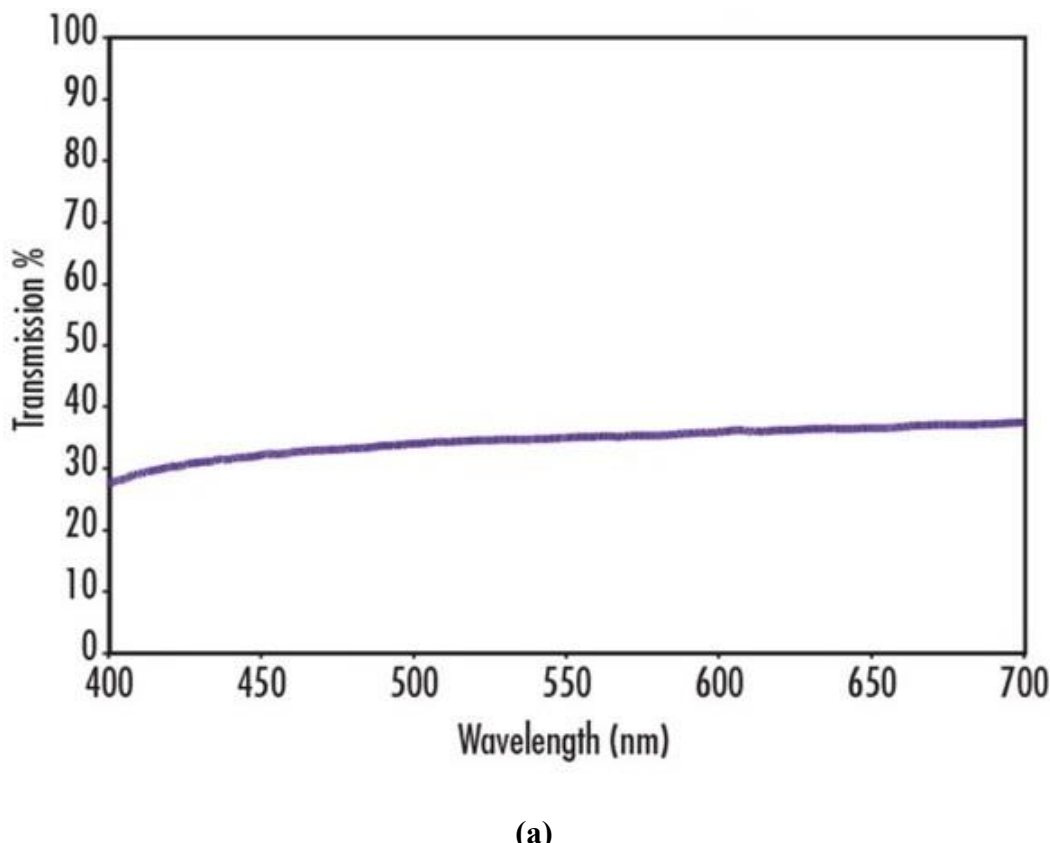


Figure 8.1: Schematic of (a) 80 Ah battery pack with upright cells and (b) Casing showing intercellular spacers and electrode slots for battery pack with inverted battery cells; IR window removed for clarity reasons

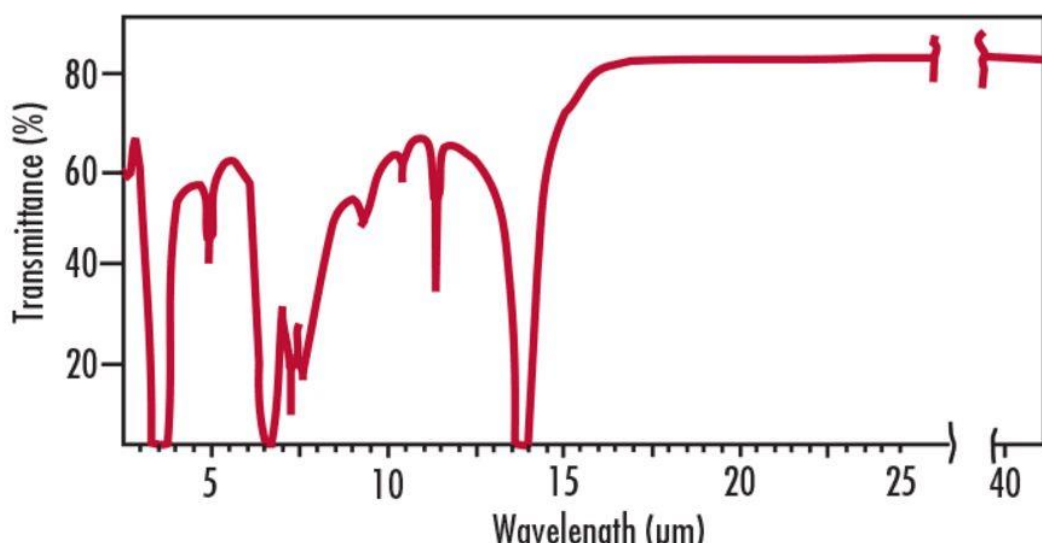
Polycarbonate, i.e., the material used for making the battery pack casing in this study, absorbs all radiations transmitted at wavelengths greater than $1.5 \mu\text{m}$. So, an IR window that transmits all radiation emitted within the spectral range of $7.5 \mu\text{m}$ and $14 \mu\text{m}$ to a thermal imaging camera was installed in the battery pack casing on the face from where the thermal distribution needs to be observed. Front side of the battery pack casing is thus replaced with a 0.381 mm thick IR material window, sourced from Edmund Optics.

The IR window has been molded from a 0.457 mm thick flexible milky white plastic sheet having consistent thickness across the surface. Transmission spectrum of the IR window

material for both the visible region and the IR region is presented in **Fig. 8.2**. In addition, important characteristics of the IR window material are presented in **Table 8.1**.



(a)



(b)

Figure 8.2: Optical spectrums for the IR window material for (a) visible region, and (b) IR region [443]

Parameter	Value
Visible (Sodium D line)	1.52
Index of refraction (η_d)	8 – 14 μm 1.53 15+ μm 1.48
Coefficient of thermal expansion ($10^{-6}/^\circ\text{C}$)	11 - 13
Young's Modulus (psi)	(60 – 80) $\times 10^3$
Flexural Modulus (psi)	(100 – 260) $\times 10^3$
Shore Hardness	D60 - 70

Table 8.1: Index of refraction and key mechanical properties of the IR window used in this investigation

The battery packs are then filled with a high capacity paraffin material (RT28HC) sourced from Rubitherm GmbH, Germany. Melting point and other important thermo-physical properties of the PCM are listed in **Table 8.2**.

Parameter	Value
Melting point	27 - 29 [°C]
Heat storage capacity	250 [kJ/kg]
Specific heat capacity	2 [kJ/kg.K]
Density of solid phase (at 15 °C)	0.88 [kg/l]
Density of liquid phase (at 40 °C)	0.77 [kg/l]
Heat conductivity (both phases)	0.2 [W/m.K]
Maximum operating temperature	50 [°C]

Table 8.2: Thermo-physical properties of PCM (RT28HC) used in the present study

A thermoelectric (TE) circuit is created by connecting a 0 – 500 Ω variable resistor in parallel to three Seebeck devices that are connected in series. Prior to use, this circuit is calibrated by applying a thermal gradient across it. It is determined that the TE circuit generates maximum

power when the resistance connected in parallel equals 2.7Ω ; leading to an update in the value of TE circuit resistance. The TE circuit is then placed on top side (casing purposefully left open from top) of the battery pack constructed with inverted battery cells. Placement is such that one side of the TE circuit is in direct contact with the bottom surface of battery cells and the PCM matrix. Subsequently, an ice tray, made of aluminium, is placed on top of the other side as shown in **Fig. 8.3**, to develop a temperature gradient across the TE circuit.

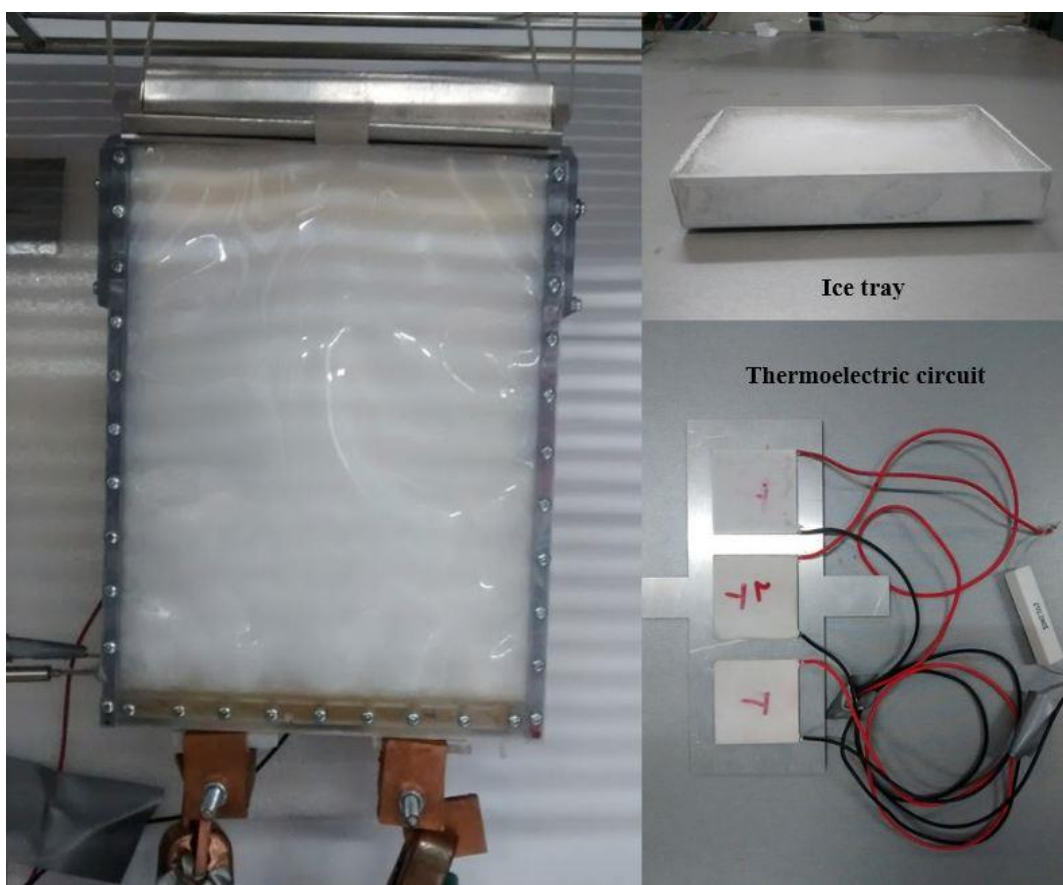


Figure 8.3: Experimental set-up involving battery pack designed with inverted battery cells and a thermoelectric circuit mounted on its top surface (with an ice tray for creating thermal gradient)

8.2.1. Test Procedure

A fully-charged battery pack will be used for testing purposes. Accordingly, battery pack with upright cells is first connected to a 4-channel, 100 A - 20 V Arbin BT 2000 data-cycler and charged using standard constant current, constant voltage (CCCV) program. As per this

program, the battery pack is charged at 0.5C until the pack voltage reaches an upper cut-off of 3.6 V. After that, constant voltage of 3.6 V is maintained and the charging current is allowed to decrease until it becomes equivalent to 0.05C. The parameter values described in the charging program correspond to manufacturer's specification for the commercial battery cell. Battery pack is then left for a minimum of 12 hours at room temperature environment (approximately 21 °C) to allow PCM regeneration. This rest phase reduces the effect of heat generated during the previous charging step on test results illustrating performance of PCM system in abusive conditions. It also simulates overnight charging routine of EV battery packs.

Ambient temperature of the battery pack is changed to 27 °C through a programmable thermal chamber at the beginning of the abusive test schedule. The fully charged battery pack is then galvanostatically discharged at 1C-rate until a lower cut-off voltage of 2.0 V is reached. At this stage, the battery pack is considered fully discharged. It is then immediately put on charging-mode, controlled by the aforementioned CCCV program. A rest phase of 1 minute is included between the discharging step and the charging step. It represents the estimated time for parking an EV in a charging station and connecting it to a charge plug. This procedure is repeated two more times, so that the battery pack undergoes three quick discharge cycles in total.

Changes in the surface temperature of battery cells in the pack during the repetitive discharge cycles are recorded using two temperature sensors with an uncertainty of ± 0.5 °C. The sensors are placed 15 mm from the bottom edge of the electrode terminals on – 1. Front Side of the first battery cell, and 2. Front side of the third cell in the battery pack, from herein referred to as the outer cell and the internal cell, respectively. Additionally, a Trotec IC080-LV infrared (IR) camera is used to capture details of phase change transformation triggered in the PCM due to heat generated by the battery pack during the abusive test.

In another instance, the whole test schedule is repeated with the battery pack 2 (with inverted battery cells). Results of this test are compared with the data gleaned after successively discharging the battery pack with upright cells three times to measure the effect of battery cell orientation on effectiveness of PCM-based TMSs.

In third instance, the TE circuit is placed on top of the battery pack with inverted cells. The battery pack is then subjected again to the abusive test schedule as above and the variations in battery cell temperatures as well as the phase change process are continuously monitored. In addition, voltage generated by the TE circuit is recorded through an auxiliary voltage sensor connected to the Arbin BT2000 data-cycler.

8.3. Results and Discussion

In this section, performance of a paraffin-based PCM is experimentally analysed for three different Li-ion battery pack designs - (a) battery pack with conventional or upright cell layout (referred as Pack 1), (b) battery pack made of inverted pouch cells (referred as Pack 2), and (c) battery pack with inverted pouch cells and thermoelectric coolers connected to one of its sides (referred as Pack 3).

Fig. 8.4 presents temperature histories recorded for two different battery cells, i.e., the outer cell and the internal cell of Pack 1. It can be noticed that the 3mm thick PCM layer acts as buffer for the battery cells, temporarily blanketing them from the effects of external environment. Consequently, it takes close to 45 minutes for surface temperature of outer cell to change from normal room temperature to approx. 27 °C. The change can be attributed to heat generated by the battery pack. A further increase in temperature of outer cell is limited by the PCM, which undergoes phase change by absorbing heat energy from it. In contrast, the internal cell temperature increases at a steeper rate stabilising in the melting range of PCM for a time span of less than 15 minutes. It resumes increasing and reaches 30 °C by the end of

discharge step 1. End of the discharge period marks a sudden drop in the internal cell temperature, which maintains a relatively steady profile during the subsequent charging step.

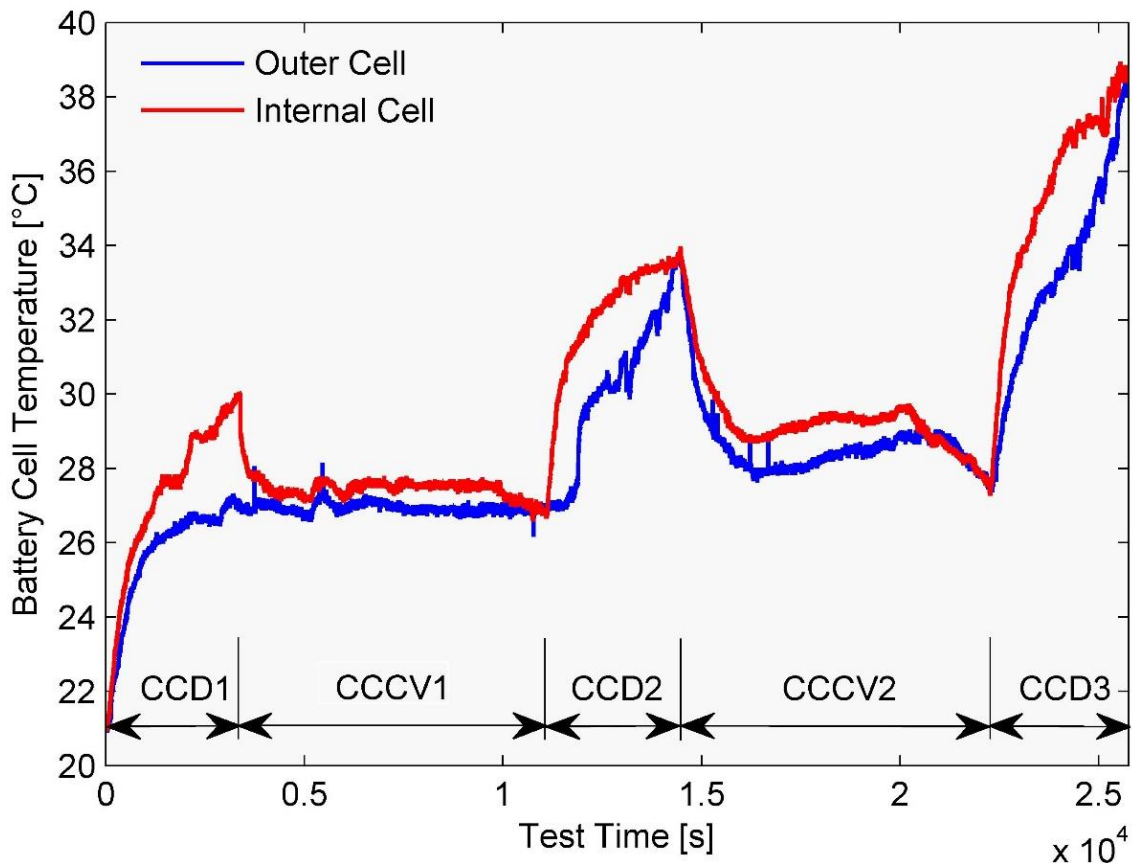
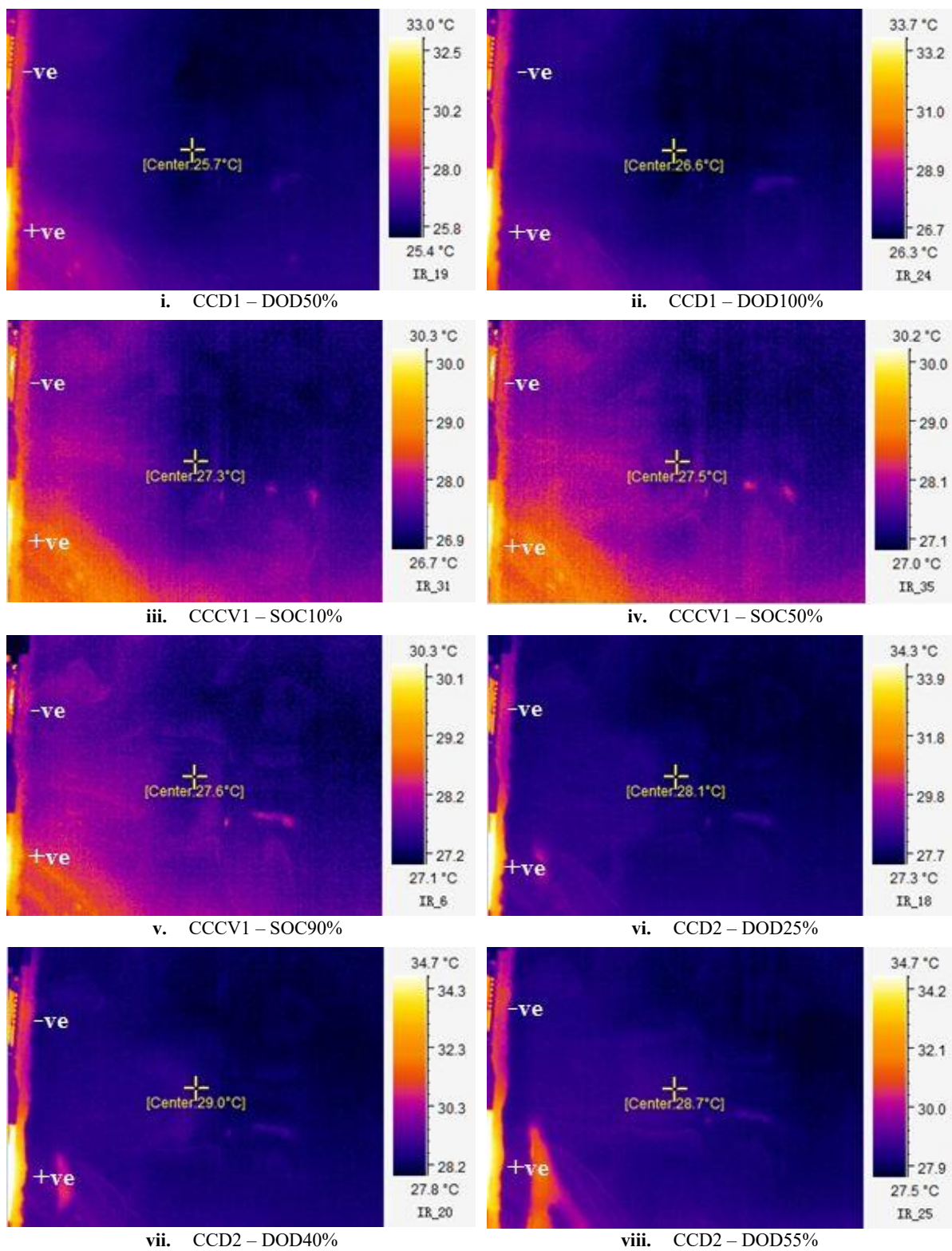
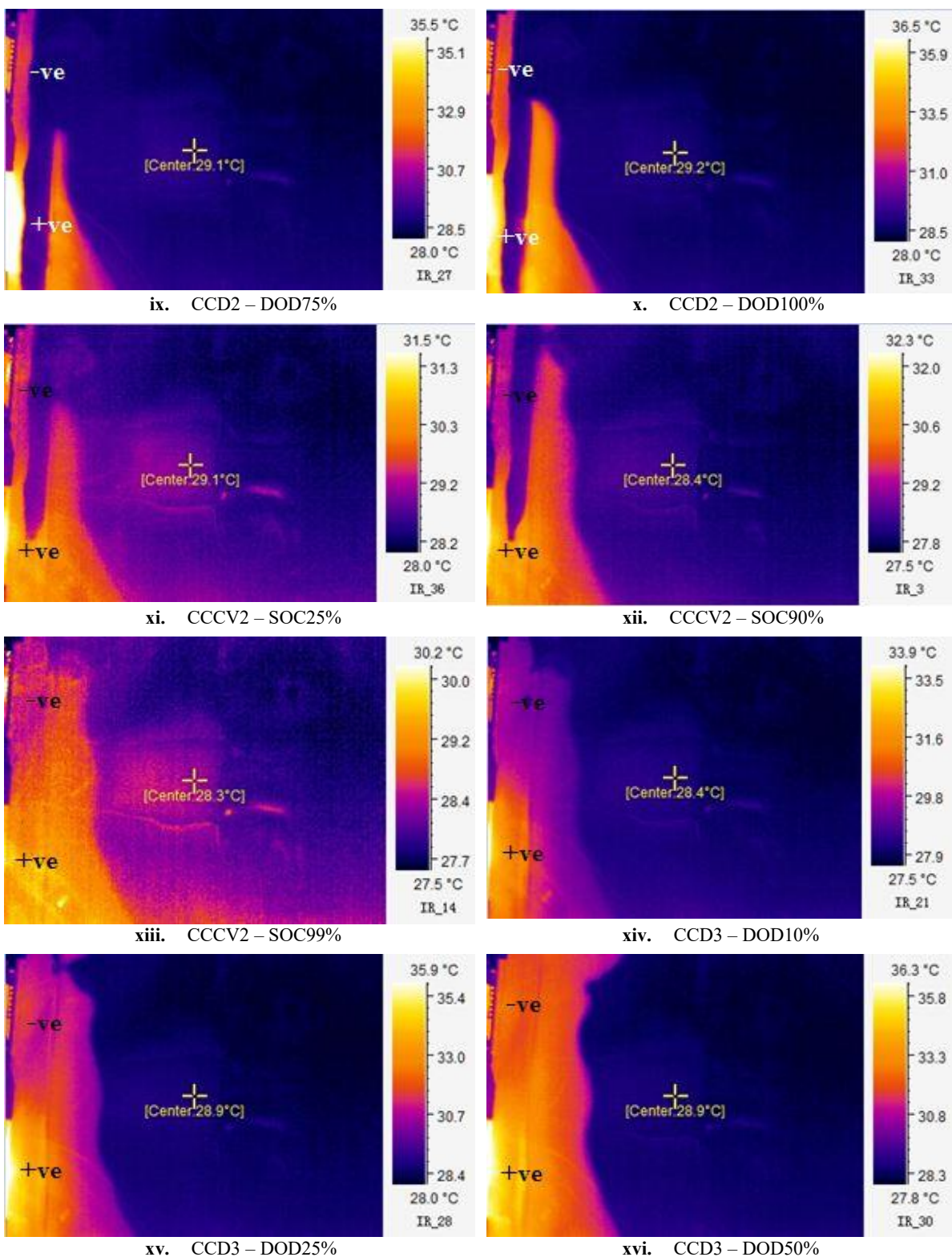


Figure 8.4: Surface temperature for the internal and the outer battery cells of the battery pack with upright cells shown as a function of time during the abuse test in an operating temperature of 27 °C; where, CCD represents constant current discharge process at 1C; CCCV is constant current constant voltage charge process at 0.5C; and the suffix indicate the respective step number in the abuse test. A one minute rest is included between each of these charge and discharge step.

Both the internal and the outer cell temperatures increase monotonically in the next discharge steps and inter-cellular gradients of 2 °C and 2.75 °C, with the outer battery cell operating at a lower temperature than the internal battery cell, are noted for discharge steps 2 and 3, respectively. Surprisingly, the inter-cellular gradient seems to have little or no effect on the maximum cell temperatures recorded for later discharge steps as approximately similar peak temperatures of 33.75 °C and 38.94 °C for both the battery cells are measured for the respective discharge steps.





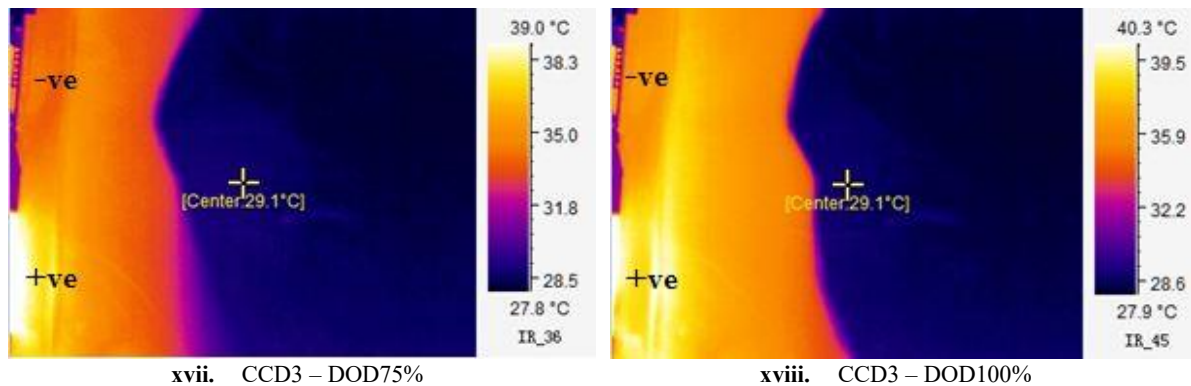


Figure 8.5: Thermal images showing temperature distribution in the PCM during abuse test of the Battery Pack with upright battery cells, in ambient temperature of 27 °C (where, CCD – Constant current discharge; DOD – Depth of discharge; SOC – State of charge and succeeding numerals indicate the step in the abuse test e.g. CCD3 means constant current discharge step 3)

Fig. 8.5 shows temporal changes in temperature of the PCM measured using infrared radiation or thermal imaging technique during the abuse test of the Pack 1. In this analysis, temperature labelled as “Center” in different images corresponds to temperature of a point in the middle of camera view-frame and is considered an indication of bulk temperature. Further, temperature at different points in the PCM matrix can be determined from the colour scheme governed by palettes shown on right hand side in each image.

It is evident from these images that more heat is generated near the positive terminal of the battery pack in comparison to the negative tab. Uneven distribution of heat generation sites in a Li-ion battery pack coupled with low thermal conductivity of PCM leads to formation of inhomogeneously distributed heat pockets across the PCM matrix as well. As a result, difference of more than 3 °C is observed in the temperature of material closer to the positive tab (bottom-left corner of thermal image) and the PCM farthest from it (diagonally opposite top-right corner) at the end of discharge step 1. The heat pocket expands multiple times in both the x - and the y - directions during the second discharge step assuming a knife-like shape, as illustrated by **Figs. 8.5(vi) – 8.5(x)**. Correspondingly, the bulk temperature increases by of 1.3 °C while a difference of more than 7 °C can be noticed between the maximum and the minimum temperature for PCM.

Volume fraction of the liquefied material increases further during the third discharge step and a clear demarcation between the solid (cool) and the liquid (hot) regions can be noticed. However, it can be seen from **Fig. 8.5(xvi)** and **Fig. 8.5(xviii)** that concentration of the hot material is significantly higher in the upper portion of the Pack 1. Segregation of the two phases causes heat accumulation in the battery pack. As a result, a non-uniform temperature gradient of 12.4 °C builds on the exterior side of the Pack 1. Point to highlight is that mass transfer or flow of molten PCM between adjacent battery packaging spaces, i.e., from space on the front side of the battery cell to the space on its opposite side is restricted. A larger thermal gradient can thus be expected in the PCM surrounding the internal battery cells of a battery pack designed by assembling battery cells in an upright position.

This phenomenon is not unique to battery packs. **Fig. 8.6** is a visible image from the later stages of abuse test study of a single 20 Ah commercial pouch cell, embedded in a PCM matrix, subjected to operating conditions similar to those used for the battery packs 1 and 2. The photograph shows that upper section of the PCM matrix is in fully melted state while some holes have formed in the middle section of the matrix, making the PCM-based TMS ineffective in removing heat from the top portion of the battery cell. In contrast, placing the battery cell in an inverted position allows using the difference in the density of the solid phase and the molten phase of the PCM for ensuring that area near the electrode terminals is surrounded by solid PCM for a relatively longer time, as shown by **Fig. 8.6(b)**. These observations align perfectly with the findings reported by Jones et al. [444] and Lamberg et al. [445] who studied melting of PCM in heated enclosures.

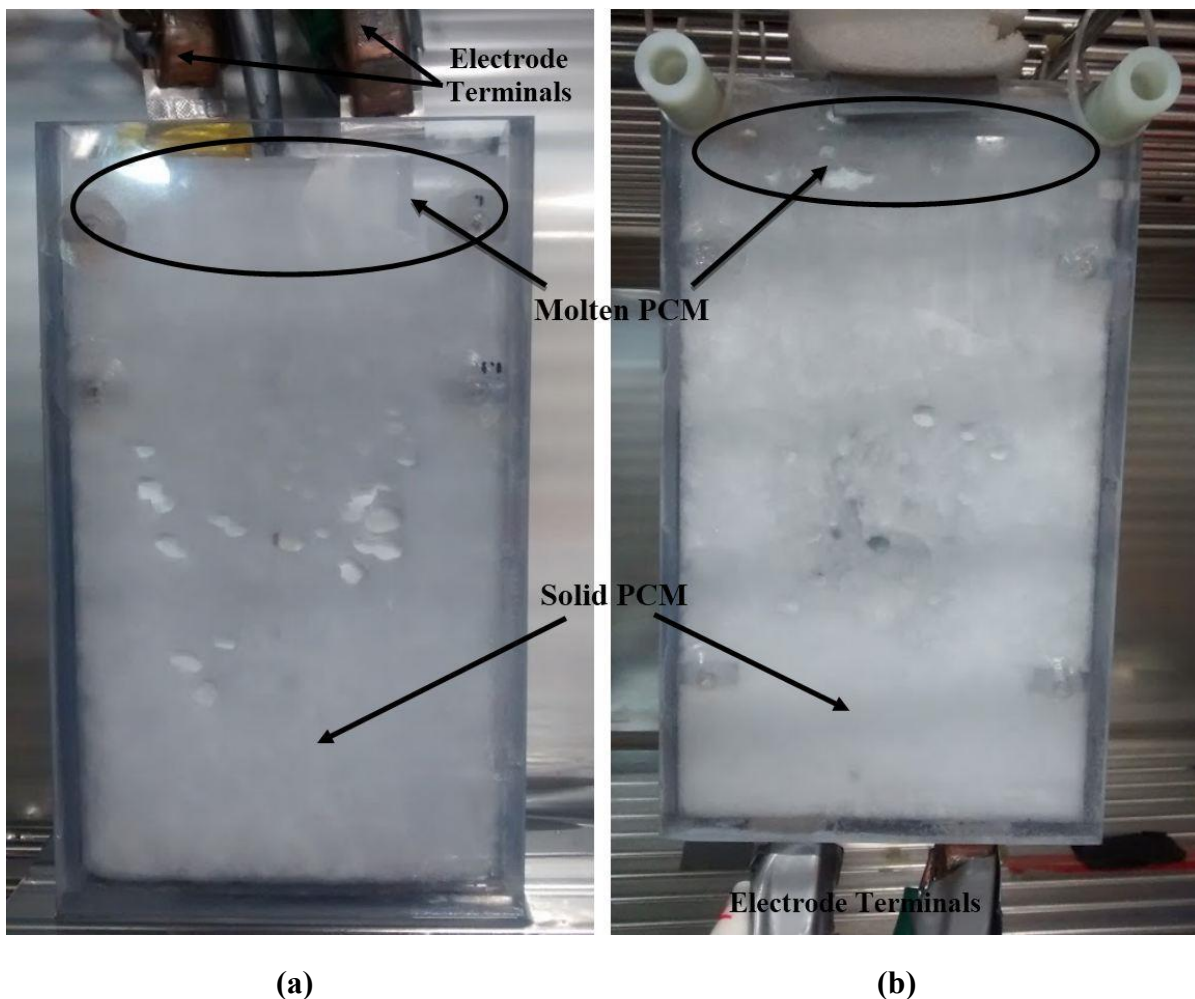


Figure 8.6: Visible images showing volume fraction of molten phase of PCM in case of abuse test of **(a)** upright battery cell and, **(b)** inverted battery cell at 27 °C

Advantages of using inverted battery cells in the design of a battery pack are illustrated via **Figs. 8.7 and 8.8**. **Fig. 8.7** depicts the surface temperature variations measured for different battery cells of Pack 2 during the abuse test. Additionally, **Fig. 8.8** presents information on thermal gradient existing in the PCM matrix at various stages during this test. It is evident from the figures that this arrangement helps not only in maintaining a stable battery cell temperature during highly demanding operating conditions but also in reducing the inter-cellular temperature gradient within the battery pack.

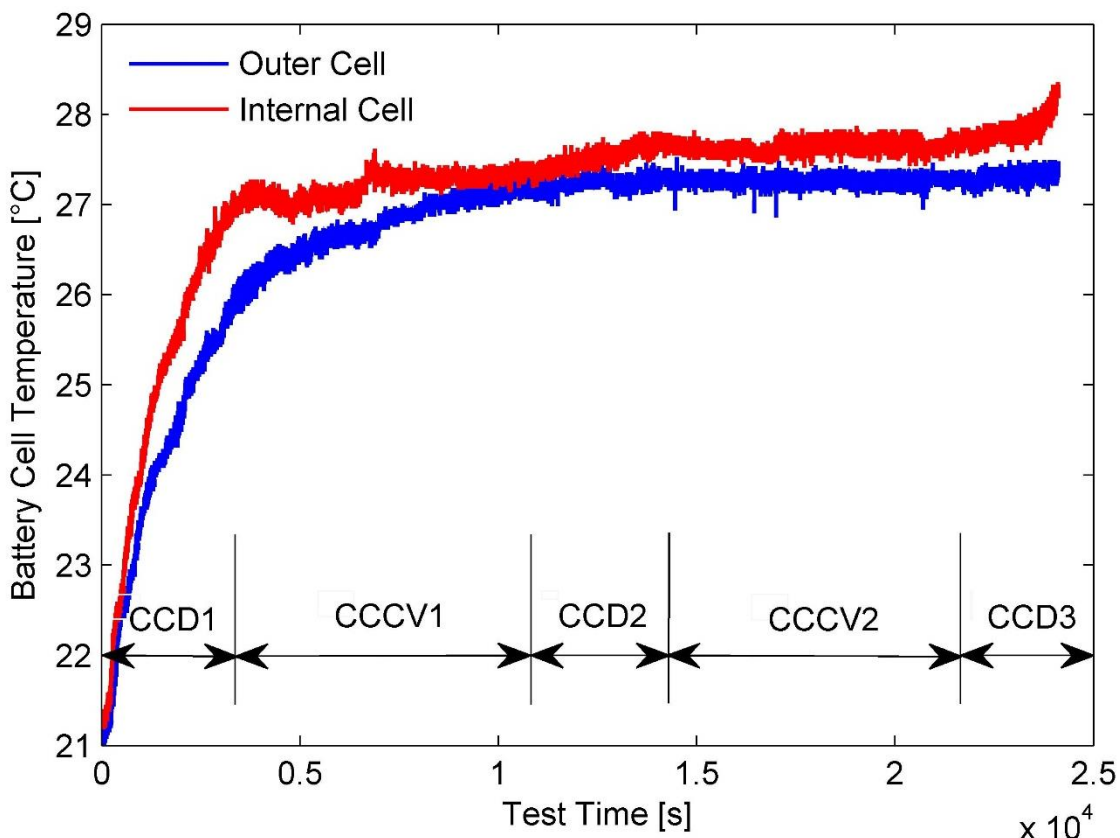
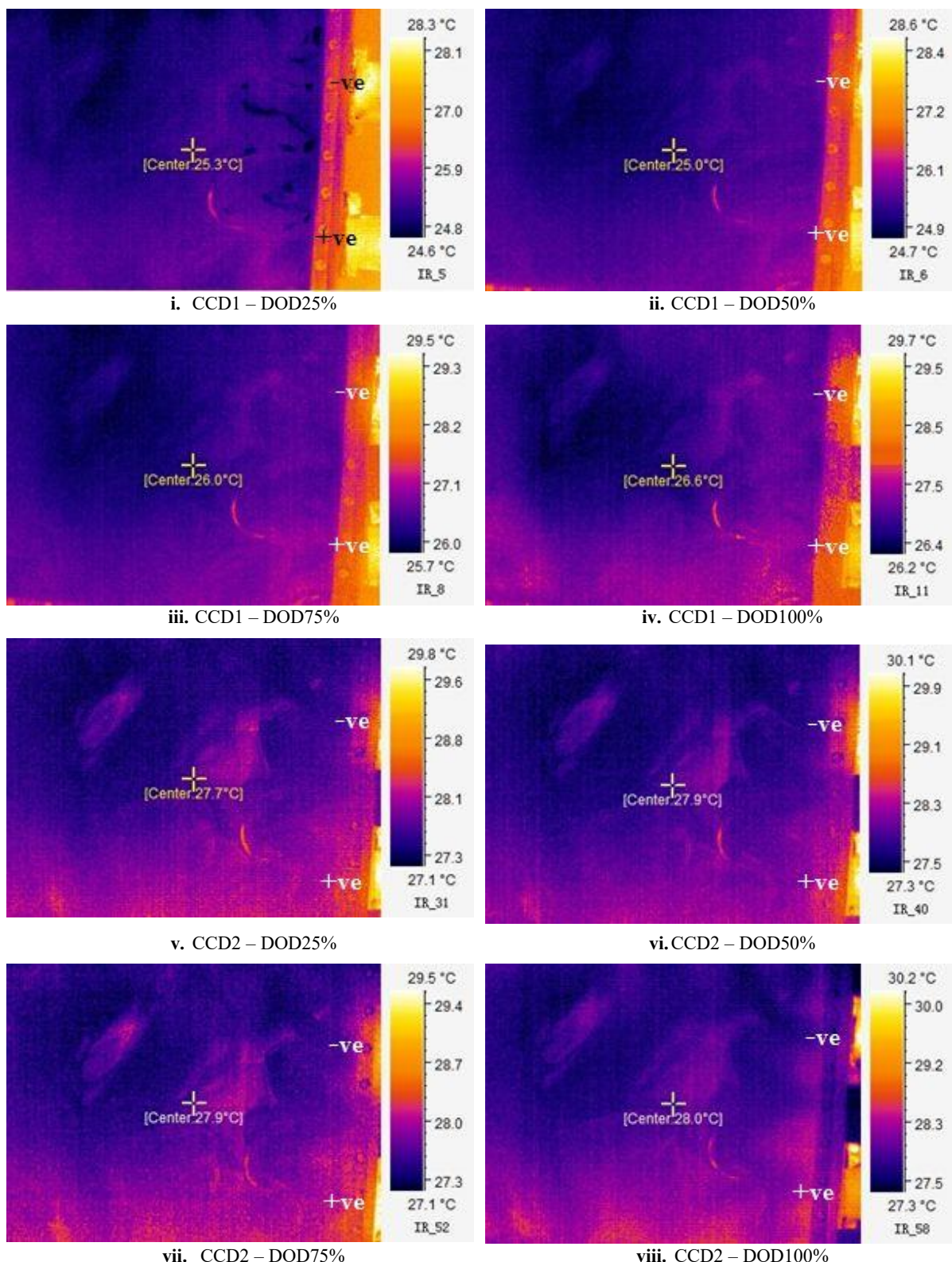


Figure 8.7: Surface temperature history for the internal and the outer battery cells of the battery pack with inverted cell orientation during its abuse test in ambient temperature of 27 °C

Scale analysis of materials having Prandtl number (Pr) greater than 1 has shown that upon being heated from the side in a rectangular enclosure melting of such materials proceed in four distinct regimes. The regimes are differentiated by the dominant heat transfer mechanism. They are: (1) conduction regime, (2) transition regime, (3) convection dominant and (4) shrinking solid [446]. Pr is a dimensionless number denoting the ratio of momentum diffusivity of a material and its thermal diffusivity. Pr values larger than 1 signify that convection is comparatively a more effective heat transfer mechanism than conduction for the chosen material. Lastly, Pr for paraffin wax compounds is of the order of 10^2 . Subsequently, they are classified as high Pr liquids [447].



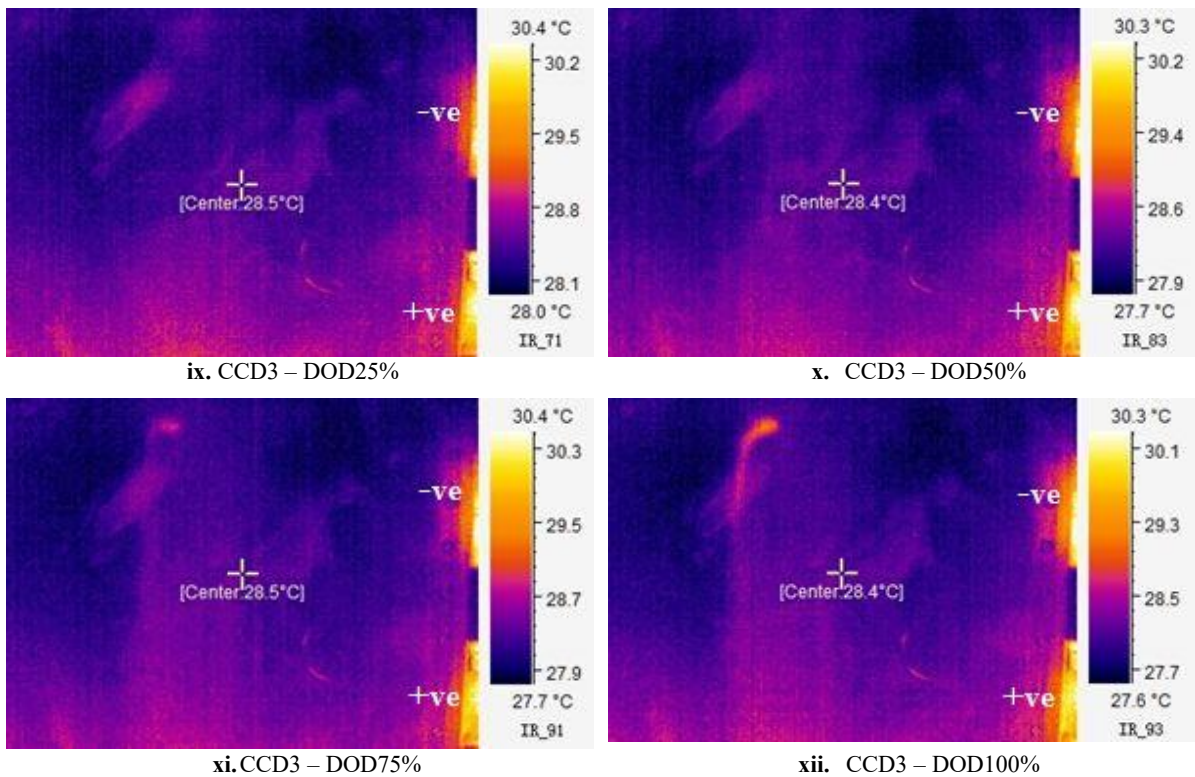


Figure 8.8: Images showing variations in temperature distribution in PCM matrix of battery pack with inverted cells at different stages of the abuse test in ambient temperature of 27 °C

Laws of pure thermal diffusion govern the melting of solid in the entire enclosure during the conduction regime. On the other hand, conduction occurs mainly in the lower part of the casing while its upper region is controlled by convection in the transition regime. Gradually, convection becomes the dominating mechanism leading to a regime of variable height that culminates with the solid-liquid interface reaching the enclosure/cool wall, which is farthest from the heating source [448].

Accordingly, thickness of the molten layer is very small and virtually uniform along the z-direction during the discharge step 1. Conduction is the primary heat transfer mode in this stage. Also, the effect of buoyancy is small and velocity of the molten PCM can be regarded as negligible. As the abuse test continues, natural convection develops in Pack 2 (the battery pack with inverted battery cells), which increases the rate of melting of the PCM. Buoyancy-driven convective currents carry the molten PCM along the vertical heating (battery) surface

to the top of the battery pack casing. In turn, the cool PCM flows down the solid-liquid interface creating a circulation effect in the battery pack. Consequently, a non-uniformity develops in the thickness of the molten PCM layer along the z-direction. **Fig. 8.6(b)** shows that the thickness of the molten PCM layer (estimated from size and concentration of holes in the PCM matrix) is largest in the top part of the battery pack casing. Magnitude of the circulation velocity depends on the thermal gradient existing in the PCM and diminishes as a more uniform temperature profile, seen in **Fig. 8.8**, is established in it.

Effectiveness of the proposed TMS is further improved through TE generators, which are solid-state integrated circuits based on Seebeck effect and used for converting waste heat to electrical power. Alternatively, solid-state integrated circuits based on Peltier effect and designed mainly for refrigeration purposes are called TE coolers. Solid-state devices offer many advantages such as scalability, reliability, adaptability, and lack of moving parts and refrigerants. Further, they can provide cooling below ambient temperature making them an attractive choice for this application.

However, cost of a 22W TE generators (approx. AUD 78 [449]) differ significantly from the cost of 51W TE coolers (approx. AUD 25 [450]). Cost benefits of TE coolers over TE generators prompted Rowe and Min [451] to investigate the applicability of TE coolers for the purpose low temperature waste heat recovery. It was found that from the cost perspective TE coolers are better suited for the application of power generation in systems with waste heat temperature below 150 °C than TE generators. Their findings were later corroborated by experiments of Chen et al. [452]. TE coolers have thus been used instead of TE generators for power generation in the present study. Module's (ZP9104) physical dimensions and other parameters are described in **Table 8.3**.

Parameter	Value
Number of TE couples	127
Length (mm)	40.0 ± 0.2
Width (mm)	40.0 ± 0.2
Height (mm)	3.50 ± 0.1
I_{max} (A)	8
U_{max} (V)	15.4
Q_{max} (W) ($\Delta T = 0$)	75.5
ΔT_{max} ($^{\circ}\text{C}$) ($Q_c = 0$)	68
R (Ω)	1.50 ± 0.08

Table 8.3: Properties of the commercially available thermoelectric module used in the present investigation

Fig. 8.9 shows Seebeck voltage induced across the TE circuit as a result of temperature difference (approx. 27°C , since a stable temperature of 0°C is maintained at cold side of the TE circuit using ice while temperature of PCM on the hot side remains close to 27°C) between its opposite sides. It simulates a real world situation where a thermal gradient is created by directing conditioned cabin air over the TE circuit or by putting the TE circuit in thermal contact with expansion valve of EV's heating, ventilation and air-conditioning system.

A sudden drop from a peak voltage of 496.2 mV is noticed in this experiment as the ice used for creating the thermal gradient across the TE circuits melts rather quickly due to – (1) high ambient temperature and (2) large inefficiency of the TE circuit. Consequently, ice tray used in the set-up was repeatedly replaced resulting in appearance of several peaks of differing heights. It is however clear that a DC (direct current) voltage of reasonable magnitude can be produced by using the waste heat accumulated in large EV battery packs. Magnitude of the induced voltage can be amplified by mounting more TE coolers on the surface of the battery pack or by using coolers with a higher figure of merit.

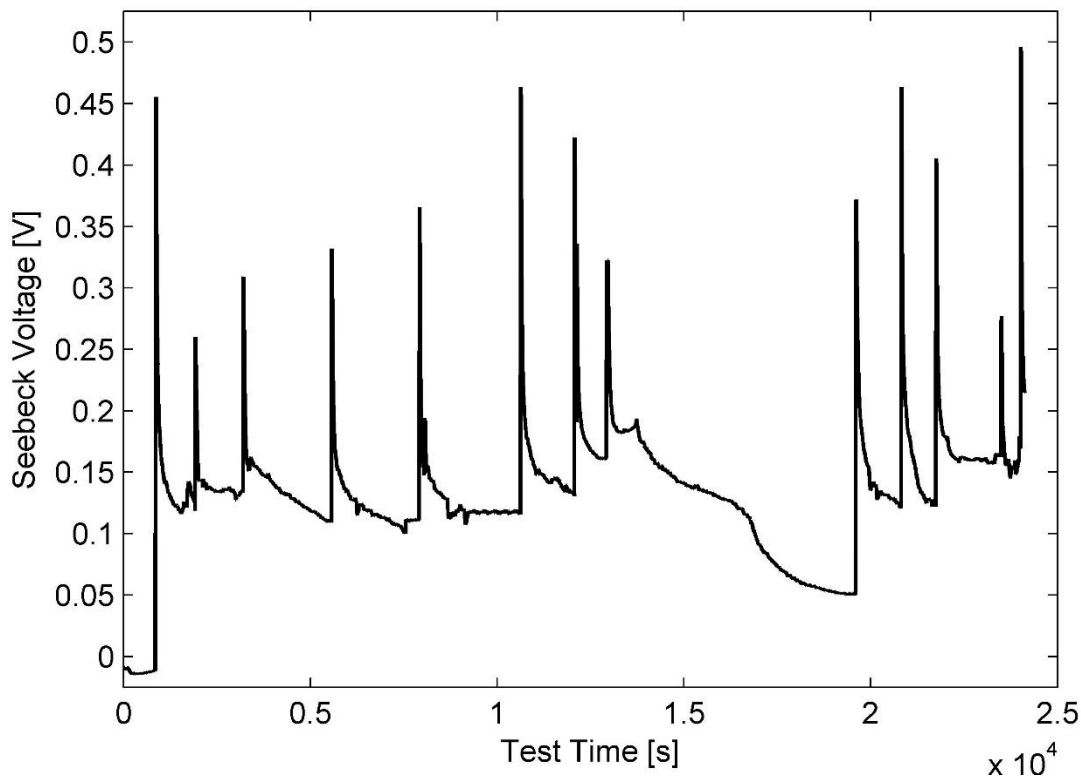
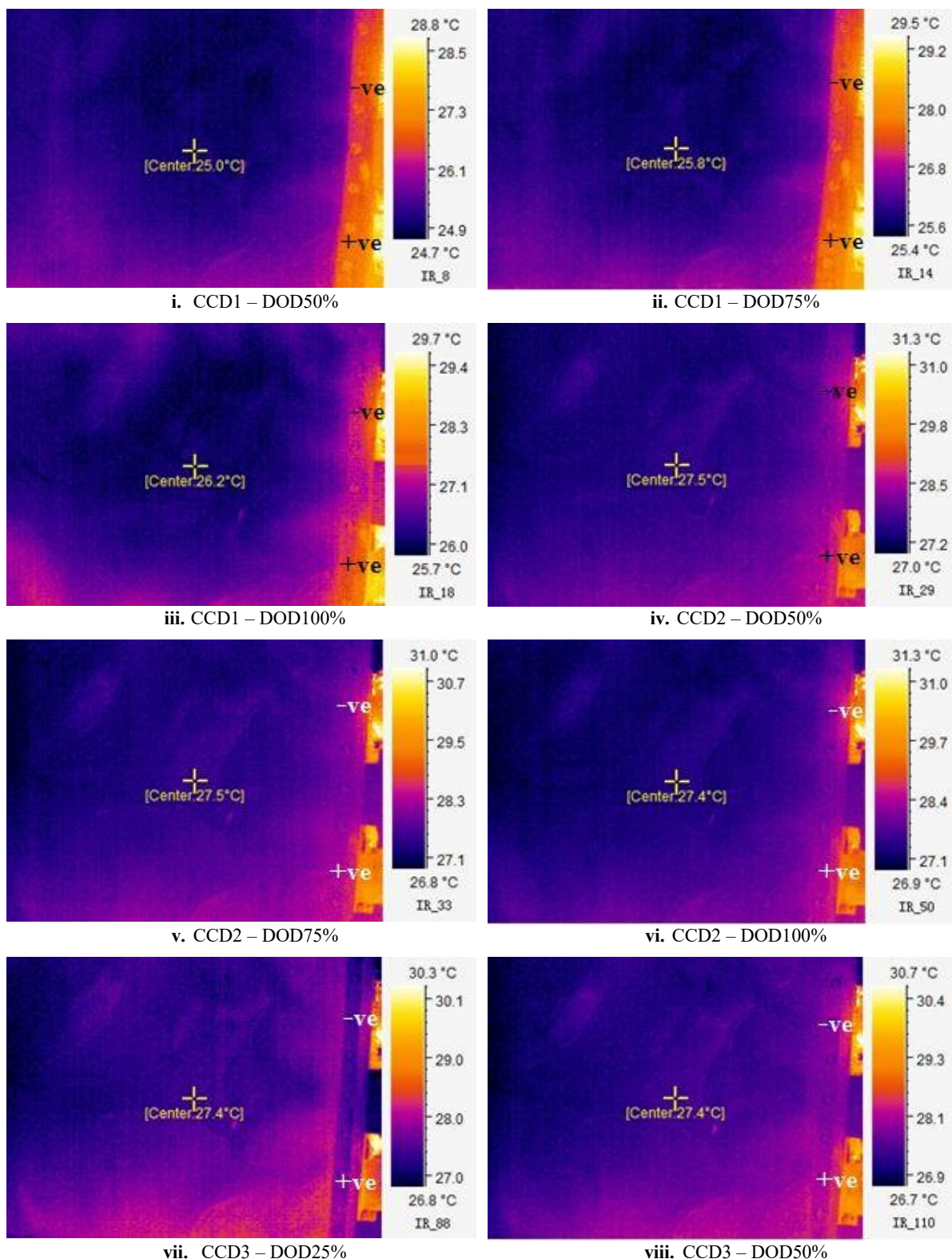


Figure 8.9: Thermoelectric voltage induced in the TE circuit due to a thermal gradient of approximately 27 °C created due to the presence of molten PCM and battery cells on one side and an ice tray on another

Waste heat recovered by the TE circuit from the PCM matrix also produces a refrigerating effect, which is visible from the thermal images shown in **Fig. 8.10**. The cooling, represented by darkish purple shade in these images, can be seen propagating in the matrix from the top of the casing towards the electrode terminals at the bottom of the battery pack. Rate of propagation is slow though, which could be because of the low thermal conductivity of the PCM matrix and improper contact between the TE devices and the battery cells. Benefits of this system cannot be neglected, as the bulk temperature in Pack 3 is lower by 0.5 °C to 1 °C than the bulk temperature recorded for Pack 2 at similar stages of the abuse test.



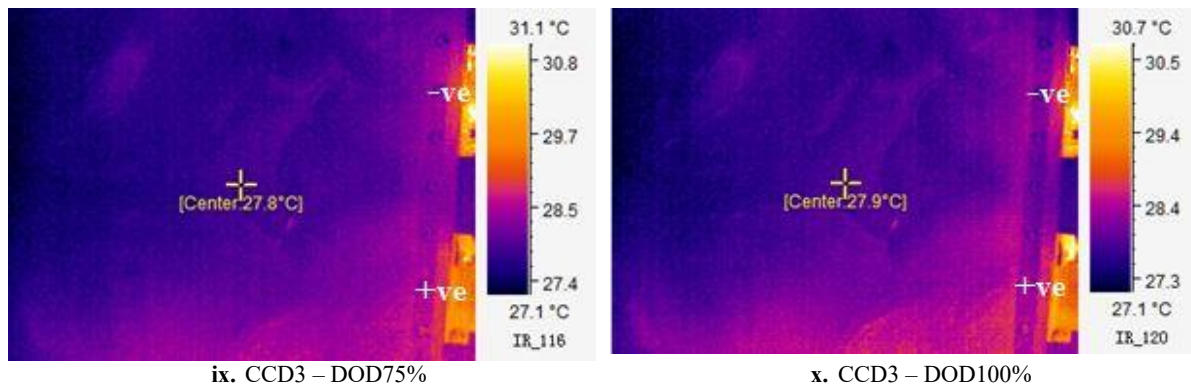


Figure 8.10: Thermal images showing temperature distribution in PCM during various stages of the abuse test of Pack 3, i.e., battery pack designed with inverted battery cells and a TE circuit attached at top surface

8.4. Conclusions

This study presents a novel mechanism for improving heat transfer characteristics of PCM-based TMSs for large battery packs, subject to repeated high rate cycling and minimal cooling periods. The proposed scheme is based on modifying cell orientation in the battery pack and dismisses the compromise made to latent heat storage capacity of PCM-based systems in order to increase their tolerance towards abuse conditions. Experimental results obtained in this study confirm that arranging battery cells in inverted position within a battery pack filled with PCM facilitates development of convective currents in the battery pack. Convection promotes better heat distribution through the PCM matrix, compensating to a degree for its low thermal conductivity. The results demonstrate that it is much easier to manage temperature irregularities in a battery pack designed with inverted battery cells than in a traditional design with battery cells arranged in an upright position. Additionally, it is found that robustness of the system can be further increased by connecting Seebeck devices on one side of the battery pack. Seebeck devices convert heat energy stored in PCM to electrical power, which may have a positive influence on driving range of EVs. Also, scalability of the components used, i.e., the TE devices and the PCM, means that it is easily accessible across cross-platform technologies.

Chapter 9

Conclusions and Future Work

Chapter 9

9.1. Overview

Large-scale electrification of road transportation sector is essential for containing the damage caused to our environment. However, high manufacturing cost of battery packs and consequently EVs has been identified as a major block. Aggressive solutions such as developing new battery chemistries and replacing components of Li-ion battery cells with cheaper materials are thus being implemented to address this issue. In addition to these solutions, mass-production of battery cells and battery packs is expected to provide further cost reduction. Therefore, design of such mass-producible battery packs is the main goal of investigation of this doctoral work.

9.2. Key Findings and Contributions of this thesis

Other than the provision of recommendations for future work, this body of work makes several significant contributions to the published literature in the domain of battery packaging and thermal management.

Firstly, it presents a conceptual analysis of a large pool of variables that may affect performance and reliability, as perceived by the end-user, of a large battery pack. It is a known fact that variability reduces mass producibility of a system. Using tools such as parameter diagram and house of quality, the relationship of two different classes of variables – noise factors and control factors with customer requirements is investigated. Subsequently, it is found that thermal management system design and battery packaging design have the largest effect on modularity of battery packs. Note, this thesis is built on a premise that implementing modular architecture would make the battery packs easily scalable; allowing OEMs to target cross-platform technologies and justify bulk production of battery packs.

Conclusions and Future Work

Secondly, it discloses mechanical features crucial for a fail-safe battery packaging design. After a careful and thorough analysis of existing EV battery pack designs along with several US patents addressing issues related to thermal runaway, mechanical vibrations and vehicle impact, it is discovered that:

- Limiting relative battery cell movement will reduce the probability of battery pack failure due to all of the three aforementioned safety risks
- In addition, to minimize the risk of thermal runaway propagation, thermal barriers should be integrated in battery packaging at cell level and at module level.
- It is necessary to include cell spacers in battery packaging design. Cell spacers perform dual function, by acting as thermal barrier at cellular level and assisting in maintaining pack integrity during vehicle impact by restricting cell motion. Other features that can help in reducing relative cell movement are deformable electrode terminals and rigid mounting frame.
- It is necessary to provide both lateral and vertical supports to battery packs in order to isolate it from damaging effects of mechanical vibrations. Including gas exhaust ducts to the battery pack structure can provide additional benefits.
- Further, a battery pack should ideally be installed in the middle of the vehicle chassis, away from the typical crush zones of a vehicle.

Thirdly, it has been revealed in this work that modularity of a battery pack is largely dependent on scalability of its thermal management system. Therefore, the relationship between battery heat generation and nominal cell capacity is experimentally explored in this thesis. A custom-designed calorimeter is used for this purpose and the effect of cell thickness is included in the analysis. Heat generation rates for $LiFePO_4$ pouch cells of different nominal capacities are measured at discharge rates of 0.33C, 1C and 3C using the custom-designed calorimeter for

ambient temperatures ranging between -10 °C and 50 °C. It is observed that in ambient temperatures lower than 35 °C, the thin battery cells generate heat at rates greater than that of thick battery cells and vice-versa at temperatures over 35 °C for all discharge rates. More importantly, it is noted that heat generation is not a function of cell nominal capacity and thickness for the Li-ion pouch cells operating in an ambient temperature of 35 °C.

Fourth, the thesis evaluates estimation accuracy of the NTG model, which is one of the most frequently used mathematical models for calculating irreversible heat generation in battery cells, and suggests procedure for improving it. The NTG model was initially developed by Tiedemann and Newman for an idealised lead-acid battery cell. It was later applied by Gu for computation of polarisation across terminals of Zn/NiOOH cell. Subsequently, the model was picked by CD-adapco for developing foundation of their proprietary battery modeling software – Battery Design Studio. Research undertaken in this thesis highlights that the OCV estimation technique defined in the structure of the NTG model, i.e., extrapolation of V-I curves, cannot account for interphasial film polarisation. As a result, the NTG model underestimates battery polarisation and irreversible heat generation rate for a 20 Ah $LiFePO_4$ pouch cell discharged at 0.5C in an ambient temperature of 27 °C by 65% and 0.22 W, respectively. Further, significant improvement in the accuracy of the NTG model is illustrated by replacing the extrapolation method based OCV estimation technique with the galvanostatic intermittent current discharge method. Rest periods equalling one hour are shown as adequate for measuring OCV using the intermittent current discharge method.

A novel methodology to estimate SEI film resistance for Li-ion battery cells is introduced in this thesis. SEI film resistance is an important parameter in the study of charge transfer kinetics of a Li-ion battery. The passive film affects the diffusion process of Li-ions. As such, it becomes essential to include film resistance in battery modelling. However, the traditional

Conclusions and Future Work

method of estimating the SEI film resistance is costly and time consuming. An indirect estimation approach is thus presented in this thesis. It is based on Ohm's law and relies on determining the interphasial polarisation from the difference of open-circuit voltage measured immediately after switching off the applied current and the equilibrium voltage. The technique is simple, easy to implement and can be used for a quick estimation of SEI film resistance with reasonable accuracy. For instance, average value of the film resistance for a 20 Ah $LiFePO_4$ test battery cell is measured as $0.004 \text{ Ohm} \cdot m^2$ using the proposed method. $\text{Ohm} \cdot m^2$ The measured value is found to be consistent with the SEI film resistance values published in the literature using the impedance spectroscopy techhniue for lithium-carbon film electrodes. The proposed technique can therefore be applied for an approximate estimation of the SEI film resistance of other battery chemistries and cell types as well with good confidence.

This thesis also proposes a simple and an easy to implement computational model for estimating heat generation rates of Li-ion battery cells of varied nominal capacities. Such a model is necessary since the existing numerical models are either too complex to serve the purpose or do not include the effect of nominal cell capacity and it would be impractical to repeat an experimental excercise every time a battery pack needs to scaled. An ANN-based modelling approach is thus selected in this work and a three layered feedforward network is designed using the Levenberg–Marquardt algorithm. An experimental dataset, generated via calorimetric study and expanded using analytical technique to address the issues related to data scarcity, is used for training the ANN. Consequently, the model takes into account the effect of discharge rate, ambient temperature and depth of discharge along with the effect of cell nominal capacity on battery heat generation. It is found that the proposed ANN architecture can predict heat generation for $LiFePO_4$ pouch cells of capacities between 8 Ah and 20 Ah with a reasonable accuracy for discharge rates between 0.33C to 3C and an ambient temperature ranging from -10 °C to 50 °C.

Lastly, proof of concept for a novel TMS for scalable Li-ion battery packs is developed in the present thesis. Performance of the disclosed TMS has been specifically tested under abuse environment, i.e., repetitive cycling at high rates with minimal rest phase. The conceptualised system is found superior than the traditional battery cooling methods for reducing peak temperatures and inter-cellular gradient in a large battery pack during conditions of abuse. Superior thermal performance is achieved by using battery cell orientation in conjunction with phase change material and thermoelectric coolers, functioning in Seebeck (or power generation) mode. It is demonstrated that placing battery cells in an inverted fashion promotes convection, which in turn improves PCM melting rate and facilitates uniform heat distribution in the PCM matrix. Moreover, the proposed hybrid TMS is scalable by virtue of the components involved. An added advantage is that parasitic load created by it is negative.

9.3. Recommendations for Future Research

Since this thesis is concentrated on designing a scalable TMS for battery packs, the effects of cell nominal capacity on battery heat generation were investigated. A comprehensive experimental study is undertaken to analyse these effects and a computational model that includes nominal cell capacity as an input is developed for the first time. However, the model is currently limited to $LiFePO_4$ pouch cells whereas other chemistries like lithium cobalt oxide, lithium nickel-manganese oxide etc. are also used in commercial battery packs. Although suggestions for possible research are made throughout the thesis where the relevant topics are discussed, it would be sensible to re-state that more work is necessary to make the computational model more robust.

Factors that could be considered for expanding the applicability of the model would include battery chemistry, battery cell type, and battery ageing-effects. In addition, variance in manufacturing methods and techniques could also have a potential impact on the quality of

Conclusions and Future Work

model predictions. It is thus expected that reliability of the ANN model output would significantly improve after including the data generated by using battery cells that are of same type, size and chemistry but sourced from different battery manufacturers in the training dataset.

Another research direction that can be considered relates to the battery packaging. Stand-alone EV battery packs have reasonable crash-worthiness rating. They are therefore sometimes used as semi-structural elements in the EV body structure to contribute towards the overall vehicle bending stiffness, e.g. the battery pack in GM Chevrolet Volt. It is for this reason that EV body structures with their typically in-built crash-protection features, discussed in Section 3.4, can be classified as over-designed when a battery pack having high crashworthiness is fitted with them. This provides a significant opportunity for vehicle lightweighting. It should thus be investigated further.

References

1. Nelson, P.A., K. Bloom, and D. I Dees, *Modeling the performance and cost of lithium-ion batteries for electric-drive vehicles*. 2011, Argonne National Laboratory (ANL), Argonne, IL (United States).
2. Pierpaolo Cazzola, M.G., Jacob Teter and Wenjing Yi, *Global EV Outlook 2016 - Beyond one million electric cars*. 2016, International Energy Agency.
3. UNFCCC, *Adoption of the Paris Agreement*. 2015, United Nations New York, NY.
4. Office, U.S.-G.E. *Paris Declaration on Electro-Mobility and Climate Change and Call to Action - Electrifying Sustainable Transport* 2015; Available from: <http://newsroom.unfccc.int/lpaa/transport/the-paris-declaration-on-electro-mobility-and-climate-change-and-call-to-action/>.
5. Pearre, N.S., W. Kempton, R.L. Guensler, and V.V. Elango, *Electric vehicles: How much range is required for a day's driving?* Transportation Research Part C: Emerging Technologies, 2011. **19**(6): p. 1171-1184.
6. Tie, S.F. and C.W. Tan, *A review of energy sources and energy management system in electric vehicles*. Renewable and Sustainable Energy Reviews, 2013. **20**: p. 82.
7. Vorrath, S. *Electric vehicle boom driving EVs to 35% new car sales in Asia by 2040*. 2016 [cited 2016 August 03]; Available from: <http://reneweconomy.com.au/2016/electric-vehicle-boom-driving-evs-35-new-car-sales-asia-2040>
8. Trigg, T., P. Telleen, R. Boyd, F. Cuenot, D. D'Ambrosio, R. Gaghen, J. Gagné, A. Hardcastle, D. Houssin, and A. Jones, *Global EV outlook: understanding the electric vehicle landscape to 2020*. Int. Energy Agency, 2013: p. 1-40.
9. Han, H., H. Park, K.C. Kil, Y. Jeon, Y. Ko, C. Lee, M. Kim, C.-W. Cho, K. Kim, U. Paik, and T. Song, *Microstructure control of the graphite anode with a high density for Li ion batteries with high energy density*. Electrochimica Acta, 2015. **166**(0): p. 367-371.
10. Lu, J., Y.-L. Chang, B. Song, H. Xia, J.-R. Yang, K.S. Lee, and L. Lu, *High energy spinel-structured cathode stabilized by layered materials for advanced lithium-ion batteries*. Journal of Power Sources, 2014. **271**(0): p. 604-613.
11. Sun, X., X. Zhang, B. Huang, H. Zhang, D. Zhang, and Y. Ma, *(LiNi0.5Co0.2Mn0.3O2 + AC)/graphite hybrid energy storage device with high specific energy and high rate capability*. Journal of Power Sources, 2013. **243**(0): p. 361-368.
12. Wang, G., Z. Ma, G. Shao, L. Kong, and W. Gao, *Synthesis of LiFePO4@carbon nanotube core-shell nanowires with a high-energy efficient method for superior lithium ion battery cathodes*. Journal of Power Sources, 2015. **291**(0): p. 209-214.
13. Zhou, G., L. Li, C. Ma, S. Wang, Y. Shi, N. Koratkar, W. Ren, F. Li, and H.-M. Cheng, *A graphene foam electrode with high sulfur loading for flexible and high energy Li-S batteries*. Nano Energy, 2015. **11**(0): p. 356-365.
14. Eroglu, D., S. Ha, and K.G. Gallagher, *Fraction of the theoretical specific energy achieved on pack level for hypothetical battery chemistries*. Journal of Power Sources, 2014. **267**(0): p. 14-19.
15. Cheng, H. and K. Scott, *Improving performance of rechargeable Li-air batteries from using Li-Nafion® binder*. Electrochimica Acta, 2014. **116**(0): p. 51-58.
16. Li, L., Y. Fu, and A. Manthiram, *Imidazole-buffered acidic catholytes for hybrid Li-air batteries with high practical energy density*. Electrochemistry Communications, 2014. **47**(0): p. 67-70.
17. Lu, X., J.P. Lemmon, J.Y. Kim, V.L. Sprenkle, and Z. Yang, *High energy density Na-S/NiCl2 hybrid battery*. Journal of Power Sources, 2013. **224**(0): p. 312-316.

References

18. Wu, M., M. Liu, G. Long, K. Wan, Z. Liang, and T.S. Zhao, *A novel high-energy-density positive electrolyte with multiple redox couples for redox flow batteries*. Applied Energy, 2014. **136**(0): p. 576-581.
19. Nykvist, B. and M. Nilsson, *Rapidly falling costs of battery packs for electric vehicles*. Nature Climate Change, 2015.
20. Everywhere, E., *Grand Challenge Blueprint*. US Department of Energy, 2013.
21. Dinger, A., R. Martin, X. Mosquet, M. Rabl, D. Rizoulis, M. Russo, and G. Sticher, *Batteries for electric cars: Challenges, opportunities, and the outlook to 2020*. Boston Consulting Group, 2010.
22. Chang, T.-R., C.-S. Wang, and C.-C. Wang, *A systematic approach for green design in modular product development*. The International Journal of Advanced Manufacturing Technology, 2013. **68**(9): p. 2729-2741.
23. Fromm, P. and P. Drews, *Modular, service-oriented design and architecture of smart vehicles for short distance person and freight transport*. 1998. p. 2192-2197.
24. Yang, W.M., S.K. Chou, K.J. Chua, J. Li, and X. Zhao, *Research on modular micro combustor-radiator with and without porous media*. Chemical Engineering Journal, 2011. **168**(2): p. 799-802.
25. Rothgang, S., T. Baumhöfer, H. van Hoek, T. Lange, R.W. De Doncker, and D.U. Sauer, *Modular battery design for reliable, flexible and multi-technology energy storage systems*. Applied Energy, 2015. **137**(0): p. 931-937.
26. Baldwin, C.Y. and K.B. Clark, *Design Rules*. 1999, Cambridge, Ma: MIT Press.
27. Hwang, B.C., M. Fernandez Jose, V. Meadows, S. Thomas, and F. Amero Willard, *5534366 Modular battery pack*. Journal of Power Sources, 1997. **67**(1–2): p. 356.
28. Technology, V. *Valence Technology: the first scalable large lithium ion battery pack*. 2016; Available from: <https://www.valence.com/why-valence/modular/>.
29. Schmid, A. *Modular Li-Ion Battery Concept*. 2013; Available from: https://www.pkm.kit.edu/downloads/Datenblatt_Batteriekonzept_EN.pdf.
30. Arbizzani, C., G. Gabrielli, and M. Mastragostino, *Thermal stability and flammability of electrolytes for lithium-ion batteries*. Journal of Power Sources, 2011. **196**(10): p. 4801-4805.
31. Campion, C.L., W. Li, and B.L. Lucht, *Thermal decomposition of LiPF₆-based electrolytes for lithium-ion batteries*. Journal of The Electrochemical Society, 2005. **152**(12): p. A2327-A2334.
32. Doughty, D.H., P.C. Butler, R.G. Jungst, and E.P. Roth, *Lithium battery thermal models*. Journal of Power Sources, 2002. **110**(2): p. 357-363.
33. Jhu, C.-Y., Y.-W. Wang, C.-Y. Wen, C.-C. Chiang, and C.-M. Shu, *Self-reactive rating of thermal runaway hazards on 18650 lithium-ion batteries*. Journal of thermal analysis and calorimetry, 2011. **106**(1): p. 159-163.
34. Kim, G.-H., A. Pesaran, and R. Spotnitz, *A three-dimensional thermal abuse model for lithium-ion cells*. Journal of Power Sources, 2007. **170**(2): p. 476-489.
35. Lamb, J., C.J. Orendorff, L.A.M. Steele, and S.W. Spangler, *Failure propagation in multi-cell lithium ion batteries*. Journal of Power Sources, 2015. **283**: p. 517-523.
36. Spinner, N.S., C.R. Field, M.H. Hammond, B.A. Williams, K.M. Myers, A.L. Lubrano, S.L. Rose-Pehrsson, and S.G. Tuttle, *Physical and chemical analysis of lithium-ion battery cell-to-cell failure events inside custom fire chamber*. Journal of Power Sources, 2015. **279**: p. 713-721.
37. Rao, Z., S. Wang, M. Wu, Z. Lin, and F. Li, *Experimental investigation on thermal management of electric vehicle battery with heat pipe*. Energy Conversion and Management, 2013. **65**: p. 92-97.
38. Sato, N., *Thermal behavior analysis of lithium-ion batteries for electric and hybrid vehicles*. Journal of Power Sources, 2001. **99**(1–2): p. 70-77.
39. Arora, S., W. Shen, and A. Kapoor, *Designing a Robust Battery Pack for Electric Vehicles Using a Modified Parameter Diagram*. 2015, SAE Technical Paper.

40. Arvidsson, M., I. Gremyr, and T. Hasenkamp. *An operationalization of robust design methodology*. in *10th QMOD Conference. Quality Management and Organizational Development. Our Dreams of Excellence; 18-20 June; 2007 in Helsingborg; Sweden*. 2008. Linköping University Electronic Press.
41. Dotsinis, I. and Z. Kang, *Robust design of structures using optimization methods*. Computer Methods in Applied Mechanics and Engineering, 2004. **193**(23): p. 2221-2237.
42. Davis, T.P., *Science, engineering, and statistics*. Applied Stochastic Models in Business and Industry, 2006. **22**(5-6): p. 401-430.
43. Phadke, M.S., *Quality engineering using robust design*. 1995: Prentice Hall PTR.
44. Thornton, A.C., S. Donnelly, and B. Ertan, *More than just robust design: Why product development organizations still contend with variation and its impact on quality*. Research in Engineering Design - Theory, Applications, and Concurrent Engineering, 2000. **12**(3): p. 127-143.
45. Goodenough, J.B., H. Abruna, and M. Buchanan. *Basic research needs for electrical energy storage*. in *Report of the basic energy sciences workshop for electrical energy storage*. 2007.
46. Tarascon, J.-M. and M. Armand, *Issues and challenges facing rechargeable lithium batteries*. Nature, 2001. **414**(6861): p. 359-367.
47. Arvidsson, M. and I. Gremyr, *Principles of robust design methodology*. Quality and Reliability Engineering International, 2008. **24**(1): p. 23-35.
48. Gremyr, I., V. Siva, H. Raharjo, and T.N. Goh, *Adapting the Robust Design Methodology to support sustainable product development*. Journal of Cleaner Production, 2014. **79**: p. 231.
49. Chen, W., J.K. Allen, K.-L. Tsui, and F. Mistree, *A procedure for robust design: minimizing variations caused by noise factors and control factors*. Journal of mechanical design, 1996. **118**(4): p. 478-485.
50. Vairaktarakis, G.L., *Optimization tools for design and marketing of new/improved products using the house of quality*. Journal of Operations Management, 1999. **17**(6): p. 645-663.
51. Park, T. and K.J. Kim, *Determination of an optimal set of design requirements using house of quality*. Journal of Operations Management, 1998. **16**(5): p. 569-581.
52. Hendricks, C., N. Williard, S. Mathew, and M. Pecht, *A failure modes, mechanisms, and effects analysis (FMMEA) of lithium-ion batteries*. Journal of Power Sources, 2015. **297**: p. 113-120.
53. Chan, L.-K. and M.-L. Wu, *A systematic approach to quality function deployment with a full illustrative example*. Omega, 2005. **33**(2): p. 119-139.
54. Bergquist, K. and J. Abeysekera, *Quality function deployment (QFD)—A means for developing usable products*. International journal of industrial ergonomics, 1996. **18**(4): p. 269-275.
55. Govers, C.P., *What and how about quality function deployment (QFD)*. International journal of production economics, 1996. **46**: p. 575-585.
56. Li, Y.L., K.S. Chin, and X.G. Luo, *Determining the final priority ratings of customer requirements in product planning by MDBM and BSC*. Expert Systems with Applications, 2012. **39**(1): p. 1243-1255.
57. Jiang, H.M., C.K. Kwong, W.H. Ip, and T.C. Wong, *Modeling customer satisfaction for new product development using a PSO-based ANFIS approach*. Applied Soft Computing Journal, 2012. **12**(2): p. 726-734.
58. Hsu, C.-C. and B.A. Sandford, *The Delphi technique: making sense of consensus*. Practical assessment, research & evaluation, 2007. **12**(10): p. 1-8.
59. Hooper, J.M. and J. Marco, *Characterising the in-vehicle vibration inputs to the high voltage battery of an electric vehicle*. Journal of Power Sources, 2014. **245**: p. 510-519.
60. Hong, S.-K., B.I. Epureanu, and M.P. Castanier, *Parametric reduced-order models of battery pack vibration including structural variation and prestress effects*. Journal of Power Sources, 2014. **261**: p. 101.

References

61. Chacko, S. and Y.M. Chung, *Thermal modelling of Li-ion polymer battery for electric vehicle drive cycles*. Journal of Power Sources, 2012. **213**: p. 296-303.
62. Alaoui, C. and Z.M. Salameh, *A novel thermal management for electric and hybrid vehicles*. IEEE transactions on vehicular technology, 2005. **54**(2): p. 468-476.
63. Neubauer, J. and E. Wood, *The impact of range anxiety and home, workplace, and public charging infrastructure on simulated battery electric vehicle lifetime utility*. Journal of Power Sources, 2014. **257**: p. 12-20.
64. Kambly, K.R. and T.H. Bradley, *Estimating the HVAC energy consumption of plug-in electric vehicles*. Journal of Power Sources, 2014. **259**: p. 117-124.
65. Brodd, R.J., *Batteries for sustainability: selected entries from the encyclopedia of sustainability science and technology*. 2012: Springer Science & Business Media.
66. Marinaro, M., M. Weinberger, and M. Wohlfahrt-Mehrens, *Toward pre-lithiated high areal capacity silicon anodes for Lithium-ion batteries*. Electrochimica Acta, 2016. **206**: p. 99-107.
67. Liang, B., Y. Liu, and Y. Xu, *Silicon-based materials as high capacity anodes for next generation lithium ion batteries*. Journal of Power Sources, 2014. **267**: p. 469-490.
68. Yehezkel, S., M. Aunat, N. Sezin, D. Starosvetsky, and Y. Ein-Eli, *Bundled and densified carbon nanotubes (CNT) fabrics as flexible ultra-light weight Li-ion battery anode current collectors*. Journal of Power Sources, 2016. **312**: p. 109-115.
69. Hu, L., J.W. Choi, Y. Yang, S. Jeong, F. La Mantia, L.F. Cui, and Y. Cui, *Highly conductive paper for energy-storage devices*. Proceedings of the National Academy of Sciences of the United States of America, 2009. **106**(51): p. 21490-21494.
70. Kim, J.S., T.H. Hwang, B.G. Kim, J. Min, and J.W. Choi, *A lithium-sulfur battery with a high areal energy density*. Advanced Functional Materials, 2014. **24**(34): p. 5359-5367.
71. Kim, U.S., C.B. Shin, and C.-S. Kim, *Modeling for the scale-up of a lithium-ion polymer battery*. Journal of Power Sources, 2009. **189**(1): p. 841-846.
72. Pesaran, A.A., G.-H. Kim, and M. Keyser, *Integration issues of cells into battery packs for plug-in and hybrid electric vehicles*. in *Proceedings of the Hybrid and Fuel Cell Electric Vehicle Symposium on EVS-24 International Battery, Stavanger, Norway*. 2009. Citeseer.
73. Saw, L.H., Y. Ye, and A.A.O. Tay, *Integration issues of lithium-ion battery into electric vehicles battery pack*. Journal of Cleaner Production, 2016. **113**: p. 1032-1045.
74. Coleman, B., J. Ostanek, and J. Heinzel, *Reducing cell-to-cell spacing for large-format lithium ion battery modules with aluminum or PCM heat sinks under failure conditions*. Applied Energy, 2016. **180**: p. 14-26.
75. Center, N.-J.-J.S., *NASA JPG JSC 20793 REV C - CREWED SPACE VEHICLE BATTERY SAFETY REQUIREMENTS*. 2014, IEEE GlobalSpec.
76. Jeevarajan, J., C. Lopez, and J. Orieukwu, *Can Cell to Cell Thermal Runaway Propagation be Prevented in a Li-ion Battery Module?* 2014.
77. Jeevarajan, J., J. Orieukwu, and C. Lopez, *Preventing Cell-to-Cell Thermal Runaway in Lithium-Ion Battery Modules*, in *NASA Tech Briefs*. 2016.
78. Dittmann, J. and N. Willenbacher, *Micro structural investigations and mechanical properties of macro porous ceramic materials from capillary suspensions*. Journal of the American Ceramic Society, 2014. **97**(12): p. 3787-3792.
79. Bitsch, B., T. Gallasch, M. Schroeder, M. Börner, M. Winter, and N. Willenbacher, *Capillary suspensions as beneficial formulation concept for high energy density Li-ion battery electrodes*. Journal of Power Sources, 2016. **328**: p. 114-123.
80. ISO, *ISO/PAS 16898:2012 Electrically Propelled road vehicles — Dimensions and designation of secondary lithium-ion cells* 2012, ISO/TC 22/SC 37 Electrically propelled vehicles.
81. Andrea, D., *Battery management systems for large lithium-ion battery packs*. 2010: Artech house.
82. EnergyTechnologyNetwork, I. *BATTERY TECHNOLOGIES*. 2015 [cited 2017 April 15]; Available from: <http://www.ieahev.org/about-the-technologies/batteries/>.

83. Marino, A. *Audi e-tron Sportsback concept Arctitecture of e-mobility*. 2017 [cited 2017 May 05]; Available from: <https://www.driveandride.com/uk/audi-e-tron-sportback-concept/>.
84. Xia, Y., T. Wierzbicki, E. Sahraei, and X. Zhang, *Damage of cells and battery packs due to ground impact*. Journal of Power Sources, 2014. **267**: p. 78-97.
85. Kukreja, J., T. Nguyen, T. Siegmund, W. Chen, W. Tsutsui, K. Balakrishnan, H. Liao, and N. Parab, *Crash analysis of a conceptual electric vehicle with a damage tolerant battery pack*. Extreme Mechanics Letters.
86. Pesaran, A.A., S. Burch, M. Keyser, and E. Institut Mech Engineers; Institut Mech, *An approach for designing thermal management systems for electric and hybrid vehicle battery packs*. Vtms 4: Vehicle Thermal Management Systems. 1999. 331-346.
87. Arora, S., W. Shen, and A. Kapoor, *Review of mechanical design and strategic placement technique of a robust battery pack for electric vehicles*. Renewable and Sustainable Energy Reviews, 2016. **60**: p. 1319-1331.
88. Tom, M., *Volvo Questions EV Safety*. Ward's Auto World, 2011. **47**(2).
89. Hunt, G., *Electric Vehicle Battery Test Procedure Manual*. 2 ed. 1996, MI, USA: United States Advanced Battery Consortium.
90. Riley, R.Q., *Automobile Ride, handling and Suspension Designs*. 2011, Robert Q. Riley Enterprises, LLC: <http://www.rqriley.com/suspensn.htm>.
91. Lu, L., X. Han, J. Li, J. Hua, and M. Ouyang, *A review on the key issues for lithium-ion battery management in electric vehicles*. Journal of Power Sources, 2013. **226**: p. 272-288.
92. Stuart, T.A. and W. Zhu, *Modularized battery management for large lithium ion cells*. Journal of Power Sources, 2011. **196**(1): p. 458-464.
93. Pesaran, A.A. and M. Keyser, *Thermal characteristics of selected EV and HEV batteries*. Sixteenth Annual Battery Conference on Applications and Advances, ed. R.S.L. Das and H. Frank. 2001. 219-225.
94. Rao, Z. and S. Wang, *A review of power battery thermal energy management*. Renewable and Sustainable Energy Reviews, 2011. **15**(9): p. 4554-4571.
95. Peter, V.-D., *GM recalls Volts to fix fire risk*, in *THE COMEBACK OF THE AMERICAN CAR*. 2012: CNN Money.
96. Vellequette, L.P., *Battery test explosion injures five at GM lab*, in *Green Cars*. 2012: Automotive News.
97. Johnson, B., "Major explosion" at GM plant near Detroit. 2012: CBS News.
98. Charles, R., *Tesla dodges full investigation after fiery crash*. 2013: CNN Money (Hongkong).
99. Bullis, K., *What the Tesla Battery Fire Means for Electric Vehicles*, in *View, Global Edition*, MIT Technology Review. 2013.
100. Todd Sperry, C.N.N., *Electric car crashes could pose new risk for first responders, group says*. 2012: Cable News Network, U.S. Edition.
101. SAE, *Vehicle Electrification Standards*. 2014, SAE International: Standardsdev.
102. Terlep, S., *GM boosts Volt defense as sales falter.(Company overview)*. 2012: The Wall Street Journal Business.
103. Vlasic, B. and N. Bunkley, *A Setback for Electric Cars.(Business/Financial Desk)*. 2011: The New York Times Business Day.
104. Committee, E.V.F., *Recommended practice for packaging of electric vehicle battery modules*. 2008: Warrendale, Pa., : SAE International.
105. Levy, S.C., *Safety and reliability considerations for lithium batteries*. Journal of Power Sources, 1997. **68**(1): p. 75-77.
106. Patraboy, T.J., M.D. Farrington, and G.J. Donaldson, *Reliability of lithium batteries in search and rescue beacons*. Journal of Power Sources, 1997. **65**(1): p. 93-99.
107. Liaw, B.Y. and M. Dubarry, *From driving cycle analysis to understanding battery performance in real-life electric hybrid vehicle operation*. Journal of Power Sources, 2007. **174**(1): p. 76-88.

References

108. Balakrishnan, P.G., R. Ramesh, and T. Prem Kumar, *Safety mechanisms in lithium-ion batteries*. Journal of Power Sources, 2006. **155**(2): p. 401-414.
109. Al Hallaj, S., H. Maleki, J.S. Hong, and J.R. Selman, *Thermal modeling and design considerations of lithium-ion batteries*. Journal of Power Sources, 1999. **83**(1): p. 1-8.
110. Wang, Q., P. Ping, X. Zhao, G. Chu, J. Sun, and C. Chen, *Thermal runaway caused fire and explosion of lithium ion battery*. Journal of Power Sources, 2012. **208**: p. 210-224.
111. Jung, D.Y., B.H. Lee, and S.W. Kim, *Development of battery management system for nickel-metal hydride batteries in electric vehicle applications*. Journal of Power Sources, 2002. **109**(1): p. 1-10.
112. Larsson, F., P. Andersson, P. Blomqvist, A. Lorén, and B.-E. Mellander, *Characteristics of lithium-ion batteries during fire tests*. Journal of Power Sources, 2014. **271**: p. 414-420.
113. Avdeev, I. and M. Gilaki, *Structural analysis and experimental characterization of cylindrical lithium-ion battery cells subject to lateral impact*. Journal of Power Sources, 2014. **271**: p. 382-391.
114. Frey; Paul (Portola Valley, C., Grace; Dustin (San Carlos, CA), *Battery pack exhaust nozzle utilizing an SMA seal retainer* 2013, Tesla Motors, Inc. (Palo Alto, CA) USA.
115. Lai, W.-J., M.Y. Ali, and J. Pan, *Mechanical behavior of representative volume elements of lithium-ion battery cells under compressive loading conditions*. Journal of Power Sources, 2014. **245**: p. 609-623.
116. Hermann; Weston Arthur (Palo Alto, C., *Rigid cell separator for minimizing thermal runaway propagation within a battery pack* 2012, Tesla Motors, Inc. (Palo Alto, CA) USA.
117. Maguire, P.D., S. Paramasivam, J.G. Gebbie, and B. Utley, *Battery cell separator*. 2014, Google Patents.
118. Higashino; Tatsuya (Yokohama, J., Saito; Kazuo (Yokohama, JP), Motohashi; Toshiyuki (Saitama, JP), *Battery pack with covering member and vehicle with the battery pack* 2009, Nissan Motor Co., Ltd. (Yokohama-shi, JP) USA.
119. Maguire, P.D., S. Paramasivam, and H. Addanki, *Battery assembly with gas discharge mechanism*. 2014, Google Patents.
120. Watanabe, K. and H. Horie, *Battery pack*. 2003, Google Patents.
121. Watanabe, K., H. Sato, K. Hosaka, and H. Horie, *Battery structure*. 2012, Google Patents.
122. Watanabe, K., T. Abe, T. Saito, O. Shimamura, K. Hosaka, H. Sato, and H. Horie, *Battery structure, assembled battery, and vehicle mounting these thereon*. 2012, Google Patents.
123. Zhou; Shijian (Rochester Hills, M., Husted; Clinton Chandler (Noblesville, IN), Benjamin; Frances A. (Indianapolis, IN), *Battery pack arrangements*. 2004, General Motors Corporation (Detroit, MI) USA.
124. Iwasa; Makoto (Chigasaki, J., Ogata; Shinya (Ebina, JP), Kadota; Hidetoshi (Yamato, JP), Hashimura; Tadayoshi (Machida, JP), Mori; Nobuhiro (Odawara, JP), *Vehicle battery mounting structure* 2010, Nissan Motor Co., Ltd. (Yokohama-shi, JP) USA.
125. *Surface vehicle two line text : (R) recommended practice for electric, fuel cell and hybrid electric vehicle crash integrity testing. (R) recommended practice for electric, fuel cell and hybrid electric vehicle crash integrity testing*, ed. E. Society of Automotive. 2014, Warrendale, Pa.: Warrendale, Pa. : SAE International.
126. Mathews, J., A.J. Carothers, P. Maguire, L.A. Shaner, and D. Zhu, *Battery mounting system for automotive vehicle*. 2006, Google Patents.
127. Charbonneau; Alexi (Redondo Beach, C., Burgess; Malcolm (Mountain View, CA), Attaluri; Vivek (Union City, CA), Gadhiya; Hitendra Laxmidas (Irvine, CA), Clarke; Alan Paul (Redondo Beach, CA), Rawlinson; Peter Dore (Worcestershire, GB), Sumpf, Jr.; Robert David (San Francisco, CA), Edwards; Bruce Philip (Menlo Park, CA), *System for absorbing and distributing side impact energy utilizing an integrated battery pack and side sill assembly*. 2012, Tesla Motors, Inc. (Palo Alto, CA): USA.
128. Lucas, M., *Structural battery duct assembly*. 2012, Google Patents.

129. Rawlinson, P.D. and H.L. Gadhiya, *Front rail configuration for the front structure of a vehicle*. 2013, Google Patents.
130. America, N.N. *Nissan Leaf Battery Pack*. [cited 2014 20/05]; Available from: <http://www.nissan-global.com>.
131. Shindou; Tatsuya (Atsugi, J., *Carrying structure for a vehicle battery pack* 2007, Nissan Motor Co., Ltd. (Yokohama-shi, Kanagawa, JP) USA.
132. Rader, R., *Safety now comes in green: 1st crash tests of electric cars*. 2011.
133. GORDON-BLOOMFIELD, N., *Nissan LEAF Electric Car Battery Pack Proves 99.9 Reliable, Busts Battery Replacement Myth*, in *TransportEvolved*. 2015, LITTLECOLLIE LTD.
134. Ottaway, L., *What makes Tesla's batteries so great?*, in *Torque News*. 2014, TorqueNews.
135. FINLEY, R., *Nissan Leaf Drive Train is 25 Times More Reliable than Conventional Cars*, in *Energy Trends Report*. 2015, Energy Trends Insider.
136. Rogowsky, M., *Rants Aside, The Volt is Actually Earning Raves -- And it's a Hit*, in *ForbesTech*. 2012, Forbes.
137. E.V., D.I.F.N., *Electrically propelled road vehicles - Battery systems - Dimensions for Lithium-Ion-Cells*. 2011, DIN SPEC 91252.
138. ISO, *Electric propelled road vehicles – Dimensions and designation of secondary lithium-ion cell*. 2012, ISO/IEC PAS 16898: Switzerland.
139. Matthe, R., L. Turner, and H. Mettlach, *VOLTEC battery system for electric vehicle with extended range*. SAE International Journal of Engines, 2011. **4**(2011-01-1373): p. 1944-1962.
140. Parrish, R., Elankumaran, K., Gandhi, M., Nance, B., Meehan, P., Milburn, D., Siddiqui, S., Brenz, A., *Voltec Battery Design and Manufacturing*. SAE International Electrification Series, 2011: p. 41-50.
141. Brooke, L., *Chevrolet Volt--Development Story of the Pioneering Electrified Vehicle*. Training, 2011. **2012**: p. 03-12.
142. Chambers, N., *Chevy Volt and Nissan LEAF Earn Top Marks on Crash Tests*, in *PluginCars*. 2011, Recargo, Inc.
143. Spotnitz, R. and J. Franklin, *Abuse behavior of high-power, lithium-ion cells*. Journal of Power Sources, 2003. **113**(1): p. 81-100.
144. Lin, C., S. Xu, G. Chang, and J. Liu, *Experiment and simulation of a LiFePO₄ battery pack with a passive thermal management system using composite phase change material and graphite sheets*. Journal of Power Sources, 2015. **275**: p. 742-749.
145. Zhu, C., X. Li, L. Song, and L. Xiang, *Development of a theoretically based thermal model for lithium ion battery pack*. Journal of Power Sources, 2013. **223**: p. 155-164.
146. MacNeil, D.D., D. Larcher, and J.R. Dahn, *Comparison of the reactivity of various carbon electrode materials with electrolyte at elevated temperature*. Journal of the Electrochemical Society, 1999. **146**(10): p. 3596-3602.
147. Suh, I.S., H. Cho, and M. Lee, *Feasibility study on thermoelectric device to energy storage system of an electric vehicle*. Energy, 2014. **76**: p. 436-444.
148. Kim, H., S.-G. Park, B. Jung, J. Hwang, and W. Kim, *New device architecture of a thermoelectric energy conversion for recovering low-quality heat*. Applied Physics A, 2014. **114**(4): p. 1201-1208.
149. Bandhauer, T.M., S. Garimella, and T.F. Fuller, *A critical review of thermal issues in lithium-ion batteries*. Journal of the Electrochemical Society, 2011. **158**(3): p. R1-R25.
150. Nagasubramanian, G., *Electrical characteristics of 18650 Li-ion cells at low temperatures*. Journal of Applied Electrochemistry, 2001. **31**(1): p. 99-104.
151. Zhang, S., K. Xu, and T. Jow, *The low temperature performance of Li-ion batteries*. Journal of Power Sources, 2003. **115**(1): p. 137-140.
152. Ehrlich, G.M., *Handbook of batteries*. McGraw-Hill, NY and London, 2002.

References

153. Smart, M.C., B.V. Ratnakumar, and S. Surampudi, *Electrolytes for Low-Temperature Lithium Batteries Based on Ternary Mixtures of Aliphatic Carbonates*. Journal of the Electrochemical Society, 1999. **146**(2): p. 486-492.
154. Ratnakumar, B.V., M.C. Smart, and S. Surampudi, *Effects of SEI on the kinetics of lithium intercalation*. 10th International Meeting on Lithium Batteries, 2001. **97-98**: p. 137-139.
155. Lin, H.P., D. Chua, M. Salomon, H.C. Shiao, M. Hendrickson, E. Plichta, and S. Slane, *Low-temperature behavior of Li-ion cells*. Electrochemical and Solid-State Letters, 2001. **4**(6): p. A71-A73.
156. Zhang, S.S., K. Xu, and T.R. Jow, *Low-temperature performance of Li-ion cells with a LiBF₄-based electrolyte*. Journal of Solid State Electrochemistry, 2003. **7**(3): p. 147-151.
157. Wang, C., A.J. Appleby, and F.E. Little, *Low-temperature characterization of lithium-ion carbon Anodes via microperturbation measurement*. Journal of the Electrochemical Society, 2002. **149**(6): p. A754-A760.
158. Blomgren, G.E., *Electrolytes for advanced batteries*. Journal of Power Sources, 1999. **81-82**: p. 112-118.
159. Joho, F., B. Rykart, R. Imhof, P. Novák, M.E. Spahr, and A. Monnier, *Key factors for the cycling stability of graphite intercalation electrodes for lithium-ion batteries*. Journal of Power Sources, 1999. **81-82**: p. 243-247.
160. Abe, K., H. Yoshitake, T. Kitakura, T. Hattori, H. Wang, and M. Yoshio, *Additives-containing functional electrolytes for suppressing electrolyte decomposition in lithium-ion batteries*. Electrochimica Acta, 2004. **49**(26): p. 4613-4622.
161. Amatucci, G., A. Du Pasquier, A. Blyr, T. Zheng, and J.-M. Tarascon, *The elevated temperature performance of the LiMn₂O₄/C system: failure and solutions*. Electrochimica Acta, 1999. **45**(1): p. 255-271.
162. Vetter, J., P. Novák, M.R. Wagner, C. Veit, K.C. Möller, J.O. Besenhard, M. Winter, M. Wohlfahrt-Mehrens, C. Vogler, and A. Hammouche, *Ageing mechanisms in lithium-ion batteries*. Journal of Power Sources, 2005. **147**(1-2): p. 269-281.
163. Petibon, R., J. Harlow, D.B. Le, and J.R. Dahn, *The use of ethyl acetate and methyl propanoate in combination with vinylene carbonate as ethylene carbonate-free solvent blends for electrolytes in Li-ion batteries*. Electrochimica Acta, 2015. **154**: p. 227-234.
164. Smart, M.C., B.V. Ratnakumar, K.B. Chin, and L.D. Whitcanack, *Lithium-ion electrolytes containing ester cosolvents for improved low temperature performance*. Journal of the Electrochemical Society, 2010. **157**(12): p. A1361-A1374.
165. Zhou, L., M. Xu, and B.L. Lucht, *Performance of lithium tetrafluorooxalatophosphate in methyl butyrate electrolytes*. Journal of Applied Electrochemistry, 2013. **43**(5): p. 497-505.
166. Herreyre, S., O. Huchet, S. Barusseau, F. Perton, J.M. Bodet, and P. Biensan, *New Li-ion electrolytes for low temperature applications*. 10th International Meeting on Lithium Batteries, 2001. **97-98**: p. 576-580.
167. Plichta, E.J. and W.K. Behl, *Low-temperature electrolyte for lithium and lithium-ion batteries*. Journal of Power Sources, 2000. **88**(2): p. 192-196.
168. Ji, Y., Y. Zhang, and C.Y. Wang, *Li-ion cell operation at low temperatures*. Journal of the Electrochemical Society, 2013. **160**(4): p. A636-A649.
169. Yang, B., H. Zhang, L. Yu, W. Fan, and D. Huang, *Lithium difluorophosphate as an additive to improve the low temperature performance of LiNi_{0.5}Co_{0.2}Mn_{0.3}O₂/graphite cells*. Electrochimica Acta, 2016. **221**: p. 107-114.
170. Smart, M.C., B.L. Lucht, S. Dalavi, F.C. Krause, and B.V. Ratnakumar, *The Effect of Additives upon the Performance of MCMB/LiNixCo_{1-x}O₂ Li-Ion Cells Containing Methyl Butyrate-Based Wide Operating Temperature Range Electrolytes*. Journal of The Electrochemical Society, 2012. **159**(6): p. A739-A751.

171. Niedzicki, L., S. Grugeon, S. Laruelle, P. Judeinstein, M. Bukowska, J. Prejzner, P. Szczeciński, W. Wieczorek, and M. Armand, *New covalent salts of the 4+ V class for Li batteries*. Journal of Power Sources, 2011. **196**(20): p. 8696-8700.
172. Xu, K., S. Zhang, and T.R. Jow, *LiBOB as additive in LiPF₆-based lithium ion electrolytes*. Electrochemical and Solid-State Letters, 2005. **8**(7): p. A365-A368.
173. Lazar, M.L. and B.L. Lucht, *Carbonate free electrolyte for lithium ion batteries containing γ-butyrolactone and methyl butyrate*. Journal of the Electrochemical Society, 2015. **162**(6): p. A928-A934.
174. Li, S., W. Zhao, Z. Zhou, X. Cui, Z. Shang, H. Liu, and D. Zhang, *Studies on electrochemical performances of novel electrolytes for wide-temperature-range lithium-ion batteries*. ACS Applied Materials and Interfaces, 2014. **6**(7): p. 4920-4926.
175. Groot, J., *State-of-health estimation of li-ion batteries: Cycle life test methods*. 2012.
176. Kong, F., R. Kostecki, G. Nadeau, X. Song, K. Zaghib, K. Kinoshita, and F. McLarnon, *In situ studies of SEI formation*. Journal of power sources, 2001. **97**: p. 58-66.
177. Richard, M.N. and J.R. Dahn, *Accelerating rate calorimetry study on the thermal stability of lithium intercalated graphite in electrolyte. I. Experimental*. Journal of the Electrochemical Society, 1999. **146**(6): p. 2068-2077.
178. Yang, H., S. Amiruddin, H. Bang, Y. Sun, and J. Prakash, *A review of Li-Ion cell chemistries and their potential use in hybrid electric vehicles*, in *J. Ind. Eng. Chem.* 2006. p. 12-38.
179. Abraham, D.P., E.P. Roth, R. Kostecki, K. McCarthy, S. MacLaren, and D.H. Doughty, *Diagnostic examination of thermally abused high-power lithium-ion cells*. Journal of Power Sources, 2006. **161**(1): p. 648-657.
180. Lisbona, D. and T. Snee, *A review of hazards associated with primary lithium and lithium-ion batteries*. Process Safety and Environmental Protection, 2011. **89**(6): p. 434-442.
181. Yang, H., S. Amiruddin, H.J. Bang, Y.-K. Sun, and J. Prakash, *A review of Li-ion cell chemistries and their potential use in hybrid electric vehicles*. Journal of industrial and engineering chemistry, 2006. **12**(1): p. 12-38.
182. Ross, P.E. *Boeing's Battery Blues*. 2013.
183. Etacheri, V., R. Marom, R. Elazari, G. Salitra, and D. Aurbach, *Challenges in the development of advanced Li-ion batteries: a review*. Energy & Environmental Science, 2011. **4**(9): p. 3243-3262.
184. MacNeil, D.D., Z. Lu, Z. Chen, and J.R. Dahn, *A comparison of the electrode/electrolyte reaction at elevated temperatures for various Li-ion battery cathodes*. Journal of Power Sources, 2002. **108**(1-2): p. 8-14.
185. Zhang, J., R. Gao, L. Sun, H. Zhang, Z. Hu, and X. Liu, *Unraveling the multiple effects of Li₂ZrO₃ coating on the structural and electrochemical performances of LiCoO₂ as high-voltage cathode materials*. Electrochimica Acta, 2016. **209**: p. 102-110.
186. Ji, Y. and C.Y. Wang, *Heating strategies for Li-ion batteries operated from subzero temperatures*. Electrochimica Acta, 2013. **107**: p. 664-674.
187. Zhang, S., K. Xu, and T. Jow, *Charge and discharge characteristics of a commercial LiCoO₂-based 18650 Li-ion battery*. Journal of Power Sources, 2006. **160**(2): p. 1403-1409.
188. Nakayama, Y., M. Mitsui, Y. Kikuchi, and K. Tojima, *Apparatus for controlling state of charge/discharge of hybrid car and method for controlling state of charge/discharge of hybrid car*. 2000, Google Patents.
189. Zhu, D., J. Mathews, B. Taenaka, and P. Maguire, *Method and system for a vehicle battery temperature control*. 2006, Google Patents.
190. Horie, H. and Y. Ohsawa, *Battery system with excellent controllability for temperature*. 2007, Google Patents.
191. Pesaran, A., A. Vlahinos, and T. Stuart. *Cooling and preheating of batteries in hybrid electric vehicles*. in *6th ASME-JSME Thermal Engineering Joint Conference*. 2003. Citeseer.

References

192. Vlahinos, A. and A.A. Pesaran, *Energy efficient battery heating in cold climates*. 2002, SAE Technical Paper.
193. Stuart, T. and A. Hande, *HEV battery heating using AC currents*. Journal of Power Sources, 2004. **129**(2): p. 368-378.
194. Mahamud, R. and C. Park, *Reciprocating air flow for Li-ion battery thermal management to improve temperature uniformity*. Journal of Power Sources, 2011. **196**(13): p. 5685-5696.
195. Li, X., F. He, and L. Ma, *Thermal management of cylindrical batteries investigated using wind tunnel testing and computational fluid dynamics simulation*. Journal of Power Sources, 2013. **238**: p. 395-402.
196. Xu, X.M. and R. He, *Research on the heat dissipation performance of battery pack based on forced air cooling*. Journal of Power Sources, 2013. **240**: p. 33-41.
197. Fan, L., J.M. Khodadadi, and A.A. Pesaran, *A parametric study on thermal management of an air-cooled lithium-ion battery module for plug-in hybrid electric vehicles*. Journal of Power Sources, 2013. **238**: p. 301-312.
198. Park, H., *A design of air flow configuration for cooling lithium ion battery in hybrid electric vehicles*. Journal of Power Sources, 2013. **239**: p. 30-36.
199. Giuliano, M.R., A.K. Prasad, and S.G. Advani, *Experimental study of an air-cooled thermal management system for high capacity lithium-titanate batteries*. Journal of Power Sources, 2012. **216**: p. 345-352.
200. Lou, Y., *Nickel-metal hydride battery cooling system research for hybrid electric vehicle*. Shanghai Jiao Tong University, Shanghai, 2007.
201. Jaura, A.K. and C.-W. Park, *Battery system for automotive vehicle*. 2007, Google Patents.
202. He, F. and L. Ma, *Thermal management of batteries employing active temperature control and reciprocating cooling flow*. International Journal of Heat and Mass Transfer, 2015. **83**: p. 164-172.
203. He, F., H. Wang, and L. Ma, *Experimental demonstration of active thermal control of a battery module consisting of multiple Li-ion cells*. International Journal of Heat and Mass Transfer, 2015. **91**: p. 630-639.
204. Wu, M.S., K.H. Liu, Y.Y. Wang, and C.C. Wan, *Heat dissipation design for lithium-ion batteries*. Journal of Power Sources, 2002. **109**(1): p. 160-166.
205. Nelson, P., D. Dees, K. Amine, and G. Henriksen, *Modeling thermal management of lithium-ion PNGV batteries*. Journal of Power Sources, 2002. **110**(2): p. 349-356.
206. Pendergast, D.R., E.P. Demauro, M. Fletcher, E. Stimson, and J.C. Mollendorf, *A rechargeable lithium-ion battery module for underwater use*. Journal of Power Sources, 2011. **196**(2): p. 793-800.
207. Pesaran, A.A., *Battery thermal management in EV and HEVs: issues and solutions*. Battery Man, 2001. **43**(5): p. 34-49.
208. Pesaran, A.A., S. Burch, and M. Keyser, *An approach for designing thermal management systems for electric and hybrid vehicle battery packs*. Proceedings of the 4th Vehicle Thermal Management Systems, 1999: p. 24-27.
209. Kim, G. and A. Pesaran. *22nd International Battery*. in *Hybrid and Fuel Cell Electric Vehicle Conference and Exhibition, Yokohama, Japan*. 2006.
210. Jarrett, A. and I.Y. Kim, *Design optimization of electric vehicle battery cooling plates for thermal performance*. Journal of Power Sources, 2011. **196**(23): p. 10359-10368.
211. Fisher, T.S. and K.E. Torrance, *Optimal shapes of fully embedded channels for conjugate cooling*. IEEE Transactions on Advanced Packaging, 2001. **24**(4): p. 555-562.
212. Fisher, T. and K. Torrance, *Constrained optimal duct shapes for conjugate laminar forced convection*. International journal of heat and mass transfer, 2000. **43**(1): p. 113-126.
213. Yu, S.H., S. Sohn, J.H. Nam, and C.J. Kim, *Numerical study to examine the performance of multi-pass serpentine flow-fields for cooling plates in polymer electrolyte membrane fuel cells*. Journal of Power Sources, 2009. **194**(2): p. 697-703.

214. Choi, J., Y.H. Kim, Y. Lee, K.J. Lee, and Y. Kim, *Numerical analysis on the performance of cooling plates in a PEFC*. Journal of Mechanical Science and Technology, 2008. **22**(7): p. 1417-1425.
215. Chen, F.C., Z. Gao, R.O. Loutfy, and M. Hecht, *Analysis of Optimal Heat Transfer in a PEM Fuel Cell Cooling Plate*. Fuel Cells, 2003. **3**(4): p. 181-188.
216. Jin, L.W., P.S. Lee, X.X. Kong, Y. Fan, and S.K. Chou, *Ultra-thin minichannel LCP for EV battery thermal management*. Applied Energy, 2014. **113**: p. 1786-1794.
217. Huo, Y., Z. Rao, X. Liu, and J. Zhao, *Investigation of power battery thermal management by using mini-channel cold plate*. Energy Conversion and Management, 2015. **89**: p. 387-395.
218. Pipe.nl, H. Dutch knowledge center for heat pipe technology - The basics. 2010 [cited 2017 April 25]; Available from: <http://www.heatpipe.nl/index.php?page=heatpipe&lang=EN>.
219. Mahefkey, E. and M. Kreitman, *An Intercell Planar Heat Pipe for the Removal of Heat During the Cycling of a High Rate Nickel Cadmium Battery*. Journal of The Electrochemical Society, 1971. **118**(8): p. 1382-1386.
220. ZHANG, G., Z. WU, Z. RAO, and L. FU, *Experimental investigation on heat pipe cooling effect for power battery [J]*. Chemical Industry and Engineering Progress, 2009. **7**: p. 013.
221. Swanepoel, G., *Thermal management of hybrid electrical vehicles using heat pipes*. 2001, University of Stellenbosch.
222. Wu, M.-S., K. Liu, Y.-Y. Wang, and C.-C. Wan, *Heat dissipation design for lithium-ion batteries*. Journal of power sources, 2002. **109**(1): p. 160-166.
223. Jang, J.-C. and S.-H. Rhi, *Battery thermal management system of future electric vehicles with loop thermosyphon*. in US-Korea conference on science, technology, and entrepreneurship (UKC). 2010.
224. Connors, M.J. and J.A. Zunner, *The use of vapor chambers and heat pipes for cooling military embedded electronic devices*. in Military Communications Conference, 2009. MILCOM 2009. IEEE. 2009. IEEE.
225. Guo, C., X. Hu, W. Cao, D. Yu, and D. Tang, *Effect of mechanical vibration on flow and heat transfer characteristics in rectangular microgrooves*. Applied Thermal Engineering, 2013. **52**(2): p. 385-393.
226. Thompson, S.M., Z.S. Aspin, N. Shamsaei, A. Elwany, and L. Bian, *Additive manufacturing of heat exchangers: A case study on a multi-layered Ti-6Al-4V oscillating heat pipe*. Additive Manufacturing, 2015. **8**: p. 163-174.
227. Ameli, M., B. Agnew, P.S. Leung, B. Ng, C. Sutcliffe, J. Singh, and R. McGlen, *A novel method for manufacturing sintered aluminium heat pipes (SAHP)*. Applied Thermal Engineering, 2013. **52**(2): p. 498-504.
228. Chen, Y.-T., S.-W. Kang, Y.-H. Hung, C.-H. Huang, and K.-C. Chien, *Feasibility study of an aluminum vapor chamber with radial grooved and sintered powders wick structures*. Applied Thermal Engineering, 2013. **51**(1): p. 864-870.
229. Ibrahim, O.T., J.G. Monroe, S.M. Thompson, N. Shamsaei, H. Bilheux, A. Elwany, and L. Bian, *An investigation of a multi-layered oscillating heat pipe additively manufactured from Ti-6Al-4V powder*. International Journal of Heat and Mass Transfer, 2017. **108**: p. 1036-1047.
230. Al Hallaj, S. and J. Selman, *A Novel Thermal Management System for Electric Vehicle Batteries Using Phase - Change Material*. Journal of the Electrochemical Society, 2000. **147**(9): p. 3231-3236.
231. Hallaj, S.A. and J.R. Selman, *Thermal management of battery systems*. 2002, Google Patents.
232. Khateeb, S.A., M.M. Farid, J.R. Selman, and S. Al-Hallaj, *Design and simulation of a lithium-ion battery with a phase change material thermal management system for an electric scooter*. Journal of Power Sources, 2004. **128**(2): p. 292-307.
233. Mills, A. and S. Al-Hallaj, *Simulation of passive thermal management system for lithium-ion battery packs*. Journal of Power Sources, 2005. **141**(2): p. 307-315.

References

234. Sabbah, R., R. Kizilel, J.R. Selman, and S. Al-Hallaj, *Active (air-cooled) vs. passive (phase change material) thermal management of high power lithium-ion packs: Limitation of temperature rise and uniformity of temperature distribution*. Journal of Power Sources, 2008. **182**(2): p. 630-638.
235. Kizilel, R., A. Lateef, R. Sabbah, M.M. Farid, J.R. Selman, and S. Al-Hallaj, *Passive control of temperature excursion and uniformity in high-energy Li-ion battery packs at high current and ambient temperature*. Journal of Power Sources, 2008. **183**(1): p. 370-375.
236. Rao, Z., S. Wang, and G. Zhang, *Simulation and experiment of thermal energy management with phase change material for ageing LiFePO₄ power battery*. Energy Conversion and Management, 2011. **52**(12): p. 3408-3414.
237. Li, W., Z. Qu, Y. He, and Y. Tao, *Experimental study of a passive thermal management system for high-powered lithium ion batteries using porous metal foam saturated with phase change materials*. Journal of power sources, 2014. **255**: p. 9-15.
238. Alrashdan, A., A.T. Mayyas, and S. Al-Hallaj, *Thermo-mechanical behaviors of the expanded graphite-phase change material matrix used for thermal management of Li-ion battery packs*. Journal of Materials Processing Technology, 2010. **210**(1): p. 174-179.
239. Fan, L. and J.M. Khodadadi, *Thermal conductivity enhancement of phase change materials for thermal energy storage: a review*. Renewable and Sustainable Energy Reviews, 2011. **15**(1): p. 24-46.
240. Shatikian, V., G. Ziskind, and R. Letan, *Numerical investigation of a PCM-based heat sink with internal fins: constant heat flux*. International Journal of Heat and Mass Transfer, 2008. **51**(5): p. 1488-1493.
241. Agyenim, F., P. Eames, and M. Smyth, *A comparison of heat transfer enhancement in a medium temperature thermal energy storage heat exchanger using fins*. Solar Energy, 2009. **83**(9): p. 1509-1520.
242. Nakaso, K., H. Teshima, A. Yoshimura, S. Nogami, Y. Hamada, and J. Fukai, *Extension of heat transfer area using carbon fiber cloths in latent heat thermal energy storage tanks*. Chemical Engineering and Processing: Process Intensification, 2008. **47**(5): p. 879-885.
243. Ettoney, H., I. Alatiqi, M. Al-Sahali, and K. Al-Hajirie, *Heat transfer enhancement in energy storage in spherical capsules filled with paraffin wax and metal beads*. Energy Conversion and Management, 2006. **47**(2): p. 211-228.
244. Ling, Z., J. Chen, X. Fang, Z. Zhang, T. Xu, X. Gao, and S. Wang, *Experimental and numerical investigation of the application of phase change materials in a simulative power batteries thermal management system*. Applied Energy, 2014. **121**: p. 104-113.
245. Mills, A., M. Farid, J. Selman, and S. Al-Hallaj, *Thermal conductivity enhancement of phase change materials using a graphite matrix*. Applied Thermal Engineering, 2006. **26**(14): p. 1652-1661.
246. Zhang, Z. and X. Fang, *Study on paraffin/expanded graphite composite phase change thermal energy storage material*. Energy Conversion and Management, 2006. **47**(3): p. 303-310.
247. Li, W., Z. Qu, Y. He, and W. Tao, *Experimental and numerical studies on melting phase change heat transfer in open-cell metallic foams filled with paraffin*. Applied Thermal Engineering, 2012. **37**: p. 1-9.
248. Zhao, C.-Y., W. Lu, and Y. Tian, *Heat transfer enhancement for thermal energy storage using metal foams embedded within phase change materials (PCMs)*. Solar Energy, 2010. **84**(8): p. 1402-1412.
249. Lafdi, K., O. Mesalhy, and S. Shaikh, *Experimental study on the influence of foam porosity and pore size on the melting of phase change materials*. Journal of Applied Physics, 2007. **102**(8): p. 083549.
250. Zhou, D. and C.Y. Zhao, *Experimental investigations on heat transfer in phase change materials (PCMs) embedded in porous materials*. Applied Thermal Engineering, 2011. **31**(5): p. 970-977.

251. Xiao, X., P. Zhang, and M. Li, *Preparation and thermal characterization of paraffin/metal foam composite phase change material*. Applied energy, 2013. **112**: p. 1357-1366.
252. Wang, H., F. Wang, Z. Li, Y. Tang, B. Yu, and W. Yuan, *Experimental investigation on the thermal performance of a heat sink filled with porous metal fiber sintered felt/paraffin composite phase change material*. Applied Energy, 2016. **176**: p. 221-232.
253. Chen, P., X. Gao, Y. Wang, T. Xu, Y. Fang, and Z. Zhang, *Metal foam embedded in SEBS/paraffin/HDPE form-stable PCMs for thermal energy storage*. Solar Energy Materials and Solar Cells, 2016. **149**: p. 60-65.
254. Hussain, A., C.Y. Tso, and C.Y. Chao, *Experimental investigation of a passive thermal management system for high-powered lithium ion batteries using nickel foam-paraffin composite*. Energy, 2016. **115**: p. 209-218.
255. Goli, P., S. Legedza, A. Dhar, R. Salgado, J. Renteria, and A.A. Balandin, *Graphene-enhanced hybrid phase change materials for thermal management of Li-ion batteries*. Journal of Power Sources, 2014. **248**: p. 37-43.
256. Babapoor, A., M. Azizi, and G. Karimi, *Thermal management of a Li-ion battery using carbon fiber-PCM composites*. Applied Thermal Engineering, 2015. **82**: p. 281-290.
257. Frusteri, F., V. Leonardi, S. Vasta, and G. Restuccia, *Thermal conductivity measurement of a PCM based storage system containing carbon fibers*. Applied Thermal Engineering, 2005. **25**(11): p. 1623-1633.
258. Wang, W., X. Yang, Y. Fang, J. Ding, and J. Yan, *Enhanced thermal conductivity and thermal performance of form-stable composite phase change materials by using β -Aluminum nitride*. Applied Energy, 2009. **86**(7): p. 1196-1200.
259. Khateeb, S.A., S. Amiruddin, M. Farid, J.R. Selman, and S. Al-Hallaj, *Thermal management of Li-ion battery with phase change material for electric scooters: experimental validation*. Journal of Power Sources, 2005. **142**(1): p. 345-353.
260. Gaultois, M., *From trash to treasure: Making electricity from waste heat*, in *The Global Scientist*, L. Williams, Editor. 2014.
261. Thielmann, J., *Thermoelectric Cooling Technology*. Will Peltier Modules Supersede the Compressor, 2013.
262. Corporation, T. *Thermoelectric Cooling & Heating*. 2017 [cited 2017 January 06]; Available from: <https://www.tellurex.com/services/thermoelectric-heating-cooling/>.
263. Corporation, F.-N. *Peltier Device: A Single Device Used for Cooling and Heating*. 2015 [cited 2017 January 06]; Available from: <https://ferrotecnordcorporation.wordpress.com/2015/12/03/peltier-device-a-single-device-used-for-cooling-and-heating/>.
264. Cosnier, M., G. Fraisse, and L. Luo, *An experimental and numerical study of a thermoelectric air-cooling and air-heating system*. International Journal of Refrigeration, 2008. **31**(6): p. 1051-1062.
265. Miranda, A., T. Chen, and C. Hong, *Feasibility study of a green energy powered thermoelectric chip based air conditioner for electric vehicles*. Energy, 2013. **59**: p. 633-641.
266. Suh, I.-S., H. Cho, and M. Lee, *Feasibility study on thermoelectric device to energy storage system of an electric vehicle*. Energy, 2014. **76**: p. 436-444.
267. Rowe, D. and H. Goldsmid, *A new upper limit to the thermoelectric figure-of-merit*, in *Thermoelectrics Handbook: Macro to Nano*. 2005, CRC Press. p. 10-1-10-10.
268. Bell, L.E., J. LaGrandeur, and S. Davis, *Battery thermal management system including thermoelectric assemblies in thermal communication with a battery*. 2015, Google Patents.
269. Tijani, M.E.H., J.C.H. Zeegers, and A.T.A.M. de Waele, *Construction and performance of a thermoacoustic refrigerator*. Cryogenics, 2002. **42**(1): p. 59-66.
270. Verma, S.S., *Eco-friendly alternative refrigeration systems*. Resonance, 2001. **6**(11): p. 63-67.
271. Tassou, S.A., J.S. Lewis, Y.T. Ge, A. Hadaway, and I. Chaer, *A review of emerging technologies for food refrigeration applications*, in *Appl. Therm. Eng.* 2010. p. 263-276.

References

272. Garrett, S.L. and T.J. Hofler, *Thermoacoustic refrigeration*. 1991.
273. Paek, I., J.E. Braun, and L. Mongeau, *Evaluation of standing-wave thermoacoustic cycles for cooling applications*. International Journal of Refrigeration, 2007. **30**(6): p. 1059-1071.
274. Chrysler, G.M. and D.T. Vader, *Electronics package with improved thermal management by thermoacoustic heat pumping*. 1994, Google Patents.
275. Zink, F., J.S. Vipperman, and L.A. Schaefer, *Environmental motivation to switch to thermoacoustic refrigeration*. Applied Thermal Engineering, 2010. **30**(2–3): p. 119-126.
276. Pecharsky, V.K. and K.A. Gschneidner Jr, *Magnetocaloric effect and magnetic refrigeration*. Journal of Magnetism and Magnetic Materials, 1999. **200**(1–3): p. 44-56.
277. Cremades, E., S. Gómez-Coca, D. Aravena, S. Alvarez, and E. Ruiz, *Theoretical study of exchange coupling in 3d-Gd complexes: large magnetocaloric effect systems*. Journal of the American Chemical Society, 2012. **134**(25): p. 10532-10542.
278. Verma, S., *Eco-friendly alternative refrigeration systems*. Resonance, 2001. **6**(10): p. 57-67.
279. Romero Gómez, J., R. Ferreiro Garcia, A. De Miguel Catoira, and M. Romero Gómez, *Magnetocaloric effect: A review of the thermodynamic cycles in magnetic refrigeration*. Renewable and Sustainable Energy Reviews, 2013. **17**: p. 74-82.
280. Debnath, J.C., *Novel magnetocaloric materials and room temperature magnetic refrigeration*. 2011.
281. Jeong, S., *AMR (Active Magnetic Regenerative) refrigeration for low temperature*. Cryogenics, 2014. **62**: p. 193-201.
282. Barclay, J.A. and W.A. Steyert, *Active magnetic regenerator*. 1982, Google Patents.
283. Kitanovski, A., J. Tušek, U. Tomc, U. Plazník, M. Ožbolt, and A. Poredoš, *Active Magnetic Regeneration*, in *Magnetocaloric Energy Conversion*. 2015, Springer. p. 97-166.
284. Yu, B.F., Q. Gao, B. Zhang, X.Z. Meng, and Z. Chen, *Review on research of room temperature magnetic refrigeration*. International Journal of Refrigeration, 2003. **26**(6): p. 622-636.
285. Zhong, X.C., P.F. Tang, Z.W. Liu, D.C. Zeng, Z.G. Zheng, H.Y. Yu, W.Q. Qiu, and M. Zou, *Magnetic properties and large magnetocaloric effect in Gd–Ni amorphous ribbons for magnetic refrigeration applications in intermediate temperature range*. Journal of Alloys and Compounds, 2011. **509**(24): p. 6889-6892.
286. Applications, C. *Magnetic Refrigeration System - The Benefits*. 2017 [cited 2017 January 04]; Available from: <http://www.cooltech-applications.com/magnetic-refrigeration-system.html>.
287. Applications, C. *Cooltech Applications Launches the First Magnetic Cooling System for Commercial Refrigeration*. 2016 [cited 2017 January 04]; Available from: <http://www.businesswire.com/news/home/20160615005178/en>.
288. Drake, S.J., M. Martin, D.A. Wetz, J.K. Ostanek, S.P. Miller, J.M. Heinzel, and A. Jain, *Heat generation rate measurement in a Li-ion cell at large C-rates through temperature and heat flux measurements*. Journal of Power Sources, 2015. **285**: p. 266-273.
289. Parise, R.J., *Quick charge battery with thermal management*. 2003, Google Patents.
290. Bandhauer, T.M. and S. Garimella, *Passive, internal thermal management system for batteries using microscale liquid–vapor phase change*. Applied Thermal Engineering, 2013. **61**(2): p. 756-769.
291. Mohammadian, S.K., Y.-L. He, and Y. Zhang, *Internal cooling of a lithium-ion battery using electrolyte as coolant through microchannels embedded inside the electrodes*. Journal of Power Sources, 2015. **293**: p. 458-466.
292. Shah, K., C. McKee, D. Chalise, and A. Jain, *Experimental and numerical investigation of core cooling of Li-ion cells using heat pipes*. Energy, 2016. **113**: p. 852-860.
293. Gauthier, M., T.J. Carney, A. Grimaud, L. Giordano, N. Pour, H.H. Chang, D.P. Fenning, S.F. Lux, O. Paschos, C. Bauer, F. Maglia, S. Lupart, P. Lamp, and Y. Shao-Horn, *Electrode-Electrolyte Interface in Li-Ion Batteries: Current Understanding and New Insights*. Journal of Physical Chemistry Letters, 2015. **6**(22): p. 4653-4672.

294. Liu, P., J. Wang, J. Hicks-Garner, E. Sherman, S. Soukiazian, M. Verbrugge, H. Tataria, J. Musser, and P. Finamore, *Aging Mechanisms of LiFePO₄ batteries deduced by electrochemical and structural analyses*. Journal of the Electrochemical Society, 2010. **157**(4): p. A499-A507.
295. Amine, K., J. Liu, and I. Belharouak, *High-temperature storage and cycling of C-LiFePO₄/graphite Li-ion cells*. Electrochemistry Communications, 2005. **7**(7): p. 669-673.
296. Biensan, P., B. Simon, J.P. Pérès, A. De Guibert, M. Broussely, J.M. Bodet, and F. Perton, *On safety of lithium-ion cells*. Journal of Power Sources, 1999. **81-82**: p. 906-912.
297. Ramadass, P., B. Haran, R. White, and B.N. Popov, *Capacity fade of Sony 18650 cells cycled at elevated temperatures: Part I. Cycling performance*. Journal of Power Sources, 2002. **112**(2): p. 606-613.
298. Maleki, H., G. Deng, A. Anani, and J. Howard, *Thermal stability studies of Li-ion cells and components*. Journal of the Electrochemical Society, 1999. **146**(9): p. 3224-3229.
299. Santhanagopalan, S., Q. Zhang, K. Kumaresan, and R.E. White, *Parameter estimation and life modeling of lithium-ion cells*. Journal of the Electrochemical Society, 2008. **155**(4): p. A345-A353.
300. Chen, K., G. Unsworth, and X. Li, *Measurements of heat generation in prismatic Li-ion batteries*. Journal of Power Sources, 2014. **261**: p. 28-37.
301. Bandhauer, T.M., S. Garimella, and T.F. Fuller, *Temperature-dependent electrochemical heat generation in a commercial lithium-ion battery*. Journal of Power Sources, 2014. **247**(0): p. 618-628.
302. Lu, W. and J. Prakash, *In situ measurements of heat generation in a Li/mesocarbon microbead half-cell*. Journal of the Electrochemical Society, 2003. **150**(3): p. A262-A266.
303. Bandhauer, T.M., S. Garimella, and T. Fuller, *A Critical Review of Thermal Issues in Lithium-Ion Batteries*, in *J. Electrochem. Soc.* 2011. p. R1-R25.
304. Bang, H., H. Yang, Y.K. Sun, and J. Prakash, *In situ studies of LixMn₂O₄ and Li_xAl_{0.17}Mn_{1.83}O_{3.97}S_{0.03} cathode by IMC*. Journal of the Electrochemical Society, 2005. **152**(2): p. A421-A428.
305. Kim, J.S., J. Prakash, and J.R. Selman, *Thermal characteristics of LixMn₂O₄ spinel*. Electrochemical and Solid-State Letters, 2001. **4**(9): p. A141-A144.
306. Kobayashi, Y., N. Kihira, K. Takei, H. Miyashiro, K. Kumai, N. Terada, and R. Ishikawa, *Electrochemical and calorimetric approach to spinel lithium manganese oxide*. Journal of Power Sources, 1999. **81-82**: p. 463-466.
307. Kobayashi, Y., H. Miyashiro, K. Kumai, K. Takei, T. Iwahori, and I. Uchida, *Precise electrochemical calorimetry of LiCoO₂/graphite lithium-ion cell understanding thermal behavior and estimation of degradation mechanism*. Journal of the Electrochemical Society, 2002. **149**(8): p. A978-A982.
308. Lu, W., I. Belharouak, S.H. Park, Y.K. Sun, and K. Amine, *Isothermal calorimetry investigation of Li_{1+x}Mn_{2-y}Al_yO₄ spinel*. Electrochimica Acta, 2007. **52**(19): p. 5837-5842.
309. Onda, K., H. Kameyama, T. Hanamoto, and K. Ito, *Experimental study on heat generation behavior of small lithium-ion secondary batteries*. Journal of the Electrochemical Society, 2003. **150**(3): p. A285-A291.
310. Saito, Y., K. Kanari, and K. Takano, *Thermal studies of a lithium-ion battery*. Journal of Power Sources, 1997. **68**(2): p. 451-454.
311. Song, L. and J.W. Evans, *Electrochemical-thermal model of lithium polymer batteries*. Journal of the Electrochemical Society, 2000. **147**(6): p. 2086-2095.
312. Yang, H. and J. Prakash, *Determination of the reversible and irreversible heats of a LiNi_{0.8}Co_{0.15}Al_{0.05}O₂/natural graphite cell using electrochemical-calorimetric technique*. Journal of the Electrochemical Society, 2004. **151**(8): p. A1222-A1229.
313. Thomas, K.E. and J. Newman, *Heats of mixing and of entropy in porous insertion electrodes*. Journal of Power Sources, 2003. **119-121**: p. 844-849.

References

314. Xiao, M. and S.-Y. Choe, *Theoretical and experimental analysis of heat generations of a pouch type LiMn₂O₄/carbon high power Li-polymer battery*. Journal of Power Sources, 2013. **241**(0): p. 46-55.
315. Schuster, E., C. Ziebert, A. Melcher, M. Rohde, and H.J. Seifert, *Thermal behavior and electrochemical heat generation in a commercial 40 Ah lithium ion pouch cell*. Journal of Power Sources, 2015. **286**: p. 580-589.
316. Lin, C., S. Xu, Z. Li, B. Li, G. Chang, and J. Liu, *Thermal analysis of large-capacity LiFePO₄ power batteries for electric vehicles*. Journal of Power Sources, 2015. **294**: p. 633-642.
317. McCullough, J.P., *Calorimetry of Non-Reacting Systems Prepared Under the Sponsorship of the International Union of Pure and Applied Chemistry Commission on Thermodynamics and the Thermochemistry*, D.W. Scott, Editor. 2013, Burlington : Elsevier Science: Burlington.
318. Reeve, T.H., *The method of fundamental solutions for some direct and inverse problems*. 2013, University of Birmingham.
319. Alifanov, O.M., *Inverse heat transfer problems*. 2012: Springer Science & Business Media.
320. Alifanov, O.M., E.A. Artiuškin, and S.V. Rumiantsev, *Extreme methods for solving ill-posed problems with applications to inverse heat transfer problems*. 1995: Begell house New York.
321. Jarny, Y., M. Ozisik, and J. Bardon, *A general optimization method using adjoint equation for solving multidimensional inverse heat conduction*. International journal of heat and mass transfer, 1991. **34**(11): p. 2911-2919.
322. Beck, J., B. Blackwell, and A. Haji-Sheikh, *Comparison of some inverse heat conduction methods using experimental data*. International Journal of Heat and Mass Transfer, 1996. **39**(17): p. 3649-3657.
323. Lesnic, D., L. Elliott, and D. Ingham, *Application of the boundary element method to inverse heat conduction problems*. International Journal of Heat and Mass Transfer, 1996. **39**(7): p. 1503-1517.
324. Huang, C.-H. and S.-P. Wang, *A three-dimensional inverse heat conduction problem in estimating surface heat flux by conjugate gradient method*. International Journal of Heat and Mass Transfer, 1999. **42**(18): p. 3387-3403.
325. Beck, J.V., B. Blackwell, and C.R.S. Clair Jr, *Inverse heat conduction: Ill-posed problems*. 1985: James Beck.
326. *Section 3 - Sealed Nickel-Cadmium Cells and Batteries*, in *Rechargeable Batteries Applications Handbook*. 1998, Newnes: Newton. p. 35-151.
327. Gu, H., *Mathematical analysis of a Zn/NiOOH cell*. Journal of The Electrochemical Society, 1983. **130**(7): p. 1459-1464.
328. Ahlberg, E., U. Palmqvist, N. Simic, and R. Sjövall, *Capacity loss in Ni-Cd pocket plate batteries. The origin of the second voltage plateau*. Journal of Power Sources, 2000. **85**(2): p. 245-253.
329. Barnard, R., G.T. Crickmore, J.A. Lee, and F.L. Tye, *The cause of residual capacity in nickel oxyhydroxide electrodes*. Journal of Applied Electrochemistry, 1980. **10**(1): p. 61-70.
330. Leger, C., C. Tessier, M. Ménétrier, C. Denage, and C. Delmas, *Investigation of the second discharge plateau of the β (III) - NiOOH/ β (II) - Ni (OH)₂ system*. Journal of The Electrochemical Society, 1999. **146**(3): p. 924-932.
331. Motupally, S., M. Jain, V. Srinivasan, and J.W. Weidner, *The role of oxygen at the second discharge plateau of nickel hydroxide*. Journal of the Electrochemical Society, 1998. **145**(1): p. 34-39.
332. Mao, Z., P. De Vidts, R.E. White, and J. Newman, *Theoretical analysis of the discharge performance of a NiOOH/H₂ cell*. Journal of the Electrochemical Society, 1994. **141**(1): p. 54-64.
333. Finley, T.D., *Battery Degradation Modeling For Vehicle Applications*. 2014.
334. Zaghib, K., A. Mauger, H. Groult, J.B. Goodenough, and C.M. Julien, *Advanced electrodes for high power Li-ion batteries*. Materials, 2013. **6**(3): p. 1028-1049.

335. Wang, W.L., E.M. Jin, and H.-B. Gu, *Electrochemical Performance of Lithium Iron Phosphate by Adding Graphite Nanofiber for Lithium Ion Batteries*. Transactions on Electrical and Electronic Materials, 2012. **13**(3): p. 121-124.
336. Wu, W., X. Xiao, and X. Huang, *The effect of battery design parameters on heat generation and utilization in a Li-ion cell*. Electrochimica Acta, 2012. **83**: p. 227-240.
337. Churikov, A.V., A.V. Ivanishchev, I.A. Ivanishcheva, V.O. Sycheva, N.R. Khasanova, and E.V. Antipov, *Determination of lithium diffusion coefficient in LiFePO₄ electrode by galvanostatic and potentiostatic intermittent titration techniques*. Electrochimica Acta, 2010. **55**(8): p. 2939-2950.
338. Laffont, L., C. Delacourt, P. Gibot, M.Y. Wu, P. Kooyman, C. Masquelier, and J.M. Tarascon, *Study of the LiFePO₄/FePO₄ Two-Phase System by High-Resolution Electron Energy Loss Spectroscopy*. Chemistry of Materials, 2006. **18**(23): p. 5520-5529.
339. Arora, S., W. Shen, and A. Kapoor, *Critical analysis of open circuit voltage and its effect on estimation of irreversible heat for Li-ion pouch cells*. Journal of Power Sources, 2017. **350**: p. 117-126.
340. Luo, X., J. Wang, M. Dooner, and J. Clarke, *Overview of current development in electrical energy storage technologies and the application potential in power system operation*. Applied Energy, 2015. **137**: p. 511-536.
341. Darcovich, K., E.R. Henquin, B. Kenney, I.J. Davidson, N. Saldanha, and I. Beausoleil-Morrison, *Higher-capacity lithium ion battery chemistries for improved residential energy storage with micro-cogeneration*. Applied Energy, 2013. **111**: p. 853-861.
342. Patoux, S., L. Daniel, C. Bourbon, H. Lignier, C. Pagano, F. Le Cras, S. Jouanneau, and S. Martinet, *High voltage spinel oxides for Li-ion batteries: From the material research to the application*. Journal of Power Sources, 2009. **189**(1): p. 344-352.
343. Hu, M., X. Pang, and Z. Zhou, *Recent progress in high-voltage lithium ion batteries*. Journal of Power Sources, 2013. **237**: p. 229-242.
344. Wang, L., Y. Cheng, and X. Zhao, *Influence of connecting plate resistance upon LiFePO₄ battery performance*. Applied Energy, 2015. **147**: p. 353-360.
345. Li, H., Z. Wang, L. Chen, and X. Huang, *Research on advanced materials for Li-ion batteries*. Advanced Materials, 2009. **21**(45): p. 4593.
346. Li, H., P. Balaya, and J. Maier, *Li-storage via heterogeneous reaction in selected binary metal fluorides and oxides*. Journal of the Electrochemical Society, 2004. **151**(11): p. A1878-A1885.
347. Saw, L.H., Y. Ye, and A.A.O. Tay, *Electro-thermal characterization of Lithium Iron Phosphate cell with equivalent circuit modeling*. Energy Conversion and Management, 2014. **87**: p. 367-377.
348. Tiedemann, W., J. Newman, and F. De Sua, *Potential Distribution in the Lead-Acid Battery Grid*. Power Sources, 1977. **6**: p. 15.
349. Tiedemann, W.H. and J. Newman, *Battery design and optimization*. Journal of Electrochemical Society, Softbound Proceeding Series, Princeton, New York, 1979. **79**(1): p. 23.
350. Newman, J. and W. Tiedemann, *Potential and current distribution in electrochemical cells interpretation of the Half - Cell voltage measurements as a function of Reference - Electrode location*. Journal of the Electrochemical Society, 1993. **140**(7): p. 1961-1968.
351. Wang, M. and H.-X. Li, *Spatiotemporal modeling of internal states distribution for lithium-ion battery*. Journal of Power Sources, 2016. **301**: p. 261-270.
352. Taheri, P., A. Mansouri, M. Yazdanpour, and M. Bahrami, *Theoretical analysis of potential and current distributions in planar electrodes of lithium-ion batteries*. Electrochimica Acta, 2014. **133**: p. 197-208.
353. Kim, U.S., J. Yi, C.B. Shin, T. Han, and S. Park, *Modelling the thermal behaviour of a lithium-ion battery during charge*. Journal of Power Sources, 2011. **196**(11): p. 5115-5121.

References

354. Sun, H., X. Wang, B. Tossan, and R. Dixon, *Three-dimensional thermal modeling of a lithium-ion battery pack*. Journal of Power Sources, 2012. **206**: p. 349-356.
355. Yi, J., U.S. Kim, C.B. Shin, T. Han, and S. Park, *Three-dimensional thermal modeling of a lithium-ion battery considering the combined effects of the electrical and thermal contact resistances between current collecting tab and lead wire*. Journal of The Electrochemical Society, 2013. **160**(3): p. A437-A443.
356. Martha, S.K., J. Nanda, Y. Kim, R.R. Unocic, S. Pannala, and N.J. Dudney, *Solid electrolyte coated high voltage layered-layered lithium-rich composite cathode: Li 1.2 Mn 0.525 Ni 0.175 Co 0.1 O 2*. Journal of Materials Chemistry A, 2013. **1**(18): p. 5587-5595.
357. Peck, S. and M. Pierce, *Development of a Temperature-Dependent Li-ion Battery Thermal Model*. 2012, SAE Technical Paper.
358. Allu, S., S. Kalnaus, W. Elwasif, S. Simunovic, J.A. Turner, and S. Pannala, *A new open computational framework for highly-resolved coupled three-dimensional multiphysics simulations of Li-ion cells*. Journal of Power Sources, 2014. **246**: p. 876-886.
359. Kim, U.S., J. Yi, C.B. Shin, T. Han, and S. Park, *Modeling the Thermal Behaviors of a Lithium-Ion Battery during Constant-Power Discharge and Charge Operations*. Journal of The Electrochemical Society, 2013. **160**(6): p. A990-A995.
360. Maia, G., E. Ticianelli, and E. Gonzalez, *A modelling approach to the optimizaton of lead-acid battery electrodes*. Journal of applied electrochemistry, 1993. **23**(11): p. 1151-1161.
361. Jung, S. and D. Kang, *Multi-dimensional modeling of large-scale lithium-ion batteries*. Journal of Power Sources, 2014. **248**: p. 498-509.
362. Peck, S., A. Velivelli, and W. Jansen, *Options for Coupled Thermal-Electric Modeling of Battery Cells and Packs*. SAE International Journal of Passenger Cars-Electronic and Electrical Systems, 2014. **7**(1): p. 273-284.
363. Spotnitz, R., *Spiral Cell Modeling with Battery Design Studio®*.
364. Uddin, A.I. and J. Ku, *Design and Simulation of Lithium-Ion Battery Thermal Management System for Mild Hybrid Vehicle Application*. 2015, SAE Technical Paper.
365. van Gils, R.W., D. Danilov, P.H.L. Notten, M.F.M. Speetjens, and H. Nijmeijer, *Battery thermal management by boiling heat-transfer*. Energy Conversion and Management, 2014. **79**: p. 9-17.
366. Huang, J., D. Qin, and Z. Peng, *Effect of energy-regenerative braking on electric vehicle battery thermal management and control method based on simulation investigation*. Energy Conversion and Management, 2015. **105**: p. 1157-1165.
367. Yuan, X.-Z.R., C. Song, H. Wang, and J. Zhang, *Electrochemical impedance spectroscopy in PEM fuel cells: fundamentals and applications*. 2009: Springer Science & Business Media.
368. Boukamp, B.A., *Impedance spectroscopy, strength and limitations (Impedanzspektroskopie, Stärken und Grenzen)*. tm-Technisches Messen/Sensoren, Geräte, Systeme, 2004. **71**(9/2004): p. 454-459.
369. Bogomolova, A., E. Komarova, K. Reber, T. Gerasimov, O. Yavuz, S. Bhatt, and M. Aldissi, *Challenges of electrochemical impedance spectroscopy in protein biosensing*. Analytical Chemistry, 2009. **81**(10): p. 3944-3949.
370. Churikov, A. and A. Ivanischev, *Application of pulse methods to the determination of the electrochemical characteristics of lithium intercalates*. Electrochimica acta, 2003. **48**(24): p. 3677-3691.
371. Catherino, H.A., *Estimation of the heat generation rates in electrochemical cells*. Journal of Power Sources, 2013. **239**(0): p. 505-512.
372. Newman, J. and K.E. Thomas-Alyea, *Electrochemical systems*. 2012: John Wiley & Sons.
373. Catherino, H.A., *An Analysis of Heat Generation in a Lithium Ion Cell*. 2015, SAE Technical Paper.

374. Takano, K., Y. Saito, K. Kanari, K. Nozaki, K. Kato, A. Negishi, and T. Kato, *Entropy change in lithium ion cells on charge and discharge*. Journal of Applied Electrochemistry, 2002. **32**(3): p. 251-258.
375. Wu, B., Z. Li, and J. Zhang, *Thermal Design for the Pouch-Type Large-Format Lithium-Ion Batteries I. Thermo-Electrical Modeling and Origins of Temperature Non-Uniformity*. Journal of The Electrochemical Society, 2015. **162**(1): p. A181-A191.
376. Al Hallaj, S., J. Prakash, and J.R. Selman, *Characterization of commercial Li-ion batteries using electrochemical-calorimetric measurements*. Journal of Power Sources, 2000. **87**(1): p. 186-194.
377. Hong, J.S., H. Maleki, S. Al Hallaj, L. Redey, and J.R. Selman, *Electrochemical - Calorimetric Studies of Lithium - Ion Cells*. Journal of The Electrochemical Society, 1998. **145**(5): p. 1489-1501.
378. Onda, K., H. Kameyama, T. Hanamoto, and K. Ito, *Experimental study on heat generation behavior of small lithium-ion secondary batteries*. J. Electrochem. Soc., 2003. **150**(3): p. A285-A291.
379. Jannesari, H., M. Emami, and C. Ziegler, *Effect of electrolyte transport properties and variations in the morphological parameters on the variation of side reaction rate across the anode electrode and the aging of lithium ion batteries*. Journal of Power Sources, 2011. **196**(22): p. 9654-9664.
380. Churikov, A.V., M.A. Volgin, and K.I. Pridatko, *On the determination of kinetic characteristics of lithium intercalation into carbon*. Electrochimica Acta, 2002. **47**(17): p. 2857-2865.
381. Churikov, A.V., I.M. Gamayunova, and A.V. Shirokov, *Ionic processes in solid-electrolyte passivating films on lithium*. Journal of Solid State Electrochemistry, 2000. **4**(4): p. 216-224.
382. Uddin, K., A.D. Moore, A. Barai, and J. Marco, *The effects of high frequency current ripple on electric vehicle battery performance*. Applied Energy, 2016. **178**: p. 142-154.
383. Ning, G., R.E. White, and B.N. Popov, *A generalized cycle life model of rechargeable Li-ion batteries*. Electrochimica Acta, 2006. **51**(10): p. 2012-2022.
384. Scrosati, B., K. Abraham, W.A. van Schalkwijk, and J. Hassoun, *Lithium batteries: advanced technologies and applications*. Vol. 58. 2013: John Wiley & Sons.
385. Arora, S., W. Shen, and A. Kapoor, *Neural network based computational model for estimation of heat generation in LiFePO₄ pouch cells of different nominal capacities*. Computers & Chemical Engineering, 2017. **101**: p. 81-94.
386. Shen, W., C. Chan, E. Lo, and K. Chau, *A new battery available capacity indicator for electric vehicles using neural network*. Energy Conversion and Management, 2002. **43**(6): p. 817-826.
387. Abada, S., G. Marlair, A. Lecocq, M. Petit, V. Sauvant-Moynot, and F. Huet, *Safety focused modeling of lithium-ion batteries: A review*. Journal of Power Sources, 2016. **306**: p. 178-192.
388. Saw, L., Y. Ye, and A. Tay, *Electrochemical-thermal analysis of 18650 lithium iron phosphate cell*. Energy Conversion and Management, 2013. **75**: p. 162-174.
389. Lai, Y., S. Du, L. Ai, L. Ai, Y. Cheng, Y. Tang, and M. Jia, *Insight into heat generation of lithium ion batteries based on the electrochemical-thermal model at high discharge rates*. International Journal of Hydrogen Energy, 2015. **40**(38): p. 13039-13049.
390. Cai, L. and R.E. White, *Mathematical modeling of a lithium ion battery with thermal effects in COMSOL Inc. Multiphysics (MP) software*. Journal of Power Sources, 2011. **196**(14): p. 5985-5989.
391. Prada, E., D. Di Domenico, Y. Creff, J. Bernard, V. Sauvant-Moynot, and F. Huet, *Simplified electrochemical and thermal model of LiFePO₄-graphite Li-ion batteries for fast charge applications*. Journal of The Electrochemical Society, 2012. **159**(9): p. A1508-A1519.
392. Guo, M., G.-H. Kim, and R.E. White, *A three-dimensional multi-physics model for a Li-ion battery*. Journal of Power Sources, 2013. **240**: p. 80-94.
393. Jokar, A., B. Rajabloo, M. Désilets, and M. Lacroix, *Review of simplified Pseudo-two-Dimensional models of lithium-ion batteries*. Journal of Power Sources, 2016. **327**: p. 44-55.

References

394. Ramadesigan, V., P.W. Northrop, S. De, S. Santhanagopalan, R.D. Braatz, and V.R. Subramanian, *Modeling and simulation of lithium-ion batteries from a systems engineering perspective*. Journal of The Electrochemical Society, 2012. **159**(3): p. R31-R45.
395. Lee, K.-J., K. Smith, A. Pesaran, and G.-H. Kim, *Three dimensional thermal-, electrical-, and electrochemical-coupled model for cylindrical wound large format lithium-ion batteries*. Journal of Power Sources, 2013. **241**: p. 20-32.
396. WORLDWIDE, C. *2016 CHEVROLET SPARK SPECIFICATIONS*. 2016 [cited 2016 July 17]; Available from: <http://media.chevrolet.com/media/us/en/chevrolet/vehicles/spark-ev/2016.tab1.html>.
397. WORLDWIDE, C. *2015 CHEVROLET SPARK SPECIFICATIONS*. 2015 [cited 2016 July 17]; Available from: <http://media.gm.com/media/us/en/chevrolet/vehicles/spark-ev/2015.tab1.html>
398. Authority, G., *2017 Chevrolet Bolt EV*. 2016.
399. Cole, J. *New Specs For 2015 e-Golf Released By VW, Launches Later This Year*. 2014 [cited 2016 July 17]; Available from: <http://insideevs.com/volkswagen-releases-details-2015-e-golf/>
400. Rovito, M. *2015 VW e-Golf ushers in an era of interchangeable drivetrains for every Volkswagen model*. 2015 [cited 2016 July 18]; Available from: <https://chargedevs.com/features/the-2015-vw-e-golf-ushers-in-an-era-of-interchangeable-drivetrains-for-every-volkswagen-model/>
401. Cole, J. *2017 Volkswagen e-Golf: 35.8 kWh Battery, 124 Mile/200km Range (Update)*. 2016 [cited 2016 July 17]; Available from: <http://insideevs.com/2017-volkswagen-e-golf-35-8-kwh-battery-124-miles200km-real-world-range/>.
402. Buchmann, I. *BU-1003: Electric Vehicle (EV)*. 2016 [cited 2016 July 17]; Available from: http://batteryuniversity.com/learn/article/electric_vehicle_ev.
403. Laboratory, I.N., *2013 Ford Focus Electric Advanced Vehicle Testing – Baseline Testing Results*. 2015.
404. Company, F.M. *FOCUS 2016 - Electric Engine Specifications*. 2016 [cited 2016 July 20]; Available from: <http://www.ford.com/cars/focus/specifications/engine/>.
405. Roper, L.D. *Mercedes B-Class ED 2015*. 2016 [cited 2016 July 19]; Available from: <http://www.roperld.com/Science/MercedesBClassED.htm>.
406. Huffman, J.P. *2014 BMW i3 vs. 2014 Mercedes-Benz B-class Electric Drive*. Car and Driver, 2014.
407. Lofton, B. *Kia Soul EV Battery System*. 2016 [cited 2016 July 17]; Available from: <https://www.evhangar.com/system/battery-systems/sys-batt-kia-soul-ev>.
408. Motors, K. *Advanced battery for Kia Soul EV*. 2014; Available from: <http://www.kiapressoffice.com/Release/35730#>.
409. Moloughney, T., *2017 BMW i3 Specs Revealed With Some Surprises*, in *The Electric BMW i3*. 2016.
410. Blanco, S. *Updated 2017 BMW i3 goes 114 miles with new 33-kWh battery*. 2016 [cited 2016 July 19]; Available from: <http://www.autoblog.com/2016/05/01/updated-bmw-i3-114-miles-new-33-kwh-battery/>
411. Mitsubishi Motors North America, I. *Main Drive Battery*. 2016 [cited 2016 July 18]; Available from: <http://www.mitsubishicars.com/imiev/specifications>.
412. Laboratory, I.N., *BEV Battery Testing Results 2012 Mitsubishi iMiev - VIN 4550*, in *Advanced Vehicle Testing Activity*. 2014.
413. fusionZONE Automotive, I. *2017 Nissan Leaf Vs Chevrolet Bolt* 2016 [cited 2016 July 20]; Available from: <http://www.premiernissanofstevenscreek.com/2017-nissan-leaf-vs-chevy-bolt>
414. Corporation, A.E.S. *Li-ion cell: High energy cell*. 2013 [cited 2016 July 18]; Available from: http://www.eco-aesc-lb.com/en/product/liion_ev/.

415. Caputo, A.C. and P.M. Pelagagge, *Parametric and neural methods for cost estimation of process vessels*. International Journal of Production Economics, 2008. **112**(2): p. 934-954.
416. Weigert, T., Q. Tian, and K. Lian, *State-of-charge prediction of batteries and battery-supercapacitor hybrids using artificial neural networks*. Journal of Power Sources, 2011. **196**(8): p. 4061-4066.
417. Kaastra, I. and M. Boyd, *Designing a neural network for forecasting financial and economic time series*. Neurocomputing, 1996. **10**(3): p. 215-236.
418. Lam, M., *Neural network techniques for financial performance prediction: integrating fundamental and technical analysis*. Decision Support Systems, 2004. **37**(4): p. 567-581.
419. Li, D.-C., L.-S. Lin, and L.-J. Peng, *Improving learning accuracy by using synthetic samples for small datasets with non-linear attribute dependency*. Decision Support Systems, 2014. **59**: p. 286-295.
420. Niyogi, P., F. Girosi, and T. Poggio, *Incorporating prior information in machine learning by creating virtual examples*. Proceedings of the IEEE, 1998. **86**(11): p. 2196-2209.
421. Li, D.-C. and Y.-S. Lin, *Using virtual sample generation to build up management knowledge in the early manufacturing stages*. European Journal of Operational Research, 2006. **175**(1): p. 413-434.
422. Bernardi, D., E. Pawlikowski, and J. Newman, *A General Energy Balance for Battery Systems*. Journal of The Electrochemical Society, 1985. **132**(1): p. 5-12.
423. Zheng, H., L. Jiang, H. Lou, Y. Hu, X. Kong, and H. Lu, *Application of artificial neural network (ANN) and partial least-squares regression (PLSR) to predict the changes of anthocyanins, ascorbic acid, Total phenols, flavonoids, and antioxidant activity during storage of red bayberry juice based on fractal analysis and red, green, and blue (RGB) intensity values*. Journal of agricultural and food chemistry, 2010. **59**(2): p. 592-600.
424. Razbani, O. and M. Assadi, *Artificial neural network model of a short stack solid oxide fuel cell based on experimental data*. Journal of Power Sources, 2014. **246**: p. 581-586.
425. Masters, T., *Advanced algorithms for neural networks: a C++ sourcebook*. 1995: John Wiley & Sons, Inc.
426. Bailey, D.L. and D. Thompson, *Developing neural-network applications*. AI expert, 1990. **5**(9): p. 34-41.
427. Katz, J.O., *Developing neural network forecasters for trading*. Technical Analysis of Stocks and Commodities, 1992. **10**(4): p. 160-168.
428. Hansen, J.V., J.B. McDonald, and R.D. Nelson, *Time Series Prediction With Genetic - Algorithm Designed Neural Networks: An Empirical Comparison With Modern Statistical Models*. Computational Intelligence, 1999. **15**(3): p. 171-184.
429. Klimasauskas, C.C., *Applying neural networks*. Neural networks in finance and investing, 1993: p. 47-72.
430. Saadat, M., M. Khandelwal, and M. Monjezi, *An ANN-based approach to predict blast-induced ground vibration of Gol-E-Gohar iron ore mine, Iran*. Journal of Rock Mechanics and Geotechnical Engineering, 2014. **6**(1): p. 67-76.
431. The MathWorks, I. *Levenberg-Marquardt backpropagation*. 2016 [cited 2016 July 28]; Available from: <http://au.mathworks.com/help/nnet/ref/trainlm.html>.
432. Fang, K., D. Mu, S. Chen, B. Wu, and F. Wu, *A prediction model based on artificial neural network for surface temperature simulation of nickel–metal hydride battery during charging*. Journal of Power Sources, 2012. **208**: p. 378-382.
433. Zhang, S.S., K. Xu, and T.R. Jow, *Charge and discharge characteristics of a commercial LiCoO₂-based 18650 Li-ion battery*. Journal of Power Sources, 2006. **160**(2): p. 1403-1409.
434. Duan, X. and G. Naterer, *Heat transfer in phase change materials for thermal management of electric vehicle battery modules*. International Journal of Heat and Mass Transfer, 2010. **53**(23): p. 5176-5182.

References

435. Karimi, G. and X. Li, *Thermal management of lithium-ion batteries for electric vehicles*. International Journal of Energy Research, 2013. **37**(1): p. 13-24.
436. Duan, X. and G.F. Naterer, *Heat transfer in phase change materials for thermal management of electric vehicle battery modules*. International Journal of Heat and Mass Transfer, 2010. **53**(23-24): p. 5176-5182.
437. Shi, S., Y. Xie, M. Li, Y. Yuan, J. Yu, H. Wu, B. Liu, and N. Liu, *Non-steady experimental investigation on an integrated thermal management system for power battery with phase change materials*. Energy Conversion and Management, 2017. **138**: p. 84-96.
438. Kizilel, R., R. Sabbah, J.R. Selman, and S. Al-Hallaj, *An alternative cooling system to enhance the safety of Li-ion battery packs*. Journal of Power Sources, 2009. **194**(2): p. 1105-1112.
439. Wang, Z., Z. Zhang, L. Jia, and L. Yang, *Paraffin and paraffin/aluminum foam composite phase change material heat storage experimental study based on thermal management of Li-ion battery*. Applied Thermal Engineering, 2015. **78**: p. 428-436.
440. Azizi, Y. and S.M. Sadrameli, *Thermal management of a LiFePO₄ battery pack at high temperature environment using a composite of phase change materials and aluminum wire mesh plates*. Energy Conversion and Management, 2016. **128**: p. 294-302.
441. Karimi, G., M. Azizi, and A. Babapoor, *Experimental study of a cylindrical lithium ion battery thermal management using phase change material composites*. Journal of Energy Storage, 2016. **8**: p. 168-174.
442. Jegadheeswaran, S. and S.D. Pohekar, *Performance enhancement in latent heat thermal storage system: a review*. Renewable and Sustainable Energy Reviews, 2009. **13**(9): p. 2225-2244.
443. Optics, E. *Infrared (IR) Material Windows - Technical Images*. 2017; Available from: <https://www.edmundoptics.com/optics/windows-diffusers/specialty-windows/infrared-ir-material-windows/#resources>
444. Jones, B.J., D. Sun, S. Krishnan, and S.V. Garimella, *Experimental and numerical study of melting in a cylinder*. International Journal of Heat and Mass Transfer, 2006. **49**(15–16): p. 2724-2738.
445. Lamberg, P., R. Lehtiniemi, and A.-M. Henell, *Numerical and experimental investigation of melting and freezing processes in phase change material storage*. International Journal of Thermal Sciences, 2004. **43**(3): p. 277-287.
446. Jany, P. and A. Bejan, *Scaling theory of melting with natural convection in an enclosure*. International Journal of Heat and Mass Transfer, 1988. **31**(6): p. 1221-1235.
447. Kowalewski, T.A. and D. Gobin, *Phase change with convection: modelling and validation*. 2004: Springer.
448. Mbaye, M. and E. Bilgen, *Phase change process by natural convection–diffusion in rectangular enclosures*. Heat and mass transfer, 2001. **37**(1): p. 35-42.
449. TEGMART. *Tegpro High Temperature TEG Power Module - 22 Watt 7 volt 56 mm*. 2017 [cited 2017 March 20]; Available from: <http://www.tegmart.com/thermoelectric-modules/22-watt-teg-power-module-by-tegpro/>.
450. JaycarElectronics. *Thermoelectric (Peltier) Module 51W/6A*. 2017 [cited March 20 2017]; Available from: <https://www.jaycar.com.au/thermoelectric-peltier-module-51w-6a/p/ZP9102>.
451. Rowe, D. and G. Min, *Evaluation of thermoelectric modules for power generation*. Journal of Power Sources, 1998. **73**(2): p. 193-198.
452. Chen, W.-H., C.-Y. Liao, C.-I. Hung, and W.-L. Huang, *Experimental study on thermoelectric modules for power generation at various operating conditions*. Energy, 2012. **45**(1): p. 874-881.

Appendix

Ambient Temperature (°C)	Polynomial Term	Depth of Discharge (%)								
		10	20	30	40	50	60	70	80	90
-10	x^2	0.0792	0.0982	0.1595	0.2315	0.3137	0.3607	0.3208	0.4577	0.4756
	x^1	-2.8208	-4.1875	-6.3833	-9.2542	-12.429	-14.975	-14.629	20.421	-22.296
	x^0	325	347.21	368.86	399.71	433.36	463.71	470.25	529.57	558.18
5	x^2	0.0262	-0.2369	-0.3292	-0.3655	-0.1905	-0.6571	-0.3155	-0.1744	-0.322
	x^1	-0.5667	7.5917	10.321	10.692	6.6667	20.9	10.042	6.1542	8.8708
	x^0	305.86	244.68	219.75	219.86	235.86	136.86	221.11	238.68	230.89
20	x^2	0.0131	0.0917	0.1131	0.0464	-0.0607	0.056	0.0321	0.0887	0.2292
	x^1	-0.4083	-2.1083	-1.9583	-0.425	3.325	0.6417	0.475	-2.2542	-7.2708
	x^0	321.18	320.5	310.43	297.3	266.29	277.29	287.39	319.11	367.5
35	x^2	0.0214	-0.0107	0.0458	-0.0446	-0.0149	-0.0685	-0.0351	0.0143	-0.1827
	x^1	-0.35	0.675	0.5542	2.3125	1.2708	3.1458	2.3792	1.1	6.3458
	x^0	311.43	306.29	305.5	279.36	288.29	268.21	267.21	273.79	238.93
50	x^2	0.0286	0.0226	0.0161	0.0244	-0.0286	-0.025	-0.094	-0.1798	0.0256
	x^1	-0.8	-0.5917	-0.0125	-0.2042	1.3	1.075	3.0917	5.9917	-0.1958
	x^0	318.57	312.79	301.07	302.07	289.43	287.5	269.29	247.57	289.43

(a)

Ambient Temperature (°C)	Polynomial Term	Depth of Discharge (%)								
		10	20	30	40	50	60	70	80	90
-10	x^2	0.0821	0.1232	0.1881	0.2167	0.2232	0.303	0.2554	0.3149	0.322
	x^1	-2.425	-4.0125	-6.4333	8.2333	-8.8125	11.504	10.588	-12.671	-13.621
	x^0	293.64	314.71	342.43	372.25	378.96	404.39	400.61	421.71	438.11

Appendix I

5	x^2	0.1071	0.1607	0.0875	0.1143	0.2542	0.1875	-0.122	0.1482	0.1601
	x^1	-3.75	-5.125	-3.0125	-4.45	-9.3458	-7.0625	1.7708	-7.5875	-7.5042
	x^0	330.64	338.96	333.25	351.04	390.75	371	315.89	388.21	382.29
20	x^2	0.0494	0.078	-0.0292	-0.094	-0.0315	0.0607	0.1518	0.2673	0.0226
	x^1	-1.2792	-2.5792	0.6708	2.3417	0.4042	-2.325	-5.5625	-9.7542	-2.3417
	x^0	317.32	331.64	312.25	304.54	318.79	335.96	363.29	396.18	341.29
35	x^2	0.1155	0.1381	0.1554	0.1363	0.1482	0.1435	0.1827	0.1827	0.2375
	x^1	-3.1917	-4.0333	-4.7875	-4.4208	-4.8375	-4.8708	-6.3458	-6.3458	-9.2125
	x^0	333.14	341.93	350.86	350.14	353.71	356.79	370.07	370.07	406.5
50	x^2	0.0357	0.0774	0.1167	0.0869	0.1226	0.1488	0.1607	0.0792	0.1113
	x^1	1	-2.7083	-3.6833	-3.1417	-4.1417	-4.7083	-5.625	-3.3208	-4.5958
	x^0	319.71	334.21	340	340.07	344.29	344.14	353.71	340.5	351.64

(b)

Ambient Temperature (°C)	Polynomial Term	Depth of Discharge (%)								
		10	20	30	40	50	60	70	80	90
5	x^2	0.2417	0.1845	0.2518	0.2458	0.1857	0.2619	0.2405	0.1274	0.2161
	x^1	-6.5583	-4.7083	-6.8625	-7.1542	-5.45	-7.9167	-7.8167	-4.8583	-7.8625
	x^0	306.5	297.86	318.04	328.25	320.46	340.57	344.89	327.21	348.57
20	x^2	0.1988	0.1571	0.2667	0.175	0.2798	0.2512	0.2554	0.206	0.1339
	x^1	-5.6083	-4.65	-8.1333	-5.775	-8.7917	-8.2417	-8.5875	-7.3083	-5.4375
	x^0	321.39	319.14	347.5	337.5	358.43	358.61	362.11	353.54	337.43
35	x^2	0.2048	0.2113	0.2173	0.2238	0.228	0.222	0.2429	0.2446	0.2732
	x^1	-5.5667	-5.8958	-6.3542	-6.6833	-7.0292	-7.0708	-7.8	-8.1625	-9.2125
	x^0	326.43	330.64	337.93	342.14	347.64	349.86	355.61	360.14	365.71
50	x^2	0.2101	0.225	0.2429	0.2167	0.2476	0.2399	0.2262	0.247	0.2583
	x^1	5.9042	-6.675	-7.3	-6.7333	-7.7667	-7.6958	-7.4167	-8.1458	-8.6917
	x^0	334.29	343	348.36	347.5	355.79	356.21	354.86	359.86	362.5

(c)

Table A1: Coefficients of the fitting polynomials used for generating virtual samples as a function of battery nominal capacity at different ambient temperatures and discharge rates of (a) 0.33C, (b) 1C and (c) 3C

Ambient Temperature (°C)	Polynomial Term	Depth of Discharge (%)								
		10	20	30	40	50	60	70	80	90
5	x^2	-9.6316	-16.85	-25.375	-29.521	-39.031	-42.142	-27.507	-41.264	-34.829
	x^1	19.526	49.277	83.748	100.08	134.37	152.32	97.779	144.81	122.81
	x^0	297.61	275.82	256.38	252.19	236.91	216.32	251.98	233.46	244.51
20	x^2	0.8189	-8.1279	-10.729	14.082	-19.951	-22.046	-23.216	-20.988	-4.0262
	x^1	-13.776	20.512	34.792	48.953	72.803	81.933	83.489	70.451	5.3549
	x^0	323.21	303.62	291.69	282.38	267.15	261.36	268.23	285.79	322.67
35	x^2	-6.5403	-8.2187	-14.368	-19.771	-18.557	-24.894	-30.44	-30.392	-46.34
	x^1	16.161	22.125	47.721	68.832	64.98	89.825	110.63	111.32	166.11
	x^0	305.38	304.59	290.15	274.44	278.08	262.07	250.81	250.08	228.23
50	x^2	-2.5281	-7.0001	-11.285	-12.776	-13.518	-13.142	-19.014	-21.157	-20.508
	x^1	3.3624	21.25	38.889	44.604	49.322	49.569	71.558	80.377	75.784
	x^0	313.17	303.25	290.4	288.67	283.2	279.57	266.46	259.78	266.72

(a)

Ambient Temperature (°C)	Polynomial Term	Depth of Discharge (%)								
		10	20	30	40	50	60	70	80	90
5	x^2	-4.0863	-1.6113	-10.794	-13.028	-13.348	-7.6178	-14.192	-13.579	-12.928
	x^1	-1.6548	-8.3047	25.177	35.238	39.768	17.221	40.145	41.941	38.463
	x^0	304.24	308.17	293.37	287.79	281.33	297.65	289.05	279.39	280.21
20	x^2	-0.2117	-5.3811	-10.836	-14.793	-13.815	-12.879	-11.202	-6.3538	-5.4272
	x^1	-12.778	8.6494	28.217	45.048	41.135	39.89	33.182	15.54	9.0839

Appendix I

	x^0	322.24	307.23	298.37	288.25	290.43	287.74	292.02	300.81	307.59
35	x^2	-4.3064	-3.4218	-7.847	-10.036	-9.8021	-13.111	-15.999	-16.931	-22.204
	x^1	6.1007	2.3122	20.138	29.02	28.708	41.318	52.622	56.101	72.442
	x^0	309.46	313.61	301.71	295.52	295.59	287.79	279.38	276.83	271.51
50	x^2	-3.5588	-4.3952	-6.9107	-7.7024	-6.8149	-7.325	-8.209	-9.2843	-11.942
	x^1	4.36	8.8306	18.893	22.184	19.885	23.175	27.336	29.512	39.017
	x^0	311.95	306.56	299.02	298.02	296.68	291.15	286.37	288.27	280.67

(b)

Ambient Temperature (°C)	Polynomial Term	Depth of Discharge (%)								
		10	20	30	40	50	60	70	80	90
5	x^2	-1.329	-3.7949	-12.509	-15.861	-10.686	-10.451	-7.0972	-4.8584	-12.828
	x^1	-7.9339	3.5547	36.786	51.319	32.869	32.93	19.514	12.059	42.061
	x^0	307.76	300.99	283.72	272.29	283.32	282.27	290.08	288.55	267.02
20	x^2	-0.487	-2.0704	-2.816	-7.5668	-6.9128	-4.3504	-5.4691	-2.5791	1.7504
	x^1	-9.4269	-2.8434	0.0139	19.392	17.776	7.6518	11.752	1.1914	-17.627
	x^0	321.41	316.16	316.8	301.92	303.39	310.45	306.47	309.39	319.38
35	x^2	-4.8619	-4.1639	-6.1672	-8.1691	-8.1223	-10.919	-12.316	-12.272	-18.658
	x^1	10.198	7.0305	14.919	23.552	23.489	33.925	39.515	38.336	61.382
	x^0	310.16	313.63	308.5	300.87	300.88	293.74	289.05	290.19	274.53
50	x^2	-2.5749	-2.7126	-5.7424	-4.7166	-5.6934	-7.9763	-8.2998	-7.6024	-7.0455
	x^1	3.4246	5.1002	16.219	12.616	17.274	26.28	28.949	25.41	22.057
	x^0	313.15	308.61	302.52	304.1	298.92	291.2	284.85	287.94	289.24

(c)

Table A2: Coefficients of the fitting polynomials used for generating virtual samples as a function of discharge rate at different ambient temperatures for LFP pouch cells of nominal capacities of (a) 8 Ah, (b) 15 Ah and (c) 20 Ah

Ambient Temperature (°C)	Polynomial Term	Depth of Discharge (%)								
		10	20	30	40	50	60	70	80	90
8	x^4	6.7e-5	6.6e-5	8.3e-5	9.6e-5	7e-5	1.4e-4	0.0001	2.3e-4	0.0003
	x^3	-0.0056	-0.0066	-0.0084	-0.0093	-0.0082	-0.0145	-0.0128	-0.0215	-0.0296
	x^2	0.1035	0.18151	0.2451	0.26633	0.2935	0.45133	0.3748	0.5663	0.7002
	x^1	0.6783	-0.5248	-1.2082	-1.8137	-3.0066	-3.5631	-3.2497	-3.3324	-2.670
	x^0	297.68	289.37	282.16	285.51	285.67	270.26	289.65	281.79	280.59
15	x^4	2e-5	-3e-6	2e-5	1.5e-5	3.7e-5	4.3e-6	-9.4e-6	9.4e-6	-3.3e-6
	x^3	-0.0023	-7 e-5	-0.0021	-0.0017	-0.0035	-0.0008	0.00028	-0.0083	-0.0011
	x^2	0.05344	0.01472	0.04312	0.06127	0.08215	0.04273	0.01497	0.196	0.0854
	x^1	0.3206	-0.0065	0.3016	-0.5548	0.04408	-0.9091	-0.4851	-0.6389	-1.159
	x^0	295.8	304.9	305.4	299.4	305.9	306.1	317	291	309.6
20	x^4	4.3e-5	2.8e-5	6.8e-5	6.5e-5	5.1e-5	8.2e-5	5.9e-5	6.8e-5	0.0002
	x^3	-0.0035	-0.0027	-0.0063	-0.0062	-0.0050	-0.0074	-0.0053	-0.0061	-0.0135
	x^2	0.05486	0.06208	0.1408	0.1568	0.1283	0.162	0.1111	0.1326	0.2697
	x^1	0.8773	0.4653	0.5157	-0.0279	-0.1029	0.3137	0.3065	0.3488	0.9225
	x^0	299.6	298.2	289.1	284.5	290.9	287.3	292.1	287.7	269.7

(a)

Ambient Temperature (°C)	Polynomial Term	Depth of Discharge (%)								
		10	20	30	40	50	60	70	80	90
8	x^4	-2.9e-5	-2.5e-6	-2.7e-5	-3.4e-5	-5.4e-5	-3.2e-5	7.6e-6	-8.2e-7	-8.7e-5
	x^3	0.0028	0.0004	0.0022	0.0026	0.0046	0.0021	0.0014	-0.0002	0.0055
	x^2	-0.0871	-0.0267	-0.0464	-0.0449	-0.0969	-0.0201	0.0538	0.0067	-0.0309
	x^1	1.204	1.022	0.3693	-0.2781	-0.2292	-0.6308	-0.2904	-0.1876	-1.775
	x^0	303.3	303.8	313.8	325	335.3	329.9	322.5	337.8	341.5
	x^4	3.9e-6	1.1e-5	5.6e-6	1.9e-5	2.0e-5	2.1e-6	2.9e-5	1.9e-5	-2.3e-5
	x^3	-2.3e-5	-0.0009	-0.0002	-0.0014	-0.0016	-0.0004	0.0024	0.0013	0.0011

Appendix I

15	x^2	-0.0283	0.0006	-0.0248	0.0045	0.0151	0.0061	-0.0627	-0.0191	0.0053
	x^1	1.396	1.141	1.194	0.9702	0.9257	0.5471	0.5363	0.1432	-0.1059
	x^0	292.2	292.6	302.4	305.2	302.9	304.4	313.6	307.4	306
20	x^4	4.1e-6	-5.6e-6	-1.2e-5	-5.9e-6	8.2e-7	1.2e-6	-1.6e-6	-3e-19	-2.8e-5
	x^3	-0.0003	0.0003	0.0011	0.0005	-0.0014	-0.0003	-0.0002	-0.0007	0.0014
	x^2	-0.0140	-0.0174	-0.0411	-0.0022	-0.0088	0.0042	0.0007	0.3481	0.0009
	x^1	1.32	1.017	0.9691	0.7497	0.8672	0.6642	0.7832	0.3287	-0.0058
	x^0	292.3	296.1	304	304.5	301.4	301.4	289.6	293.3	296.1

(b)

Ambient Temperature (°C)	Polynomial Term	Depth of Discharge (%)								
		10	20	30	40	50	60	70	80	90
8	x^3	0.0007	0.0008	0.0011	0.0001	0.0001	0.0001	0.0008	0.0004	-0.0005
	x^2	-0.0719	-0.0837	-0.1061	-0.0909	-0.0998	-0.0941	-0.0741	-0.0426	0.0415
	x^1	2.7565	2.9852	3.4389	2.8241	3.1074	2.8231	2.2565	1.6602	-0.5519
	x^0	257.43	259.06	264.57	274.78	275.58	282.11	288.23	289.22	301.29
15	x^3	0.0005	0.0008	0.0002	0.0009	0.0001	0.0005	0.0003	0.00026	9.9e-5
	x^2	-0.0559	-0.0711	-0.0283	-0.0778	-0.0185	-0.0507	-0.03	-0.0261	-0.0143
	x^1	2.4519	2.4361	1.5278	2.4306	0.9981	1.7065	1.2319	1	0.7546
	x^0	251.58	258.25	264.8	265.94	275.96	273.42	276.4	278.62	275.82
20	x^3	0.0002	-0.0001	-3.7e-5	-9.9e-5	0.0001	0.0001	-2.5e-5	-1.2e-5	-0.0006
	x^2	-0.0293	0.0009	-0.0061	0.00037	-0.0185	-0.0161	-0.0063	-0.0076	0.0422
	x^1	1.7574	0.8148	0.8389	0.6093	0.9815	0.8278	0.687	0.7796	-0.4639
	x^0	263.92	273.42	277.46	280.46	281.29	283.25	281.48	277.29	279.08

(c)

Table A3: Coefficients of the fitting polynomials used for generating virtual samples as a function of ambient temperature for LFP pouch cells of different nominal capacities and discharge rates of (a) 0.33C, (b) 1C and (c) 3C

Appendix II: Authorship declaration and copyright forms

Paper 1



Swinburne Research

Authorship Indication Form For PhD (including associated papers) candidates

NOTE

This Authorship Indication form is a statement detailing the percentage of the contribution of each author in each associated 'paper'. This form must be signed by each co-author and the Principal Coordinating Supervisor. This form must be added to the publication of your final thesis as an appendix. Please fill out a separate form for each associated paper to be included in your thesis.

DECLARATION

We hereby declare our contribution to the publication of the 'paper' entitled:

REVIEW OF MECHANICAL DESIGN AND STRATEGIC PLACEMENT
TECHNIQUE OF A ROBUST BATTERY PACK FOR ELECTRIC VEHICLES

First Author

Name: SHASHANK ARORA Signature: _____

Percentage of contribution: 100 % 95 % SP Date: 15/05/2017

Brief description of contribution to the 'paper' and your central responsibilities/role on project:

Second Author

Name: WEIXIANG SHEN Signature: W.S.

Percentage of contribution: 0 % 5 % SP Date: 15/05/2017

Brief description of your contribution to the 'paper': Thesis Supervisor

Third Author

Name: AJAY KAPOOR Signature: Ajay Kapoor

Percentage of contribution: 0 % Date: 15/05/2017

Brief description of your contribution to the 'paper': Thesis Supervisor

Fourth Author

Name: _____ Signature: _____

Percentage of contribution: _____ Date: ____/____/____

Brief description of your contribution to the 'paper':

Principal Coordinating Supervisor: Name: Prof. AJAY KAPOOR Signature: Ajay Kapoor
Date: 15/05/2017

In the case of more than four authors please attach another sheet with the names, signatures and contribution of the authors.

Appendix II

Paper 2



Swinburne Research

Authorship Indication Form For PhD (including associated papers) candidates

NOTE

This Authorship Indication form is a statement detailing the percentage of the contribution of each author in each associated 'paper'. This form must be signed by each co-author and the Principal Coordinating Supervisor. This form must be added to the publication of your final thesis as an appendix. Please fill out a separate form for each associated paper to be included in your thesis.

DECLARATION

We hereby declare our contribution to the publication of the 'paper' entitled:

NEURAL NETWORK BASED COMPUTATIONAL MODEL FOR ESTIMATION OF HEAT GENERATION IN LiFePO₄ POUCH CELLS OF DIFFERENT NOMINAL CAPACITY
First Author

Name: SHASHANK ARORA Signature: _____

Percentage of contribution: 100 % 95.1 SA Date: 15/05/2017

Brief description of contribution to the 'paper' and your central responsibilities/role on project:

Second Author

Name: WEIXIANG SHEN Signature: E

Percentage of contribution: 0 % 54 SA Date: 15/05/2017

Brief description of your contribution to the 'paper': Thesis Supervisor

Third Author

Name: AJAY KAPOOR Signature: Ajay Kapoor

Percentage of contribution: 0 % Date: 15/05/2017

Brief description of your contribution to the 'paper': Thesis Supervisor

Fourth Author

Name: _____ Signature: _____

Percentage of contribution: ____ % Date: ____ / ____ / ____

Brief description of your contribution to the 'paper':

Principal Coordinating Supervisor: Name: Prof. AJAY KAPOOR Signature: Ajay Kapoor
Date: 15/05/2017

In the case of more than four authors please attach another sheet with the names, signatures and contribution of the authors.

Paper 3



Swinburne Research

Authorship Indication Form For PhD (including associated papers) candidates

NOTE

This Authorship Indication form is a statement detailing the percentage of the contribution of each author in each associated 'paper'. This form must be signed by each co-author and the Principal Coordinating Supervisor. This form must be added to the publication of your final thesis as an appendix. Please fill out a separate form for each associated paper to be included in your thesis.

DECLARATION

We hereby declare our contribution to the publication of the 'paper' entitled:

CRITICAL ANALYSIS OF OPEN CIRCUIT VOLTAGE AND ITS EFFECT ON
ESTIMATION OF IRREVERSIBLE HEAT FOR LI-ION POUCH CELLS

First Author

Name: SHASHANK ARORA Signature: _____

Percentage of contribution: 100% 95% SP Date: 15/05/2017

Brief description of contribution to the 'paper' and your central responsibilities/role on project:

Second Author

Name: WEIXIANG SHEN Signature: S

Percentage of contribution: 0% 5% SP Date: 15/05/2017

Brief description of your contribution to the 'paper': Thesis Supervisor

Third Author

Name: AJAY KAPOOR Signature: Ajay Kapoor

Percentage of contribution: 0% Date: 15/05/2017

Brief description of your contribution to the 'paper': Thesis Supervisor

Fourth Author

Name: _____ Signature: _____

Percentage of contribution: _____ % Date: ____ / ____ / ____

Brief description of your contribution to the 'paper':

Principal Coordinating Supervisor: Name: <u>Prof. AJAY KAPOOR</u>	Signature: <u>Ajay Kapoor</u>
Date: <u>15/05/2017</u>	

In the case of more than four authors please attach another sheet with the names, signatures and contribution of the authors.

**ELSEVIER LICENSE
TERMS AND CONDITIONS**

May 08, 2017

This Agreement between Shashank Arora ("You") and Elsevier ("Elsevier") consists of your license details and the terms and conditions provided by Elsevier and Copyright Clearance Center.

License Number	4104560309852
License date	May 08, 2017
Licensed Content Publisher	Elsevier
Licensed Content Publication	Renewable and Sustainable Energy Reviews
Licensed Content Title	Review of mechanical design and strategic placement technique of a robust battery pack for electric vehicles
Licensed Content Author	Shashank Arora,Weixiang Shen,Ajay Kapoor
Licensed Content Date	July 2016
Licensed Content Volume	60
Licensed Content Issue	n/a
Licensed Content Pages	13
Start Page	1319
End Page	1331
Type of Use	reuse in a thesis/dissertation
Intended publisher of new work	other
Portion	full article
Format	both print and electronic
Are you the author of this Elsevier article?	Yes
Will you be translating?	No
Order reference number	
Title of your thesis/dissertation	Design of a modular battery pack for electric vehicles
Expected completion date	May 2017
Estimated size (number of pages)	210
Elsevier VAT number	GB 494 6272 12
Requestor Location	Shashank Arora H38, Swinburne University of Technology John Street Hawthorn, Victoria 3122 Australia Attn: Shashank Arora
Total	0.00 AUD
Terms and Conditions	

INTRODUCTION

1. The publisher for this copyrighted material is Elsevier. By clicking "accept" in connection with completing this licensing transaction, you agree that the following terms and conditions apply to this transaction (along with the Billing and Payment terms and conditions

established by Copyright Clearance Center, Inc. ("CCC"), at the time that you opened your Rightslink account and that are available at any time at <http://myaccount.copyright.com>).

GENERAL TERMS

2. Elsevier hereby grants you permission to reproduce the aforementioned material subject to the terms and conditions indicated.

3. Acknowledgement: If any part of the material to be used (for example, figures) has appeared in our publication with credit or acknowledgement to another source, permission must also be sought from that source. If such permission is not obtained then that material may not be included in your publication/copies. Suitable acknowledgement to the source must be made, either as a footnote or in a reference list at the end of your publication, as follows:

"Reprinted from Publication title, Vol /edition number, Author(s), Title of article / title of chapter, Pages No., Copyright (Year), with permission from Elsevier [OR APPLICABLE SOCIETY COPYRIGHT OWNER]." Also Lancet special credit - "Reprinted from The Lancet, Vol. number, Author(s), Title of article, Pages No., Copyright (Year), with permission from Elsevier."

4. Reproduction of this material is confined to the purpose and/or media for which permission is hereby given.

5. Altering/Modifying Material: Not Permitted. However figures and illustrations may be altered/adapted minimally to serve your work. Any other abbreviations, additions, deletions and/or any other alterations shall be made only with prior written authorization of Elsevier Ltd. (Please contact Elsevier at permissions@elsevier.com). No modifications can be made to any Lancet figures/tables and they must be reproduced in full.

6. If the permission fee for the requested use of our material is waived in this instance, please be advised that your future requests for Elsevier materials may attract a fee.

7. Reservation of Rights: Publisher reserves all rights not specifically granted in the combination of (i) the license details provided by you and accepted in the course of this licensing transaction, (ii) these terms and conditions and (iii) CCC's Billing and Payment terms and conditions.

8. License Contingent Upon Payment: While you may exercise the rights licensed immediately upon issuance of the license at the end of the licensing process for the transaction, provided that you have disclosed complete and accurate details of your proposed use, no license is finally effective unless and until full payment is received from you (either by publisher or by CCC) as provided in CCC's Billing and Payment terms and conditions. If full payment is not received on a timely basis, then any license preliminarily granted shall be deemed automatically revoked and shall be void as if never granted. Further, in the event that you breach any of these terms and conditions or any of CCC's Billing and Payment terms and conditions, the license is automatically revoked and shall be void as if never granted. Use of materials as described in a revoked license, as well as any use of the materials beyond the scope of an unrevoked license, may constitute copyright infringement and publisher reserves the right to take any and all action to protect its copyright in the materials.

9. Warranties: Publisher makes no representations or warranties with respect to the licensed material.

10. Indemnity: You hereby indemnify and agree to hold harmless publisher and CCC, and their respective officers, directors, employees and agents, from and against any and all claims arising out of your use of the licensed material other than as specifically authorized pursuant to this license.

11. No Transfer of License: This license is personal to you and may not be sublicensed, assigned, or transferred by you to any other person without publisher's written permission.

12. No Amendment Except in Writing: This license may not be amended except in a writing signed by both parties (or, in the case of publisher, by CCC on publisher's behalf).

13. Objection to Contrary Terms: Publisher hereby objects to any terms contained in any purchase order, acknowledgment, check endorsement or other writing prepared by you, which terms are inconsistent with these terms and conditions or CCC's Billing and Payment terms and conditions. These terms and conditions, together with CCC's Billing and Payment terms and conditions (which are incorporated herein), comprise the entire agreement between you and publisher (and CCC) concerning this licensing transaction. In the event of

any conflict between your obligations established by these terms and conditions and those established by CCC's Billing and Payment terms and conditions, these terms and conditions shall control.

14. Revocation: Elsevier or Copyright Clearance Center may deny the permissions described in this License at their sole discretion, for any reason or no reason, with a full refund payable to you. Notice of such denial will be made using the contact information provided by you. Failure to receive such notice will not alter or invalidate the denial. In no event will Elsevier or Copyright Clearance Center be responsible or liable for any costs, expenses or damage incurred by you as a result of a denial of your permission request, other than a refund of the amount(s) paid by you to Elsevier and/or Copyright Clearance Center for denied permissions.

LIMITED LICENSE

The following terms and conditions apply only to specific license types:

15. **Translation:** This permission is granted for non-exclusive world **English** rights only unless your license was granted for translation rights. If you licensed translation rights you may only translate this content into the languages you requested. A professional translator must perform all translations and reproduce the content word for word preserving the integrity of the article.

16. **Posting licensed content on any Website:** The following terms and conditions apply as follows: Licensing material from an Elsevier journal: All content posted to the web site must maintain the copyright information line on the bottom of each image; A hyper-text must be included to the Homepage of the journal from which you are licensing at <http://www.sciencedirect.com/science/journal/xxxxx> or the Elsevier homepage for books at <http://www.elsevier.com>; Central Storage: This license does not include permission for a scanned version of the material to be stored in a central repository such as that provided by Heron/XanEdu.

Licensing material from an Elsevier book: A hyper-text link must be included to the Elsevier homepage at <http://www.elsevier.com>. All content posted to the web site must maintain the copyright information line on the bottom of each image.

Posting licensed content on Electronic reserve: In addition to the above the following clauses are applicable: The web site must be password-protected and made available only to bona fide students registered on a relevant course. This permission is granted for 1 year only. You may obtain a new license for future website posting.

17. **For journal authors:** the following clauses are applicable in addition to the above:

Preprints:

A preprint is an author's own write-up of research results and analysis, it has not been peer-reviewed, nor has it had any other value added to it by a publisher (such as formatting, copyright, technical enhancement etc.).

Authors can share their preprints anywhere at any time. Preprints should not be added to or enhanced in any way in order to appear more like, or to substitute for, the final versions of articles however authors can update their preprints on arXiv or RePEc with their Accepted Author Manuscript (see below).

If accepted for publication, we encourage authors to link from the preprint to their formal publication via its DOI. Millions of researchers have access to the formal publications on ScienceDirect, and so links will help users to find, access, cite and use the best available version. Please note that Cell Press, The Lancet and some society-owned have different preprint policies. Information on these policies is available on the journal homepage.

Accepted Author Manuscripts: An accepted author manuscript is the manuscript of an article that has been accepted for publication and which typically includes author-incorporated changes suggested during submission, peer review and editor-author communications.

Authors can share their accepted author manuscript:

- immediately
 - via their non-commercial person homepage or blog
 - by updating a preprint in arXiv or RePEc with the accepted manuscript

- via their research institute or institutional repository for internal institutional uses or as part of an invitation-only research collaboration work-group
- directly by providing copies to their students or to research collaborators for their personal use
- for private scholarly sharing as part of an invitation-only work group on commercial sites with which Elsevier has an agreement
- After the embargo period
 - via non-commercial hosting platforms such as their institutional repository
 - via commercial sites with which Elsevier has an agreement

In all cases accepted manuscripts should:

- link to the formal publication via its DOI
- bear a CC-BY-NC-ND license - this is easy to do
- if aggregated with other manuscripts, for example in a repository or other site, be shared in alignment with our hosting policy not be added to or enhanced in any way to appear more like, or to substitute for, the published journal article.

Published journal article (JPA): A published journal article (PJA) is the definitive final record of published research that appears or will appear in the journal and embodies all value-adding publishing activities including peer review co-ordination, copy-editing, formatting, (if relevant) pagination and online enrichment.

Policies for sharing publishing journal articles differ for subscription and gold open access articles:

Subscription Articles: If you are an author, please share a link to your article rather than the full-text. Millions of researchers have access to the formal publications on ScienceDirect, and so links will help your users to find, access, cite, and use the best available version. Theses and dissertations which contain embedded PJsAs as part of the formal submission can be posted publicly by the awarding institution with DOI links back to the formal publications on ScienceDirect.

If you are affiliated with a library that subscribes to ScienceDirect you have additional private sharing rights for others' research accessed under that agreement. This includes use for classroom teaching and internal training at the institution (including use in course packs and courseware programs), and inclusion of the article for grant funding purposes.

Gold Open Access Articles: May be shared according to the author-selected end-user license and should contain a [CrossMark logo](#), the end user license, and a DOI link to the formal publication on ScienceDirect.

Please refer to Elsevier's [posting policy](#) for further information.

18. For book authors the following clauses are applicable in addition to the above:

Authors are permitted to place a brief summary of their work online only. You are not allowed to download and post the published electronic version of your chapter, nor may you scan the printed edition to create an electronic version. **Posting to a repository:** Authors are permitted to post a summary of their chapter only in their institution's repository.

19. Thesis/Dissertation: If your license is for use in a thesis/dissertation your thesis may be submitted to your institution in either print or electronic form. Should your thesis be published commercially, please reapply for permission. These requirements include permission for the Library and Archives of Canada to supply single copies, on demand, of the complete thesis and include permission for Proquest/UMI to supply single copies, on demand, of the complete thesis. Should your thesis be published commercially, please reapply for permission. Theses and dissertations which contain embedded PJsAs as part of the formal submission can be posted publicly by the awarding institution with DOI links back to the formal publications on ScienceDirect.

Elsevier Open Access Terms and Conditions

You can publish open access with Elsevier in hundreds of open access journals or in nearly 2000 established subscription journals that support open access publishing. Permitted third party re-use of these open access articles is defined by the author's choice of Creative Commons user license. See our [open access license policy](#) for more information.

Terms & Conditions applicable to all Open Access articles published with Elsevier:

Any reuse of the article must not represent the author as endorsing the adaptation of the article nor should the article be modified in such a way as to damage the author's honour or reputation. If any changes have been made, such changes must be clearly indicated.

The author(s) must be appropriately credited and we ask that you include the end user license and a DOI link to the formal publication on ScienceDirect.

If any part of the material to be used (for example, figures) has appeared in our publication with credit or acknowledgement to another source it is the responsibility of the user to ensure their reuse complies with the terms and conditions determined by the rights holder.

Additional Terms & Conditions applicable to each Creative Commons user license:

CC BY: The CC-BY license allows users to copy, to create extracts, abstracts and new works from the Article, to alter and revise the Article and to make commercial use of the Article (including reuse and/or resale of the Article by commercial entities), provided the user gives appropriate credit (with a link to the formal publication through the relevant DOI), provides a link to the license, indicates if changes were made and the licensor is not represented as endorsing the use made of the work. The full details of the license are available at <http://creativecommons.org/licenses/by/4.0>.

CC BY NC SA: The CC BY-NC-SA license allows users to copy, to create extracts, abstracts and new works from the Article, to alter and revise the Article, provided this is not done for commercial purposes, and that the user gives appropriate credit (with a link to the formal publication through the relevant DOI), provides a link to the license, indicates if changes were made and the licensor is not represented as endorsing the use made of the work. Further, any new works must be made available on the same conditions. The full details of the license are available at <http://creativecommons.org/licenses/by-nc-sa/4.0>.

CC BY NC ND: The CC BY-NC-ND license allows users to copy and distribute the Article, provided this is not done for commercial purposes and further does not permit distribution of the Article if it is changed or edited in any way, and provided the user gives appropriate credit (with a link to the formal publication through the relevant DOI), provides a link to the license, and that the licensor is not represented as endorsing the use made of the work. The full details of the license are available at <http://creativecommons.org/licenses/by-nc-nd/4.0>.

Any commercial reuse of Open Access articles published with a CC BY NC SA or CC BY NC ND license requires permission from Elsevier and will be subject to a fee.

Commercial reuse includes:

- Associating advertising with the full text of the Article
- Charging fees for document delivery or access
- Article aggregation
- Systematic distribution via e-mail lists or share buttons

Posting or linking by commercial companies for use by customers of those companies.

20. Other Conditions:

v1.9

Questions? customercare@copyright.com or +1-855-239-3415 (toll free in the US) or +1-978-646-2777.

**ELSEVIER LICENSE
TERMS AND CONDITIONS**

May 08, 2017

This Agreement between Shashank Arora ("You") and Elsevier ("Elsevier") consists of your license details and the terms and conditions provided by Elsevier and Copyright Clearance Center.

License Number	4104560198073
License date	May 08, 2017
Licensed Content Publisher	Elsevier
Licensed Content Publication	Computers & Chemical Engineering
Licensed Content Title	Neural network based computational model for estimation of heat generation in LiFePO4 pouch cells of different nominal capacities
Licensed Content Author	Shashank Arora, Weixiang Shen, Ajay Kapoor
Licensed Content Date	9 June 2017
Licensed Content Volume	101
Licensed Content Issue	n/a
Licensed Content Pages	14
Start Page	81
End Page	94
Type of Use	reuse in a thesis/dissertation
Portion	full article
Format	both print and electronic
Are you the author of this Elsevier article?	Yes
Will you be translating?	No
Order reference number	
Title of your thesis/dissertation	Design of a modular battery pack for electric vehicles
Expected completion date	May 2017
Estimated size (number of pages)	210
Elsevier VAT number	GB 494 6272 12
Requestor Location	Shashank Arora H38, Swinburne University of Technology John Street Hawthorn, Victoria 3122 Australia Attn: Shashank Arora
Total	0.00 AUD

Terms and Conditions

INTRODUCTION

1. The publisher for this copyrighted material is Elsevier. By clicking "accept" in connection with completing this licensing transaction, you agree that the following terms and conditions apply to this transaction (along with the Billing and Payment terms and conditions established by Copyright Clearance Center, Inc. ("CCC"), at the time that you opened your Rightslink account and that are available at any time at <http://myaccount.copyright.com>).

GENERAL TERMS

2. Elsevier hereby grants you permission to reproduce the aforementioned material subject to the terms and conditions indicated.

3. Acknowledgement: If any part of the material to be used (for example, figures) has appeared in our publication with credit or acknowledgement to another source, permission must also be sought from that source. If such permission is not obtained then that material may not be included in your publication/copies. Suitable acknowledgement to the source must be made, either as a footnote or in a reference list at the end of your publication, as follows:

"Reprinted from Publication title, Vol /edition number, Author(s), Title of article / title of chapter, Pages No., Copyright (Year), with permission from Elsevier [OR APPLICABLE SOCIETY COPYRIGHT OWNER]." Also Lancet special credit - "Reprinted from The Lancet, Vol. number, Author(s), Title of article, Pages No., Copyright (Year), with permission from Elsevier."

4. Reproduction of this material is confined to the purpose and/or media for which permission is hereby given.

5. Altering/Modifying Material: Not Permitted. However figures and illustrations may be altered/adapted minimally to serve your work. Any other abbreviations, additions, deletions and/or any other alterations shall be made only with prior written authorization of Elsevier Ltd. (Please contact Elsevier at permissions@elsevier.com). No modifications can be made to any Lancet figures/tables and they must be reproduced in full.

6. If the permission fee for the requested use of our material is waived in this instance, please be advised that your future requests for Elsevier materials may attract a fee.

7. Reservation of Rights: Publisher reserves all rights not specifically granted in the combination of (i) the license details provided by you and accepted in the course of this licensing transaction, (ii) these terms and conditions and (iii) CCC's Billing and Payment terms and conditions.

8. License Contingent Upon Payment: While you may exercise the rights licensed immediately upon issuance of the license at the end of the licensing process for the transaction, provided that you have disclosed complete and accurate details of your proposed use, no license is finally effective unless and until full payment is received from you (either by publisher or by CCC) as provided in CCC's Billing and Payment terms and conditions. If full payment is not received on a timely basis, then any license preliminarily granted shall be deemed automatically revoked and shall be void as if never granted. Further, in the event that you breach any of these terms and conditions or any of CCC's Billing and Payment terms and conditions, the license is automatically revoked and shall be void as if never granted. Use of materials as described in a revoked license, as well as any use of the materials beyond the scope of an unrevoked license, may constitute copyright infringement and publisher reserves the right to take any and all action to protect its copyright in the materials.

9. Warranties: Publisher makes no representations or warranties with respect to the licensed material.

10. Indemnity: You hereby indemnify and agree to hold harmless publisher and CCC, and their respective officers, directors, employees and agents, from and against any and all claims arising out of your use of the licensed material other than as specifically authorized pursuant to this license.

11. No Transfer of License: This license is personal to you and may not be sublicensed, assigned, or transferred by you to any other person without publisher's written permission.

12. No Amendment Except in Writing: This license may not be amended except in a writing signed by both parties (or, in the case of publisher, by CCC on publisher's behalf).

13. Objection to Contrary Terms: Publisher hereby objects to any terms contained in any purchase order, acknowledgment, check endorsement or other writing prepared by you, which terms are inconsistent with these terms and conditions or CCC's Billing and Payment terms and conditions. These terms and conditions, together with CCC's Billing and Payment terms and conditions (which are incorporated herein), comprise the entire agreement between you and publisher (and CCC) concerning this licensing transaction. In the event of any conflict between your obligations established by these terms and conditions and those

established by CCC's Billing and Payment terms and conditions, these terms and conditions shall control.

14. Revocation: Elsevier or Copyright Clearance Center may deny the permissions described in this License at their sole discretion, for any reason or no reason, with a full refund payable to you. Notice of such denial will be made using the contact information provided by you. Failure to receive such notice will not alter or invalidate the denial. In no event will Elsevier or Copyright Clearance Center be responsible or liable for any costs, expenses or damage incurred by you as a result of a denial of your permission request, other than a refund of the amount(s) paid by you to Elsevier and/or Copyright Clearance Center for denied permissions.

LIMITED LICENSE

The following terms and conditions apply only to specific license types:

15. **Translation:** This permission is granted for non-exclusive world English rights only unless your license was granted for translation rights. If you licensed translation rights you may only translate this content into the languages you requested. A professional translator must perform all translations and reproduce the content word for word preserving the integrity of the article.

16. **Posting licensed content on any Website:** The following terms and conditions apply as follows: Licensing material from an Elsevier journal: All content posted to the web site must maintain the copyright information line on the bottom of each image; A hyper-text must be included to the Homepage of the journal from which you are licensing at <http://www.sciencedirect.com/science/journal/xxxxx> or the Elsevier homepage for books at <http://www.elsevier.com>; Central Storage: This license does not include permission for a scanned version of the material to be stored in a central repository such as that provided by Heron/XanEdu.

Licensing material from an Elsevier book: A hyper-text link must be included to the Elsevier homepage at <http://www.elsevier.com>. All content posted to the web site must maintain the copyright information line on the bottom of each image.

Posting licensed content on Electronic reserve: In addition to the above the following clauses are applicable: The web site must be password-protected and made available only to bona fide students registered on a relevant course. This permission is granted for 1 year only. You may obtain a new license for future website posting.

17. **For journal authors:** the following clauses are applicable in addition to the above:

Preprints:

A preprint is an author's own write-up of research results and analysis, it has not been peer-reviewed, nor has it had any other value added to it by a publisher (such as formatting, copyright, technical enhancement etc.).

Authors can share their preprints anywhere at any time. Preprints should not be added to or enhanced in any way in order to appear more like, or to substitute for, the final versions of articles however authors can update their preprints on arXiv or RePEc with their Accepted Author Manuscript (see below).

If accepted for publication, we encourage authors to link from the preprint to their formal publication via its DOI. Millions of researchers have access to the formal publications on ScienceDirect, and so links will help users to find, access, cite and use the best available version. Please note that Cell Press, The Lancet and some society-owned have different preprint policies. Information on these policies is available on the journal homepage.

Accepted Author Manuscripts: An accepted author manuscript is the manuscript of an article that has been accepted for publication and which typically includes author-incorporated changes suggested during submission, peer review and editor-author communications.

Authors can share their accepted author manuscript:

- immediately
 - via their non-commercial person homepage or blog
 - by updating a preprint in arXiv or RePEc with the accepted manuscript
 - via their research institute or institutional repository for internal institutional uses or as part of an invitation-only research collaboration work-group

- directly by providing copies to their students or to research collaborators for their personal use
- for private scholarly sharing as part of an invitation-only work group on commercial sites with which Elsevier has an agreement
- After the embargo period
 - via non-commercial hosting platforms such as their institutional repository
 - via commercial sites with which Elsevier has an agreement

In all cases accepted manuscripts should:

- link to the formal publication via its DOI
- bear a CC-BY-NC-ND license - this is easy to do
- if aggregated with other manuscripts, for example in a repository or other site, be shared in alignment with our hosting policy not be added to or enhanced in any way to appear more like, or to substitute for, the published journal article.

Published journal article (JPA): A published journal article (PJA) is the definitive final record of published research that appears or will appear in the journal and embodies all value-adding publishing activities including peer review co-ordination, copy-editing, formatting, (if relevant) pagination and online enrichment.

Policies for sharing publishing journal articles differ for subscription and gold open access articles:

Subscription Articles: If you are an author, please share a link to your article rather than the full-text. Millions of researchers have access to the formal publications on ScienceDirect, and so links will help your users to find, access, cite, and use the best available version. Theses and dissertations which contain embedded PJsAs as part of the formal submission can be posted publicly by the awarding institution with DOI links back to the formal publications on ScienceDirect.

If you are affiliated with a library that subscribes to ScienceDirect you have additional private sharing rights for others' research accessed under that agreement. This includes use for classroom teaching and internal training at the institution (including use in course packs and courseware programs), and inclusion of the article for grant funding purposes.

Gold Open Access Articles: May be shared according to the author-selected end-user license and should contain a [CrossMark logo](#), the end user license, and a DOI link to the formal publication on ScienceDirect.

Please refer to Elsevier's [posting policy](#) for further information.

18. **For book authors** the following clauses are applicable in addition to the above:

Authors are permitted to place a brief summary of their work online only. You are not allowed to download and post the published electronic version of your chapter, nor may you scan the printed edition to create an electronic version. **Posting to a repository:** Authors are permitted to post a summary of their chapter only in their institution's repository.

19. **Thesis/Dissertation:** If your license is for use in a thesis/dissertation your thesis may be submitted to your institution in either print or electronic form. Should your thesis be published commercially, please reapply for permission. These requirements include permission for the Library and Archives of Canada to supply single copies, on demand, of the complete thesis and include permission for Proquest/UMI to supply single copies, on demand, of the complete thesis. Should your thesis be published commercially, please reapply for permission. Theses and dissertations which contain embedded PJsAs as part of the formal submission can be posted publicly by the awarding institution with DOI links back to the formal publications on ScienceDirect.

Elsevier Open Access Terms and Conditions

You can publish open access with Elsevier in hundreds of open access journals or in nearly 2000 established subscription journals that support open access publishing. Permitted third party re-use of these open access articles is defined by the author's choice of Creative Commons user license. See our [open access license policy](#) for more information.

Terms & Conditions applicable to all Open Access articles published with Elsevier:

Any reuse of the article must not represent the author as endorsing the adaptation of the article nor should the article be modified in such a way as to damage the author's honour or reputation. If any changes have been made, such changes must be clearly indicated. The author(s) must be appropriately credited and we ask that you include the end user license and a DOI link to the formal publication on ScienceDirect.

If any part of the material to be used (for example, figures) has appeared in our publication with credit or acknowledgement to another source it is the responsibility of the user to ensure their reuse complies with the terms and conditions determined by the rights holder.

Additional Terms & Conditions applicable to each Creative Commons user license:

CC BY: The CC-BY license allows users to copy, to create extracts, abstracts and new works from the Article, to alter and revise the Article and to make commercial use of the Article (including reuse and/or resale of the Article by commercial entities), provided the user gives appropriate credit (with a link to the formal publication through the relevant DOI), provides a link to the license, indicates if changes were made and the licensor is not represented as endorsing the use made of the work. The full details of the license are available at <http://creativecommons.org/licenses/by/4.0>.

CC BY NC SA: The CC BY-NC-SA license allows users to copy, to create extracts, abstracts and new works from the Article, to alter and revise the Article, provided this is not done for commercial purposes, and that the user gives appropriate credit (with a link to the formal publication through the relevant DOI), provides a link to the license, indicates if changes were made and the licensor is not represented as endorsing the use made of the work. Further, any new works must be made available on the same conditions. The full details of the license are available at <http://creativecommons.org/licenses/by-nc-sa/4.0>.

CC BY NC ND: The CC BY-NC-ND license allows users to copy and distribute the Article, provided this is not done for commercial purposes and further does not permit distribution of the Article if it is changed or edited in any way, and provided the user gives appropriate credit (with a link to the formal publication through the relevant DOI), provides a link to the license, and that the licensor is not represented as endorsing the use made of the work. The full details of the license are available at <http://creativecommons.org/licenses/by-nc-nd/4.0>.

Any commercial reuse of Open Access articles published with a CC BY NC SA or CC BY NC ND license requires permission from Elsevier and will be subject to a fee.

Commercial reuse includes:

- Associating advertising with the full text of the Article
- Charging fees for document delivery or access
- Article aggregation
- Systematic distribution via e-mail lists or share buttons

Posting or linking by commercial companies for use by customers of those companies.

20. Other Conditions:

v1.9

Questions? customercare@copyright.com or +1-855-239-3415 (toll free in the US) or +1-978-646-2777.

**ELSEVIER LICENSE
TERMS AND CONDITIONS**

May 08, 2017

This Agreement between Shashank Arora ("You") and Elsevier ("Elsevier") consists of your license details and the terms and conditions provided by Elsevier and Copyright Clearance Center.

License Number	4104091236263
License date	May 08, 2017
Licensed Content Publisher	Elsevier
Licensed Content Publication	Journal of Power Sources
Licensed Content Title	Critical analysis of open circuit voltage and its effect on estimation of irreversible heat for Li-ion pouch cells
Licensed Content Author	Shashank Arora,Weixiang Shen,Ajay Kapoor
Licensed Content Date	15 May 2017
Licensed Content Volume	350
Licensed Content Issue	n/a
Licensed Content Pages	10
Start Page	117
End Page	126
Type of Use	reuse in a thesis/dissertation
Portion	full article
Format	both print and electronic
Are you the author of this Elsevier article?	Yes
Will you be translating?	No
Order reference number	
Title of your thesis/dissertation	Design of a modular battery pack for electric vehicles
Expected completion date	May 2017
Estimated size (number of pages)	210
Elsevier VAT number	GB 494 6272 12
Requestor Location	Shashank Arora H38, Swinburne University of Technology John Street Hawthorn, Victoria 3122 Australia Attn: Shashank Arora
Total	0.00 AUD

Terms and Conditions

INTRODUCTION

1. The publisher for this copyrighted material is Elsevier. By clicking "accept" in connection with completing this licensing transaction, you agree that the following terms and conditions apply to this transaction (along with the Billing and Payment terms and conditions established by Copyright Clearance Center, Inc. ("CCC"), at the time that you opened your Rightslink account and that are available at any time at <http://myaccount.copyright.com>).

GENERAL TERMS

2. Elsevier hereby grants you permission to reproduce the aforementioned material subject to the terms and conditions indicated.

3. Acknowledgement: If any part of the material to be used (for example, figures) has appeared in our publication with credit or acknowledgement to another source, permission must also be sought from that source. If such permission is not obtained then that material may not be included in your publication/copies. Suitable acknowledgement to the source must be made, either as a footnote or in a reference list at the end of your publication, as follows:

"Reprinted from Publication title, Vol /edition number, Author(s), Title of article / title of chapter, Pages No., Copyright (Year), with permission from Elsevier [OR APPLICABLE SOCIETY COPYRIGHT OWNER]." Also Lancet special credit - "Reprinted from The Lancet, Vol. number, Author(s), Title of article, Pages No., Copyright (Year), with permission from Elsevier."

4. Reproduction of this material is confined to the purpose and/or media for which permission is hereby given.

5. Altering/Modifying Material: Not Permitted. However figures and illustrations may be altered/adapted minimally to serve your work. Any other abbreviations, additions, deletions and/or any other alterations shall be made only with prior written authorization of Elsevier Ltd. (Please contact Elsevier at permissions@elsevier.com). No modifications can be made to any Lancet figures/tables and they must be reproduced in full.

6. If the permission fee for the requested use of our material is waived in this instance, please be advised that your future requests for Elsevier materials may attract a fee.

7. Reservation of Rights: Publisher reserves all rights not specifically granted in the combination of (i) the license details provided by you and accepted in the course of this licensing transaction, (ii) these terms and conditions and (iii) CCC's Billing and Payment terms and conditions.

8. License Contingent Upon Payment: While you may exercise the rights licensed immediately upon issuance of the license at the end of the licensing process for the transaction, provided that you have disclosed complete and accurate details of your proposed use, no license is finally effective unless and until full payment is received from you (either by publisher or by CCC) as provided in CCC's Billing and Payment terms and conditions. If full payment is not received on a timely basis, then any license preliminarily granted shall be deemed automatically revoked and shall be void as if never granted. Further, in the event that you breach any of these terms and conditions or any of CCC's Billing and Payment terms and conditions, the license is automatically revoked and shall be void as if never granted. Use of materials as described in a revoked license, as well as any use of the materials beyond the scope of an unrevoked license, may constitute copyright infringement and publisher reserves the right to take any and all action to protect its copyright in the materials.

9. Warranties: Publisher makes no representations or warranties with respect to the licensed material.

10. Indemnity: You hereby indemnify and agree to hold harmless publisher and CCC, and their respective officers, directors, employees and agents, from and against any and all claims arising out of your use of the licensed material other than as specifically authorized pursuant to this license.

11. No Transfer of License: This license is personal to you and may not be sublicensed, assigned, or transferred by you to any other person without publisher's written permission.

12. No Amendment Except in Writing: This license may not be amended except in a writing signed by both parties (or, in the case of publisher, by CCC on publisher's behalf).

13. Objection to Contrary Terms: Publisher hereby objects to any terms contained in any purchase order, acknowledgment, check endorsement or other writing prepared by you, which terms are inconsistent with these terms and conditions or CCC's Billing and Payment terms and conditions. These terms and conditions, together with CCC's Billing and Payment terms and conditions (which are incorporated herein), comprise the entire agreement between you and publisher (and CCC) concerning this licensing transaction. In the event of any conflict between your obligations established by these terms and conditions and those

established by CCC's Billing and Payment terms and conditions, these terms and conditions shall control.

14. Revocation: Elsevier or Copyright Clearance Center may deny the permissions described in this License at their sole discretion, for any reason or no reason, with a full refund payable to you. Notice of such denial will be made using the contact information provided by you. Failure to receive such notice will not alter or invalidate the denial. In no event will Elsevier or Copyright Clearance Center be responsible or liable for any costs, expenses or damage incurred by you as a result of a denial of your permission request, other than a refund of the amount(s) paid by you to Elsevier and/or Copyright Clearance Center for denied permissions.

LIMITED LICENSE

The following terms and conditions apply only to specific license types:

15. **Translation:** This permission is granted for non-exclusive world English rights only unless your license was granted for translation rights. If you licensed translation rights you may only translate this content into the languages you requested. A professional translator must perform all translations and reproduce the content word for word preserving the integrity of the article.

16. **Posting licensed content on any Website:** The following terms and conditions apply as follows: Licensing material from an Elsevier journal: All content posted to the web site must maintain the copyright information line on the bottom of each image; A hyper-text must be included to the Homepage of the journal from which you are licensing at <http://www.sciencedirect.com/science/journal/xxxxx> or the Elsevier homepage for books at <http://www.elsevier.com>; Central Storage: This license does not include permission for a scanned version of the material to be stored in a central repository such as that provided by Heron/XanEdu.

Licensing material from an Elsevier book: A hyper-text link must be included to the Elsevier homepage at <http://www.elsevier.com>. All content posted to the web site must maintain the copyright information line on the bottom of each image.

Posting licensed content on Electronic reserve: In addition to the above the following clauses are applicable: The web site must be password-protected and made available only to bona fide students registered on a relevant course. This permission is granted for 1 year only. You may obtain a new license for future website posting.

17. **For journal authors:** the following clauses are applicable in addition to the above:

Preprints:

A preprint is an author's own write-up of research results and analysis, it has not been peer-reviewed, nor has it had any other value added to it by a publisher (such as formatting, copyright, technical enhancement etc.).

Authors can share their preprints anywhere at any time. Preprints should not be added to or enhanced in any way in order to appear more like, or to substitute for, the final versions of articles however authors can update their preprints on arXiv or RePEc with their Accepted Author Manuscript (see below).

If accepted for publication, we encourage authors to link from the preprint to their formal publication via its DOI. Millions of researchers have access to the formal publications on ScienceDirect, and so links will help users to find, access, cite and use the best available version. Please note that Cell Press, The Lancet and some society-owned have different preprint policies. Information on these policies is available on the journal homepage.

Accepted Author Manuscripts: An accepted author manuscript is the manuscript of an article that has been accepted for publication and which typically includes author-incorporated changes suggested during submission, peer review and editor-author communications.

Authors can share their accepted author manuscript:

- immediately
 - via their non-commercial person homepage or blog
 - by updating a preprint in arXiv or RePEc with the accepted manuscript
 - via their research institute or institutional repository for internal institutional uses or as part of an invitation-only research collaboration work-group

- directly by providing copies to their students or to research collaborators for their personal use
- for private scholarly sharing as part of an invitation-only work group on commercial sites with which Elsevier has an agreement
- After the embargo period
 - via non-commercial hosting platforms such as their institutional repository
 - via commercial sites with which Elsevier has an agreement

In all cases accepted manuscripts should:

- link to the formal publication via its DOI
- bear a CC-BY-NC-ND license - this is easy to do
- if aggregated with other manuscripts, for example in a repository or other site, be shared in alignment with our hosting policy not be added to or enhanced in any way to appear more like, or to substitute for, the published journal article.

Published journal article (JPA): A published journal article (PJA) is the definitive final record of published research that appears or will appear in the journal and embodies all value-adding publishing activities including peer review co-ordination, copy-editing, formatting, (if relevant) pagination and online enrichment.

Policies for sharing publishing journal articles differ for subscription and gold open access articles:

Subscription Articles: If you are an author, please share a link to your article rather than the full-text. Millions of researchers have access to the formal publications on ScienceDirect, and so links will help your users to find, access, cite, and use the best available version. Theses and dissertations which contain embedded PJsAs as part of the formal submission can be posted publicly by the awarding institution with DOI links back to the formal publications on ScienceDirect.

If you are affiliated with a library that subscribes to ScienceDirect you have additional private sharing rights for others' research accessed under that agreement. This includes use for classroom teaching and internal training at the institution (including use in course packs and courseware programs), and inclusion of the article for grant funding purposes.

Gold Open Access Articles: May be shared according to the author-selected end-user license and should contain a [CrossMark logo](#), the end user license, and a DOI link to the formal publication on ScienceDirect.

Please refer to Elsevier's [posting policy](#) for further information.

18. **For book authors** the following clauses are applicable in addition to the above:

Authors are permitted to place a brief summary of their work online only. You are not allowed to download and post the published electronic version of your chapter, nor may you scan the printed edition to create an electronic version. **Posting to a repository:** Authors are permitted to post a summary of their chapter only in their institution's repository.

19. **Thesis/Dissertation:** If your license is for use in a thesis/dissertation your thesis may be submitted to your institution in either print or electronic form. Should your thesis be published commercially, please reapply for permission. These requirements include permission for the Library and Archives of Canada to supply single copies, on demand, of the complete thesis and include permission for Proquest/UMI to supply single copies, on demand, of the complete thesis. Should your thesis be published commercially, please reapply for permission. Theses and dissertations which contain embedded PJsAs as part of the formal submission can be posted publicly by the awarding institution with DOI links back to the formal publications on ScienceDirect.

Elsevier Open Access Terms and Conditions

You can publish open access with Elsevier in hundreds of open access journals or in nearly 2000 established subscription journals that support open access publishing. Permitted third party re-use of these open access articles is defined by the author's choice of Creative Commons user license. See our [open access license policy](#) for more information.

Terms & Conditions applicable to all Open Access articles published with Elsevier:

Any reuse of the article must not represent the author as endorsing the adaptation of the article nor should the article be modified in such a way as to damage the author's honour or reputation. If any changes have been made, such changes must be clearly indicated. The author(s) must be appropriately credited and we ask that you include the end user license and a DOI link to the formal publication on ScienceDirect.

If any part of the material to be used (for example, figures) has appeared in our publication with credit or acknowledgement to another source it is the responsibility of the user to ensure their reuse complies with the terms and conditions determined by the rights holder.

Additional Terms & Conditions applicable to each Creative Commons user license:

CC BY: The CC-BY license allows users to copy, to create extracts, abstracts and new works from the Article, to alter and revise the Article and to make commercial use of the Article (including reuse and/or resale of the Article by commercial entities), provided the user gives appropriate credit (with a link to the formal publication through the relevant DOI), provides a link to the license, indicates if changes were made and the licensor is not represented as endorsing the use made of the work. The full details of the license are available at <http://creativecommons.org/licenses/by/4.0>.

CC BY NC SA: The CC BY-NC-SA license allows users to copy, to create extracts, abstracts and new works from the Article, to alter and revise the Article, provided this is not done for commercial purposes, and that the user gives appropriate credit (with a link to the formal publication through the relevant DOI), provides a link to the license, indicates if changes were made and the licensor is not represented as endorsing the use made of the work. Further, any new works must be made available on the same conditions. The full details of the license are available at <http://creativecommons.org/licenses/by-nc-sa/4.0>.

CC BY NC ND: The CC BY-NC-ND license allows users to copy and distribute the Article, provided this is not done for commercial purposes and further does not permit distribution of the Article if it is changed or edited in any way, and provided the user gives appropriate credit (with a link to the formal publication through the relevant DOI), provides a link to the license, and that the licensor is not represented as endorsing the use made of the work. The full details of the license are available at <http://creativecommons.org/licenses/by-nc-nd/4.0>.

Any commercial reuse of Open Access articles published with a CC BY NC SA or CC BY NC ND license requires permission from Elsevier and will be subject to a fee.

Commercial reuse includes:

- Associating advertising with the full text of the Article
- Charging fees for document delivery or access
- Article aggregation
- Systematic distribution via e-mail lists or share buttons

Posting or linking by commercial companies for use by customers of those companies.

20. Other Conditions:

v1.9

Questions? customercare@copyright.com or +1-855-239-3415 (toll free in the US) or +1-978-646-2777.
